NORTHWESTERN UNIVERSITY

Experiment-based Simulations for Heterogeneous Hierarchical Materials: Application to Metal Additive Manufacturing

A DISSERTATION

SUBMITTED TO THE GRADUATE SCHOOL
IN PARTIAL FULFILLMENT OF THE REQUIREMENTS

for the degree

DOCTOR OF PHILOSOPHY

Field of Mechanical Engineering

By

Orion Landauer Kafka

EVANSTON, ILLINOIS

March 2020

ABSTRACT

Experiment-based Simulations for Heterogeneous Hierarchical Materials:

Application to Metal Additive Manufacturing

Orion Landauer Kafka

Modeling the mechanical performance of metal produced with additive manufacturing (AM) has proven to be a challenging task. In the as-built state, these materials have been shown to exhibit strong heterogeneity and anisotropy. Even after post-processing, such as heat treatment or hot isostatic pressing and depending on the alloy, some of these characteristics remain. Contemporary testing and modeling approaches are not particularly adept at identifying, capturing, or predicting these relatively complicated behaviors. This shortcoming in the currently available methods is particularly the case for fatigue and failure.

This dissertation begins by presenting an experimental exploration of AM materials, looking predominately at spatial heterogeneity and how that might relate to porosity generated during directed energy deposition (i.e. Laser Engineered Net Shaping) processing. The results from these, and related, experiments indicated that in order to explain and predict performance in fatigue and fracture, the two most important factors would likely be porosity (typically between 2 µm and several hundred microns equivalent diameter) and grains (typically columnar and varying from micron-size to millimeter-size).

In order to capture these effects well, a crystal plasticity finite element model was developed to explore the fatigue performance of Inconel 718/718+. This model provided some insight into the relative importance of grain orientations and potential impacts of unusually large grains. However,

the substantial computational expense involved made it difficult to explore effects of heterogeneity at a realistic scale (e.g. variations occurring over more than 10 times the average grain size). Further, although this type of model is useful for exploring materials, it is also too expensive to practically model part-scale systems of interest to practical users of AM.

Thus, the final two chapters will introduce and demonstrate two key developments. First, the combination of reduced order modeling methods with material models suited to the study of crystalline metals (the crystal plasticity law mentioned above) and its integration within a process-structure-properties-performance prediction framework for AM. Second, a one-way or two-way coupled concurrent multiscale model (depending on the requirements of the mechanics simulated) capable of capturing varying microstructures throughout a part-scale. In the case of AM, this variability is linked both to randomness and more importantly to processing conditions, and a change in processing conditions will change the distribution of, in this case, porosity represented by a database of experimental images at the microscale. This model is shown in both fatigue and fracture initiation prediction settings. No other system can currently produce comparable results, nor can any other approach with equivalent capabilities compete in terms of speed. As a design and optimization tool, this allows for consideration of not only minimum and/or mean properties, but also estimation of the spread of properties that can be expected and more importantly the local properties to any region or feature of interest. In terms of AM, this will allow for more generalized design, for example consideration of functional grading, realistic reinforcement to counter possible defects, and toolpaths to account for the specific impact such choices have on both local and overall performance.

Acknowledgments

First I would like to thank my parents, Thomas Kafka and Almy Landauer, and grandparents. My entire family has been amazingly supportive of my journey thus far. My brother, Alexander K. Landauer, a nearly-constant companion for our first 22 years, has also been fundamentally important to my ability to persevere. My research adviser, Professor Wing Kam Liu, also deserves mention in the opening sentences: without his guidance and willingness to allow me to craft my own direction none of the following chapters would exist.

I thank my committee members as well: Gregory Olson for his inspirational suggestions and helping set my direction, Gregory Wagner for more detail-oriented suggestions and critiques along the way, and Jian Cao for assistance in the experimental and manufacturing aspects of my research. I would also like to thank QuesTek Innovations for hosting me for an internship over the summer of 2018, most importantly Jiadong Gong my supervisor. My work there is responsible for most of Chapter 3.

I extend my gratitude to my many co-authors and co-workers over the years, starting with my undergraduate research adviser Kathleen Issen who saw my potential and began my training in research. John Moore, and Wentao Yan and Jacob Smith help me get started in crystal plasticity modeling and additive manufacturing respectively. I starting in the second year of my PhD I collaborated extensively with Cheng Yu, who shared with me many of his codes. Sarah Wolff helped me throughout the course of the experiments, and without her the work at Argonne National Laboratory would not have happened. Puikei Cheng helped design and conduct the experiments at Argonne and helped with some of the related data analysis. Wentao Yan and Stephen Lin taught me about process modeling for AM, and later on Zhengtao Gan as well. Kevontrez Jones helped me by providing process modeling as well, particularly later in my PhD. Yanping Lian helped with

process-structure modeling. Xianghui Xiao guided the work at beamline 2BM of the Advanced Photon Source and was an invaluable resource. Newell Moser, Miguel Bessa, Ying Li, and Wylie Stromberg were all mentors in various areas leading by example (or, sometime, counterexample). Unfortunately, I do not have space to list everyone; I am thankful of your help even if you name is not here.

I would also like to thank my all friends, those from my days homeschooling all the way to those I met while at Northwestern, alas too numerous to name (although you know who you are). Our gatherings, chance encounters, and day-to-day discussions have been enlightening, enriching, and empowering.

Finally, I am deeply grateful of the funding agencies and organizations that made my work possible throughout my PhD (although not all contributed to the project described in my thesis). I would like to acknowledge and thank them in chronological order as follows:

- Northwestern University: New PhD student Murphy Fellowship – Fall 2014, Winter 2015
- National Institute of Standards and Technology: Center for Hierarchical Materials Design (CHiMaD, Grant Nos. 70NANB13Hl94 and 70NANB14H012) – Spring 2015, Fall 2018
- National Science Foundation: Graduate Research Fellowship Program for three years under Grant No. DGE-1324585a, from Summer 2015 through Spring 2018
- Northwestern University: Crown Family Internship – Summer 2018
- Northwestern University: Murphy Professor Fellowship (W. Liu) – Winter, Spring, Summer 2019
- National Science Foundation: Data driven multiscale damage (Grant No. MOMS/CMMI-1762035 for which I co-wrote the grant proposal with Professor Liu's suggestions and advice) – Fall 2019

Sample preparation made use of the MatCI Facility, which receives support from the MRSEC Program (NSF DMR-1720139) of the Materials Research Center at Northwestern University. Sample preparation and testing at the APS was also in part paid for by the Digital Manufacturing and Design Innovation Institute (DMDII) through award number 15-07.

Preface

This dissertation is submitted in partial completion of the degree of Doctor of Philosophy in the field of Mechanical Engineering at Northwestern University. The majority of the dissertation represents publication-ready, but as yet unpublished, work. Specifically, Chapters 2 and 5 are mostly prepared but unpublished manuscripts, and Chapter 3 mostly consists of results from my internship at QuesTek (in report format). Some of this work also served as preliminary results for the NSF proposal that resulted in Grant No. MOMS/CMMI-1762035. Some portions of published articles central to the efforts outlined herein have a been included where necessary (part of Chapter 3, the majority of Chapter 4). The following articles were used are cited where appropriate:

- Orion L. Kafka, Cheng Yu, Modesar Shakoor, Zeliang Liu, Gregory J. Wagner, and Wing Kam Liu. Data-Driven Mechanistic Modeling of Influence of Microstructure on High-Cycle Fatigue Life of Nickel Titanium. *JOM*, 70(7):1154–1158, 2018.
- Zeliang Liu, Orion L. Kafka, Cheng Yu, and Wing Kam Liu. Data-Driven Self-consistent Clustering Analysis of Heterogeneous Materials with Crystal Plasticity, *Computational Methods in Applied Sciences*, volume 46. 2018. (Book Chapter) (Using only sections that I wrote or was a primary contributor on.)
- Wentao Yan*, Yanping Lian*, Cheng Yu*, Orion L. Kafka*, Zeliang Liu, Wing Kam Liu, and Gregory J. Wagner. An integrated process–structure–property modeling framework for additive manufacturing. *Computer Methods in Applied Mechanics and Engineering*, 339:184–204, 2018. *Equal contributions

My work has been highly collaborative and the results presented in some cases represent outcomes arrived at with the help of one or more of these collaborators. In these cases, I have made every attempt to identify in the text those persons who assisted in the acquisition of those results

or outcomes. If you are one of those collaborators and feel unfairly represented, either with an overage or underage of credit, please realize that I have made a sincere effort avoid that and I do apologize if I have not been successful.

Table of Contents

ABSTRACT 3

Acknowledgments 5

Preface 7

List of Figures 12

List of Tables 24

Chapter 1. Introduction 26

1.1. Vision and motivation 26

1.2. Fatigue in AM 30

1.3. Process-structure-properties modeling for AM 32

1.4. Objectives and roadmap 33

Chapter 2. Experimental characterization 35

2.1. Background and motivation 35

2.2. Initial DED material characterization efforts 36

2.3. XCT with in-situ mechanical testing 46

2.4. Results 59

2.5. Discussion 70

2.6. Summary and Conclusions 72

Chapter 3. Material modeling: crystal plasticity finite elements and fatigue calibration 76

3.1. Background and motivation 76

3.2. CPFE modeling for fatigue prediction of polycrystals 80

3.3. Computing N_{inc}: test-coupon-inspired geometry 90

3.4. Discussion of results 98

3.5. Summary and Conclusions 101

Chapter 4. Reduced order modeling for CP and application for integrated process-structure-properties-performance modeling 103

4.1. Background and motivation 103

4.2. Reduced order model for crystalline materials 104

4.3. Structure-properties modeling directly from modeling of AM processes 109

4.4. Integrated framework results 121

4.5. Summary and Conclusions 126

Chapter 5. Heterogeneous material representation with image-based two-scale modeling 128

5.1. Background and motivation 128

5.2. Methodology 129

5.3. Numerical demonstrations 141

5.4. Discussion 153

5.5. Conclusions and summary 156

Chapter 6. Conclusions and future work 157

6.1. Summary and conclusion 157

6.2. Ongoing projects and future work 159

References 165

Appendix A. Codes and scripts for post-processing 2BM data 178

A.1. Tomopy reconstruction script 178

A.2. Matlab image processing 190

A.3. DREAM3D porosity analysis pipeline 198

Appendix B. Experimental procedures 204

B.1. Sample preparation for in-situ tensile coupons 204

B.2. Procedures for in-situ testing at 2BM 205

Appendix C. Image-based multiscale code 214

C.1. Fatigue 214

List of Figures

1.1 Overall process-structure-properties-performance prediction schematic; the majority of the work described in this thesis fall into the box on the right 33

2.1 Schematic diagram showing the various sub-samples cut from each half-Charpy 37

2.2 LENS surface profiles: (a) surface roughness of with Alicona (2.162 mm by 2.851 mm patch) (b) Top-down view with SEM. (c) Alicona for small-scale roughness failures to capture reentrant features (0.284 mm by 0.215 mm) 38

2.3 Example XCT images of voids made with different processing conditions collected from the middle (M in Figure 2.1) of the three different half Charpy specimens with the same powder flow rate but different laser powers. (left) GED = 78.82 J/mm^2, (center) GED = 120.76 J/mm^2, (right) GED = 170.53 J/mm^2 40

2.4 Main effects plot and interaction plots for void count versus position, power, and travel speed; increasing laser power and decreasing travel speed tend to decrease the number of voids, while position is loosely related to number of voids but it depends on the laser power. The GED of each of these specimens is given in Table 2.1 41

2.5 (a) Volume distribution of voids in IN718; (b) distribution of C/A aspect ratio voids seem to either be flattened at about a 1/4 to 1/3 ratio or approaching roughly spherical, consistent with voids produced by different mechanisms: perhaps either lack of fusion or boiling . . . 42

2.6 Example grains in the 475 W, SS316L build in Table 2.1 as measured with x-ray diffraction at 34-IDE; (a) 3D view, showing grain configurations in the build, scan, and hatch direction, (b) slightly large “top down” view of the same specimen, showing “waviness” as a result of multiple tracks altering the preferred grain growth direction.. 44

2.7 (a) Inverse pole figure coloring (showing grain orientations) looking into the cross-section of a 32IDE build, the top surface is unpolished, and so shows roughness from the build. Grains seems to be oriented with [101] preference, but only slightly (if at all) tilted in the scan direction, contrary to what was observed in Figure 2.6. (b) In-to-the-depth scan at 80 Z-height in (a) looking at a plane "top down" from the build configuration. No strong pattern is observed, which match the similar observation in Figure 2.6. (c) Residual strains, plotted as a scaled difference from the expected d-spacing, red is more tensile and blue is more compressive. Some tensile hotspots (potentially dangerous) and substantial variations are observed 45

2.8 (a) Grains in a build with higher laser power, but otherwise similar conditions, than in Figure 2.7. (b) Residual strains, again colored using scaled difference from the expected d-sapcing. Generally similar patterns are observed with Figure 2.7 45

2.9 A photography of two of the thin walls (Wall 3 (left) and Wall 2 (right)) that were then cut up to make miniature tensile coupons. Note there are noticeable geometry inaccuracies, even from this perspective. 48

2.10 Coupon locations in each thin wall build. 50

2.11 Relative locations and orientations of tensile specimens. Green are vertical (long axis aligned with the build direction), and purple are horizontal (long axis along the scan direction). . . . 50

2.12 Details of nominal miniature specimen geometry, dimensions in mm 51

2.13 Labeled specimens in their respective thin wall slices prior to testing 51

2.14 EBSD image of grains in IN718, near one of the tensile coupons; columnar structure with preferential orientation. Image collected by Zilin Jiang 53

2.15 X-ray micro-Laue diffraction (34IDE) images of the top corner of the no-dwell and one-minute dwell builds. Colored using the same IPF legend as Figure 2.6 54

2.16 Number of voids versus location in the XCT image with respect to the material manufacturing coordinates for specimens (a) H3-2 (b) V3-4, two characteristic examples. Note that some large spikes on the edges are likely edge effects (perhaps artificial, even), so should be interpreted differently than bulk porosity. 55

2.17 Crosshead displacement versus time for specimen V3-4, as an example of the "start-stop" or interrupted in-situ loading pattern 56

2.18 Schematic diagram (not to scale, top down view), of the specimen location with respect to the DIC camera and x-ray beam.. 58

2.19 Stress-strain curves for (a) continuous testing of processing condition 1, (b) stop-start testing of processing condition 2, (c) stop-start of processing condition 3 60

2.20 Stress-strain curves for (a) continuous testing horizontal specimens in processing condition 1 (10 specimens), (b) stop-start testing horizontal specimens in processing condition 2 (3 specimens), (c) stop-start testing of horizontal specimens in processing condition 3 (four specimens), (d) continuous testing vertical specimens in processing condition 1 (10 specimens), (e) stop-start testing vertical specimens in processing condition 2 (3 specimens), (f) stop-start testing vertical specimens in processing condition 3 (4 specimens). Min/max as well as one standard deviation are shown for each.. 60

2.21 Maximum elongation for (a) processing condition 1, (b) processing condition 2, (c) processing condition 3. Data points represent real data (jittered for visibility). Note that only processing conditions 2 and 3 can be compared with each other, because the both are based on stop-start testing, whereas processing conditions 1 was not. The red line is the mean, the salmon region is one standard deviation, the blue region is a 95% confidence interval and the whiskers plot outliers.. 61

2.22 A similar boxplot to Figure 2.21, this time showing elastic modulus for (a) processing condition 1, (b) processing condition 2, (c) processing condition 3. Because modulus was measured before any of the stops, these all can be compared fairly. 62

2.23 Young's modulus, yield strength, and ultimate tensile strength versus location for horizontal specimens, wall 1 63

2.24 Young's modulus, yield strength, and ultimate tensile strength versus location for vertical specimens, wall 1 63

2.25 Thermal FE model of the thin wall build, showing solidification cooling rate (with GAMMA [**115**]); more details of the thermal modeling, which was conducted by Kevontrez Jones, are given in Chapter 5 64

2.26 Stress-strain plot of four in-situ test specimens at the same location (4) in vertical and horizontal configuration (V vs H) and walls 2 and 3 (V3-4 is a vertical specimen in wall 3 at position 4). For reference they are compared to the behavior of an annealed, wrought Inconel 718 specimen tested on the same equipment with the same specimen geometry (black line). 65

2.27 Initial configuration of voids in the for specimens highlighted in Figure 2.26 (reproduced here at lower resolution than was measured and used in analysis, so smaller voids are missing) 66

2.28 Two deformed configurations for specimens V3-4 and H2-4, one at the onset of plasticity (left side) and the other at the final scan before failure (as indicated on the stress-strain curve in Figure 2.26 by the last drop in stress before failure). The large blue bands are the encroaching edges of the specimen as it thins during deformation. Notice that in the vertical configuration, where more elongation occurs, the voids have deformed substantially before failure but in the horizontal case similar void evolution has not occurred.. 67

2.29 Combined macroscopic and microscopic measures of deformation (strain) for V3-4: stress-strain curve with numbers indicating where the correspondingly numbered surface strain maps from DIC and XCT scans. The top edge of each CT scan is about 0.15 mm from the end of the upper fillet. 68

2.30 Images of a single, large void deforming in specimen H1-8, along with the overall engineering stress state at which the respective images were taken; the void elongates along the loading direction and new voids (either grown above the observation threshold or newly nucleated) appear. In this case we were lucky enough to capture a void in the primary deformation zone 69

2.31 Stress versus time (which shows the hold periods), with the points at which the single-void deformation images shown in Figure 2.30 were taken circled 70

2.32 Optical microscope image of a fracture surface of specimen V3-4 71

2.33 XCT scan of the two opposing fracture surfaces of specimen V3-4; left is the bottom, right is the top; scans show the classic "cup-and-cone" failure pattern indicative of ductile rupture in fcc metals. 71

3.1 Undeformed configuration for on instantiation of the calibration volume. This has 64 cubic grains with random ψ, θ, and ϕ Euler angles, arranged in a cube. Colored by ϕ, so different colors are different grains (although some grains have similar ϕ). 82

3.2 Deformed configuration of calibration volume subjected to uniaxial tension in the vertical direction (applied with symmetry boundary conditions and a prescribed vertical (Y) displacement for the top surface), colored by (a) von Mises stress (b) effective plastic strain. Deformation is scaled to be clearly apparent. 83

3.3 Calibrated overall RVE response with CP (dashed) and "average" experimental tension test results (solid) from heat treated AM IN718+ (two different powder lots; data from Honeywell) 83

3.4 (a) Cyclic stress strain response of simulated (blue) and measured (black) IN718+. (b) detail showing match at minimum stress; (c) match at peak stress. This is for stress ratio $R = -1$, strain amplitude 0.3%, 0.33 Hz, cycles 1 to 30,000, periodically plotted for the experiments (once loop every 3,000 cycles), and the first 4 cycles from the simulation. These results show good similarity between the model and experiment within this strain range for the CP law calibrated to tensile results 85

3.5 (left) raw FIP and (right) volume averaged FIP at 0.3% strain amplitude for the reference RVE. Locally, FIP values vary because some local plasticity occurs (e.g. in grains oriented to be "soft" with respect to the direction of load), even when overall loading does not show hysteresis or a bulk plastic response. 86

3.6 All collected HCF data from literature (green points), and fitted stress-life curves for all data (black curve) and data points grouped by experiment (gray curve) plotted on log-x axes 88

3.7 Stress-life curve similar to Figure 3.6, now with censored (run-out removed) data 89

3.8 FIP predictions versus statistical model of fatigue life, used for calibrating the FIP parameters. The FIP points shown minimize the cost function in Eq. (3.15). A perfect fit would overlay the blue crosses and red dots. Because this FIP is designed for HCF, it seems reasonable that for lower number of cycles the fit is mismatched (i.e. low-cycle mechanisms are not captured) 91

3.9 SEM images of an example failure surface for IN718 printed with DMLS and machined into a test coupon under cyclic loading. In this case, strain amplitude was 0.218%, testing was at 426.7 °C, and failure measured by a 50% drop in stress occurred at 100,186 cycles. Failure seems to be due to intergranular separation or cleavage (the large planar feature near the initation point by be a grain boundary that has separated) 92

3.10 A 3D perspective of the failure surface shown in Figure 3.9 93

3.11 Quarter-cylinder model with one large grain. (a) colors represent different grain orientations (random orientations and colors) (b) meshed volume.. 93

3.12 FIP contours at three strain amplitude (columns) and for two different materials calibrations (rows). (The color legends are hard to see here: lighter implies greater fatigue risk or lower estimated N_{inc}). 94

3.13 Strain-life curve for the reference statistical model (solid blue line) and the FIP predictions (points) at several strain amplitudes and for three different material instantiations with random grain orientations. 94

3.14 Side-by-side comparisons: (1) green dots instan 1/2/3 are different specified orientations of the large grain (instan 1 = 90,45,0; instan 2 = 0,45,0; instan 3 = 0,0,0) with the same orientations for all other grains as in instan 1 of Figure 3.13; (2) brown dots the same, but with instan 3 of Figure 3.13 for all other grains instead of instan 1; (3) red dots are reproduced from Figure 3.13 95

3.15 (a) Example microstructure with approximately equiaxial grains, colored by magnitude of the ψ Euler angle, and (b) the mesh for this microstructure 96

3.16 Contours of filtered FIP for two different sets of random orientations (instantiations 2 and 3 below) 96

3.17 Strain-life comparison of meshes with equiaxial grains (brown hues) and a longer grain (green hues). This replots data from Figure 3.13 97

3.18 (left) Scatter of plot of equiaxial and large grain meshes for 15 different instantiations each at 0.25% strain amplitude (right) box-and-whisker plot showing a difference in mean and variance/outliers between the cases 97

3.19 Example of voids measured with XCT at 2BM. Specimen B-1-6; demarcations at 435 µm increments 99

3.20 Ellipsoid generated from the mean size and aspect ratios found with XCT 99

3.21 Cylinder model with mesh outlined and coloring by grain orientation vector magnitude (to show different grains). An ellipsoid with mean aspect ratio and 95^{th} percentile size has been removed from the center of the cylinder (centered due to the symmetry boundaries on the top and flat sides). 100

3.22 Filtered FIP field for the cylinder with a void. For this geometry, the model predicts the void as the most potent fatigue nucleation cite. 100

3.23 Strain-life plot for polycrystalline microstructure with a void. 101

4.1 A schematic showing the essential components of the SCA method for predicting fatigue using CP like the FE method did in Chapter 3. The figures here show a demonstrative RVE from a parametric study of inclusions and voids in NiTi, with half of the matrix phase shown and the inclusion and void phases hidden. This is a tidier and easier to understand example than the AM images provide. From Kafka et al. [**54**]. 107

4.2 Three-by-three diagram showing heightened FIP surrounding voids in polycrystalline volumes. Each of the three different voids cases at different power levels were modeled with three different instantiations of grains 108

4.3 Maximum averaged FIP within one grain in each of the void and grain cases. Larger voids in the 475 W case then to increase the measured FIP, but grains have a very noticeable impact as well. The interplay between the voids and grain imply that in some cases (e.g. 645 W, realization 1 versus 875 W, realization 2) voids one would expect to produce a higher FIP are entirely mitigated by the grain configuration 109

4.4 A single void deforming in a single crystal. The two rows show "side" and "top" views, with each sub-row showing the comparison of measurement (red) and model (pink). The single crystal orientation in the model was selected to optimize the similarity with fixed material properties 110

4.5 Schematic diagram of the module-hub framework conceptual layout, with images of our current implementation demonstrating the modules: a SEBM process with microstructure-based fatigue life assessment. The data used by the framework at each point in space is described by spatial coordinates and any relevant field data for the current working modules, as shown graphically by a schematic of a representative voxel. The cellular automaton model is shaded gray to indicate that results both with and without it are given, to demonstrate the flexibility of the framework. 112

4.6 A schematic of the flat file database used to store record data for the proposed framework. The fields are abbreviated to more clearly show the structure of the database. 113

4.7 (a) a 2D section of the CA result with the relative locations of four cubic VOIs at different locations through the height of a two-layer build (color coded green, purple, and black to upper, middle, and lower) and one near the intersection of two tracks of the same build (red; for FIP with/without void). The white dashed lines show approximate melt region boundaries for each layer. (b) these VOIs in 3D with the surrounding material removed. (c) the single crystal voxel mesh used for FIP prediction. (d) clustering used for the single crystal, with a void (white) case. (e) the clusters used for the polycrystal case. (f) the clusters used for the polycrystal with void case. 123

4.8 Stress-strain curves predicted by SCA with CP at the strain rate of 10^{-4} s^{-1}. (a) for the upper VOI showing the anisotropy of overall response, for all VOIs. The response for each VOI is given for x-direction loading (b), y-direction loading (c) and z-direction loading (d). 124

4.9 Experimental strain life data (points) for HCF replotted from [**48**], and four predictions of fatigue life at two strain amplitudes each: (1) a single crystal without any defects (baseline data), (2) a single crystal with a void predicted with the thermal-CFD model and (3) the full polycrystalline fatigue VOI shown in Figure 4.7 (4) this same growth pattern, including a void. 126

5.1 Overall diagram of the computational scheme. Geometry, build process parameters, material, and loading conditions must be specified. These are used to conduct a thermal analysis and a macroscale stress analysis. For each material point X within these two models, an element-wise sub-model is constructed to represent a possible state at that point. This uses local thermal history and strain history to determine the microstructure (void geometry) and deformation history. These are used to predict the microscale evolution of state variables such as plasticity and damage, which are homogenized (e.g. by taking the l_∞ norm of the domain) and used as element-wise estimators of part-level susceptibility to failure. . . 131

5.2 Diagram of the defect estimation and database building process. In the first part, a relationship between solidification cooling rate (SCR) and void volume fraction (V_f) is determined using process modeling and X-ray computed tomography. Second, 2(a) the subsets of the images acquired with X-ray tomography are selected based on V_f, such that the expected range of V_f for any arbitrary part (with known or predicted thermal history) is spanned. 2(b) A database of these possible microstructures is generated, 2(c) including computing the training stage of the mechanical model. 135

5.3 For each macroscale material point (in this case, within the dogbone specimen use in the numerical example in Section 5.3), the thermal history and strain history are passed to a microscale solver; a microstructure is selected from the database developed in Section 5.2.3.1 based on the thermal history, and deformation boundary conditions are applied according to the strain history. A crystal-plasticity-based microscale solution is computed, and a homogenized response (e.g. the l_∞-norm of the fatigue indicating parameter, if a fatigue problem is chosen) is returned to the macroscale. 138

5.4 (a) example component geometry specification (ASTM E606 fatigue specimen) (b) the two meshes and (c) details of the specimen meshes, including the difference between stress (left) and thermal (right) meshes.. 143

5.5 The continuous radius fatigue test specimen, showing the thermal processing prediction partway through the build. The peak temperature and temperatures gradients appear physically reasonable. 144

5.6 Estimated fatigue lives for multiple realizations of the fatigue coupon, run at different applied strain amplitudes, mimicking theoretical experimental conditions. Two different processing conditions (conditions 1 and 2 in Tab. 5.2) were modeled.. 146

5.7 Contour plots for each of the points shown in the fatigue-life diagram, showing distributions of estimated fatigue life 147

5.8 Compact tension example: (a) mesh, pin loading from rigid pins excluded from this visualization (b) solidification cooling rate prediction 150

5.9 Contour plots of (a) number of voids in the microscale for each element, (b) average void size for within the microscale, (c) minimum nearest neighbor distance, (d) average nearest neighbor distance (a value of zero in (c) and (d) indicates only one void is present); (e) histogram of minimum nearest neighbor distance, (f) histogram of average nearest neighbor distance. 151

5.10 (a-e) PK1 YY (or 1 in Voigt notation) stress contours of the microscales at the elements highlighted in (g); note that some voids interact and cause larger failed zones or increase stresses; (f) contours of stress in the YY direction after fracture has begun, note "failed" elements with decreased stresses at crack tip; (g) heat map showing the prevalence of failure, the color shows the number of clusters failed at the microscale, 0 = no failures, 20 = completely failed. 152

5.11 Contours of YY stress plotted for (a) Instance 1 of the fracture specimen; (b) Instance 2 of the fracture specimen. As with the fatigue example, (slightly) different local patterns of failure are caused by different microstructures selected based on thermal conditions. Failed elements are outlined heavily. Note that failure is not necessarily in the highest stress elements, because of the triaxiality/Lode angle failure criterion used on the microscale . . 153

6.1 Design constraint: in-situ blocking angle. 161

6.2 Contours of applied force on the voltage versus frequency plot show the physical limitation of the actuator itself. 161

6.3 Design constraint: cyclic frequency versus force apply for the piezo-actuator 162

6.4 (a) Draft drawing of the fatigue test coupon to be used; dimensions are in inches, tolerances are generally ± 0.0002 inches unless otherwise marked. Roughly a miniaturized ASTM E606 standard test geometry. (b) A machined test coupon 163

6.5 Drawings of the fatigue test machine as built; digital 3D embodiment by Fengchun Li. . . 164

List of Tables

2.1 Build conditions and some physical measurements of the half-Charpy specimens sectioned for imaging at 2BM; data from NIU 37

2.2 List of voids sizes in IN718 from Honeywell, as detected by XCT at 2BM (note that median equals 50th percentile) 42

2.3 Nominal composition of IN718, wt% 47

2.4 Optical and VIC2D DIC settings used to compute surface displacements 57

2.5 Summary of the key experimental findings 74

3.1 The 12 active FCC slip systems considered by the CP constitutive law. 81

3.2 Constitutive parameters for the CP material law, fit to room temperature tensile data for fully heat treated AM IN718+ using a 64 grain SVE approach 82

3.3 Coffin-Manson type fit parameters for uncensored and censored literature data for IN718 . 87

3.4 Calibrated FIP parameters 90

4.1 Input and output for powder spreading model 116

4.2 Build parameters for cases 1 and 2 117

4.3 Input and output for thermal-CFD model 117

4.4 Input and output for grain growth model 117

4.5 Input and output for mechanical response model 119

4.6 Calibrated elastic and plastic crystal plasticity parameters for primary α phase. Parameters with a * are from [**123**]. Others are selected to match experimental results 119

4.7 Offline and online model parameters 120

4.8 Input and output for fatigue prediction 121

5.1 Thermo-physical properties of IN718 [**88**] 142

5.2 Set of process parameters for thermal analysis of IN718 142

5.3 Primary crystal plasticity model parameters 144

CHAPTER 1

Introduction

1.1. Vision and motivation

In general, the mechanical performance of structural and functional materials has increased over time. Commensurately, the complexity of the materials and the systems with which they interface – from initial conception to final disposal – has risen. This parallels the increase in knowledge of the materials and systems and an ability to predict the behavior of these systems. In order to make accurate and efficient predictions of material behavior, two primary criteria are customary: (1) fundamental understanding of the governing equations is required and (2) a solution method that captures the relevant mechanics of materials science. New materials and new manufacturing methods introduce variables that must be understood and either considered or discarded based on sound reasoning in either case. If new variables are to be considered, this must be done in as efficacious a manner as possible to enable expeditious development and deployment. The preceding generalities might be evident, but the specific steps required in any given instance less so.

Metal-based Additive Manufacturing (AM) is an emerging and potentially transformative technology. There are many classes of advanced manufacturing techniques called AM, with different material delivery strategies (e.g. powder bed, powder deposition, wirefeed) and energy sources (e.g. laser, electron beam). Direct material deposition (DMD), Laser Powder Deposition (LPD), Laser Engineered Net Shaping (LENS) methods use a co-focal laser heat source and powder delivery nozzle to deliver material to a molten pool. An inert gas is typically used for shielding and powder delivery. Repeated transversal of the nozzle over a substrate or previously deposited material builds material layer-by-layer to produce a free-form geometry in a pattern specified by a 3D model file. This approach removes the need for special tooling, allowing for rapid and agile product realization by simplifying tooling and assembly. The DMD process in particular provides relatively large

working volume and can be used for repair and modification of existing components, in addition to whole part fabrication.

Such capabilities are appealing in a wide range of applications, with the most impact where the need for topological, part, and system design freedom outweighs the need for bulk production speed. This is of interest in many fields, including the transportation, aerospace, military, and biomedical sectors. For example, the ability to rapidly fabricate individualized, complex devices can improve clinical outcomes and reduce overall cost [**18**]. Ventola *et al.* [**125**] concluded that there is much promise in AM for medical applications, but it still requires improvement to become widely viable. AM has been used to fabricate customized parts (size, shape, mechanical properties): orthopedic prostheses and implants e.g. [**16**]. Most medical applications of metal AM have used powder bed techniques, for example for implants [**50, 106**] or orthopedic replacements [**18, 49, 81, 86**]. However, the LENS process has also been shown to be effective in producing biocompatible structures, e.g. with NiTi and titanium [**114**]. Designed local material microstructure and composition is another exciting possibility for AM. Finally, AM can fabricate materials with complex nano- or meso-scale geometry (so-called "architectured material"), which can enhance macroscale behavior or enable functional materials, e.g. [**128, 43, 145**].

Current literature largely agrees that existing test standards and prediction methods, particularly for fatigue and failure, often are inappropriate for AM materials, e.g. [**9**]. There is controversy over the effects of surface roughness, residual stresses, and defects in AM parts and the usefulness of various patches or remedies that have been suggested; fundamentally, a lack of mechanistic understanding of material response prohibits further developments. A deeper understanding of the material built with AM is needed to construct tools that predict the impact of systemic and stochastic deviations on the performance of AM components. The lack of such tools is inhibiting the growth of AM technologies in the sectors where they might make the most difference [**21, 34, 109**]. It also makes standardization and qualification a challenge, particularly in environments where failure is costly and/or dangerous [**34**].

Existing limitations of AM are primarily related to (1) build quality of the material, most notably pores, inclusions, and surface finish e.g [**10, 20**], (2) lack of sufficient thermal control and measurement capabilities for bulk and localized material during processing e.g. [**57**], and (3) scalability to mass production. Prior efforts to quantify material performance in AM have often relied upon full-scale mechanical test coupons and largely either bulk, homogenized descriptions (e.g. relative density) or 2D material micrographs of inherently inhomogeneous 3D features. The assumptions built into these bulk material measures or tests that rely on homogeneous properties or features are often inappropriate for the complicated material that results from the complex processing history typical of AM material. The AM process, i.e. material atomization followed by track-by-track (re-)melting with many localized reheating cycles, introduces a more complicated, multifaceted thermal and material processing history than is seen in conventional (i.e. casting or subtractive manufacturing) processes. This complicated material history leads to difficulty in understanding microstructures and defects that might occur (e.g. local composition variation, voids, "unusual" grains and/or phases), which in turn makes estimating mechanical properties difficult, and leads to a general lack of mechanical performance quantification and thorough computational modeling. This, in turn, hampers the efficacy and impact of AM within engineering communities. This host of factors drives a strong need for accurate, mechanistically driven simulation of component performance, e.g. as suggested by [**65, 69, 116, 133, 144**].

Despite the challenges, or perhaps because of them, understanding of the mechanical properties of AM metals has advanced in the past few years. Many of these advances have been experimental (e.g. [**27, 55, 129, 132, 117**]), and predictions of the properties of AM materials such as Ti-6Al-4V, SS316L, and Ni-based superalloys have been reported [**119, 134, 135**]. One common factor, resulting from the manufacturing process itself, is that the material may widely vary point-to-point within a single component, between builds with the same conditions and parameters, and for builds with different parameters. The challenges to modeling associated with these various sources of variability have been noted, e.g. by [**95**]. Experimental efforts have noted this variability, too; for example, Gong et al. and Sheridan et al. [**31, 113**] show significant variance between builds

with different parameters and within builds with the same parameters, highlighting the importance of processing parameters, but also process-induced randomness. This kind of variability and randomness, particularly where defects are concerned, results in heterogeneous material for which standard testing, prediction, and validation methods may be ill-suited [**65**] or lead to potentially inaccurate conclusions.

These difficulties span multiple length scales. Just as parts or sub-scale coupons are heterogeneous and random, the geometric and orientation factors of grains vary with processing conditions, location, size of the overall build, size of the specific feature, feed material (even between lots or manufacturers of the same nominal composition material), powder size, and a host of other factors; e.g. Antonysamy et al. [**4**] show varying grain structure based on the grains in precursor particles. Because the process has vastly different thermal history (e.g. peak temperatures and solidification rates) than other, more conventional, material processing routes (e.g. casting, forging), different precipitates or secondary phases might occur which influence mechanical performance. In some cases this can be beneficial, e.g. [**136**], and in others detrimental, e.g. [**63**].

Multiscale modeling is one approach that might be able to capture the heterogeneous, non-uniform material responses. For example, Horstemeyer [**45**] provides a case of fatigue modeling in heterogeneous materials made by casting using a hierarchical multiscale and the multi-stage fatigue model developed by McDowell et al. [**82**]. More recent works, such as those by Yan, Lian, Yu, Kafka et al. [**141**] (discussed in some detail in Chapter 3) and Herroitt et al. [**42**] have focused on applying models throughout the processing and subsequent service life for additive manufacturing to relate processing, structure, and performance. Although not multiscale themselves, these works suggest the complexity involved with these processes and the level of detail that might be required to understand them.

However, the common assumptions and methods used for multiscale or microstructure-sensitive modeling of materials are often not appropriate for capturing the performance of additively manufactured (AM) metal, because of the variability and other factors described above. Current approaches often rely upon a representative volume element (RVE) or some other form of representative structure (e.g. a representative unit cell or other simple, often periodic, structure); prediction of response with these structures might also be predicated upon simplifying assumptions, such as idealization of the microstructure (e.g. as an ellipsoid), periodicity, or statistical (spatial) uniformity. Models that predict minimum performance or capture worst-case scenarios often struggle to make predictions that are quantitatively useful in process design - one of the main goals of structure-properties-performance modeling. These difficulties relate to an underlying challenge with AM: the localized process produces a mix of process-dependent and random microstructures. These depend on time- and length-scales related to the melt pool (typically sub-second, sub-millimeter) and have an impact across the time and space of the full build (often hours and tens of centimeters).

1.2. Fatigue in AM

A reduction in fatigue life is often observed for AM parts, as well as an increase in scatter, compared to conventionally processed materials, e.g. [**32, 105, 118**]. Both these effects are at least in part due to the occurrence of residual stresses, possible deleterious phases (e.g. α'-phase in Ti-6Al-4V, depending on heat treatment) or morphologies, voids, surface roughness, and very large grains depending on the regime of fatigue (high or low cycle) [**9**]. There is a competition between voids/interior defects and surface defects, as noted by e.g. [**65**], particularly important in high cycle fatigue (HCF). Beretta and Romano [**9**] provide a relatively thorough dissection of the differences in fatigue behavior between AM and conventionally processed materials, focusing on Al-Si-10Mg and Ti-6Al-4V. Two important takeaways are that (1) post-processing heat treatments can change grain sizes which impacts fatigue life, and (2) AM fatigue properties are governed by defects - in the absence of these defects AM material can be as strong or stronger than traditionally processed material. The first point tells us that a CP model will be important to understand, and

predict, fatigue. The second gives us some hope that designers could use predictive tools to increase performance of AM materials.

There are several techniques to measure as-built AM surfaces, which if they exist tend to dominate fatigue life. Sectioning and SEM is often used as a reference to measure surfaces, but it destroys the sample. To avoid this, Senin et al. [**110**], for instance, assessed surface profiles for LPBF measured with X-ray computed tomography (XCT). To quantify surface effects in more conventionally processed materials Hallberg et al. [**38**] used electron backscatter diffraction (EBSD) measurements of crystallography to construct 2D axisymmetic CP models. They then used these CP models to study grain morphology effects. They concluded that a CP model is required to obtain sufficient accuracy to predict fatigue, especially if there exist non-equiaxed (columnar) grains, which are also common in as-built AM materials. Studies also have considered mechanical performance of as-built, heat-treated, polished, or post-processed materials and the potential impact of surface roughness, e.g. [**20, 132**].

In AM components that have undergone surface processing, bulk failures seem to dominate fatigue life especially in the high cycle regime [**132**]. Hot isostatic pressing (HIP) has been used to reduce the size of interior defects, which can improve fatigue life [**65**]. Fatigue cracks have been seen experimentally to initiate at defects (typically voids), but also inter-granularly. In AM material, for example Ti-6Al-4V made with LPBF, grain morphology might depend on build parameters, as well as the prior grains in powder and substrate; for example, Antonysamy et al. [**4**] show epitaxial grain growth from a partially-melted particle. AM materials also typically express strong anisotropy both in monotonic and fatigue loading, as shown by experimental studies that quantify the performance of popular alloys and AM technologies.

Attempts to model and predict fatigue in AM have included, e.g., the $\sqrt{\text{area}}$ method [**65**], stress-concentration methods [**99**], or various different fatigue indicator parameters (FIP) [**134**]. In order for AM materials to be applied in critical or load-bearing capacities, e.g. as structural components in aircraft where the possibilities for light-weighting provide a strong motivation, an effective lifetime performance model is required [**34**].

1.3. Process-structure-properties modeling for AM

Many models have been developed to understand AM holistically from various perspectives including temperature field [**47, 103, 140**], molten pool flow [**59, 62, 101, 138**], residual stress [**29, 41, 44, 97**] and mechanical properties [**40, 65**]. However, most models in the current literature are not connected, at least not directly, making comprehensive process-structure-property (PSP) relationships difficult to capture. Recent reviews and opinion papers, e.g. [**80, 108**], have called for the integration of process-structure and structure-property-performance tools for predictive computational modeling to further enable AM. By providing predictive models that mimic the stages of production and use of a part, these tools could allow for higher confidence in AM parts and an integration of part and process design to maximize the potential of AM. Francois *et al.* [**24**] demonstrate a number of recent advances in modeling for process to structure, structure to properties, and properties to part performance. However, they do not propose a means of connecting these tools. Indeed, they state that such a combination would benefit the AM community. Collins *et al.* present a predominantly continuum scale process-structure-properties integration for a Titanium alloy [**17**]. Only the macroscale is considered, which may be insufficient to assess damage or failure. Moreover, no generalized structure or framework is provided, resulting in limited applicability outside of the specific simulations presented [**17**]. Recent perspectives articles on which I am a co-author, e.g. [**116, 141, 142**], have included statements to similar effect, and with a similar shortcoming: lack of the demonstration of a definitive framework and implementation.

Although modeling process-structure relationship is not a focus of this dissertation, it is such an important feature of the larger landscape in AM some mention must be included. Indeed, many of the key scientific and engineering challenges in AM reside in the mechanics of the processes itself. Thus, although the focus here is on models that link structure to properties, the precursor to structure must also be taken into consideration. In the efforts described in Chapter 4, this progression of process-structure-properties is indeed central in that one of the core ideas is to develop structure-properties methods that can account of the various structures predicted by process modeling. This broader perspective on process-structure-properties-performance modeling is shown in Figure 1.1.

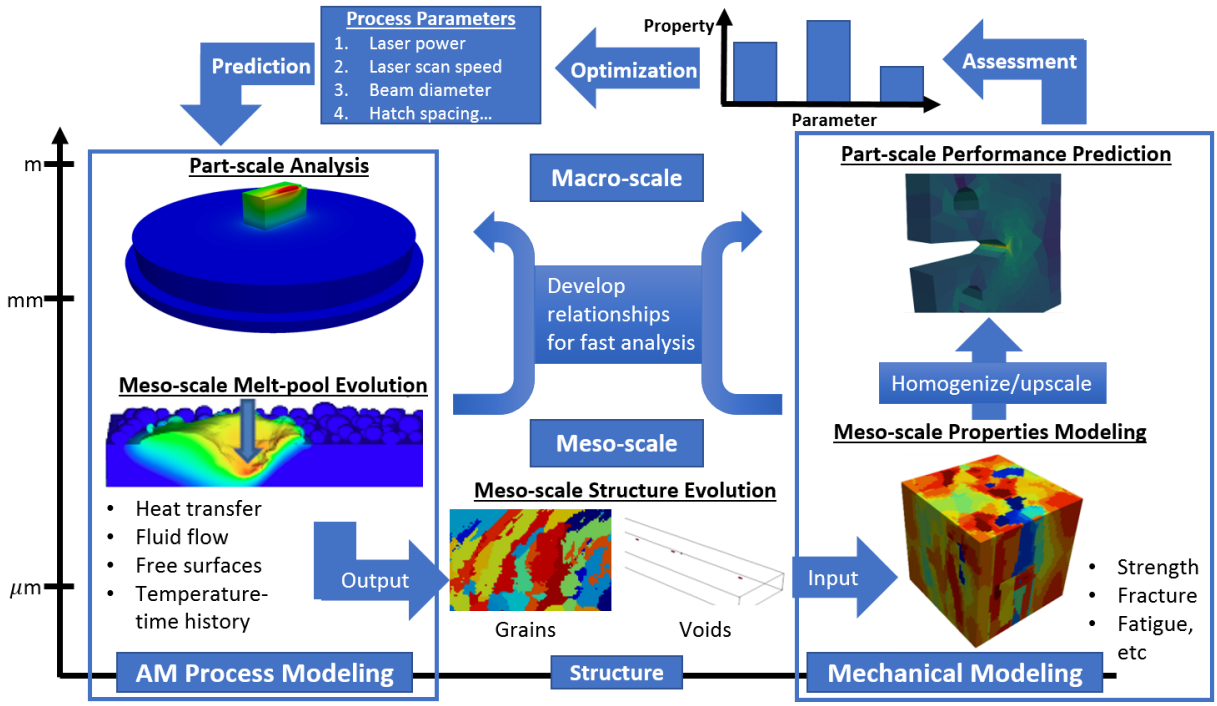

Figure 1.1. Overall process-structure-properties-performance prediction schematic; the majority of the work described in this thesis fall into the box on the right

1.4. Objectives and roadmap

The goal of this dissertation is to present a series of efforts related to first understanding, and second modeling the microstructures and mechanical responses of that arise in additively manufactured metal. In so doing, a new mechanical modeling method will be developed that captures the heterogeneous mechanical response by using specifically selected experimental images.

Chapter 2 will show experimental characterization efforts, including most notably in-situ x-ray observation of the deformation of AM materials with significant void populations. Chapter 3 introduces various modeling techniques to be used and initial calibration and validation work with those techniques. Chapters 4 and 5 will illustrate the design and development of several new modeling methods, using work in Chapters 2 and 3 as building blocks. These new methods are bespoke and designed to capture the unique aspects of AM metals and more generally heterogeneous metallic systems. Developing these models supports new material system design and engineering tasks. Chapters 4 and 5 build on the experimental results of the Chapter 2, including the use

of x-ray images the basis for a multiscale model. Finally, Chapter 6 will present ongoing efforts towards novel experimental and modeling techniques, concluding with a section for summary and future prospects.

CHAPTER 2

Experimental characterization

2.1. Background and motivation

Many AM technologies exist, and each has slightly different impacts upon the material and associated challenges. The majority of the work presented here will relate specifically to the Laser Engineered Net Shaping (LENS) process. LENS is part of the class of directed energy deposition (DED) AM techniques where powder is delivered with a shielding gas to a molten pool created by a laser. This offers more flexibility than powder-bed type AM, but the LENS process is more stochastic. Previous studies have identified significant anisotropy in as-built and stress-relieved LENS components, e.g. [**130**]. Many of the general ideas presented here are applicable to more than one type of AM process, although the data upon which most of this work is based comes from LENS material.

This chapter has three main goals. First, I will to use advanced material characterization techniques to develop an understanding of the complex, 3D microstructures that arise in AM materials. This involves using synchrotron x-ray based methods (as well as more conventional tools) to create 3D images of various microstructural features and quantification of these 3D images. Second, this characterization is conducted to facilitate modeling that is based directly or indirectly upon the experimental results. The goal here is to inform our various modeling methods with experimental data as much as possible, with the goal of developing robust "image-based" capabilities. Third, I will better understand the mechanical behavior of AM material, particularly as it relates to processing conditions or, more generally, observed characteristics of the material through experimental measurement. For instance, we know that variations in performance are typically induced by the periodic local material melting and re-solidification process, but we do not know the extent of these variations or how to control the process to minimize them. In some cases, homogeneous properties

are even (usually incorrectly) use to represent the material at the part, or continuum, scale. Specifically, I will show an experimental study that emphasizes the lack of homogeneous and isotopic behavior on the continuum scale.

The highlights of this chapter are:

- Microstructural and mechanical characterization of heterogeneous metal built with AM
- Deformation of voids observed in-situ with X-ray tomography, which provides physical insight and allows for direct validation of simulation predictions of void deformations
- Database of void images constructed to use as input for future models

2.2. Initial DED material characterization efforts

2.2.1. Materials

In an initial preliminary study, test coupons of SS316L was exhumed from several different approximately 15 mm×15 mm×15 mm "half Charpy" builds with varying processing parameters. The experimental conditions and some materials information for each of these builds are given in Table 2.1. These specimens were sectioned using a high speed metallurgical saw (kerf about 0.5 mm) into the 13 different bars shown in Figure 2.1. These were nominally 2.0 mm in each of the short dimensions, although this varied due to lack of geometric accuracy of the build (mostly rounded corners). This dimension was selected to enable x-ray penetration, which for SS316L was about 2 mm.

Test coupons made from IN718 were also measured. For these, the material was cut from the threaded section of two fatigue specimens built using DMLS and provided by Honeywell; comparatively little is known about these specimens, other than that they were prepared for said fatigue testing, and thus likely represent relatively high quality (well built) material. Likely these are fully heat-treated specimens. In any case, four bars of similar dimensions to those cut from the half Charpy builds were produced for each of the two fatigue specimens (eight total bars).

Table 2.1. Build conditions and some physical measurements of the half-Charpy specimens sectioned for imaging at 2BM; data from NIU

Build ID	HC-875-5-1.4	HC-875-20-4.7	HC-645-5-1.4	HC-475-5-1.05
Input Power (W)	875	875	645	475
Measured Power (W)	675	675	478	312
Travel speed (in/min)	5	20	5	5
Powder Flow (g/min)	2.88	7.32	2.88	2.47
Hatch Spacing (µm)	1,486	1,243	1,156	958
Layer Height (µm)	464.5	456	484	201
Build Height (µm)	15,672	17,187	—	17,187
Build Length (µm)	13,462	13,657	—	12,742
Build Width (µm)	28,321	29,396	—	28,998
Average Volume (mm^3)	5,695	5,943	5,424	6,023
Avg. Vickers Hardness (.2 kg)	210.88	231.32	213.09	227.23
Theoretical Energy (kJ)	2,631.14	835.89	2,189.23	4,610.84
Measured Energy (kJ)	588.02	165.94	566.8	1,022.06
Theoretical Energy Density (J/mm^3)	462.01	140.66	403.62	765.49
Measured Energy Density (J/mm^3)	103.25	27.92	104.5	169.68
Net Heat Input (J/mm)	71.27	15.83	58.47	32.67
Global Energy Density (J/mm^2)	170.53	42.63	120.76	78.82

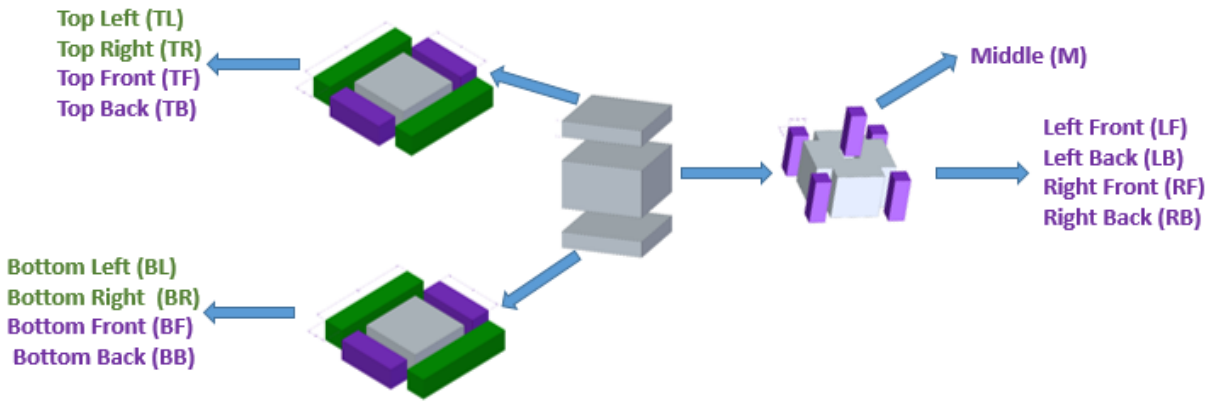

Figure 2.1. Schematic diagram showing the various sub-samples cut from each half-Charpy

2.2.2. Surface feature characterization

Preliminary surface characterization was performed as part of a Predictive Science and Engineering Design (PSED) cluster project, although the surface roughness facet of AM was not pursued extensively beyond that project. I.e., the specimens tested later in this chapter were all machined surfaces. Figure 2.2 shows some example as-built surface characterizations collected using (a) an

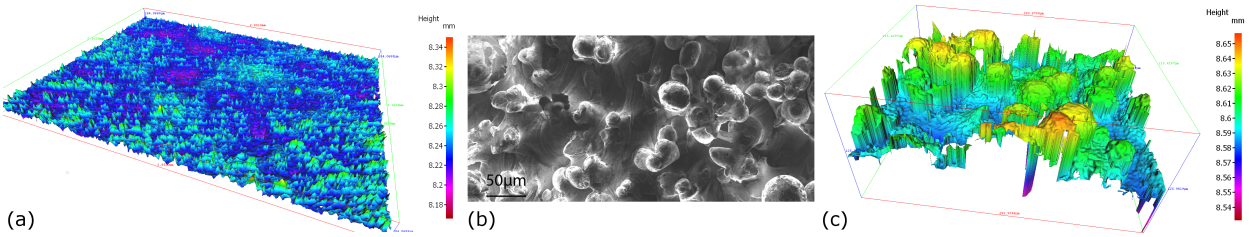

Figure 2.2. LENS surface profiles: (a) surface roughness of with Alicona (2.162 mm by 2.851 mm patch) (b) Top-down view with SEM. (c) Alicona for small-scale roughness failures to capture reentrant features (0.284 mm by 0.215 mm)

Alicona InfiniteFocus focus-varying microscope and (b) SEM of powder bed AM surfaces (the example here is SS316L built with selective laser melting, measured with assistance from Hui Yang). The smaller scale variations are highlighted in Fig. 2.2(c), although the Alicona system cannot capture high wall angle (beyond about 87°) or reentrant features. Large surface roughnesses with characteristics sizes of both the particles and the layer height have been reported for all types of AM using different measurement techniques (e.g. tomography, interferometry, serial sectioning and microscopy). For instance, Senin et al. [**110**] and Townsend et al. [**124**] both compare surface profiles for laser powder-bed fusion (LPBF) measured using X-ray computed tomography (XCT), confocal and focus-variation microscopy, and coherence scanning interferometry. In terms of different metal AM processes, the surface roughness of powder bed tends to be lower than that produced by DED-type processes (due at least in part to the smaller characteristics feature sizes in powder bed).

2.2.3. Void measurement using x-ray computed tomography

The initial characterization of voids within LENS-built material was conducted using synchrotron X-ray computed tomography (XCT) 3D using Beamline 2BM at the Advanced Photon Source (APS) in Argonne National Laboratory. A proto-study was first conducted in June 2016 via a Rapid Access proposal to test if sufficient contrast and resolution were attainable using the techniques available at 2BM. These experiment were set up and with the PSED team: Puikei Cheng, Cheng Yu, Sarah Wolff, Xu Zhang, and Hui Yang. The goals of the study were first to determine if 2BM

would be effective, and second to assess the voids that occurred in two different materials built with two different machines; stainless steel 316L (SS316L) from Northern Illinois University (NIU) and Inconel 718 (IN718) from Honeywell: the specimen outlined above. Both goals were attained: voids in the metals were observable and was possible to characterize them in 3D given suitable image post-processing.

XCT at 2BM was conducted using settings recommended by Dr. Xianghui Xiao, the beamline scientist. For this first series of imaging experiments, a voxel edge length of 0.87 µm for a minimum detectable feature size of perhaps 1.7 µm in each dimension. The dimensions of the final, binarized images were $2560 \times 2560 \times 1990$ voxels.

Image processing to obtain porosity information from x-ray imaging involves the following series of steps:

(1) X-ray reconstruction using Tomopy [**37**]; see Appendix A.1 for a listing of an example python script for Tomopy)
(2) Image filtering and segmentation; see Appendix A.2 for a listing of the associated MATLAB script
(3) Binary image analysis using DREAM3D [**35**] for feature analysis; see Appendix A.3 for an example pipeline (in json format) for DREAM3D

Unfortunately, even after the all image filtering steps some so-called "ring" artifacts remained, which pollute attempts to quantify voids. To address this, a semi-manual process to remove these was conducted, which involved visually identifying which voids were erroneous and algorithmically removing those voids from the reconstructed images. After this process was completed, a final table of voids with the characteristics of each was compiled for each XCT scanned volume. The statistics computed include various descriptive parameters for each void identified within the material (surface features were removed from the analysis): aspect ratios of equivalent ellipsoids (B/A and C/A), Euler angles (3) and axis lengths (2), centroid x, y, and z locations, equivalent diameters, Omega3 factor (as defined by [**75, 79**]), and size (number of voxels in void).

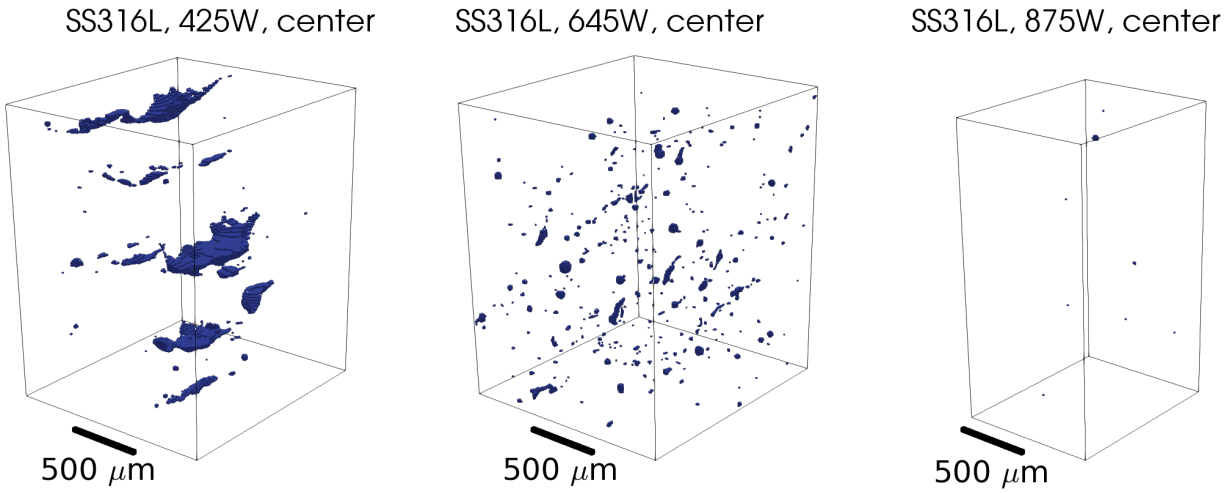

Figure 2.3. Example XCT images of voids made with different processing conditions collected from the middle (M in Figure 2.1) of the three different half Charpy specimens with the same powder flow rate but different laser powers. (left) GED = $78.82\,\mathrm{J/mm^2}$, (center) GED = $120.76\,\mathrm{J/mm^2}$, (right) GED = $170.53\,\mathrm{J/mm^2}$

Example images of voids for each of the three different processing conditions for SS316L are shown in Figure 2.3. These images were also used in initial demonstrations of the reduced order modeling technique that will be outlined in Chapter 4, and statistics collected from the IN718 will be used in Chapter 3 to construct equivalent ellipsoid models.

2.2.4. Void data characterization and analysis

Using the data from this collection of images, some insight into process-structure relationships was gained at least for voids. Some general trends, in the form of main effects plots, are presented in Figure 2.4. These results show that increasing power and decreasing travel speed tends to decrease porosity – not surprising considering it is likely that the low-power builds were creating lack of fusion voids. In addition, position seems to make more of a difference when laser power is lower, perhaps related to heat-soak in the center reducing lack of fusion defect potential. However, due to the limited number images, lack of information on the local processing conditions, and precise localization of individual voids in the full build, localized data proved impossible to generate reliably for these specimens. In addition, because some of the data points were rendered unreliably, difficult to interpret, or difficult to gather data from because of geometry in the XCT images, a more limited

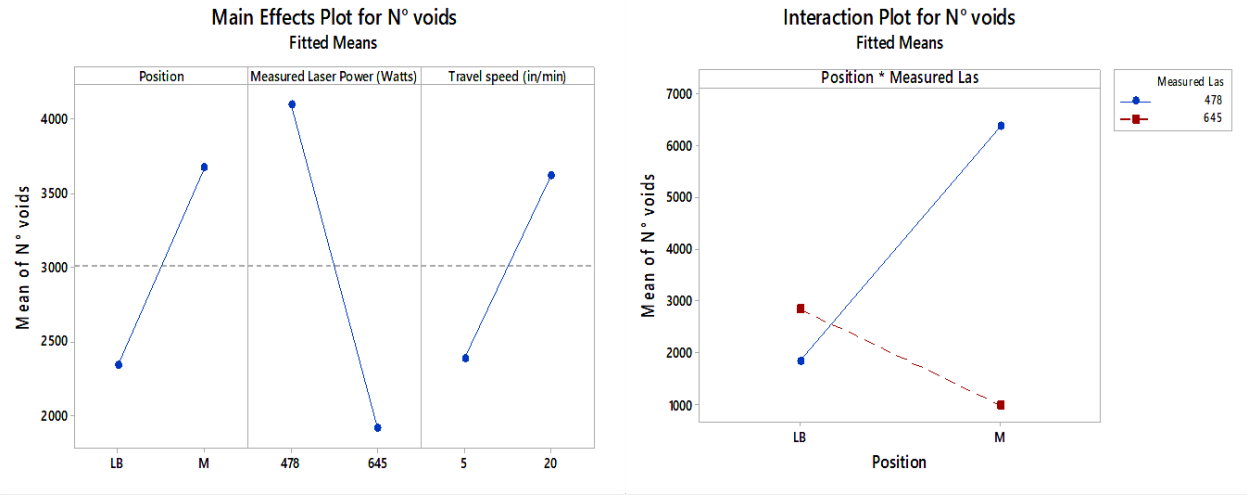

Figure 2.4. Main effects plot and interaction plots for void count versus position, power, and travel speed; increasing laser power and decreasing travel speed tend to decrease the number of voids, while position is loosely related to number of voids but it depends on the laser power. The GED of each of these specimens is given in Table 2.1

selection of the specimens shown in Table 2.1 were used for the analysis. The analysis of these specimens (specifically, the main effects and interaction plots) were conducted in collaboration with Mouad Fergoug.

For the IN718 samples, voids were characterized by size and aspect ratio, as illustrated in Figure 2.5(a) and 2.5(b) respectively. The first histogram indicates that the void sizes fit well with a Weibull distribution. Particles sizes in terms of percentile largest are given in Table 2.2. This data was later used to construct representative finite element models. For example, the aspect ratio data presented suggests there are two populations of voids, some with roughly equal C/A and some with C/A of between 1/4 and 1/3, probably indicating different mechanisms of void formation active in the observed regions of the build. This data will be used to construct a "mean equivalent ellipsoid" in Chapter 3, which will be embedded into an FE model representative of a uniaxial fatigue test specimen.

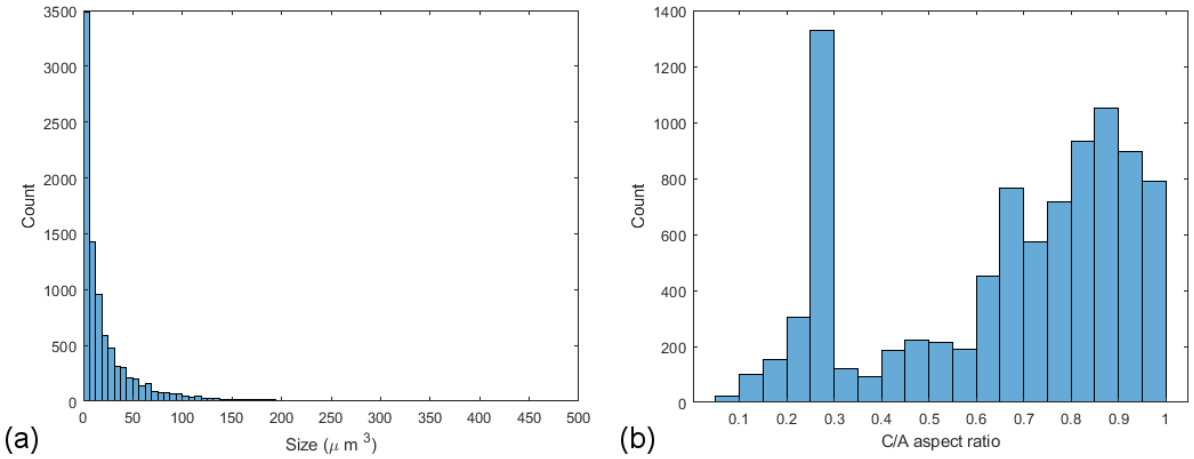

Figure 2.5. (a) Volume distribution of voids in IN718; (b) distribution of C/A aspect ratio voids seem to either be flattened at about a 1/4 to 1/3 ratio or approaching roughly spherical, consistent with voids produced by different mechanisms: perhaps either lack of fusion or boiling

Table 2.2. List of voids sizes in IN718 from Honeywell, as detected by XCT at 2BM (note that median equals 50th percentile)

Percentile	99th	95th	50th	5th	1st	Mean
Size (µm^3)	249.1	106.0	10.54	1.976	1.317	29.18

2.2.5. Measuring crystallography

Although crystallographic information was not captured directly for all these specimens, a small region of SS3316L from the 475 W specimen was measured at beamline 34IDE at the APS. Beamline 34IDE uses X-ray micro-Laue Diffraction to measure grain orientation and residual strains with high accuracy. This technique can obtain 2D and 3D measurements using a point-scanning technique with maximum spatial resolution of about 200 nm. More details of the operating principle can be found in [**46**]. In brief, the x-ray forms a diffraction pattern that contains signal from all the grains through the penetration depth of the beam, in this case about 300 µm. Software provided by the beamline scientists allows us to reconstruct the grains based on their intensity in the diffraction pattern. This provides a 2D map. To collect 3D information, a wire is translated through the diffracted beam isolating the signal from subsequent grains through the penetrated depth; from that the into-the-depth information can be extracted. In general, because this is a point-scanning

method that requires physical motion of the specimen (and wire in 3D), data collection is a lengthy process. This work was conducted with the help from Wenjun Liu, one of the APS beamline scientists at 34IDE, in configuring system and analyzing the resulting data. Puikei Cheng and Sarah Wolff were collaborators.

Although too small (because of the time required to collect data) to be generally representative, the results presented below give some idea of the grains one might expect. A 3D visualization (from measuring two faces of a rectangle) is shown in Figure 2.6(a), and the top 2D surface of that is shown in Figure 2.6(b). This shows the complex, 3D nature of grains that can occur, complicating heterogeneity that a modeling effort will need to capture beyond the voids. The grains shown here are colored with an IPF map, so different colors mean different crystallographic orientation, and similar colors have similar orientation. In this case some preferred texture is observed (reds and greens), although no orientation clearly dominates. The grains themselves have a strong preferential orientation in the build direction. Physically this seems to follow from predominantly epitaxial growth from prior grains following the direction of strongest temperature gradient during solidification. The observation that grains tend to grow epitaxially from the substrate is similar to patterns found in other studies of AM, such as the work of [**4**] in Ti-6Al-4V.

The same technique was used to measure SS316L specimens built at beamline 32IDE with in-situ observation of the DED-style build using custom hardware. The work at 32IDE to build this material was conducted by Sarah Wolff and is reported elsewhere, i.e. [**131**]. Two of her specimens were scanned. For these cases, both grain orientations and volumetric residual strains were measured (as change in d-spacing from a pre-calculated reference d-spacing). A qualitative measure of residual strain is used; while it would be possible to report specific numbers, i.e. for d-spacing shift or even the associated strain value, there are some limitations. First, the technique we are used only measured scalar strains in the direction of the diffracted beam. It would be possible to measure full, 3D strain tensors, but much more time and effort intensive. Second, the overall state shown here represents an average or effective measure through the beam penetration depth; from preliminary studies, we know that substantial variations exist through that depth. Because of

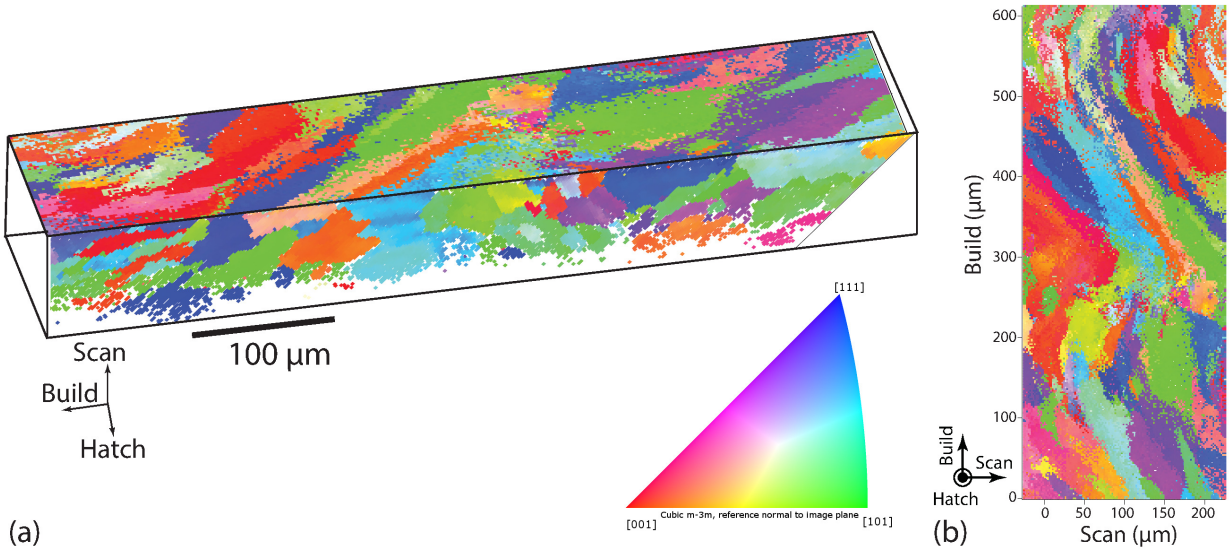

Figure 2.6. Example grains in the 475 W, SS316L build in Table 2.1 as measured with x-ray diffraction at 34-IDE; (a) 3D view, showing grain configurations in the build, scan, and hatch direction, (b) slightly large "top down" view of the same specimen, showing "waviness" as a result of multiple tracks altering the preferred grain growth direction.

these two factors the specific numbers we can report likely do not represent the true state of strain of any particular material point well. Thus, I have opted to show only a relative scale bar to avoid suggesting a more complete understanding than in fact exists.

In the first specimen, shown in Figure 2.7, about 2 mm of material along the track was measured to a depth of 150 µm with a skip spacing of 5 µm for diffraction and 8 µm for residual strains. For the second specimen, shown in Figure 2.8, a 3 mm by 300 µm region was measured with the same spacing. In these specimens, we observe less of the preferential orientation in terms of both crystallography and shape that was seen in the builds conducted using commercial equipment. The results shown in Figure 2.7 are for a 300 W build (codenamed V18) and Figure 2.8 shows a 400 W build (codenamed V21), where all other settings were held the same.

From the figures, it seems that the same waviness observed in the build that used a commercial system was not present, probably because of different scan strategies (s versus z), but the grains were still preferentially oriented. They seem to favor the [100] direction, and sometimes tilt in the direction of laser travel (X, the scan direction). Figure 2.7(b) shows an into-the-depth scan, looking

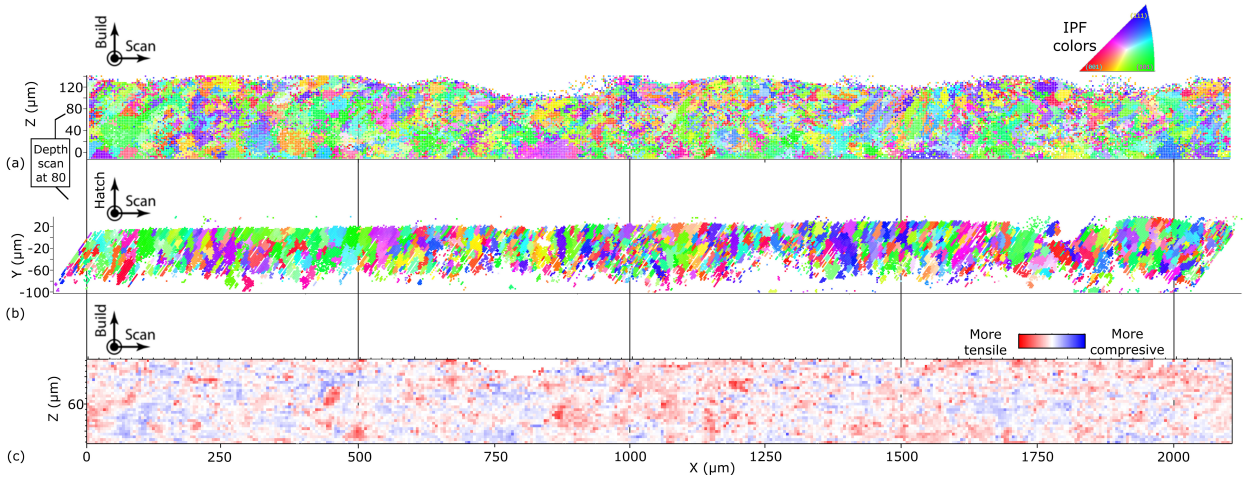

Figure 2.7. (a) Inverse pole figure coloring (showing grain orientations) looking into the cross-section of a 32IDE build, the top surface is unpolished, and so shows roughness from the build. Grains seems to be oriented with [101] preference, but only slightly (if at all) tilted in the scan direction, contrary to what was observed in Figure 2.6. (b) In-to-the-depth scan at 80 Z-height in (a) looking at a plane "top down" from the build configuration. No strong pattern is observed, which match the similar observation in Figure 2.6. (c) Residual strains, plotted as a scaled difference from the expected d-spacing, red is more tensile and blue is more compressive. Some tensile hotspots (potentially dangerous) and substantial variations are observed

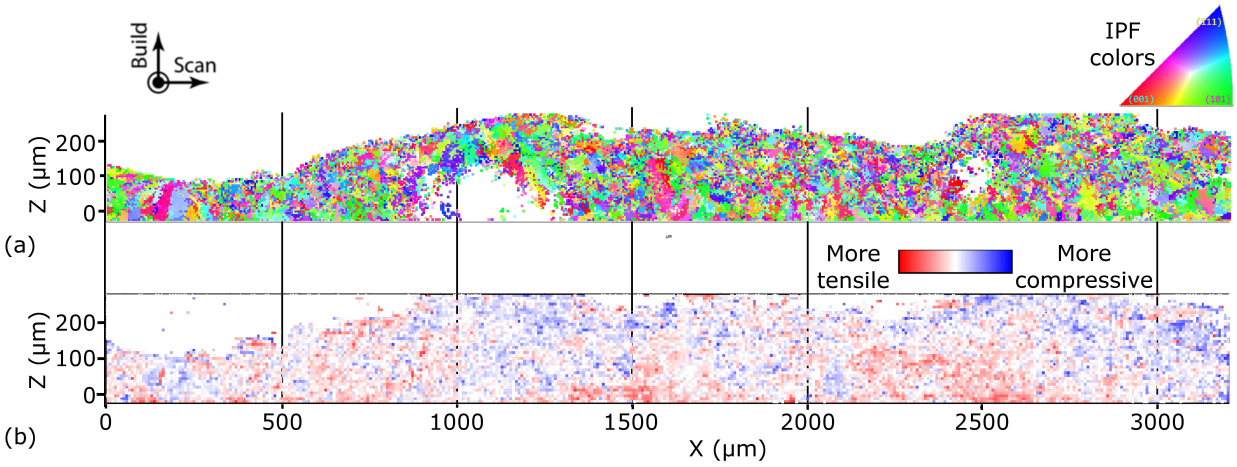

Figure 2.8. (a) Grains in a build with higher laser power, but otherwise similar conditions, than in Figure 2.7. (b) Residual strains, again colored using scaled difference from the expected d-sapcing. Generally similar patterns are observed with Figure 2.7

into the line at Z=80 in Figure 2.7(a) (similar to the 3D perspective shown in Figure 2.6). This shows little pattern or preference along this cross section, which is similar to the results shown in Figure 2.6(a). Figure 2.8 shows largely similar results, although grain sizes might be slightly

smaller. These experiments and analysis of 32IDE-built material were conducted in collaboration with Puikei Cheng. Residual strains seem to favor tensile states, with some "hotspots." The presence of these hotspots might be of future interest as potential fatigue or damage initiation cites under loading. If more homogeneous residual strains could be achieved, it might positively impact performance although further study (experimental or with simulations) are required to test this hypothesis.

2.3. XCT with in-situ mechanical testing

These prior characterizations of voids in the material were useful to understand the impact of processing parameter choices, and the 3D shapes of voids that might occur. One goal was to produce images that could (relatively) easily be used as geometric input to micro-scale models. This will be achieved, and the results of some image-based modeling using crystal plasticity on these example images are shown in Chapter 3. However, in order to understand the impact of voids from AM on the performance of the material, another series of experiments were carried out at the APS, this time using an *in-situ* load frame (on loan from beamline 1ID). This provides important calibration and validation data for microscale modeling, while also providing insight to the mechanisms active during deformation, predominately void-driven ductile damage.

Ideally, diffraction and tomography could be conducted simultaneously with in-situ mechanical testing. This would provide more complete information about the nature of the specimens, and more complete data to pass to the numerical simulations, especially crystal plasticity models. In fact, this capability exists at beamline 1ID (albeit with more restrictions on specimen geometry and conditions). However, time on beamline 1ID is highly limited (and coveted), so in light of the lengthy testing process we will make due with only having XCT data, not diffraction as well.

2.3.1. Materials and Methods

The nickel-based superalloy Inconel 718 with nominal composition given in Table 2.3 was studied. This is a commonly used alloy in AM, and is relatively ease to print (and weld), because it is a

quench supressable alloy that can be printed in a soft state an later heat treated to achieve full strength. In this case, the material was gas atomized to a particle size of 50 µm to 150 µm.

Table 2.3. Nominal composition of IN718, wt%

Al	B	C	Cr	Co	Cu	Fe	Mn	Mo	Ni	Cb+Ta	P
0.2-0.8	<0.006	<0.08	17-21	<1.0	<0.3	17 (bal)	<0.35	2.8-3.3	50-55	4.75-5.5	<0.015
	Si	S	Ti								
	<0.35	<0.015	0.65-1.15								

Three single-track, "thin wall," builds using a DMG MORI LaserTec 65 3D tool were deposited on stainless steel grade 304 substrates. This tool uses a direct diode laser, in this case operated at 1800 W, 1020 nm wavelength, and approximately 3 mm focal spot size. Each build resulted in a thin wall, nominally 120 mm long, 60 mm high, and about 3.5 mm wide with a layer height of 0.5 mm. Argon shield and conveying gas at 7 L/min protected the melt pool while delivering powder coaxially to the laser. Three walls were built with different build patterns; each wall was built using a zig-zag tool path and 1000 mm/min scan speed, but two walls shared a 18.0 g/min powder flow rate while the third had about a 27.0 g/min powder flow rate. Using the definition of Global Energy Density (GED) used to compute GED in Table 2.1, $GED = \frac{power}{(scanSpeed)(laserRadius)}$, the nominal GED of all three builds is 0.01 J/mm^2; however, because this is a thin wall build, it may not be particularly comparable to other GED measurements. I.e. if an "optimal" GED were known for IN718 for a cubic build, this would be influenced by the hatch spacing, and thus not necessarily be also the optimal GED for these builds. Of the two walls with the same flow rate, one had no dwell time between layers and one had a 60 s dwell between layers. Real-time thermal monitoring was conducted using an infrared camera, although that data is not reported here. See, e.g., Bennett et al. [**8**] for more details on the thermal monitoring. These builds were conducted by my collaborator Jennifer Bennett.

After building, a 1 hr at 1065 °C stress relieving heat treatment followed by air cooling to room temperature was conducted, per AMS standard 5664F and the suggestion of EOS, an AM machine manufacturer that uses IN718. It is important to note that this is a solutionizing heat treatment, an thus the specimens were eventually tested in the solutionized state (with an unknown amount

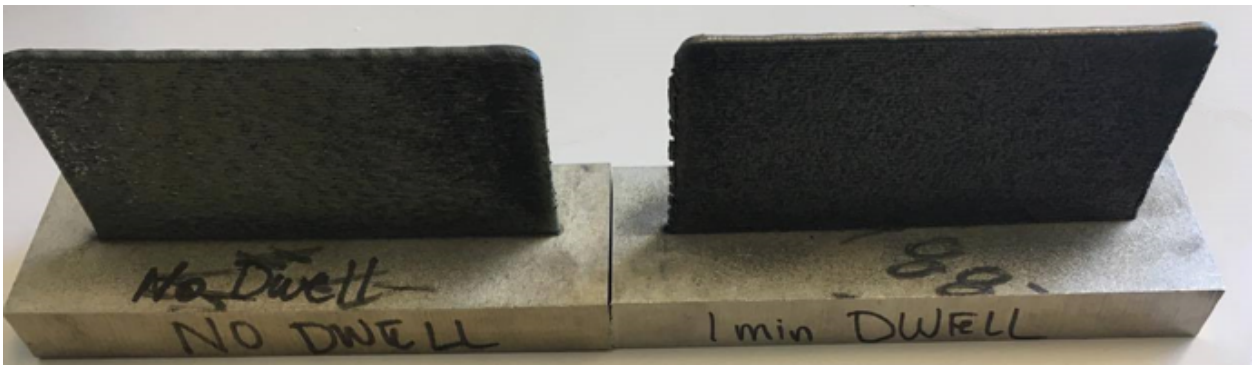

Figure 2.9. A photography of two of the thin walls (Wall 3 (left) and Wall 2 (right)) that were then cut up to make miniature tensile coupons. Note there are noticeable geometry inaccuracies, even from this perspective.

of precipitation strengthening, which would have resulted from the air cooling step). This residual stress relief enabled subsequent specimen machining from the builds with limited distortion. A photograph of two of the thin walls prior to stress relief in Figure 2.9 shows the real geometry of the builds, including inexact geometric features such as slightly warped top and side surfaces and rounded corners. This meant that any real-space position measurements had some unavoidable inaccuracy.

2.3.1.1. Specimen selection and preparation. Once the walls were built, miniature ASTM E8 pin-loaded tensile coupons (designed bespoke for these tests) were exhumed from each wall. With little *a priori* knowledge of the distribution from which we were sampling, a Sobol sequence was used to define the points at which the specimens were collected from the walls. This maximized the information gathered from the specimens. To test for anisotropy, half the coupons were exhumed with the gage section parallel to the build direction and half perpendicular to the build direction. To maximize the similarity, in terms of processing history, between the horizontal and vertical specimens, the ≈3 mm thick wall was sectioned longitudinally to produce two 0.8 mm to 1 mm thick sheets (change in thickness resulted from warping). Horizontal and vertical specimens were then cut from the same coordinates of each sheet, such that the distance between gage sections in the precursor material was minimized. This specimen extraction procedure is shown schematically in Figures 2.10 and 2.11. All specimen machining steps, after the wall was built, were conducted

using contracted wire electric discharge machining (wire-EDM) to minimize disturbance of the material prior to testing.

By machining specimens from builds we limit the influence of edge effects (predominantly geometrical and thermal) from the process on the underlying mechanical behavior of the material. This more closely represents the service condition of the material, locally, than if each tensile specimen were built individually as has occasionally been done in other studies. This is particularly important to consider because, unlike with a powder-bed process, LENS does not surround the part with particles that may mitigate the free surface thermal effects.

Each specimen extracted from the wall had a nominal gage section 2.5 mm long, 1.2 mm wide, and 0.8 mm thick, as shown in Figure 2.12. All specimens were measured after machining and etching (described in the next section), as some variations from the nominal geometry were expected due to warping of the thin sheets after release from the baseplate. The actual, measured gage section size (measured three times at three different locations in each direction) was used to compute engineering stresses for each specimen. An image of the specimens prior to testing is shown in Figure 2.13, where each specimen in uniquely labeled using a letter/number convention that will be referenced in later sections. The first character, H or V, refers to the orientation (horizontal or vertical) with respect to the build direction. The second character refers to the wall: 1 = 90% powder flow rate, no dwell; 2 = 60% powder flow rate, 60 s dwell; 3 = 60% powder flow rate, no dwell. Finally, within each wall slice the specimens are number in accordance with the Sobol sequence, thus higher numbers are more "disposable" in terms of providing information regarding the spatial distribution of material properties. The numbers that end in a 0 were "manually" added after the sequencing to probe the extremes of the build, either at the top of edges of the build.

2.3.1.2. Surface preparation. To remove possible effects of the wire-EDM procedure, the specimens were chemically processed after machining. All specimens were immersed for approximately 90 minutes in Kalling's Etchant, which removed about 50 µm (0.05 mm) of surface material from all faces. Prior to immersion, both pin-connector ends of each specimen were coated in etch-resist

to protect them from the surface removal. The etch-resist was removed after the specimens were retrieved from the immersion.

The final stage of specimen surface preparation was to apply a speckle pattern to the gage sections, to enable surface DIC. This was required because the constricted environment of the in-situ

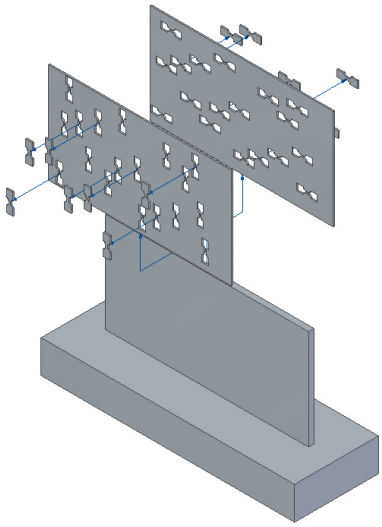

Figure 2.10. Coupon locations in each thin wall build

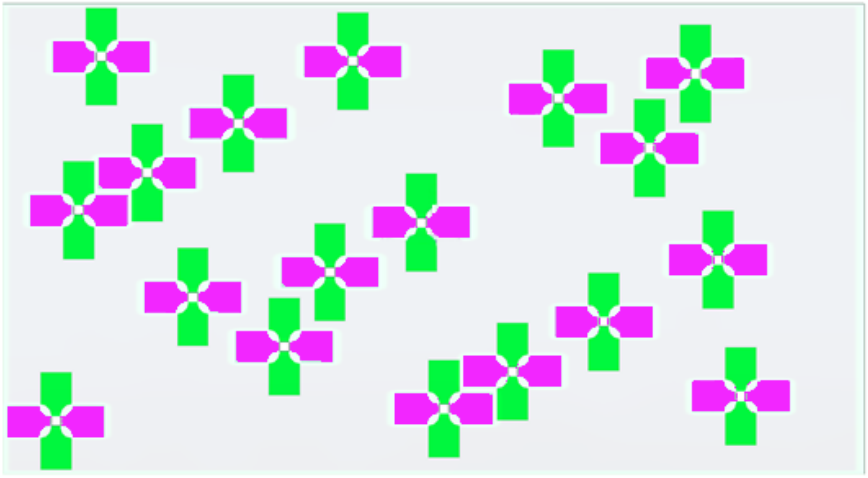

Figure 2.11. Relative locations and orientations of tensile specimens. Green are vertical (long axis aligned with the build direction), and purple are horizontal (long axis along the scan direction).

test would not allow a contact-based strain measurement system. To generate speckle patterns of sufficient detail, one of the larger surfaces of the gage section was first painted black, then a dispersion of 6 µm alumina powder in ethanol was applied with an air brush to the still-wet layer of paint. The "outward" face was chosen, and consistently faced towards to x-ray source in the experiments to remain as consistent between specimens as possible. This created a fine, high-contrast, white-on-black speckle pattern with ideal minimum subset size of about 60 µm. The quality of speckle patterns made this way was tested by assessing the ability of DIC to reproduce a known rigid body

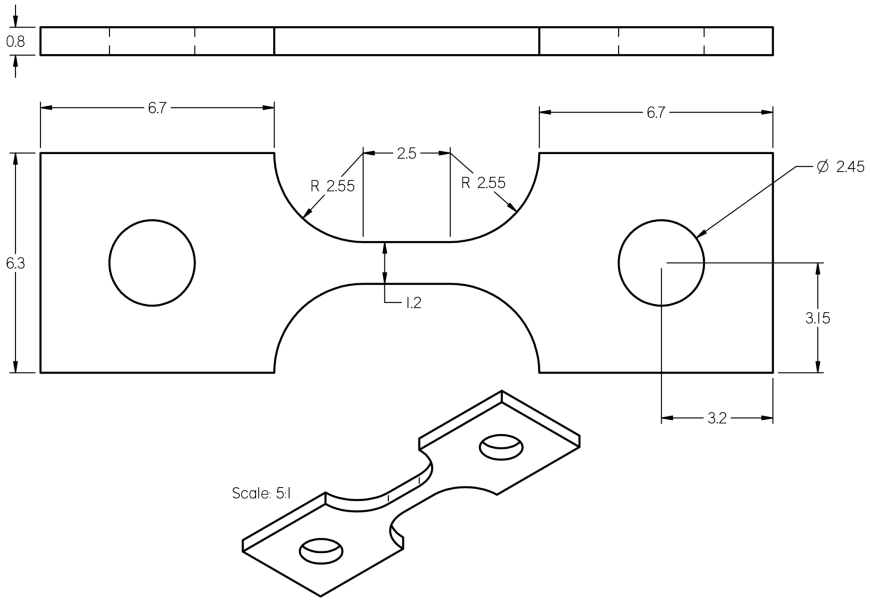

Figure 2.12. Details of nominal miniature specimen geometry, dimensions in mm

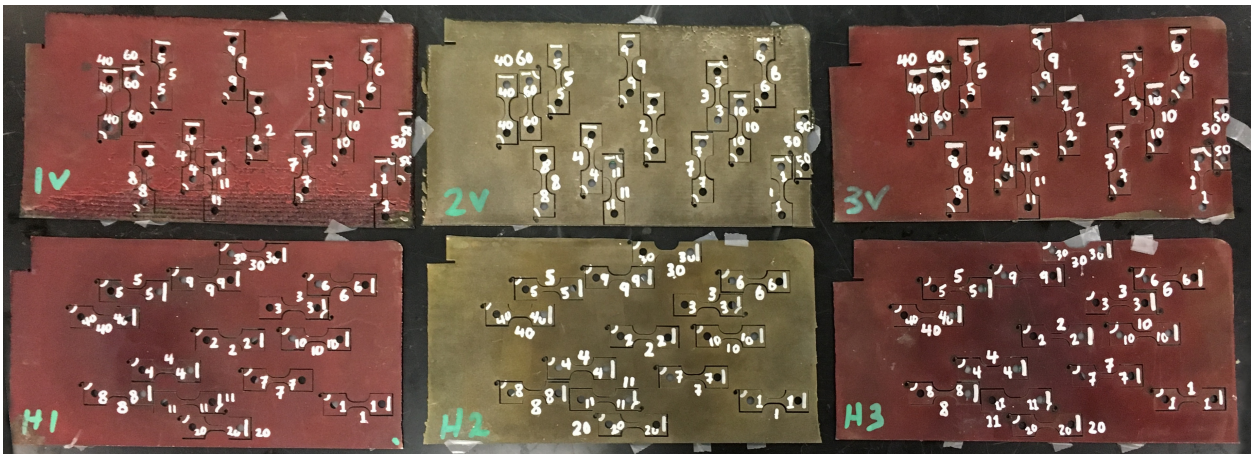

Figure 2.13. Labeled specimens in their respective thin wall slices prior to testing

motion, measured with subsequent images taken under light microscope observation and/or using the optical system used during testing (both ways were roughly equivalent).

2.3.1.3. Crystallography. Crystallographic analysis was performed using both electron backscatter diffraction (EBSD) and x-ray micro-Laue diffraction at beamline 34IDE of the APS. Both characterizations were limited in total area observed and specific location due to operational and personnel limitations. However, from the few images collected, a pattern of large columnar grains with high aspect ratio and a preferred crystallographic orientation is fairly clear. For example, Figure 2.14 shows an EBSD map that indicates columnar grain structures near where one of the test coupons was removed from the thin wall. Micro-Laue diffraction at 34IDE was conducted on a small region cut from the top corner of the thin wall, and Figure 2.15 shows two dominate features: first, similar elongated grains with a predominate orientation is seen; second, the final layer of the build exhibits a unique orientation, likely due to the lack of re-solidification during processing of that layer (however, the this is purely supposition).

Note that EBSD represent a nearly-purely surface measurement. Compare this to micro-Laue diffraction, where x-ray penetration depth is between 50 µm and 75 µm for IN718 and the grain that produces the strongest signal (see [**46**] for a more detailed description of what this means) is shown. This results in the somewhat less "clean" grain boundaries in Figure 2.15. The EBSD scan was run by Zilin Jiang, as part of a Predictive Science and Engineering Design cluster project that I helped mentor (not the same one that I was part of for the XCT measurements described earlier).

2.3.1.4. Porosity. Histograms relating voids to their location within the XCT scan region (within the gage section) are shown in Figure 2.16. These are characteristic examples: many samples show similar patterns. The strongest relationship is in the build direction, where a periodic increase in voids every 400 µm to 600 µm corresponds to the layer height. Specifically, there seems to be between three and five times more voids in the between layers compared to within layers. There is also a peak in the center of the hatch, which physically corresponds to about 1/4 of the way through into the melt pool (because this is half of the wall); it is unclear why this occurs.

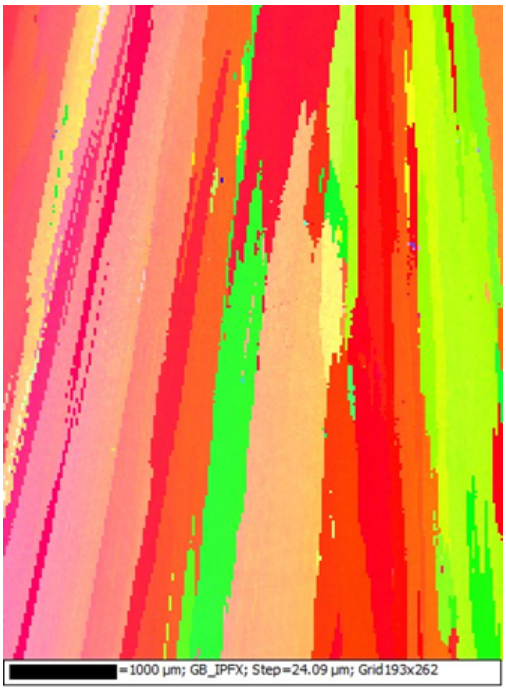

Figure 2.14. EBSD image of grains in IN718, near one of the tensile coupons; columnar structure with preferential orientation. Image collected by Zilin Jiang

2.3.2. Mechanical testing procedure

Specimens were tested *in-situ* at beamline 2-BM of the APS. A custom-build, miniature screw-actuated load frame on loan from beamline 1ID was used to conduct tensile loading within the hutch. Quasi-static testing was conducted under displacement control, such that a nominal initial strain rate 5×10^{-4}/s was achieved based on initial specimen length and a continuous crosshead displacement rate. This was obtained with a crosshead displacement rate of 1.25 µm/s, kept constant during all subsequent deformation steps.

2.3.2.1. Continuous and interrupted loading. Two different displacement protocols were used: an interrupted in-situ modality was employed to enable XCT imaging during deformation, and a continuous loading through failure was used to enable more direct comparison to standard E8 tests of IN718. In the former, displacement was applied to the specimen until an engineering stress, measured load over pre-determined cross-sectional area, of 575 MPa was reached. This is usually

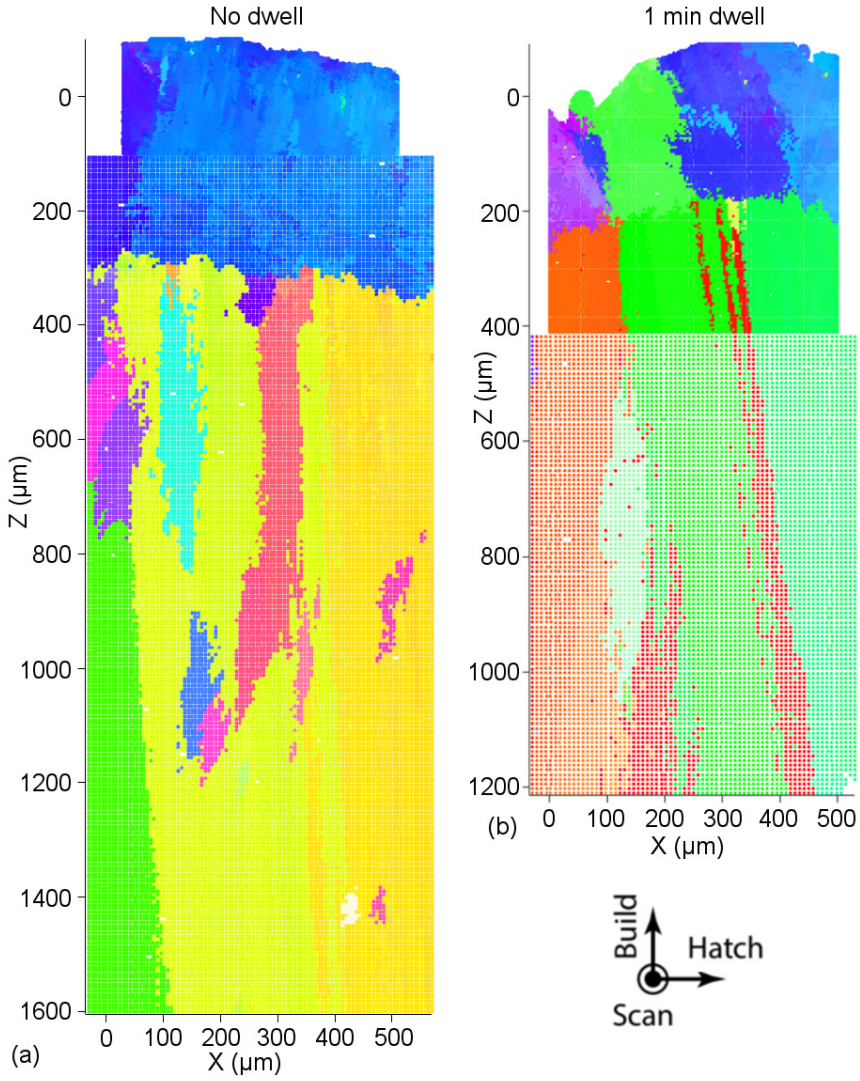

Figure 2.15. X-ray micro-Laue diffraction (34IDE) images of the top corner of the no-dwell and one-minute dwell builds. Colored using the same IPF legend as Figure 2.6

quite close to the yield stress. At this point, deformation was stopped for approximately 8.5 minutes (about 500 seconds). This allows about four minutes of creep prior to a 4.5 minute scan; the initial creep period avoids including the stage 1 creep in the XCT scan, and scanning can take place during stage 2 where creep rate is minimum (and stage 2 is very long at this load level). After the scan, displacement was increased again until stress had increased by 75 MPa, at which point another pause followed by a scan was conducted. This procedure of load-wait-scan was repeated until the ultimate tensile strength was reached. At this point, due to the more rapid change in

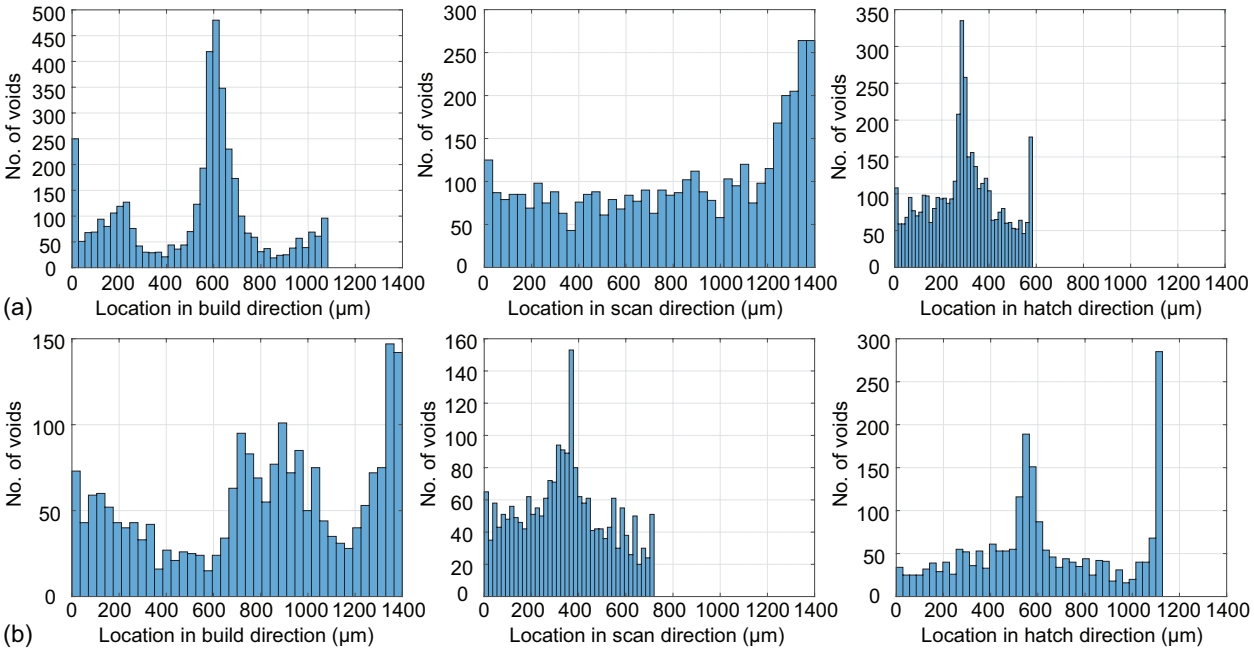

Figure 2.16. Number of voids versus location in the XCT image with respect to the material manufacturing coordinates for specimens (a) H3-2 (b) V3-4, two characteristic examples. Note that some large spikes on the edges are likely edge effects (perhaps artificial, even), so should be interpreted differently than bulk porosity.

behavior during the softening regime, scans were taken after every 15 MPa of load drop. An example displacement versus time graph is shown in Figure 2.17 to illustrate displacement history common for "start-stop" specimens. In two cases rupture occurred during either the primary creep hold time or during scanning.

Continuous loading applied the 5×10^{-4}/s strain rate (more accurately, the crosshead displacement rate of 1.25 μm/s) until the specimen failed.

It is unclear if these hold periods will impact the overall mechanical response of the material. Thus, for the time being I have to assume that they do. While this has not been directly studied, to my knowledge, in Inconel 718, reports in other alloys are conflicted. For example, Maire *et al.* [**77**] reports that for an Aluminum AA2143 metal matrix composite hold periods can change the overall behavior, whereas [**148**] shows that in Nickel-rich stainless steel no change is evident between tests with hold periods and those without. Inconel is generally creep-resistant and in these tests we see stable, repeatable recovery of pre-pause behavior upon the continuation of deformation. This

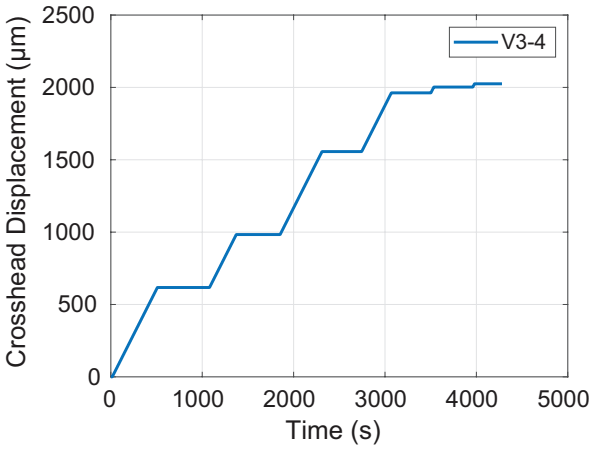

Figure 2.17. Crosshead displacement versus time for specimen V3-4, as an example of the "start-stop" or interrupted in-situ loading pattern

would suggest there is little influence of the interim creep stage on overall behavior (though localized creep behavior, e.g. near voids, may be more profoundly altered). However, because of the lack of conclusive evidence to support this, we will avoid comparison between these two modalities where an influence might be possible (i.e. UTS, toughness, or elongation at failure will not be compared, but Young's modulus during initial loading is comparable).

2.3.2.2. DIC. During deformation and at all times other than during an XCT scan, speckle pattern images of the specimen surface were collected with a Point Gray Research Grasshopper3 camera, sensor size 3376×2704 pixels, at 1 frame/s and with exposure time 0.5 s. An Infinity K2/DistaMax long distance microscope with K2 Close-Focus Objective CF-2 optic was used to provide detailed images of the gage section of the miniature test specimen (working distance about 30 cm). Lighting was provided by a LitePanels Astra LED 1x1 light panel with custom light directing hood to avoid influencing the x-ray detector. LED lighting avoids heating the specimens or surrounding air appreciably. Specular reflections were mitigated with cross-polarization: a linear polarizing film was placed between the light source and specimen, and another linear polarizing filter was affixed to the CF-2 objective lens. The use of cross-polarization has been shown to reduce error in displacement measurement by about 50% [**64**]. Two-dimensional digital image correlation with the VIC 2D software package [**127**] was used to compute surface displacement. Details of

Table 2.4. Optical and VIC2D DIC settings used to compute surface displacements

Optical parameter	Value
Camera body	Point Gray Research Grasshopper3
Sensor size, px	3376×2704
Lens	Infinity K2/DistaMax
Objective	K2 Close-Focus with CF-2
DIC parameter	**Value**
Software	VIC-2D Version 6.06, build 665
Subset size	35
Step size	7
Subset weights	Gaussian
Interpolation	Optimized 6-tap
Criterion	Normalized squared differences
Incremental mode	
Consistency margin, maximum margin	0.02 px
Confidence margin, maximum margin	0.05 px
Matchability threshold, maximum margin	0.1
Strain computation filter size	15
Strain measure	Lagrange

the DIC settings that generally provided good quality correlations for these images are provided in Table 2.4. Out of plane motion was minimal. From the displacement, strain evolution over the test duration was computed using both a local and a global approximation (both were used and compared both in VIC2D and in a custom MATLAB script to help ensure an accurate estimate of strain) to determine surface strains from displacements. Figure 2.29 shows snapshots of surface strain for specimen V3-4 (my perennial example, although such data is available for nearly all specimens) collected and reconstructed through this process. Load frame displacement was tracked and used to verify the DIC results. These strains were registered against load cell readings based on timing and starting/ending points. Thus, engineering stress versus strain curves were reconstructed as well as load-displacement.

2.3.3. XCT observation

In specimens tested using the interrupted in-situ protocol, XCT observations were conducted at every pause in the displacement increase. XCT observation was only conducted before and after (of

the two sides of the fractured specimens) testing in specimens tested using the continuous displacement increase modality. At beamline 2-BM, fast XCT is achieved by rotating the stage containing the load frame and specimen 180°, with sinographs collected every 1.0°using a rolling 100 ms exposure. Partial blocking of the specimens due to the load-carrying columns of the load frame was mitigated during reconstruction using a custom reconstruction script provided by the beamline. A 10x optic was used to provide a 0.65 µm effective voxel size. This setup is shown schematically in Figure 2.18. Tomographic reconstruction was conducted using a slightly customized (to output 8-bit images instead of 32-bit) Tomopy 1.0.1 [**37**] in a high-throughput, parallel processing environment to generate 8-bit 3D tiff image stacks. Image thresholding, or binarization, was conducted after applying a series of edge-preserving, smoothing filters to reduce noise and enhance contrast between the material and pore phases. Constancy between all reconstructions was enhanced by using a streamlined batch processing workflow with minimal outside influence. Series of segmented image stacks provide an insight into the deformation processes of pores within the tensile specimens. Segmented images were also processed in DREAM.3D [**35**] to identify features (voids) and from there determine feature statistics and descriptors.

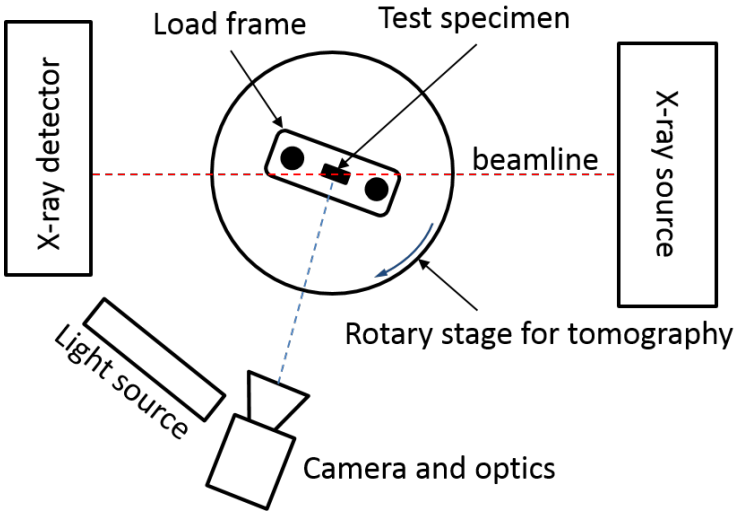

Figure 2.18. Schematic diagram (not to scale, top down view), of the specimen location with respect to the DIC camera and x-ray beam.

The full reconstruction images processing scripts are included in Appendix A. Detailed procedures for everything from specimen preparation to testing are given in Appendix B. Load/strain data and data processing MATLAB scripts are available upon reasonable request.

2.4. Results

2.4.1. Stress-strain curves

Engineering stress versus strain curves for each of the specimens tested were reconstructed using load sensor data, the DIC surface strain measurements, and initial measurements of the specimens as outlined above. In some cases data was deemed to be unreliable or simply missing, and those specimens are excluded from the current measurement (e.g. if the correlation factors for DIC were low, the strain measure probably is bad).

For each thin wall, the strain-point-wise averaged (i.e. at each fixed point in strain the stress values of all the specimens are averaged together) stress-strain curves are shown in Figure 2.19; (a) shows the results for wall 1 (90% flow rate, no dwell continuous displacement rate), (b) shows the results for wall 2 (60% flow rate, 60 s dwell, stop-start testing), and (c) shows the results for wall 3 (60% flow, no dwell, stop-start testing). Recall that a stress-based criterion was used to determine when to scan. This means that there is some spread in the strain values at which scans are taken. Thus, for wall 2 and wall 3, there are some points where the stress measured during loading and stress measured during hold periods are sometimes averaged together. This results in the increased variability and decreased smoothness of the averaged stress-strain response of walls 2 and 3 compared to wall 1. The same curves are re-plotted each on their own axes for the horizontal walls 1-3 and vertical walls 1-3 in Figure 2.20(a-f) respectively. This also shows the minimum and maximum across the reported data. These curves show that in general there are noticeable differences between orientations and between processing conditions. In wall 1 these differences are statistically significant throughout most of the stress-strain curve; walls 2 and 3 have somewhat artificially increase CIs, so are not statistically significant but this might be because of the added variability from averaging over the hold and non-hold periods as explained above.

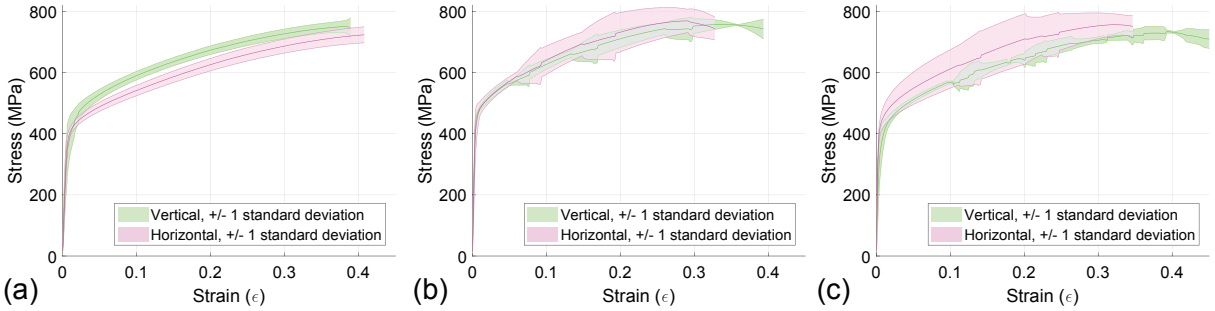

Figure 2.19. Stress-strain curves for (a) continuous testing of processing condition 1, (b) stop-start testing of processing condition 2, (c) stop-start of processing condition 3

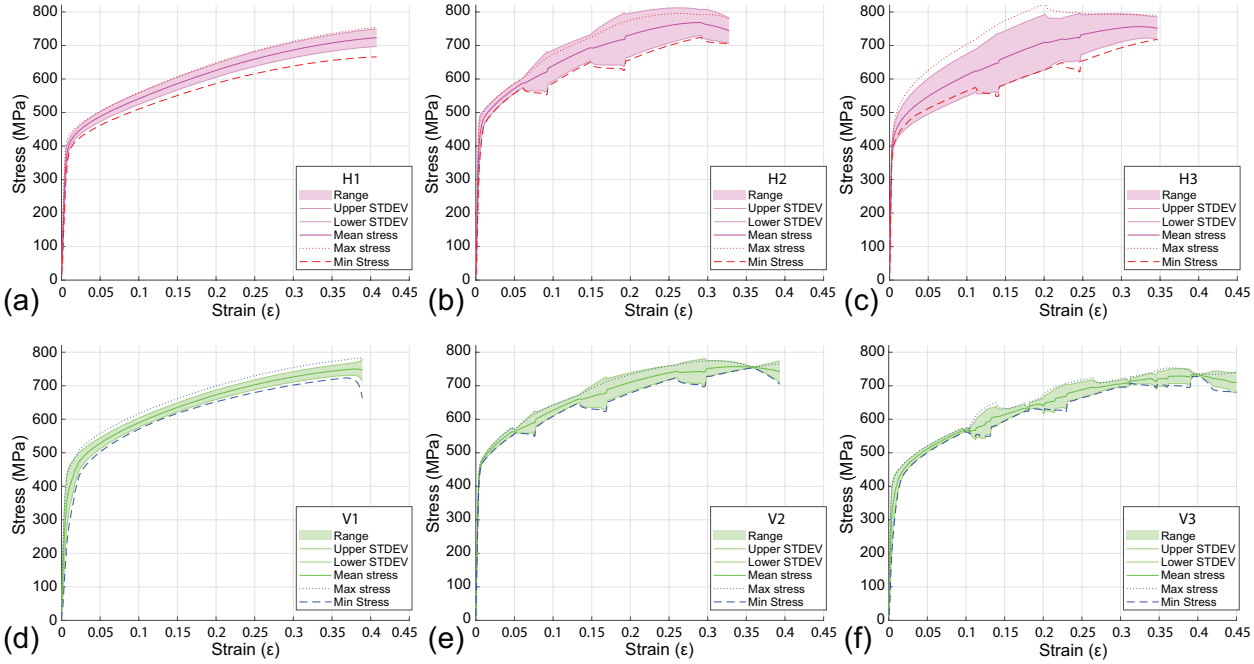

Figure 2.20. Stress-strain curves for (a) continuous testing horizontal specimens in processing condition 1 (10 specimens), (b) stop-start testing horizontal specimens in processing condition 2 (3 specimens), (c) stop-start testing of horizontal specimens in processing condition 3 (four specimens), (d) continuous testing vertical specimens in processing condition 1 (10 specimens), (e) stop-start testing vertical specimens in processing condition 2 (3 specimens), (f) stop-start testing vertical specimens in processing condition 3 (4 specimens). Min/max as well as one standard deviation are shown for each.

2.4.2. Parameterizations of stress-strain curves

To quantify the differences noted in the stress-strain curves above, common parameters can be extracted from each. Quantifying differences in such parameters can also make location dependence more easily observed, as the location dependence was lost in the averaging used to construct the earlier stress-strain curves. Commonly used single-point descriptors of the stress-strain response, i.e. 0.2% offset yield stress, Young's modulus, and elongation at failure are used to parameterize the stress strain curves for more direct comparison of location-dependent heterogeneity. Figure 2.21 shows a comparison of the elongation at failure within each wall, and between the three walls, for both vertical and horizontal specimens. Figure 2.22 shows a similar comparison for Young's modulus between the vertical and horizontal specimens for each processing condition. The red line is the mean value, each dot represents an individual specimen (jittered to be more distinct), the salmon colored region represents one standard deviation, the blue region represents a 95% confidence interval, and the outliers are plotted on the whiskers. Note that these values (SD and CI) make most sense if the data are normally distributed, but this is not necessarily the case. Plotted using the MATLAB File Exchange function "notBoxPlot".

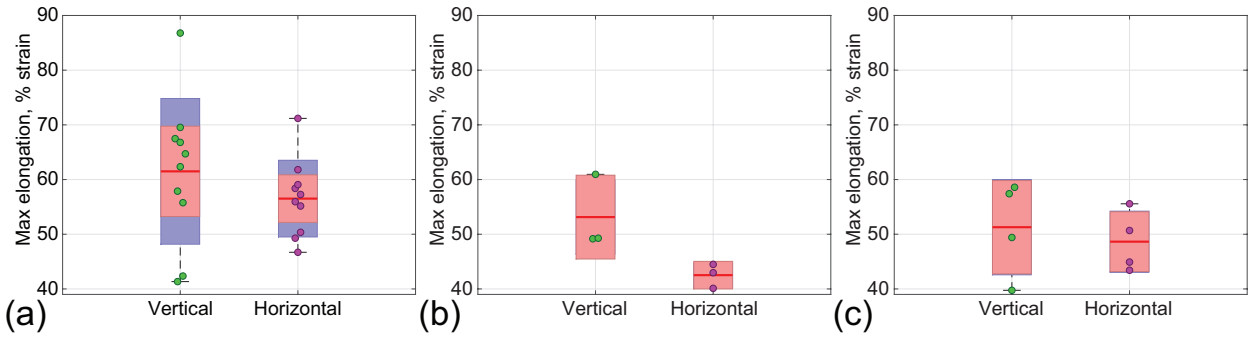

Figure 2.21. Maximum elongation for (a) processing condition 1, (b) processing condition 2, (c) processing condition 3. Data points represent real data (jittered for visibility). Note that only processing conditions 2 and 3 can be compared with each other, because the both are based on stop-start testing, whereas processing conditions 1 was not. The red line is the mean, the salmon region is one standard deviation, the blue region is a 95% confidence interval and the whiskers plot outliers.

2.4.3. Relationships with location, orientation, processing conditions

In order to better understand the distribution of mechanical properties within the wall, I plotted the Young's modulus (E), Yield stress (σ_y) and ultimate tensile strength (UTS) versus position for both the horizontal and vertical specimens. To aid in visualization, a polynomial surface is fit to the points, as shown in Figures 2.24 and 2.23 for wall 1.

For Young's modulus, notice that there are some similar trends between the two orientations, although the magnitude and details differ. In both, specimens that are low and far along horizontally tend to be stronger, as are specimens centered vertically and on the close side horizontally. It is unclear if these trends correlate directly to processing conditions, although it does seem there might be a similar pattern to the solidification cooling rate throughout the wall, as predicted by a thermal FE model shown in Figure 2.25. The stiffness of the horizontal specimens is about a factor of two higher, which corresponds to the difference seen in Figure 2.22(a). For yield stress the trends are switched: the horizontal wall tends to be slightly weaker, although the difference is not as dramatic (perhaps 15 MPa to 20 MPa). The UTS is more dependent on position, and perhaps slightly lower, for the horizontal specimens. The differences in stiffness and yield strength are indicative of the preferentially oriented grains (the effective grain boundary density in larger for horizontal specimens); however, the spread of results and relationship with location may be indicate impacts of both grains and voids to some extent. In particular, if voids are preferentially patterned this may

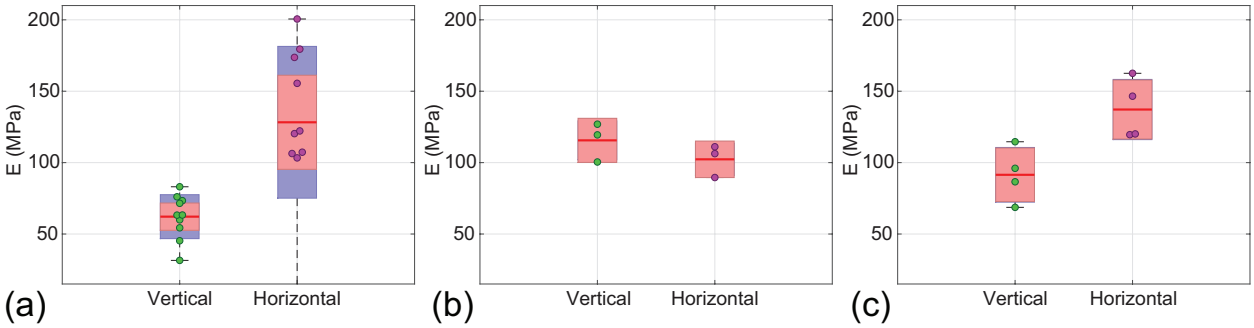

Figure 2.22. A similar boxplot to Figure 2.21, this time showing elastic modulus for (a) processing condition 1, (b) processing condition 2, (c) processing condition 3. Because modulus was measured before any of the stops, these all can be compared fairly.

reduce the effective cross-sectional area in one set versus the other. Such patterns are indicated in Figure 2.16 and are seen in, e.g., Figure 2.29 where bands of voids roughly corresponding with the layer spacing (and for V-specimens oriented across the gage section) are observed. One possible factor is that the effective cross-sectional area is reduced because of these bands of voids. The differences in UTS might be explained the same way, although the higher variability may indicate that (random) voids have a stronger role, especially in the horizontal direction. A similar pattern, with "horizontally" aligned load states stiffer though with lower yield strength than vertically aligned loading, is also captured using crystal plasticity modeling, i.e. Figure 4.8 in Chapter 4.

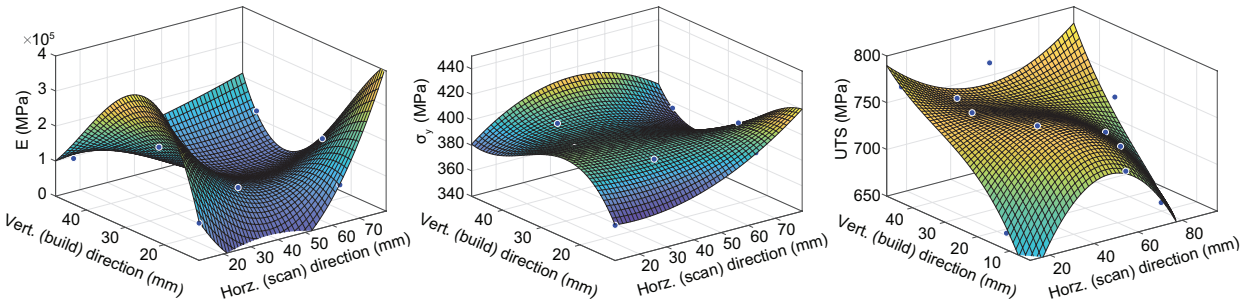

Figure 2.23. Young's modulus, yield strength, and ultimate tensile strength versus location for horizontal specimens, wall 1

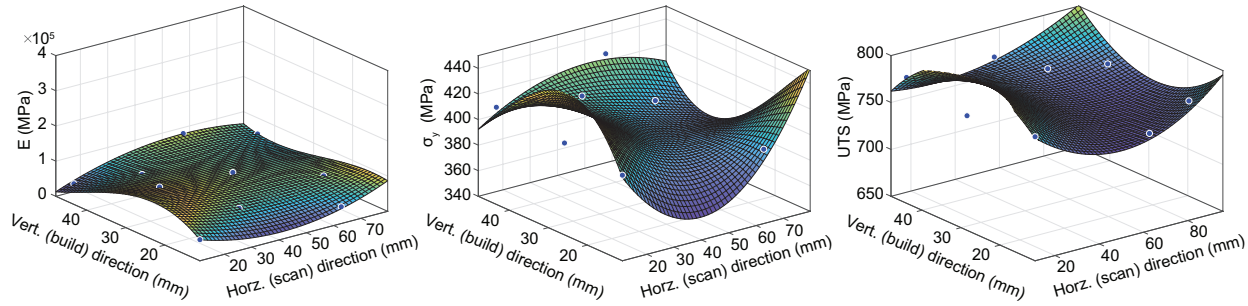

Figure 2.24. Young's modulus, yield strength, and ultimate tensile strength versus location for vertical specimens, wall 1

2.4.4. Deformation observations

Several example stress-strain curves are given in Figure 2.26. For reference, a wrought IN718 test result for annealed material using the same specimen geometry and equipment is plotted as well.

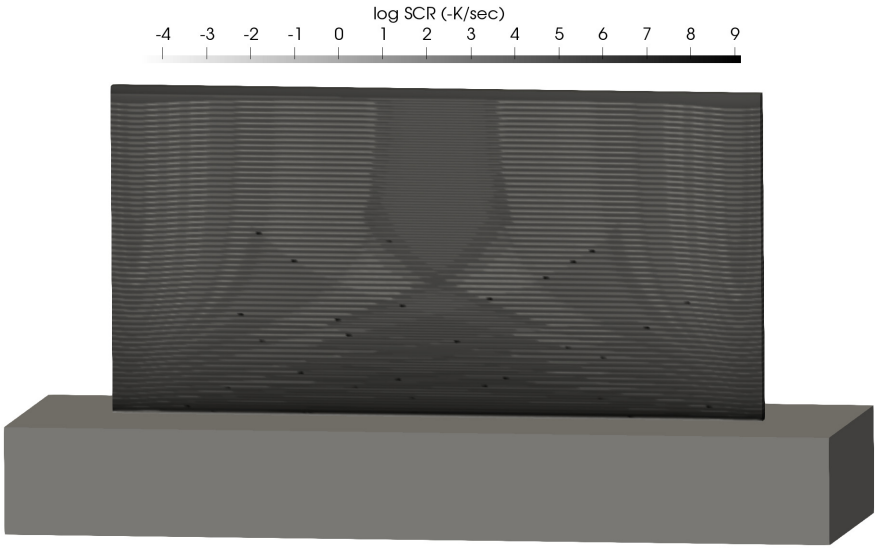

Figure 2.25. Thermal FE model of the thin wall build, showing solidification cooling rate (with GAMMA [**115**]); more details of the thermal modeling, which was conducted by Kevontrez Jones, are given in Chapter 5

All the AM coupons are tougher than the wrought material, with longer elongation but lower peak stress, lower stiffness, and much lower stress at the onset of plastic deformation.

Several frames of deformation throughout the history of one specimen are given as an example of the data collected during in-situ monitoring. These are color-coded to match the initial geometries of these same specimens, as shown in Figure 2.27. These evolve during deformation, as shown in Figure 2.28; here, voids at the onset of plasticity and near failure are shown.

2.4.5. Correlating macroscale and microscale measures with XCT scans

Continuing the example of specimen V3-4, Figure 2.29 shows a combined view of the overall stress-strain response and corresponding DIC maps and XCT scans at the prescribed stress levels. The total cross-section reduces as strain increases, an effect that is exacerbated here by visualizing only the largest rectangle that does not include any of the air space around the specimen. Were a larger area visualized (e.g. as shown in Figure 2.28), non-homogeneous deformation that results in a non-smooth exterior surface would be seen. From this, we can observe that deformation occurs in

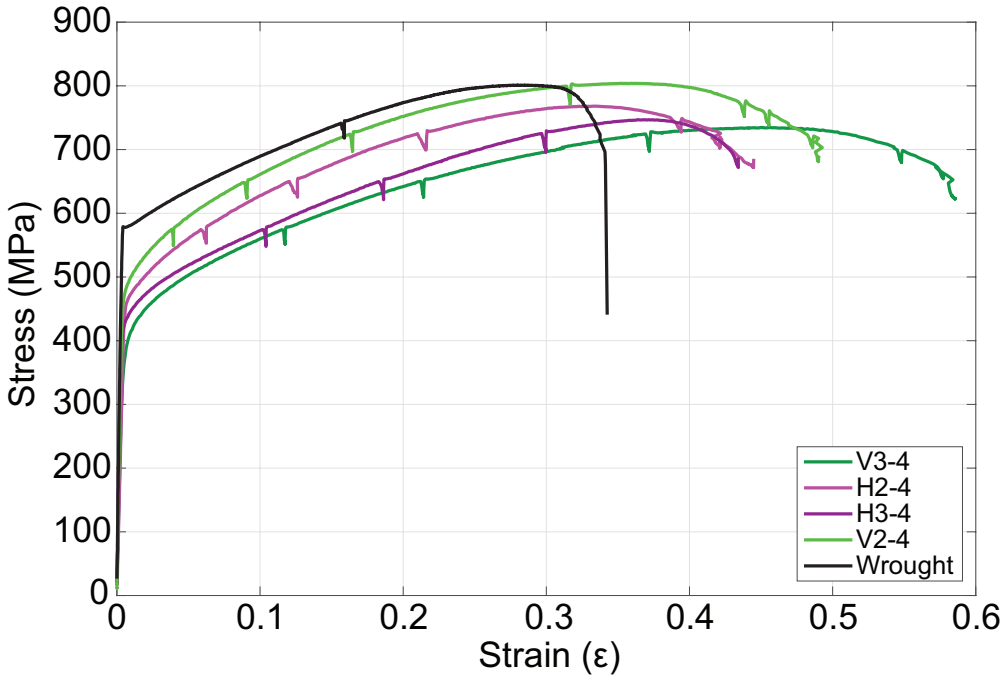

Figure 2.26. Stress-strain plot of four in-situ test specimens at the same location (4) in vertical and horizontal configuration (V vs H) and walls 2 and 3 (V3-4 is a vertical specimen in wall 3 at position 4). For reference they are compared to the behavior of an annealed, wrought Inconel 718 specimen tested on the same equipment with the same specimen geometry (black line).

individual (very large) grains giving the surface a jagged appearance. However, to more clearly see the voids those surfaces have been removed here. These scans do not capture the precise location of failure, so unlike in the H1-8 example, substantial void deformation is not observed. We know this because the surface strain maps show substantial localization at what is likely the lower extent of the XCT region. However, void motion and stretching can be seen.

Notice that between snapshots, voids sometimes move out of the lower extent of the box and the band of more dense smaller voids moves downwards. This is probably partly due to rigid body motion, which is uncompensated, and can be introduced during the scanning procedure, but part of this is strain in the specimen. Future work is to compensate for the motion of the stage and XCT system; doing so will be required to measure strains, if we eventually want to reconstruct 3D strain fields. Careful reconstruction and comparison of surface features might help with that.

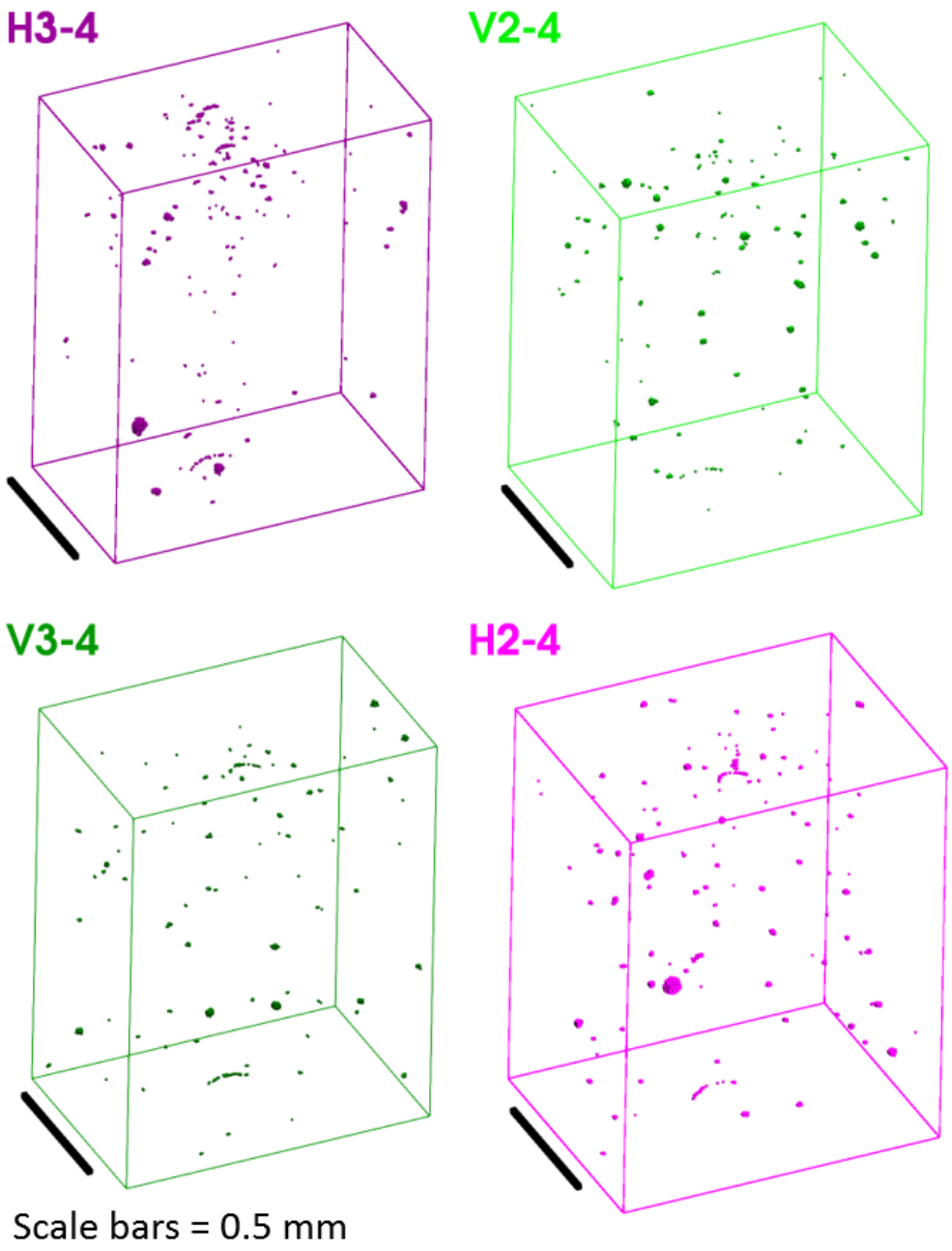

Figure 2.27. Initial configuration of voids in the for specimens highlighted in Figure 2.26 (reproduced here at lower resolution than was measured and used in analysis, so smaller voids are missing)

2.4.6. Defect tracking

The deformation progress of a single void throughout the strain-history was tracked, through the series of 4 snapshots shown in Figure 2.30. The stress-time points at which these snapshots were

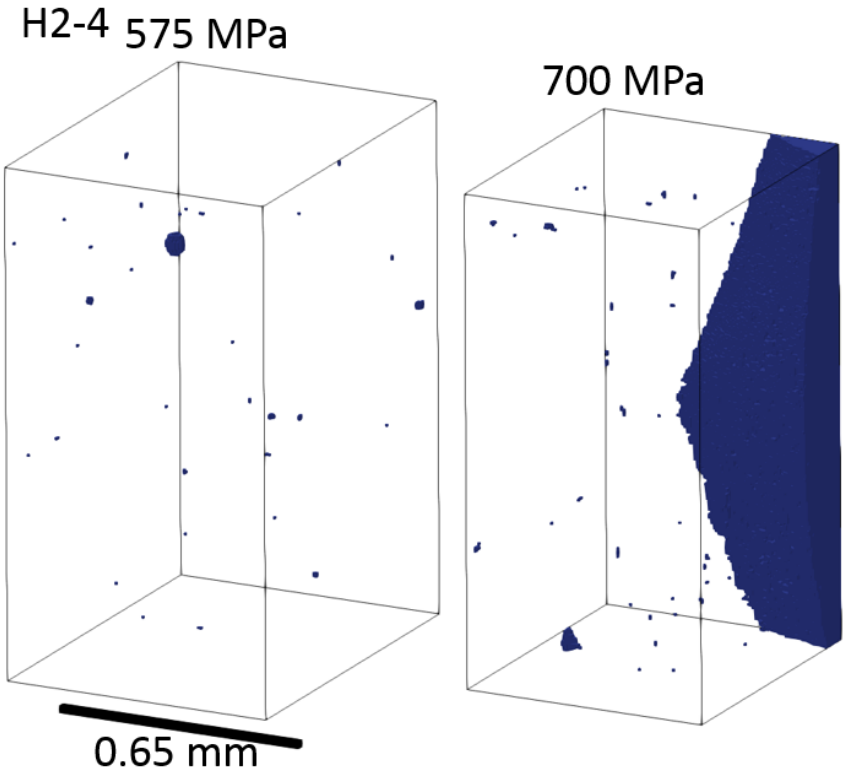

Figure 2.28. Two deformed configurations for specimens V3-4 and H2-4, one at the onset of plasticity (left side) and the other at the final scan before failure (as indicated on the stress-strain curve in Figure 2.26 by the last drop in stress before failure). The large blue bands are the encroaching edges of the specimen as it thins during deformation. Notice that in the vertical configuration, where more elongation occurs, the voids have deformed substantially before failure but in the horizontal case similar void evolution has not occurred.

taken are circled in the stress-time curve shown in Figure 2.31; the subset image shows the total volume imaged, and the relative location of this void of interest within a slice of the gage region around it is boxed. Plotting stress versus time allows direct observation of the creep region during the XCT scan. From this, we can also see that the creep is nearly perfectly recovered upon continued displacement. In this case, the scan captures a region that eventually experiences localization (necking). The plastic flow in a single crystal in that region results in the observed deformation. This was confirmed by CP simulations of this subset image, as will be shown in Chapter 4.

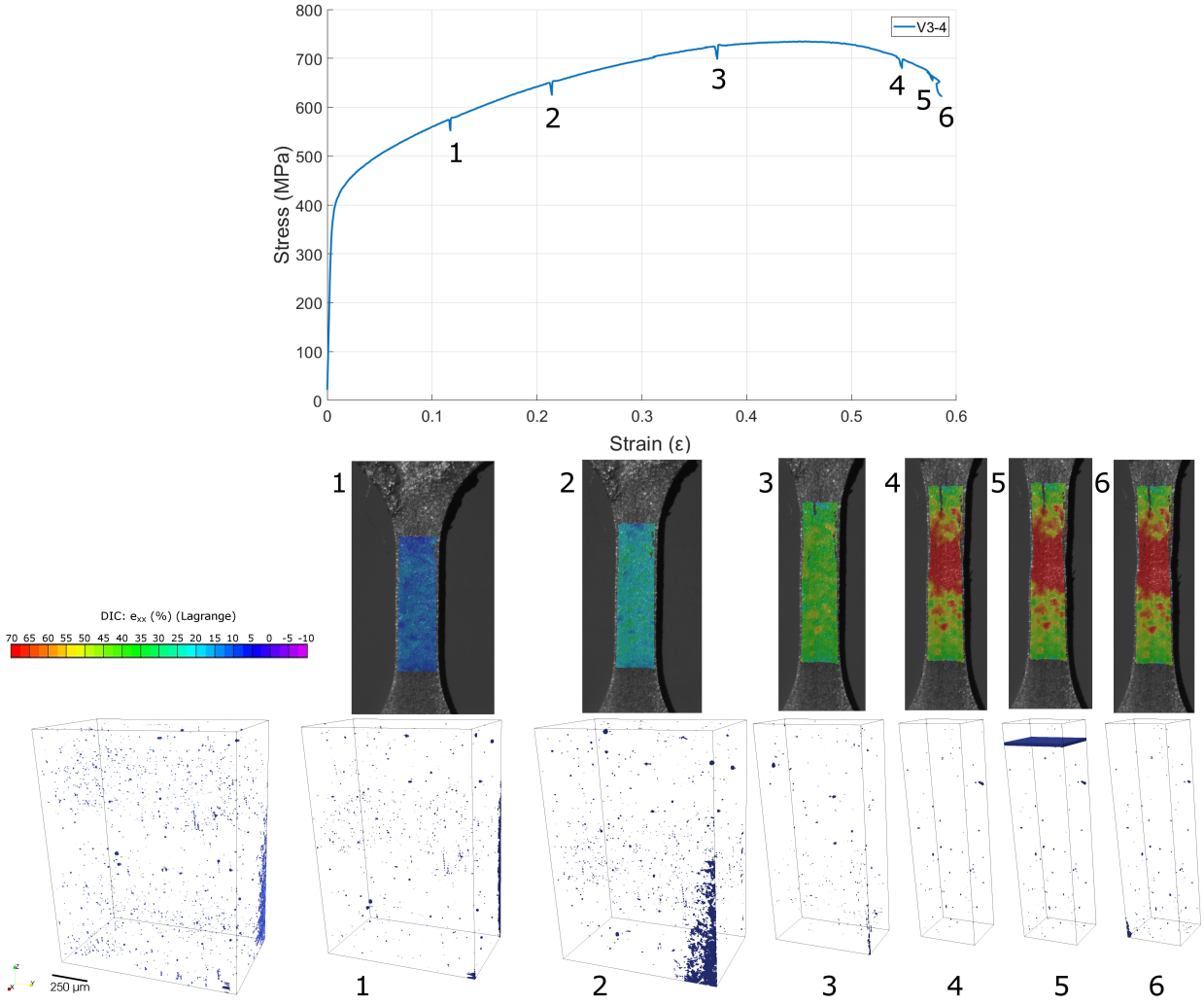

Figure 2.29. Combined macroscopic and microscopic measures of deformation (strain) for V3-4: stress-strain curve with numbers indicating where the correspondingly numbered surface strain maps from DIC and XCT scans. The top edge of each CT scan is about 0.15 mm from the end of the upper fillet.

2.4.7. Fracture surface observations

As an example, a fracture surface of specimen V3-4 after failure is shown via optical microscopy (OM) in Figure 2.32. From what we can see with these OM measurements this appears to follow the common patterns of void-induced ductile failure. However, future investigation could include SEM or otherwise more thorough fractographic analysis along with comparison to XCT scans of these regions. Two example XCT scans are shown in Figure 2.33 (rendered here at reduced resolution). These surfaces confirm the OM measurements, and from these the single-crystal nature of some of

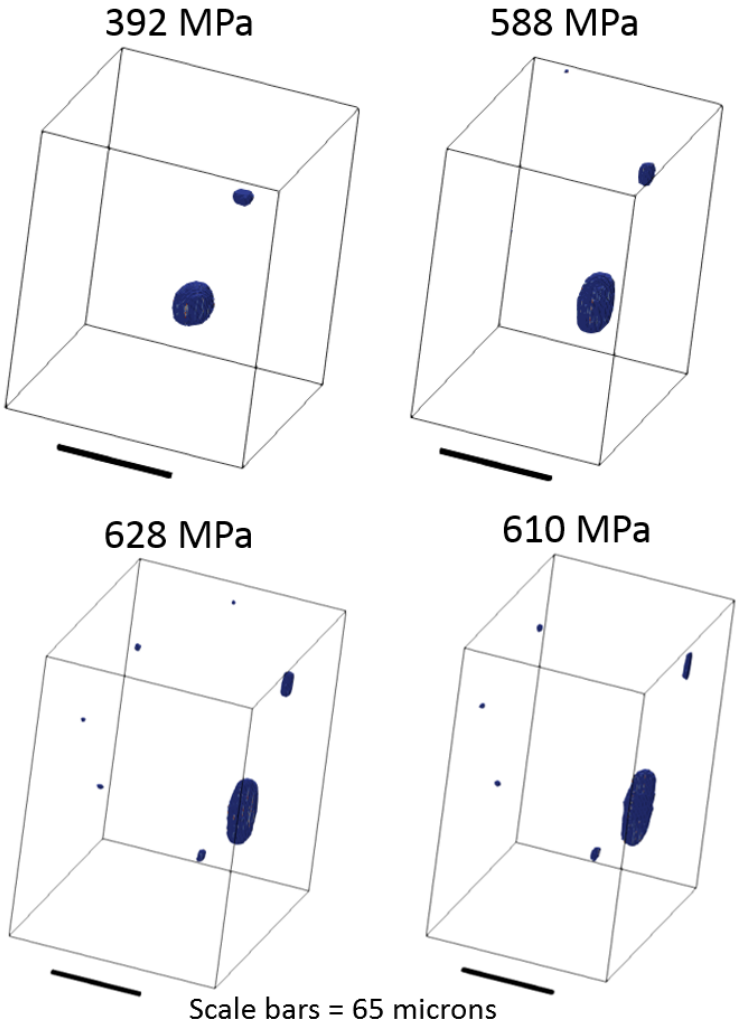

Figure 2.30. Images of a single, large void deforming in specimen H1-8, along with the overall engineering stress state at which the respective images were taken; the void elongates along the loading direction and new voids (either grown above the observation threshold or newly nucleated) appear. In this case we were lucky enough to capture a void in the primary deformation zone

the surfaces are more apparent. Although not shown here (because of the rendering used), voids can be seen in the near surface and subsurface regions, which might be linked to the development of localization in this region. More quantitative analysis of these voids could be conducted to measure if they are significantly different from voids occurring elsewhere.

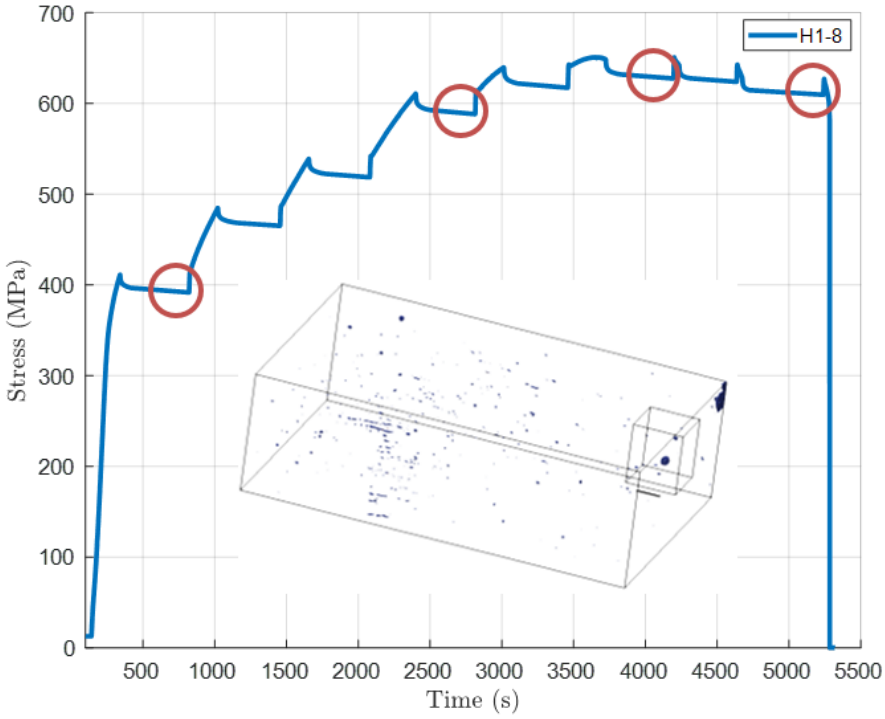

Figure 2.31. Stress versus time (which shows the hold periods), with the points at which the single-void deformation images shown in Figure 2.30 were taken circled

2.5. Discussion

Only highlights of the complete results obtained have been shown, along with aggregated data. Full testing included about 88 total in-situ specimens, of which some 74 were actually tested and 14 were for various reasons untested or had unreliable results. In total 68 more specimens were imaged without in-situ (including the SS316L and Honeywell specimens). As complete of data as could be obtained (there were some operational difficulties) represent a very rich corpus of evidence that could be further explored in several different ways. The void images obtained through XCT can be used directly for mechanical modeling, and two examples of such direct use are shown in the following chapters. Unfortunately, none of the data present a clear or obvious picture of the deformation mechanisms or failure mechanisms, exactly. While voids are present, we do not observe a strong pattern of final failure occurring near the most densely pack or largest void (at least in

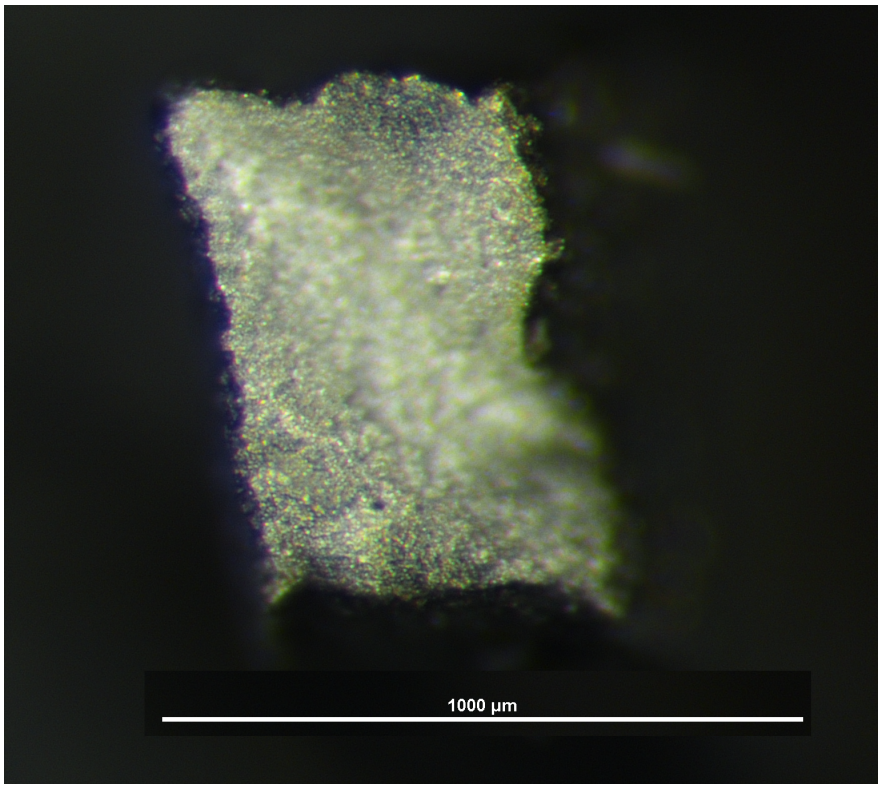

Figure 2.32. Optical microscope image of a fracture surface of specimen V3-4

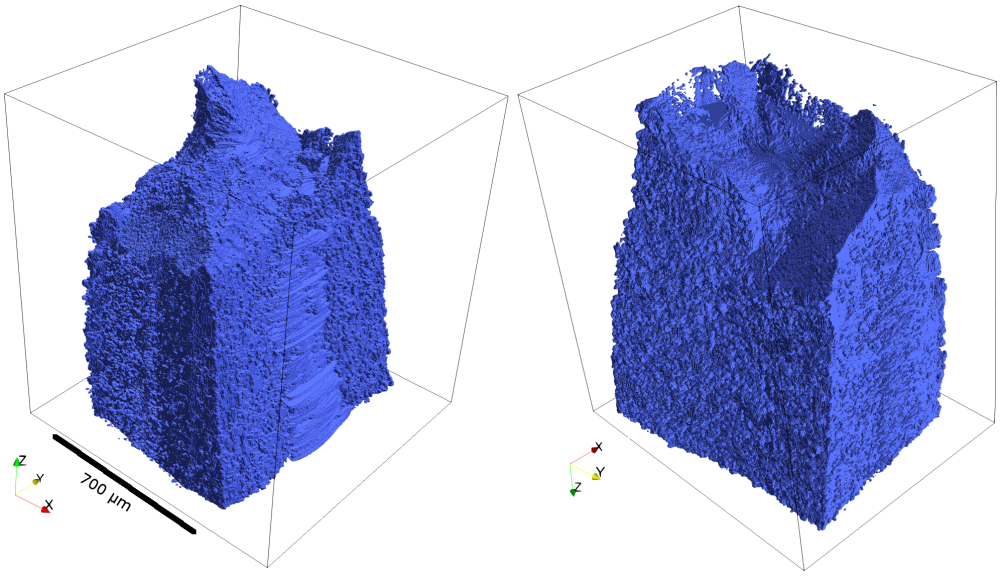

Figure 2.33. XCT scan of the two opposing fracture surfaces of specimen V3-4; left is the bottom, right is the top; scans show the classic "cup-and-cone" failure pattern indicative of ductile rupture in fcc metals.

the imaged region). While voids do have an impact on the propensity for failure, there are multiple competing mechanisms and we have only been able to measure one.

In order to make the most use of the in-situ testing the use of a DVC, or more likely a particle-tracking based algorithm, to reconstruct 3D strain fields in the measured volume would be informative. This would allow for even more direct comparison between models and experiments. Chapter 4 will show one case in which the void in Figure 2.30 is directly compared to a model. However, if a robust method for reconstructing full strain fields were used, this could be extended to a larger volume of material. This could increase confidence in the overall model, and perhaps provide deeper insight into the mechanics observable through void deformations. Implementation of this would require a technique to identify a reference, or zero, point in each of the volumes. Because the deformation between states is large and there may be large rigid body motions, this is not an entirely trivial task although it might be possible. An attempt to reconstruct deformation fields could follow from that.

One possible future work would be to use the existing data to further calibrate, or possibly validate, the failure prediction modeling shown in future chapters, most notably Chapter 5. For example, a further study of the existing data to examine the failure conditions of fracture surfaces could be developed. Currently, Chapter 5 uses data from another study of conventionally manufactured IN718, [**102**], but similar data could probably be gathered from our tests, given a more thorough inspection and analysis of the fracture surfaces (e.g. measurement of local plastic strain and the stress state at failure).

2.6. Summary and Conclusions

This chapter has shown a series of micro/meso-structural and mechanical characterizations of AM material, predominantly LENS IN718, though also SS316L. Largely 3D measurements show the complex, heterogeneous nature of the material. These quantitative 3D measurements provide relatively unique insight into the deformation behavior of the material in ways that would not be possible to understand without in-situ monitoring. Voids are mostly randomly distributed, though

under some circumstances correlations to processing conditions can be made. In single-track, thin-wall IN718 builds, material properties vary from location to location and with orientation. While it is difficult to quantify the precise nature of these effects, some insight is gained by observing the deformation of voids within these specimens. Specifically, we show that for this process and material, voids tend to be on the sub-grain scale and elongate with the material. Final ductile fracture does not appear, at least currently and at this scale, to be solely driven by voids; while voids certainly play a role, there are other important factors, e.g. grain boundary cleavage, that may also be important to consider. The factors measured here, and this elusive interplay between voids and grains, inspired the simulations presented the following chapters that attempt to determine the varying role of voids and grains. In this way, simulations can probe the system response in ways that would be much more challenging using experimental methods (e.g. varying the size of an individual grain while keeping the others constant).

While the methods used here are generally not novel in themselves, neither are they commonplace. In general, these were the first (or nearly first) applications of these methods to AM metals, which present unique challenges and opportunities. The application of in-situ tensile testing and synchrotron x-ray imaging in particular to metal AM and the exploration its heterogeneous, spatially varying nature required innovative uses of these techniques to achieve the desired results. Perhaps most importantly for future chapters, these experiments developed a large database of 3D images of voids in AM material. This database contains about 600,000 individual voids, in a total inspected volume of perhaps $145\,\mathrm{mm}^3$ at a resolution of either $0.65\,\mu\mathrm{m}$, or $0.87\,\mu\mathrm{m}$ voxel edge length for a smaller subset of the data. In this database, each void is uniquely identified and its characteristics are measured, as was shown for a subset of the data in the analysis in Section 2.2.3. A summary of the key outcomes from these experiments, and their utility throughout the remaining chapters, are summarized in Table 2.5.

Possible areas for future exploration and analysis abound, even using these existing datasets. For example, further study of the reduction of area versus elongation would provide a quantifiable measure for ductility. Measurement of final cross section could be done on either the specimens

Table 2.5. Summary of the key experimental findings

Experiments	Novelty	Used to	In Chapter
3D measurements of voids in Honeywell IN718	Prior measurements mostly 2D, lower resolution, or smaller area	Make representative "mean ellipse" for CPFE fatigue model	3
Measured grains in SS316L and IN718	3D grain measurements and residual stresses for AM	Make polycrystalline microstructures with synthetic reconstruction	4
3D void measurements in SS316L	3D void measurements (previously 2D or smaller area) and their relationship with processing conditions	Make polycrystalline plus voids microstructures	4
3D void measurements in LENS IN718 thin-walls	Spatial dependence of voids in a simply build and between processing conditions	Construct porosity relationship with location and thermal history, and the void image database	2, 5
In-situ void deformation measurements	No other reports of void-driven 3D deformation observations in AM material	Validate single crystal models, potential future work	4, 6

themselves, or using reconstructed XCT scans of of the fracture regions. We could also analyze more closely the void growth patterns, and how void appear in the failure regions after fracture. If we identify which specimens we capture the eventual fracture region within the initial scan, we could track the progression of voids throughout the process in those examples. We could also explore direct analysis of grain sizes, and the difference in "effective" grain size with different orientation though more complete measurement of grains either in the coupons themselves or nearby where they were cut from. A more fair comparison of mechanical properties with wrought material could be made by solutionalizing the wrought material before testing it.

While some work has been done to compare ultimate tensile strength to thermal indicators (i.e. [**8**]), future analysis could also include comparisons between measured mechanical performance indicators (e.g. stiffness, ultimate strength, yield strength, ductility) and spatial location or thermal history for the various different coupons and walls to deduce trends or build predictive relationship. Unfortunately, there is a lot of noise in the data that makes this difficult. For example, the variability within each specimen might be as large as the variability between specimens. This would require a close inspection of individual specimens, although this is challenging because exact

location and details of the thermal history are difficult to deduce in the small region of the gage section.

CHAPTER 3

Material modeling: crystal plasticity finite elements and fatigue calibration

3.1. Background and motivation

The previous chapter demonstrated that there are important factors that control deformation and failure at the scale of voids and grains (the 1 µm to 100 µm regime) in AM materials. In order to predict the response of these materials, these factors need to be captured. For example, anisotropic elastic response, yield strength, ultimate strength, and elongation can be related to differences in grain orientations and size/shape as well as void distribution and size/shape. In order to accurately and predictively model these effects, a material law that captures the relevant behavior is required. To do this, a crystal plasticity (CP) model is chosen. Succinctly, the CP model here provides a mechanistic basis for anisotropy by considering only deformations permissible on a single crystal (the so-called "active slip systems") at each material point in the analysis. The highlights of this chapter are:

- Crystal plasticity finite element material model calibrated to IN718 data
- High cycle fatigue model calibrated to experimental IN718 data in literature
- Physically-inspired model geometry simulated under several conditions
- Model predictions indicate that grain orientation and size (specifically, variations from mean size) can effect both overall fatigue life and variability in fatigue life
- Simulations show that voids of the mean size observed with XCT likely contribute to a reduction in fatigue life, as they are stronger stress raisers (promoting local plastic flow) than grain boundary (at least as modeled here)

3.1.1. Crystal plasticity (CP) finite element constitutive law

The following description of the crystal plasticity law is extracted, in lightly edited form, from [**72**], a book chapter that I wrote with Zeliang Liu and Cheng Yu. This is, in fact, largely the same material model used by [**89**] and is derived from [**83**] and [**100**] with some additions and bug fixes. The final chapter of [**7**] includes a thorough discussion of CP material modeling, and the interested reader is directed to that chapter for more. The mechanical model outlined here is the so-called CP material law, such as those described in the overview of Roters *et al.* [**107**].

3.1.1.1. A brief overview of the CP model. Crystal plasticity in conjunction with the finite element method (termed CPFEM or CPFE) has been applied to solve both microscopic and macroscopic problems, following from the early combinations of classical plasticity and the finite element method, e.g. [**94**]. It has two primary variants: polycrystal and single crystal plasticity. In the polycrystal formulation, each material point is assumed to represent a collection of crystals such that the overall response of the point is homogeneous. In single crystal plasticity, each material point is assumed to represent a single crystal, or a point in a single crystal, the deformation of which is governed by the particularities of single crystal deformation mechanics (e.g. active slip systems and/or dislocation motion). The former approach is more commonly used for macroscopic problems, where a relatively large solution volume is desired. The later shall be the focus of this chapter, and has been used to solve microscopic problems, e.g. those related to void mechanics within metals. There are many versions of crystal plasticity laws in both form. Here the basic kinematics and constitutive law of the version of McGinty and McDowell [**83**] are applied, and are discussed below.

3.1.1.2. Kinematics. The deformation gradient $\mathbf{F}$ can be multiplicatively decomposed as:

$$\mathbf{F} = \mathbf{F}^e\mathbf{F}^p \tag{3.1}$$

where the plastic part $\mathbf{F}^p$ maps points in the reference configuration onto an intermediate configuration which is then mapped to a current configuration through the elastic part $\mathbf{F}^e$. Note that

physically $\mathbf{F}^p$ is associated with the dislocation motion and $\mathbf{F}^e$ is a combination of the elastic stretch and rigid body rotation.

The effect of dislocation motion is modeled by relating the plastic velocity gradient $\tilde{\mathbf{L}}^p$ in the intermediate configuration (usually denoted by $\tilde{\square}$) to simple shear deformation $\gamma^{(\alpha)}$:

$$\tilde{\mathbf{L}}^p = \sum_{\alpha=1}^{N_{\text{slip}}} \dot{\gamma}^{(\alpha)} (\tilde{\mathbf{s}}^{(\alpha)} \otimes \tilde{\mathbf{n}}^{(\alpha)}) \tag{3.2}$$

where $\otimes$ is the dyadic product, N_{slip} is the number of slip systems, $\dot{\gamma}^{(\alpha)}$ is a shear rate, $\tilde{\mathbf{s}}^{(\alpha)}$ is the slip direction, and $\tilde{\mathbf{n}}^{(\alpha)}$ is the slip plane normal, all for a crystal slip systems (α) in the intermediate configuration. The relationship between $\tilde{\mathbf{L}}^p$ and $\mathbf{F}^p$ is given by

$$\tilde{\mathbf{L}}^p = \dot{\mathbf{F}}^p \cdot \left(\mathbf{F}^p\right)^{-1}. \tag{3.3}$$

3.1.1.3. Constitutive law. The final task in constructing the crystal plasticity framework is defining the constitutive laws of elasto-plasticity. We choose a basis of the Green-Lagrange strain $\mathbf{E}^e$ and Second Piola-Kirchhoff stress $\mathbf{S}^e$, from the many conjugate pairs available, which are related by:

$$\mathbf{S}^e = \tilde{\mathbf{C}} \cdot \mathbf{E}^e = \frac{1}{2} \tilde{\mathbf{C}} \cdot [(\mathbf{F}^e)^{\mathrm{T}} \mathbf{F}^e - \mathbf{I}], \tag{3.4}$$

where the elastic stiffness tensor $\tilde{\mathbf{C}}$ is defined in the intermediate configuration.

A phenomenological power law for the plastic shear rate in each slip system given by

$$\dot{\gamma}^{(\alpha)} = \dot{\gamma}_0 \left| \frac{\tau^{(\alpha)} - a^{(\alpha)}}{\tau_0^{(\alpha)}} \right|^{(m-1)} \left(\frac{\tau^{(\alpha)} - a^{(\alpha)}}{\tau_0^{(\alpha)}} \right) \tag{3.5}$$

is used, where $\tau^{(\alpha)}$ is the resolved shear stress, $a^{(\alpha)}$ is a backstress that describes kinematic hardening, $\dot{\gamma}_0$ is a reference shear rate, $\tau_0^{(\alpha)}$ is a reference shear stress that accounts for isotropic hardening, and m is the material strain rate sensitivity. Shear stress is resolved onto the slip directions with:

$$\tau^{(\alpha)} = \boldsymbol{\sigma} : (\mathbf{s}^{(\alpha)} \otimes \mathbf{n}^{(\alpha)}), \tag{3.6}$$

where $\boldsymbol{\sigma}$, $\mathbf{s}^{(\alpha)}$ and $\mathbf{n}^{(\alpha)}$ are the Cauchy stress, slip direction and slip plane normal respectively, all of which are in the current configuration. The Cauchy stress is given by:

$$\boldsymbol{\sigma} = \frac{1}{J_e}[\mathbf{F}^e \cdot \mathbf{S}^e \cdot (\mathbf{F}^e)^{\mathrm{T}}], \tag{3.7}$$

where J_e is the determinate of $\mathbf{F}^e$. The relationship between $\mathbf{s}^{(\alpha)}$ and $\tilde{\mathbf{s}}^{(\alpha)}$ is given by

$$\mathbf{s}^{(\alpha)} = \mathbf{F}^e \cdot \tilde{\mathbf{s}}^{(\alpha)}, \tag{3.8}$$

and the relationship between $\mathbf{n}^{(\alpha)}$ and $\tilde{\mathbf{n}}^{(\alpha)}$ is given by

$$\mathbf{n}^{(\alpha)} = \tilde{\mathbf{n}}^{(\alpha)} \cdot (\mathbf{F}^e)^{-1}, \tag{3.9}$$

which ensures that the slip plane normal vector remains orthogonal to the slip direction in the current configuration.

The reference shear stress $\tau_0^{(\alpha)}$ evolves based on the expression:

$$\dot{\tau}_0^{(\alpha)} = H \sum_{\beta=1}^{N_{\text{slip}}} q^{\alpha\beta} \dot{\gamma}^{(\beta)} - R_d \tau_0^{(\alpha)} \sum_{\beta=1}^{N_{\text{slip}}} |\dot{\gamma}^{(\beta)}|, \tag{3.10}$$

where H is a direct hardening coefficient and R_d is a dynamic recovery coefficient and $q^{\alpha\beta}$ is the latent hardening ratio given by:

$$q^{\alpha\beta} = \chi + (1 - \chi)\delta_{\alpha\beta} \tag{3.11}$$

where χ is a latent hardening parameter. The backstress $a^{(\alpha)}$ evolves based on the expression:

$$\dot{a}^{(\alpha)} = A_h \dot{\gamma}^{(\alpha)} - A_d a |\dot{\gamma}^{(\alpha)}|, \tag{3.12}$$

where A_h and A_d are direct and dynamic hardening factors respectively.

A computational crystal plasticity algorithm needs to solve a set of non-linear equations from Eq. (3.1) to Eq. (3.12). Different numerical methods can be used to solve these equations. McGinty and McDowell [**83**] gave an implicit time integration algorithm for the material law with the finite element method.

3.2. CPFE modeling for fatigue prediction of polycrystals

3.2.1. Crystal plasticity model calibration for AM IN718+

A representative volume element (RVE) approach was taken to calibrate the tensile response of the crystal plasticity constitutive law used. This model uses the 12 primary FCC active slip systems associated with the primary matrix phase of IN718. The slip systems used are given in Table 3.1. The material parameters were calibrated to tensile experiments conducted on AM IN718+ with two different powder lots, which shows the amount of consistency between production runs of the precursor material. The calibrated material parameters are given in Table 3.2.

In order to obtain these calibrated parameters, a cubic RVE with 64 cubic grains (four grains in each direction) was constructed using Abaqus CAE. A python script was written to apply the material parameters and three random Euler angles to each grain, resulting in an isotropic RVE with randomly oriented grains (based on a spherical distribution). This represents a heat-treated material similar to that used to generate the experimental test data. The mesh, with one instantiation of orientations, is shown in 3.1. A mesh with five elements per side for each grain was used (and thus 8,000 total elements). Abaqus's C3D8R element – a reduced integration hexahedral element with hourglass control – was selected. The hourglass control avoids potential issues with hourglassing in reduced integration elements, while simultaneously treating near-incompressibility better than a fully-integrated element (less pressure-locking possible) and saving about a factor of eight in computational time. A validation study indicated that the results with fully-integrated C3D8 elements were largely similar.

The RVE was loaded in tension by applying symmetry boundary conditions (BC) to three orthogonal faces, and a displacement BC to a face parallel to one of the symmetry-condition faces.

Table 3.1. The 12 active FCC slip systems considered by the CP constitutive law

Slip system	Slip plan normal	Slip direction
1	(111)	$[\bar{1}01]$
2	(111)	$[\bar{1}10]$
3	(111)	$[0\bar{1}1]$
4	$(\bar{1}\bar{1}1)$	[011]
5	$(\bar{1}\bar{1}1)$	$[\bar{1}10]$
6	$(\bar{1}\bar{1}1)$	[101]
7	$(\bar{1}11)$	[101]
8	$(\bar{1}11)$	[110]
9	$(\bar{1}11)$	$[0\bar{1}1]$
10	$(1\bar{1}1)$	[011]
11	$(1\bar{1}1)$	[110]
12	$(1\bar{1}1)$	$[\bar{1}01]$

In this case, the displacement BC was applied to the top face and displaced upward. This symmetry condition means that the middle grains are virtually twice the size of the other grains, but this does not seem to substantially effect the uniaxial tension calibration, other than perhaps to promote localization in the bottom layer of grains. This configuration is thought to represent the undamaged, defect-free nature of the tension tests. A deformed configuration, after loading, is shown with contours of von Mises equivalent stress in 3.2a and effective plastic strain 3.2b, as one example of the calibration tests. In this case, deformation on the free surface varies because of the different grain orientation of the grains on the surface of the RVE.

To conduct the calibration, the overall stress-strain response of the RVE was computed with a C++ API script for Abaqus by averaging the stress and strain components of interest (e.g. for this RVE with z-direction loading, the z-component was taken) across all elements for each time step ("frame" in Abaqus's terminology). This choice is not unique: many stress measures could be chosen. Stress in the direction of loading give a reasonable comparison to the measured stress in the tension test. The calibrated overall stress-strain response of the RVE is shown in 3.3.

Table 3.2. Constitutive parameters for the CP material law, fit to room temperature tensile data for fully heat treated AM IN718+ using a 64 grain SVE approach

C_{11}(MPa)	C_{12}(MPa)	C_{44}(MPa)	$\dot{\gamma}_0$	m*	g_0 (MPa)	H(MPa)	R_d	χ
257,000	127,000	94,000	0.00242	58.8	358.0	760.0	5.3	6.5
a_0	A_h(MPa)	A_d						
0.0	753.0	8.5						

*From [**19**], which has a similar CP formulation

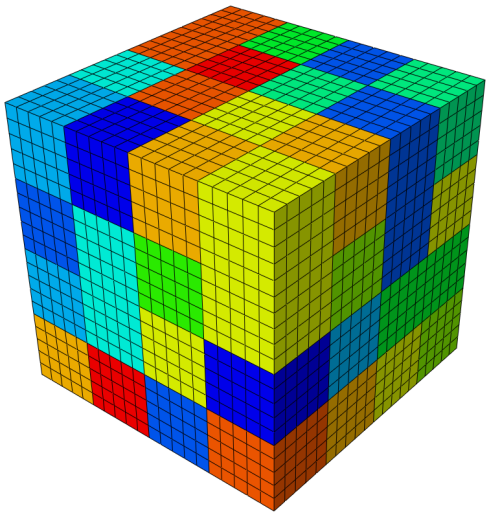

Figure 3.1. Undeformed configuration for on instantiation of the calibration volume. This has 64 cubic grains with random ψ, θ, and ϕ Euler angles, arranged in a cube. Colored by ϕ, so different colors are different grains (although some grains have similar ϕ).

3.2.2. Fatigue Indicating Parameter (FIP): computing and calibrating

3.2.3. Computing FIP

A fatigue indicating parameter (FIP) is used to estimate the fatigue life from plastic deformation after a few cycles of fatigue loading. The Fatemi-Socie FIP [**22**], modified by McDowell to be applicable to microstructural analysis [**112**], used here is defined as:

$$\text{FIP} = \frac{\Delta\gamma^p}{2}\left(1+\kappa\frac{\sigma_n}{\sigma_y}\right) = \gamma^f\left(2N_{\text{inc}}\right)^c \tag{3.13}$$

where $\Delta\gamma^p$ is the stabilized cyclic change in plastic shear strain, κ is a normal stress factor (here it is 0.55), σ_n is the stress normal to $\Delta\gamma^p$, σ_y is the yield stress, γ^f and c are Coffin-Manson-type

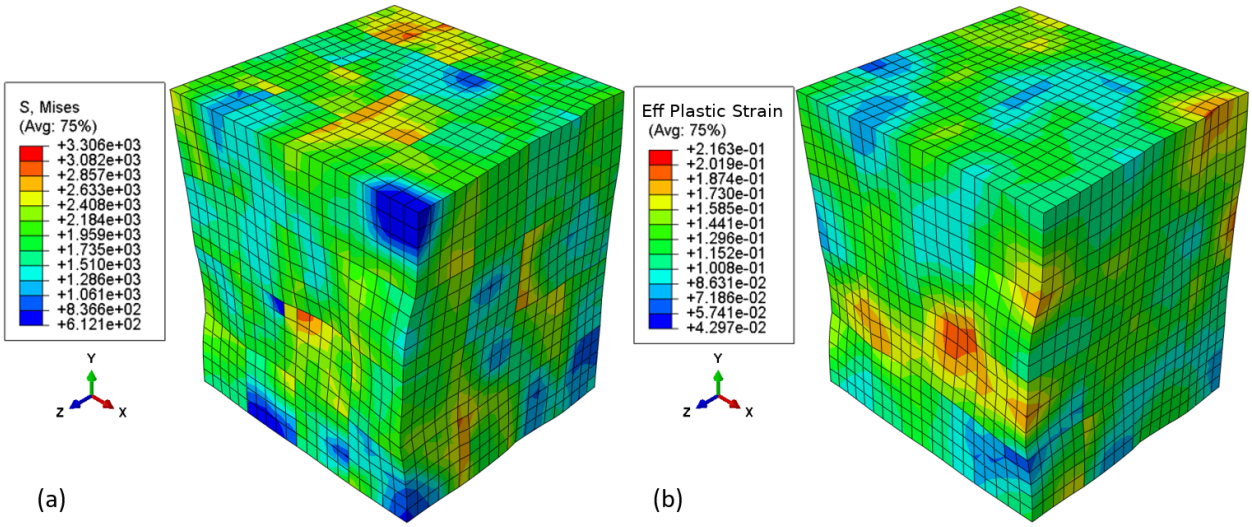

Figure 3.2. Deformed configuration of calibration volume subjected to uniaxial tension in the vertical direction (applied with symmetry boundary conditions and a prescribed vertical (Y) displacement for the top surface), colored by (a) von Mises stress (b) effective plastic strain. Deformation is scaled to be clearly apparent.

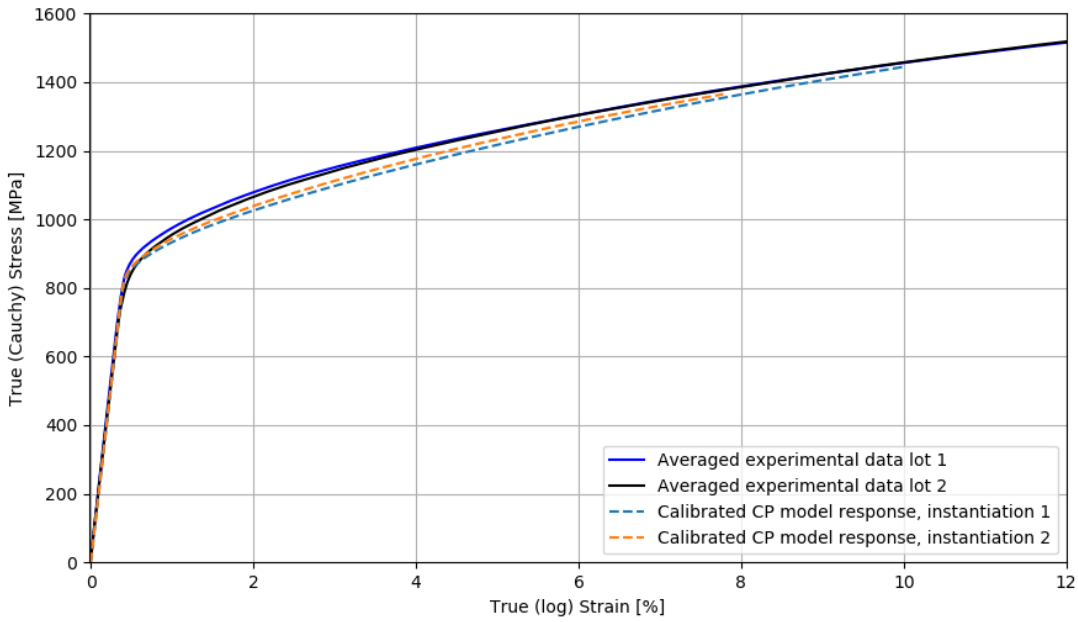

Figure 3.3. Calibrated overall RVE response with CP (dashed) and "average" experimental tension test results (solid) from heat treated AM IN718+ (two different powder lots; data from Honeywell)

multiplicative and exponential fitting parameters. To estimate the fatigue life of a microstructure, the maximum value of FIP, which corresponds to a minimum value of N_{inc} is found. However,

this maximum represents a localized parameter, and to set a length scale and avoid some mesh dependency associated with local responses, a local volume averaging is applied. An averaging volume about 0.1 times the size of the feature of interest is typical.

The same cubic RVE used to calibrate the material parameters under tension was used to calibrate the FIP parameters, this time loaded in fully reversed tension-compression fatigue. The overall stress-strain response of the material is shown by the hysteresis loops in Figure 3.4. From this, the FIP was determined. Specifically, first $\Delta\gamma^p$ was computed using the 3^{rd} and 4^{th} cycles of loading (at which point the $\Delta\gamma^p$ field is usually saturated). This was used to compute the normal stress, σ_n. FIP was computed elementwise using Eq. (3.13). A local volume averaging of FIP was computed. For each element, a spherical kernel was constructed. Elements with centroid within this sphere were weighted by their volume and included in the averaging filter. I.e., $\text{FIP}_j^{filt} = \frac{\sum_{e=1}^{n}(\text{FIP}_e \times V_e)}{V_{filt}}$ where FIP_j^{filt} is the "filtered" (as indicated by the superscript "filt") FIP at the current element j; n is the number of elements in the kernel around that element, FIP_e is the FIP is an element in the kernel (including the current element), V_e is that element's volume, and V_{filt} is the total volume of all elements in the filter. Basic mesh and mechanical response data were collected using Abaqus C++ API calls, using a similar code to that used to extract the tensile calibration data but modified to work with the local cyclic data used for FIP (rather than monotonic averaged data for tensile calibration). This data was written to files that were read using a Python script, which performed the computations required to arrive at the unfiltered and filter FIP values. Element volume was computed as the volume of the convex hull of the nodes assigned to that element. In this case, the diameter of the kernel was selected to be 0.1 times edge length of the RVE. These FIP values then exported to a VTK file an visualized using ParaView. The RVE with contours of unfiltered (a) and filtered FIP (b) field is shown in Figure 3.5. The maximum FIP in the region corresponds to the minimum fatigue life, and can be used to calibrate the FIP to observed fatigue life.

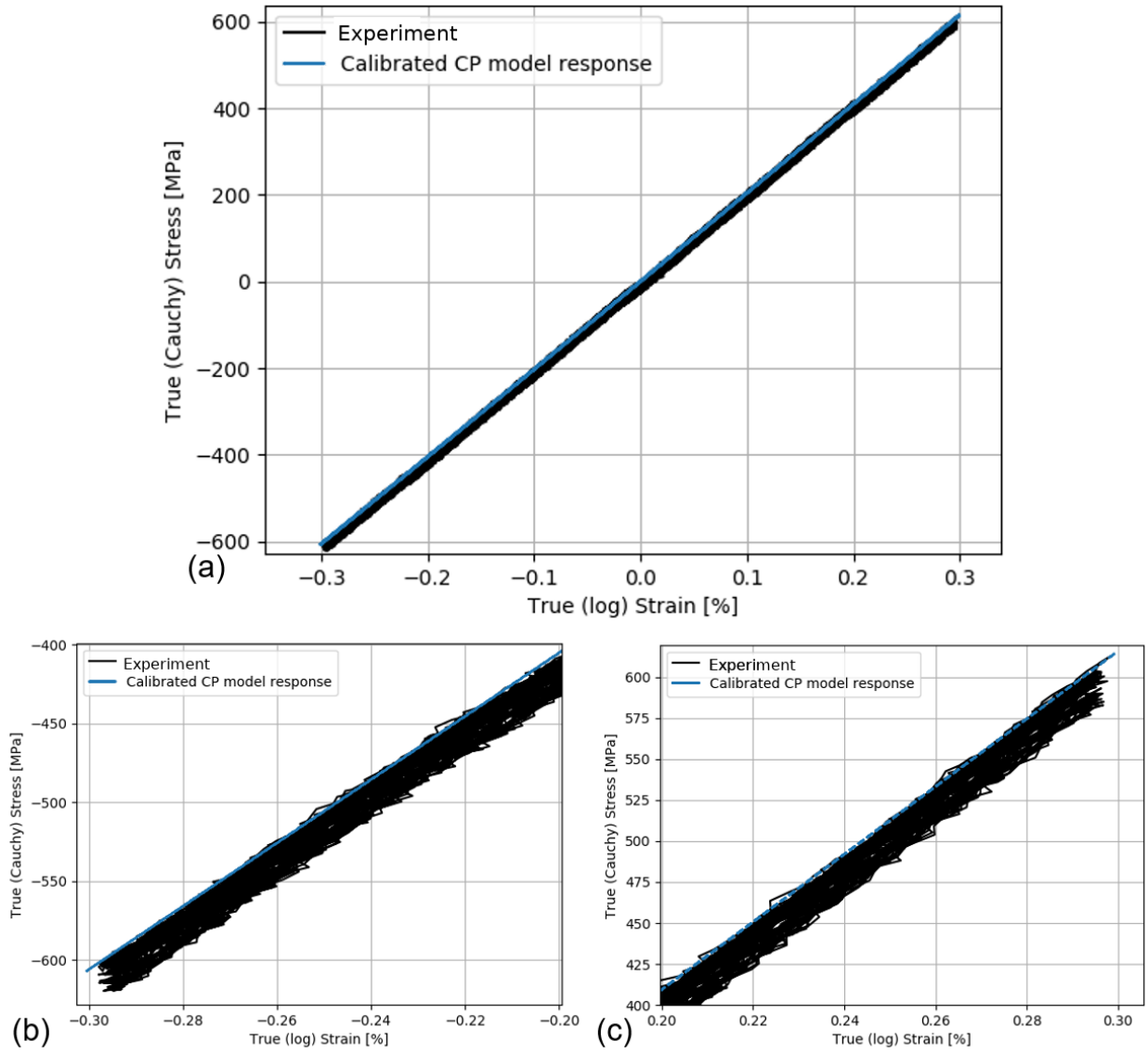

Figure 3.4. (a) Cyclic stress strain response of simulated (blue) and measured (black) IN718+. (b) detail showing match at minimum stress; (c) match at peak stress. This is for stress ratio $R = -1$, strain amplitude 0.3%, 0.33 Hz, cycles 1 to 30,000, periodically plotted for the experiments (once loop every 3,000 cycles), and the first 4 cycles from the simulation. These results show good similarity between the model and experiment within this strain range for the CP law calibrated to tensile results

3.2.4. Statistical model for HCF of IN718 and modification for AM IN718+

There is very little open literature data on fatigue of IN718+, much less AM IN718+, for high-cycle conditions. The experimental data we have for AM IN718+ mostly does not extend to the high-cycle regime. Thus, literature data for IN718 under high cycle conditions was collected

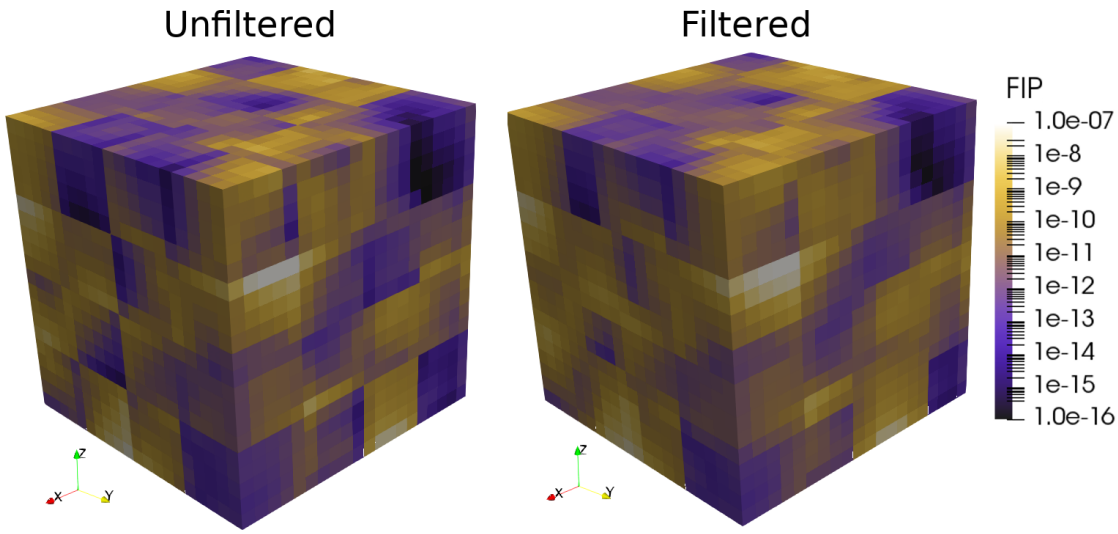

Figure 3.5. (left) raw FIP and (right) volume averaged FIP at 0.3% strain amplitude for the reference RVE. Locally, FIP values vary because some local plasticity occurs (e.g. in grains oriented to be "soft" with respect to the direction of load), even when overall loading does not show hysteresis or a bulk plastic response.

from the sources listed in the references: [**2, 3, 6, 11, 12, 13, 14, 15, 19, 25, 28, 36, 51, 52, 56, 61, 73, 76, 78, 87, 90, 93, 96, 120, 122, 137, 149**]; of these, the most notably useful were [**6, 15, 73, 137, 149**]. Data were collected and adjusted where needed to align with the stress ratio $R = \frac{\sigma_{min}}{\sigma_{max}} = -1$ condition used for calibration and other tests (using the standard Basquin's equation for mean stress adjustment). Two different approaches to generating a statistical model were taken: in the first, data in each paper was fitted independently with a Coffin-Manson type power-law curve ($y = ax^b$) and the average and standard deviations of those Coffin-Manson parameters was computed. In the second, all data points were taken to be equal, and a Coffin-Manson curve was fitted to the entire collection of points. The statistics (confidence levels, standard deviations, etc.) of the Coffin-Manson parameters obtained this way were also computed. In each case, two approaches to run-out points were taken: either these points were censored or included directly as failures. The former approach is typically preferred, because runouts are not actual failure data points. However, for our purposes taking runouts as failure may give us a closer approximation to the HCF slope than ignoring this data. It is also a more conservative estimate,

Table 3.3. Coffin-Manson type fit parameters for uncensored and censored literature data for IN718

Parameter	Estimate	Std. error	t-value	Pr($>\|t\|$)
a uncensored (multiplier)	130.4	11.22	11.62	<2e-16
b uncensored (exponent)	-0.03210	0.005808	-5.681	1.15e-7
a censored	157.7	16.75	9.416	2.93e-15
b censored	-0.04656	0.007443	-6.256	1.13e-8

as failures are considered prematurely in the model. For this reason, fits to both the censored and complete datasets are computed.

The fitted exponential Coffin-Manson curves for censored and uncensored data was adjusted by a multiplicative factor such that the curve matched with experimental data from Honeywell (unavailable for release here). This adjustment is shown graphically in Figures 3.6 and 3.7 as dotted lines (teal and magenta).

All the data collected (green circles) are displayed in Figure 3.6, with corresponding fit curves to all points equally (black) with a 95% confidence interval (dashed blue), mean of sets from each paper (gray) and a 95% confidence interval to that (dashed gray; the upper bound is outsize the window), the all-point (including runouts) curve adjusted to cross the AM IN718+ HCF data point (curve is magenta dotted) and its lower 95% confidence interval bound (dotted teal line). The censored data is plotted identically in Figure 3.7. The parameters used to generate these plots are given in Table 3.3. Finally, these results were normalized to the same effective strain amplitude and a Weibull distribution was fit to assess the chance of failure.

3.2.5. Calibrating the FIP constants

In order to calibrate the FIP, one must first have an idea of the stress- or strain-life behavior of the material; once some data is collected, preferably data where the fatigue mechanism of the tests is the same as those that one wishes to predict, parameters of the FIP can be calibrated. Doing this involves adjusting the γ^f and c parameters in Eq. (3.14) such that the N_{inc} predictions fall near the data points available, under a known reference condition (e.g. prescribed strain amplitude

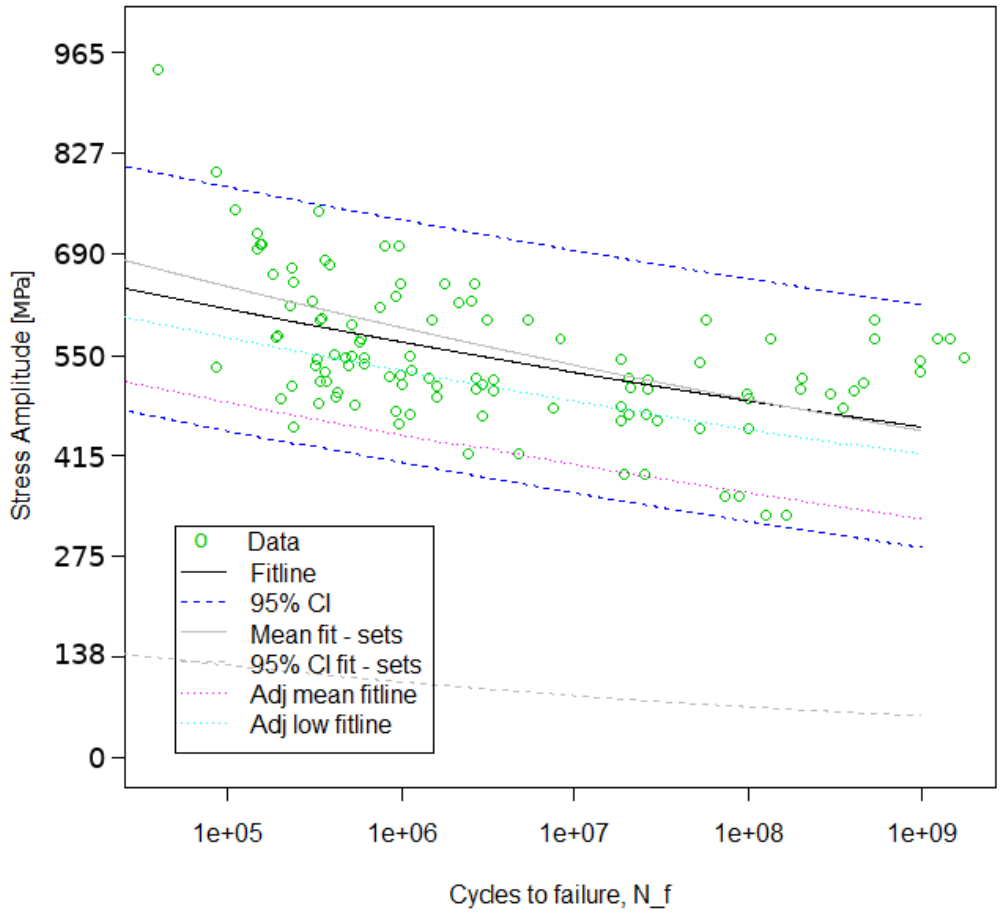

Figure 3.6. All collected HCF data from literature (green points), and fitted stress-life curves for all data (black curve) and data points grouped by experiment (gray curve) plotted on log-x axes

and microstructure). The effect of deviations from this reference condition can then be predicted in terms of an estimated number of incubation cycles at a specified strain amplitude.

$$N_{\text{inc}} = \frac{1}{2}\left(\frac{\text{FIP}}{\gamma^f}\right)^{\frac{1}{c}} \tag{3.14}$$

In practice, this calibration involves minimizing a cost function based on the distance in cycles between the minimum N_{inc} predicted by the FIP model (an approximation for the number of cycles to failure), and an N_f based on experimental data. This is thus under the assumption that N_{inc} dominates total lifetime, so N_{inc} and N_f are comparable. The cost function used here is given in

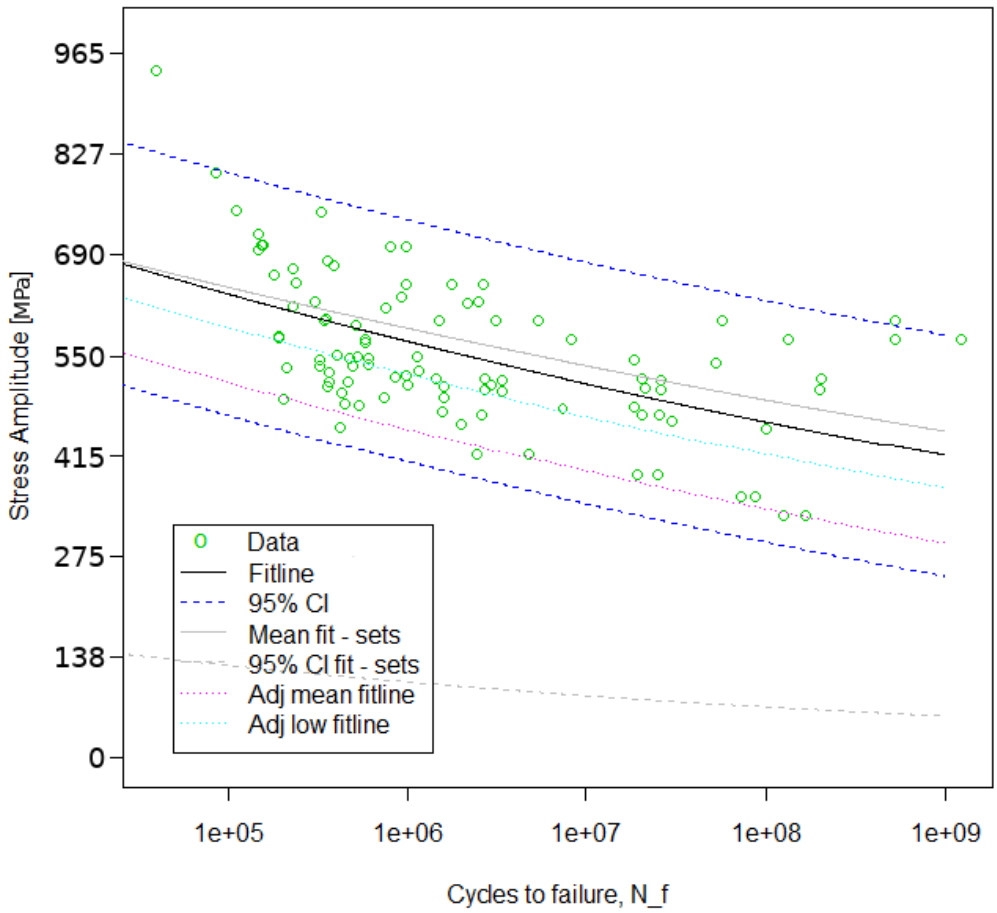

Figure 3.7. Stress-life curve similar to Figure 3.6, now with censored (run-out removed) data

Eq. (3.15). It defines the Euclidean distance, Δ, in log10 space between the fatigue lives, where K is the total number of observations, $N^i_{inc,sim}$ is the i^{th} FIP-based measure of life, and $N^i_{f,exp}$ is the i^{th} experiment-based measure of life. A logarithmic distance measure is used to avoid over-weighting low strain amplitude (high life) points and under-weighting high strain amplitude (low life) points, because fatigue lives follow a vaguely exponential trend (linear when plotted in log-log coordinates).

$$\Delta = \sqrt{\sum_{i=1}^{K} \left[\left(\log_{10}\left(N^i_{inc,sim}\right) - \log_{10}\left(N^i_{f,exp}\right) \right)^2 \right]} \tag{3.15}$$

Table 3.4. Calibrated FIP parameters

γ^f	c
0.60902	-1.6186

One can find the γ^f and c that minimizes the total distance for all points under consideration using standard function minimization techniques; a method to do this has been implemented in Python using *scipy.optimize.minimize* and its toolbox of minimization routines (specifically, the Nelder-Mead method seems to work well for this function).

For this, the $N_{f,exp}$ values were computed from the statistical model developed in Section 3.2.4. A Coffin-Manson-type (exponential) curve was fit to the failure data and used to interpolate the cycles to failure at the strain amplitudes used in the simulation. Figure 8 shows a strain-life plot with log-x axis; the red line is the curve based on experimental data, and the blue crosses are the calibration points using FIP computed from the reference volume shown in Figure 3.5. If log-y is used this is a straight line (but the divisions are difficult to read). The FIP parameters that minimize Eq. (3.15) for the reference RVE case are given in Table 3.4.

The data were also used to define a 3-parameter Weibull distribution failure model. These data could be used to define a percent survival chance given a number of cycles (or cycles given a desired survival chance). Future work could involve defining a desired failure chance and basing the experimental values for number of cycles on that, before defining the exponential interpolation.

3.3. Computing N_{inc}: test-coupon-inspired geometry

Once the FS FIP parameters are calibrated for a reference case, they can be used to predict fatigue life under other cases using the same approach. Although we hope for an accurate prediction, the variability and model uncertainty likely restrict observations based on this prediction to trends rather than absolute values.

In this case, an image-inspired geometry was constructed based on observed fracture surfaces occurring at what appeared as large (perhaps, this is a relative term) planar features, probably grain boundaries, as shown in Figures 3.9 and 3.10. The testing was conducted by the Engineering

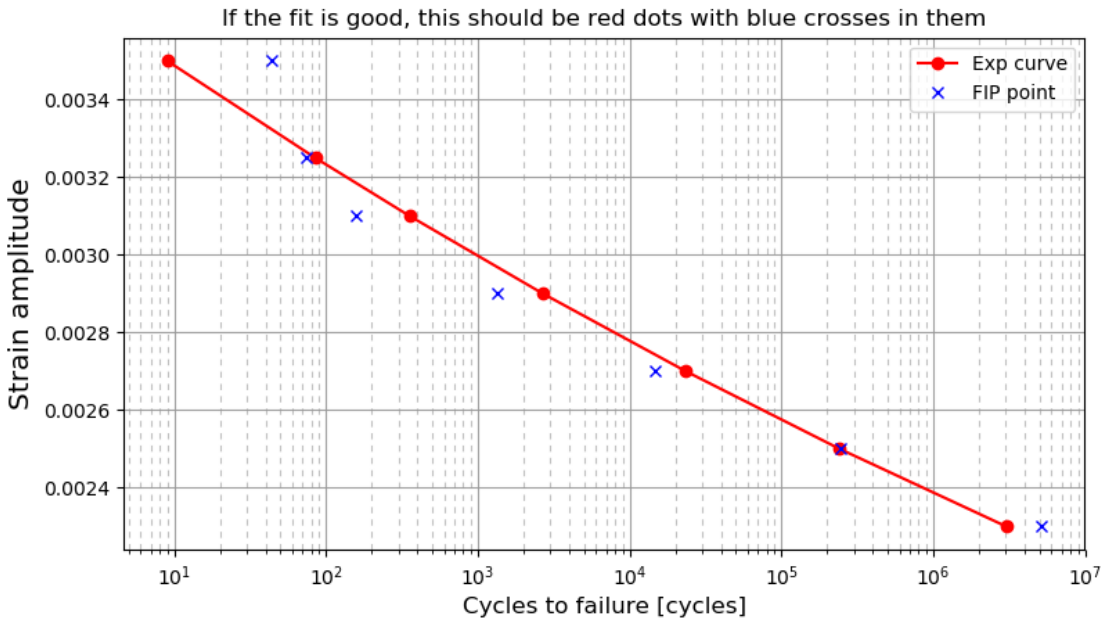

Figure 3.8. FIP predictions versus statistical model of fatigue life, used for calibrating the FIP parameters. The FIP points shown minimize the cost function in Eq. (3.15). A perfect fit would overlay the blue crosses and red dots. Because this FIP is designed for HCF, it seems reasonable that for lower number of cycles the fit is mismatched (i.e. low-cycle mechanisms are not captured)

Test Services' Materials Laboratory at Honeywell, who provided a post-failure specimen. A large grain (maybe about 200 µm) was seen to protrude from the fracture surface near the point of fatigue initiation in Figure 3.9. A similar failure feature was noted in higher cycle fatigue tests, micrographs of which are not reproduced here. This indicates a potential for cleavage-type failures in the interface between grains, particularly large grains.

A sample geometry and mesh inspired by these images are shown in Figure 3.11. This geometry is constructed so a single long grain is present near the free surface at the edge of the cylinder. This may be like features seen in the SEM micrographs reproduced in the above figures. The mesh has 105 different grains, each with a random orientation drawn from a spherical distribution. This represents the case of a heat treated, recrystallized specimen with random orientation and approximately equiaxial (except for the one larger grain) grains. Again, symmetry boundary conditions were used on three faces (sides and top), this time to create a cylinder. An axial displacement

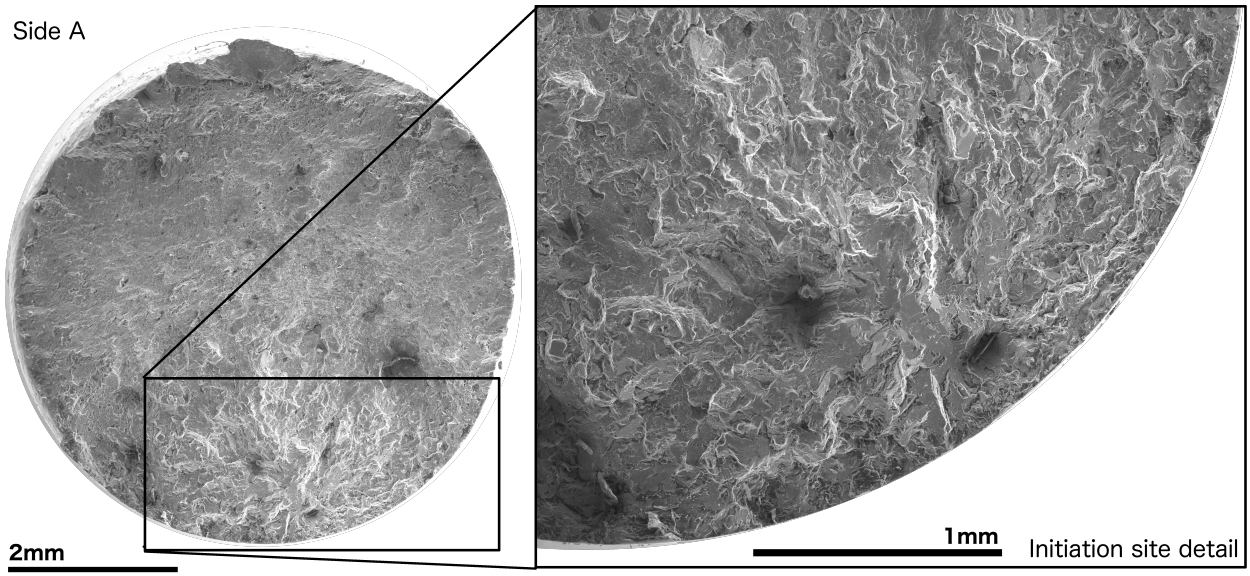

Figure 3.9. SEM images of an example failure surface for IN718 printed with DMLS and machined into a test coupon under cyclic loading. In this case, strain amplitude was 0.218%, testing was at 426.7 °C, and failure measured by a 50% drop in stress occurred at 100,186 cycles. Failure seems to be due to intergranular separation or cleavage (the large planar feature near the initation point by be a grain boundary that has separated)

boundary condition was applied to the fourth (bottom) and used to impose constant strain rate cyclic loading at 0.33 Hz.

The computed FIP fields with two different sets of grain orientations under different strain amplitudes is shown in Figure 3.12. This results in the predicted fatigue lives are given in Figure 3.13, where three different cases of lives are shown.

These results show that there is some sensitivity to grain orientation. This is expected, because stress concentration caused by misorientation (orientation discontinuity at a grain boundary) is the major driver of plastic strain inhomogeneity. To further explore this sensitivity, and particularly the role of the single large grain in that sensitivity, two existing instantiations (1 and 3 from above) were modified. For both cases, the large grain was manually set to orientations (90, 45, 0), (0, 45, 0) and (0, 0, 0) in terms of Euler angles with respect to the load axis. The resulting strain life points are compared to the strain life behavior with random orientation shown previously by replotting all the points on a single set of axes in Figure 3.14.

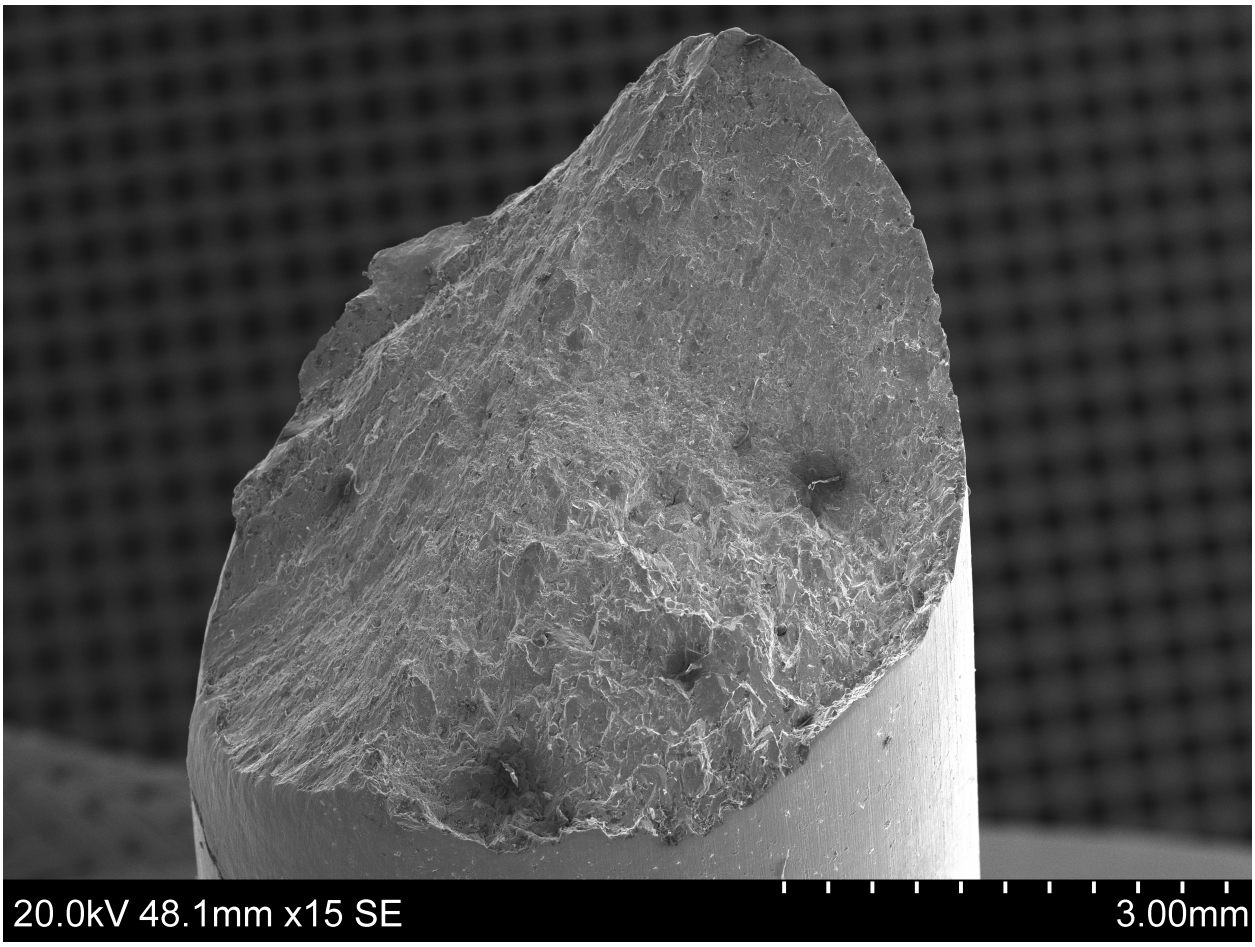

Figure 3.10. A 3D perspective of the failure surface shown in Figure 3.9

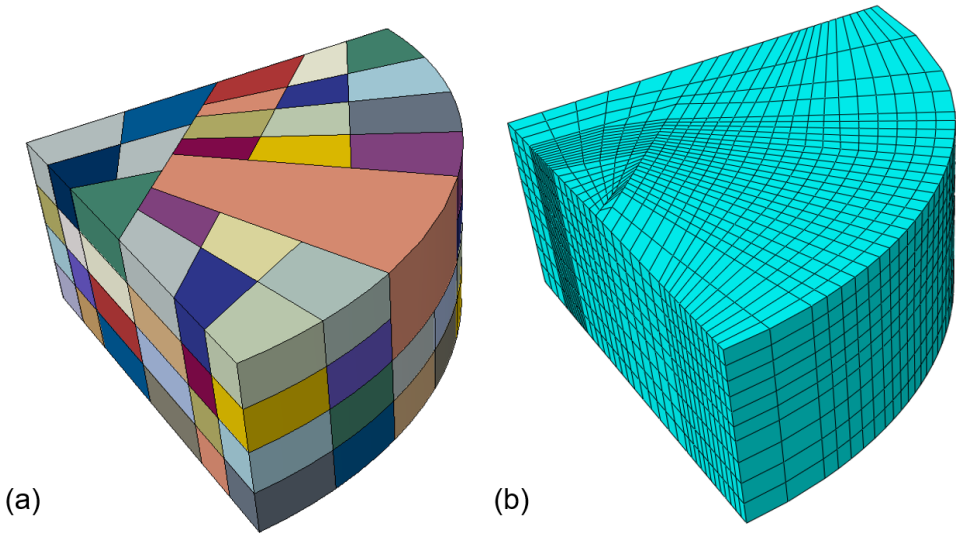

Figure 3.11. Quarter-cylinder model with one large grain. (a) colors represent different grain orientations (random orientations and colors) (b) meshed volume.

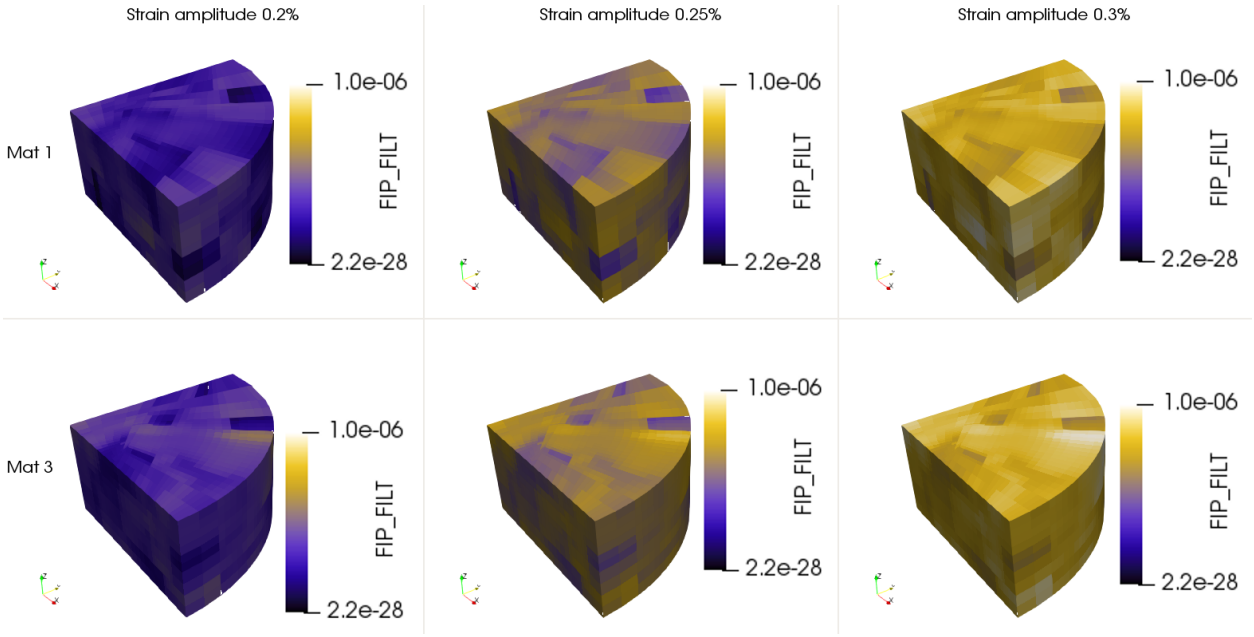

Figure 3.12. FIP contours at three strain amplitude (columns) and for two different materials calibrations (rows). (The color legends are hard to see here: lighter implies greater fatigue risk or lower estimated N_{inc})

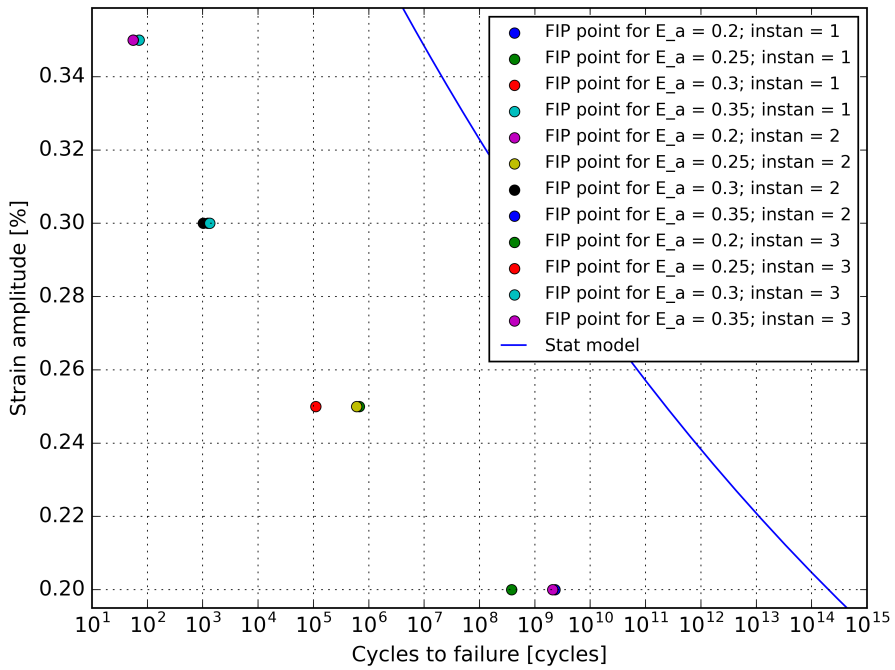

Figure 3.13. Strain-life curve for the reference statistical model (solid blue line) and the FIP predictions (points) at several strain amplitudes and for three different material instantiations with random grain orientations.

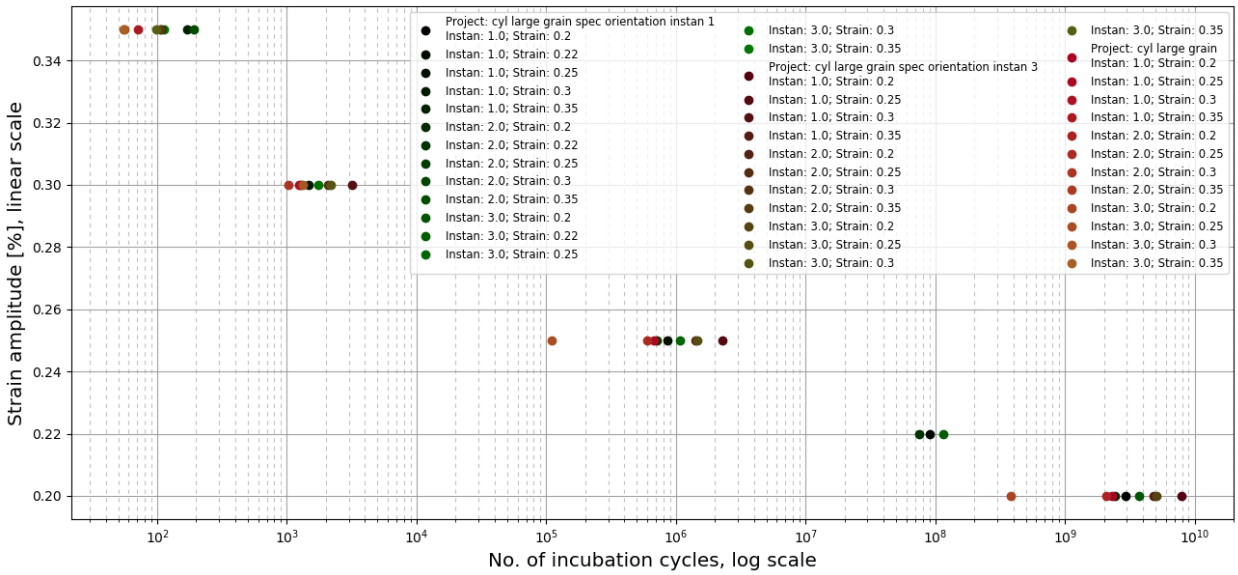

Figure 3.14. Side-by-side comparisons: (1) green dots instan 1/2/3 are different specified orientations of the large grain (instan 1 = 90,45,0; instan 2 = 0,45,0; instan 3 = 0,0,0) with the same orientations for all other grains as in instan 1 of Figure 3.13; (2) brown dots the same, but with instan 3 of Figure 3.13 for all other grains instead of instan 1; (3) red dots are reproduced from Figure 3.13

A similar mesh with a larger grain replaced by several small grains was constructed for comparison. This mesh is shown in Figure 3.15. When the same boundary conditions are applied to this new mesh, contours of FIP as shown in Figure 3.16 for several different cases are produced. This is plotted with the results from the mesh with an irregularly large grain in Figure 3.17. These results seem to indicate, albeit with relatively small confidence due to the small number of cases, that in general the large grain has relatively little impact compared to the overall grain orientations on the maximum FIP value predicted.

From this it seemed that the mesh with a large grain may have higher variability in response. To test this, 15 instantiations at 0.25% strain amplitude were run for both cases. These results show that the mesh with a larger grain has higher mean life, but also more variance. This is show in Figure 3.18.

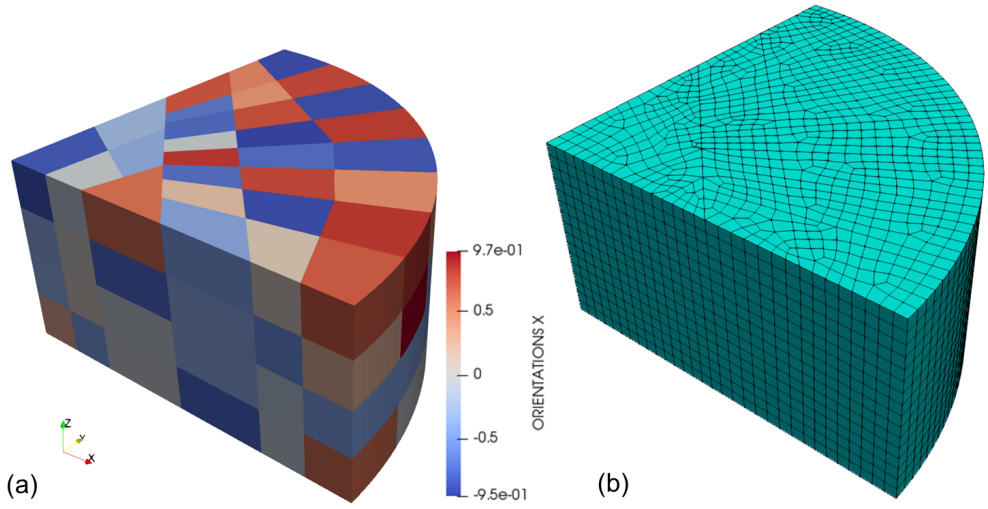

Figure 3.15. (a) Example microstructure with approximately equiaxial grains, colored by magnitude of the ψ Euler angle, and (b) the mesh for this microstructure

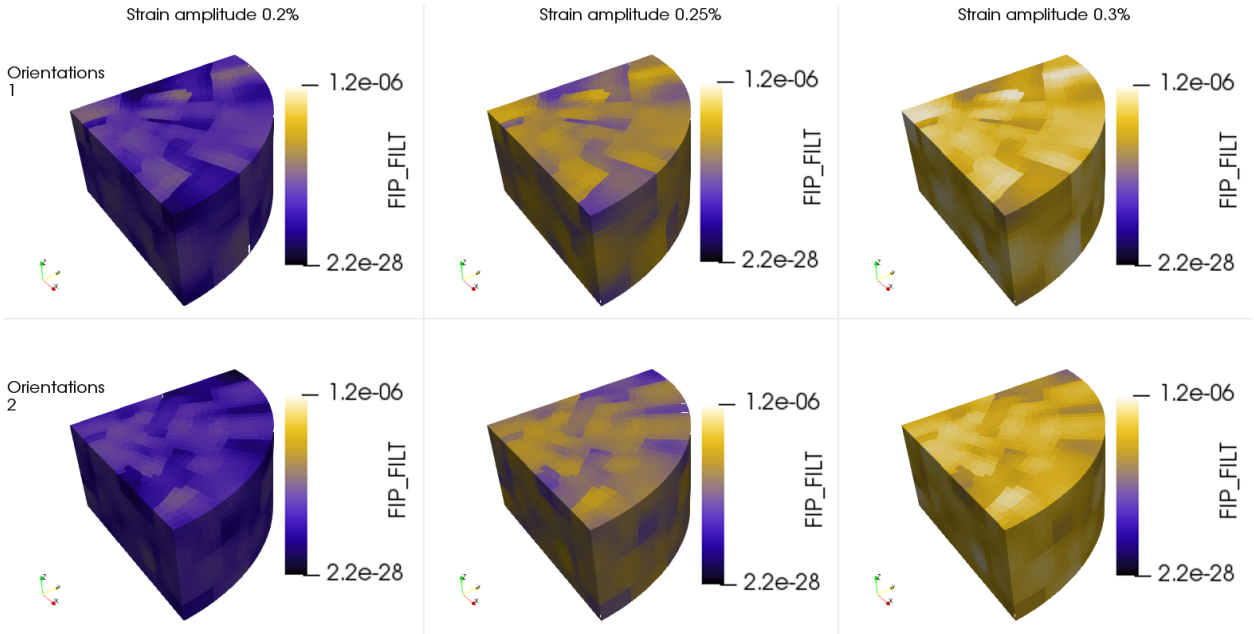

Figure 3.16. Contours of filtered FIP for two different sets of random orientations (instantiations 2 and 3 below)

3.3.1. Influence of a void on estimated life

The effect of introducing a void was also studied. To do this, a relative void size and shape was found experimentally, using statistics extracted from x-ray micro-computed tomography at Beamline 2-BM at the APS, as described in Chapter 2. This method produced 3D images of voids

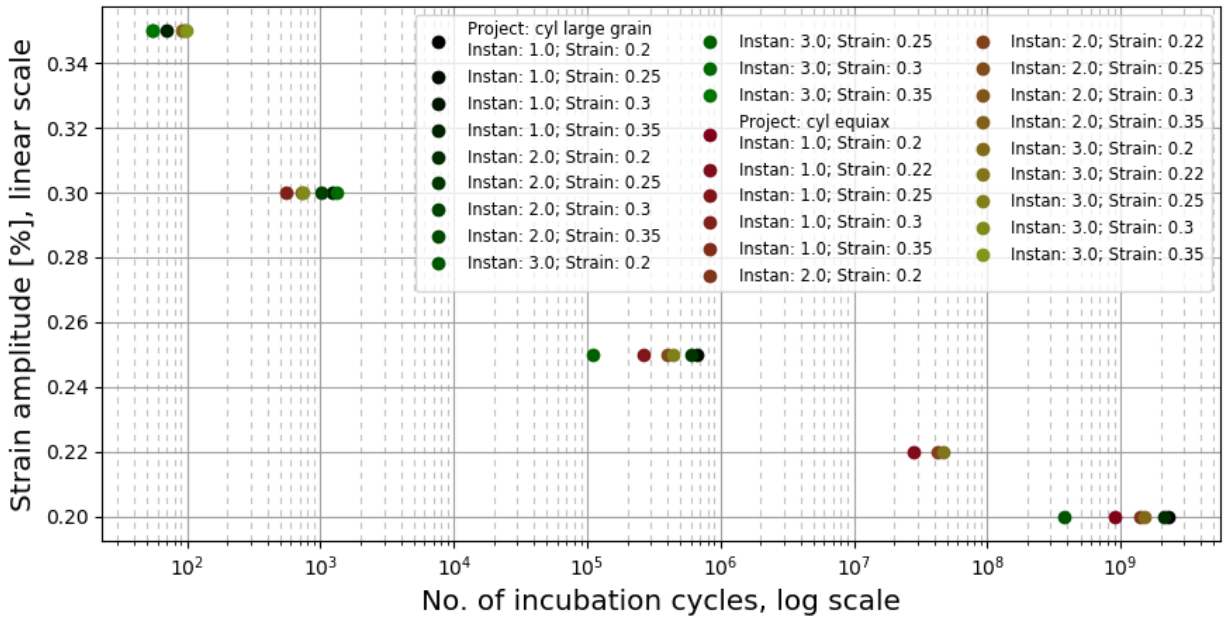

Figure 3.17. Strain-life comparison of meshes with equiaxial grains (brown hues) and a longer grain (green hues). This replots data from Figure 3.13

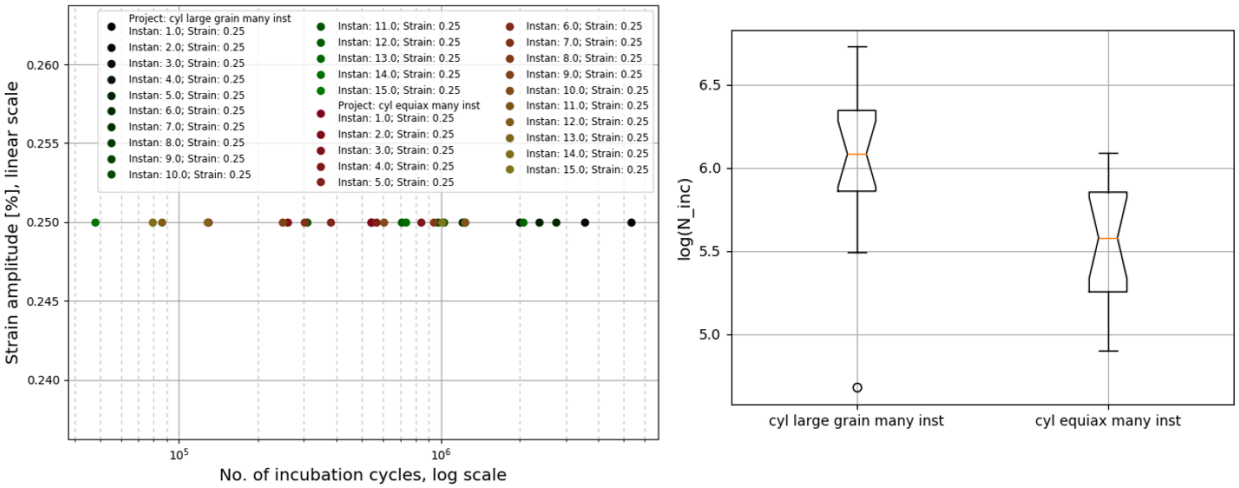

Figure 3.18. (left) Scatter of plot of equiaxial and large grain meshes for 15 different instantiations each at 0.25% strain amplitude (right) box-and-whisker plot showing a difference in mean and variance/outliers between the cases

in the material with voxel edge length of 0.87 microns. The total observed area across eight 3D images of volumes exhumed from two fatigue coupons of IN718 (specimens B-1-6-LCF-800-3 and B-3-5-LCF-800-2 from Honeywell, obtained for imaging in Spring 2016) was about 64 mm^3. After a series of post-processing steps including reconstruction, thresholding, feature identification, and

data cleanup this generated a dataset of 9761 voids. An example cleaned 3D image rendered as a smoothed surface in ImageJ is shown in Figure 3.19. (Specifically, this is from inside the threaded region of B-1-6). General descriptive statistics of the "features" (voids) identified were computed using a semi-automated pipeline in DREAM3D [**35**]. Size by voxel count was one measure used. Equivalent ellipsoids were fit to each void, from which aspect ratios C/A and B/A (where A, B, and C are the axes, and $A > B > C$) were extracted. There are a few points to note. First, there is an inconsistency – the void information is from IN718, not IN718+. It is currently unknown if there is a significantly different void population between these two alloys. Indeed, it is unknown if this sample is representative of anything outside of the volume inspected, as significant variation in voids has been observed in AM metals in general, including IN718. Second, the experimental portion of this work was conducted for the Predictive Science and Engineering Design (PSED) PhD research cluster at Northwestern University in 2016. A rendering of the "mean void" in terms of shape and size of an ellipsoid is shown in Figure 3.20.

The size data was used in combination with the aspect ratios to modify the equiaxed grain mesh shown in Figure 3.15 with a void of reasonable shape and size with respect to the grains. A void of about 95^{th} percentile size (relative to the grains) was used to make the mesh shown in Figure 3.21. The same process as before was repeated, resulting in the FIP contours in Figure 3.22 and strain-life prediction in Figure 3.23.

3.4. Discussion of results

The specific orientation of the larger grain having little overall impact, as shown in Section 3.3 is reasonable: failure location in the model is dominated by the misorientation between grains (as the only driver of changes in plastic strain is stress concentrations caused by local changes in material properties). There is no reason that any specific orientation would promote or demote the occurrence of potent misorientations.

The results comparing microstructures with and without a large grain indicate a significantly (with 95% CI) higher mean life if there is a large grain. This is not very meaningful, however,

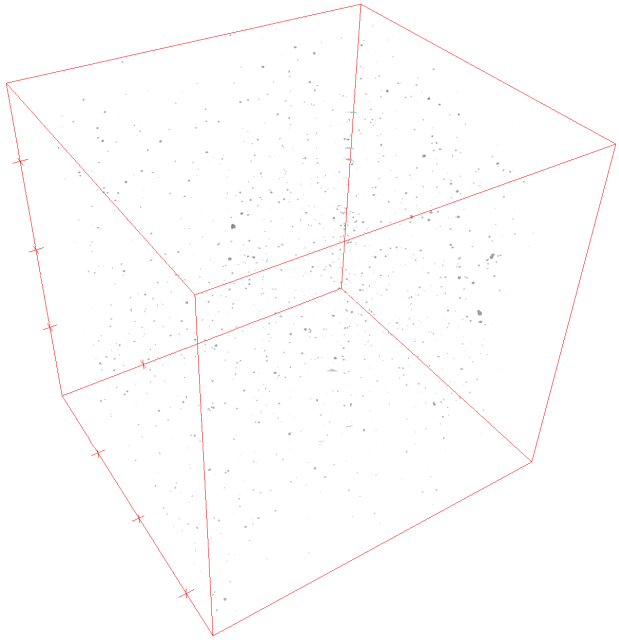

Figure 3.19. Example of voids measured with XCT at 2BM. Specimen B-1-6; demarcations at 435 µm increments

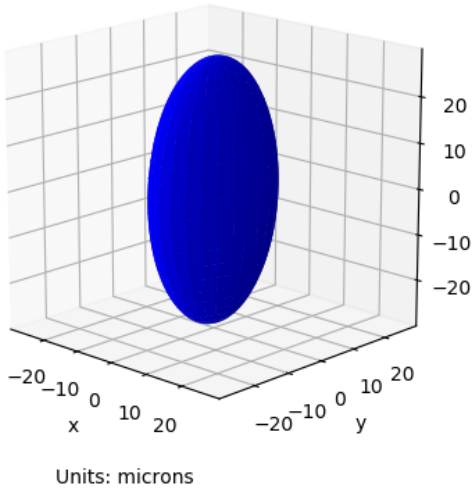

Figure 3.20. Ellipsoid generated from the mean size and aspect ratios found with XCT

because it is probably an expression of the finite number of grains in this model: with fewer grains, there is less likelihood that any two grains are oriented in such a way as to cause a drop in the estimated life. An enrichment of this method may introduce a mechanism to more specifically capture the effects of grain boundaries, which could help with this issue. Another alternative

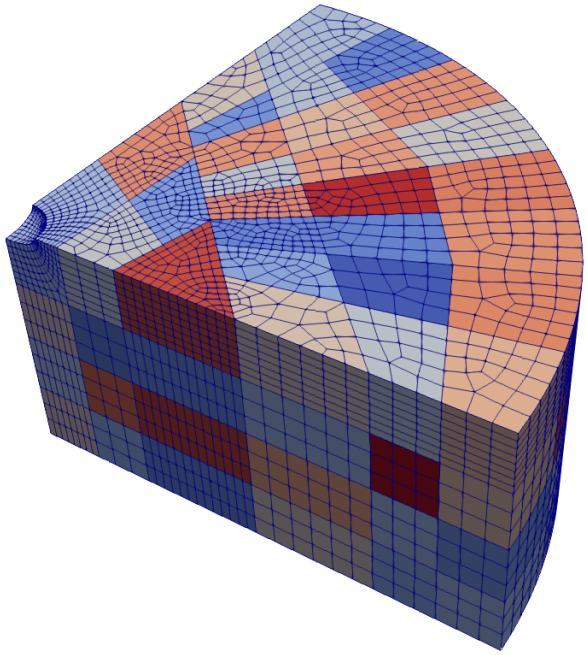

Figure 3.21. Cylinder model with mesh outlined and coloring by grain orientation vector magnitude (to show different grains). An ellipsoid with mean aspect ratio and 95$^{\text{th}}$ percentile size has been removed from the center of the cylinder (centered due to the symmetry boundaries on the top and flat sides)

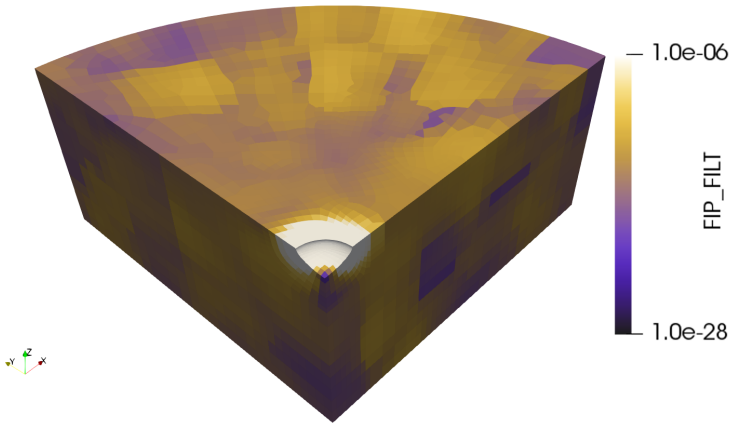

Figure 3.22. Filtered FIP field for the cylinder with a void. For this geometry, the model predicts the void as the most potent fatigue nucleation cite.

would be to model a system with many more grains, although the computational expense may be prohibitive. This would require a system where adding or removing 6 to 8 grains would cause a negligible change in the overall statistics. The increase in variability probably represents the effective decrease in size of the volume in terms of number of grains.

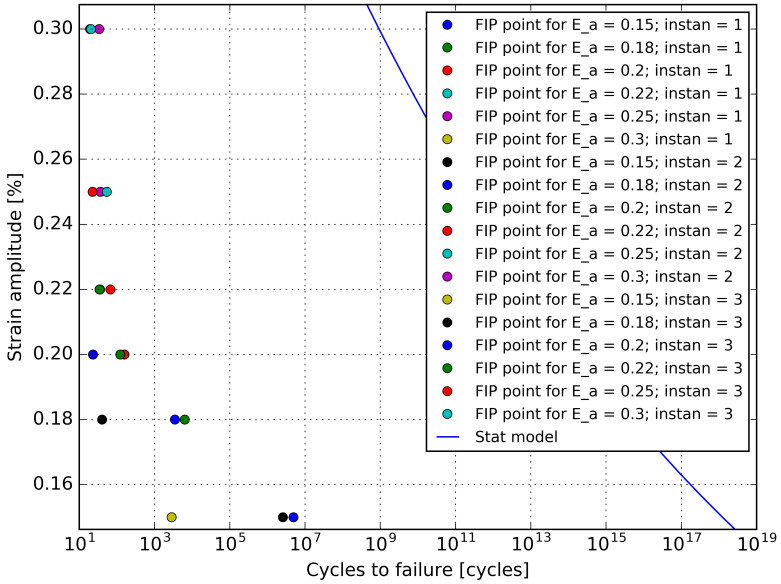

Figure 3.23. Strain-life plot for polycrystalline microstructure with a void

3.5. Summary and Conclusions

This chapter introduced the basics of the crystal plasticity material model and showed one example of calibrating such a model to tensile test results for IN718. Because of the mechanics that CP is based on, reversed cyclic deformations could be relatively well fitted, despite only calibrating to tensile data. A method for computing high cycle fatigue life, and a calibration of this method for IN718 was outlined. Finally, several case studies examining features, irregular grains and voids, that tend to appear in experiments were explored using CPFE.

One important point to take away here is that failures do not seem to always occur on the large grain (when there is one), or that having a large grain changes the estimated fatigue life, at least when computed with this method. This remains true even when particularly weak or strong orientations of that grain are expressed (as in Figure 3.17). One possible option the more accurately model the increase likelihood of a persistent slip band (PSB) occurring within a larger grain and driving nearby failure would be to manually include a planar feature within that with large grain with artificially lower strength. This would promote shear in that area, as a PSB does,

and potentially lead to increase plastic strains in that region and near the boundaries of the planar feature.

The model that includes a void here clearly shows that the void dominates fatigue life. However, this raises an interesting question: at what size does the void become less of an influential factor than the grain boundaries in determining fatigue life? The admittedly simple approach to grain boundaries used here might make such a prediction inaccurate, but it is certainly an interesting future direction with practically useful implications.

For analysis on the microstructural scale, dealing with a relatively small number of grains and/or voids, this analysis works well. This type of modeling and analysis can be used to develop further understanding of the complicated interactions, and the relative importance of each. However, to understand the performance of part-scale builds the inherent heterogeneity of AM materials poses a significant challenge to this kind of an approach. A worst-case analysis (which the above might be considered) is likely overly conservative – in systems where light weight is important this is undesirable. Furthermore, this kind of analysis can be useful for optimization of individual weak spots in the material but not if multi-scale factors are involved. For example, one might wonder what the relative importance of a given microstructure is when the macroscopic topology changes. One might also consider localized improvements, e.g. via alterations to the build history or local chemical composition. In order to understand the impact this would have upon the macroscopic, or part-scale, performance more information is required. Specifically, some way of including microscopic performance indicators in a macroscopic model. The tools used to do this, and ultimately a model that incorporates variable microstructures throughout a macroscale model is shown in the following chapters.

CHAPTER 4

Reduced order modeling for CP and application for integrated process-structure-properties-performance modeling

4.1. Background and motivation

One issue with the CPFE modeling of Chapter 3 is that it is slow: for each step for each material point a system of ODEs must be solved to update the CP material law. Even using relatively large implicit time steps it becomes impractical to model even 100s of grains (much less an entire part) or resolve inclusions with high enough accuracy (i.e. fine enough mesh) to compute the FIP field confidently. In addition, even if one could spend the time to do a large CPFE model, it is unclear what physical system would best represent the AM process. While we have seen an example of gaining insight on a known process and parameter set using image-based modeling in Chapter 3, this does not necessarily transfer to other processes.

Thus, this chapter has two distinct goals. First, a reduced order modeling technique is developed for polycrystalline material, based on previous works. Second, an integrated system to combine process-structure and structure-properties-performance modeling is developed. This will allow for more direct process plan assessment, or eventually process design, using a fully integrated modeling framework. The highlights for this chapter are the following:

- A reduced order model that implements the same methods as the fatigue estimator used in the previous chapter and applicable to metals at the single grain or polygrain scale is developed
- The method is integrated with an AM process-structure modeling framework, so that a fully model-based workflow can capture the effects of AM processing choices on final performance

- In keeping with the results from the previous chapter we show that introducing a void, in this case though suboptimal choice of processing parameters, decreases fatigue performance

4.2. Reduced order model for crystalline materials

The following is an excerpt from [**54**], in which I describe the "crystal plasticity self-consistent clustering method" concisely for a relatively general audience. The formulation for CPSCA in a small strain setting was first introduced in my co-authored publication [**72**], when the term CPSCA was coined. One major contribution of this book chapter, beyond introducing the crystal plasticity law, was to formulate SCA for an arbitrary number of phases. Prior to this SCA, originally developed for carbon fiber reinforced polymer composites, was formulated only for two- or three-phase microstructures. Subsequent works on which I was a co-author, namely [**111**] and [**147**], extended the formulation to the finite deformation setting (this reformulation was the work of Shakoor and Yu, so is only mentioned briefly). This increased accuracy, because a simplifying assumption used to compute $\mathbf{F}$ from the strains could be avoided (i.e. using $\mathbf{F} = \boldsymbol{\epsilon} + \mathbf{I}$, which potentially. erroneously enforces symmetry of the $\mathbf{F}$ tensor). More importantly, it allows us to solve problems in which finite deformations (deformations that result in perhaps 5% or more strain) dominate. The interested reader is directed to the relevant papers for the finite strain formulation and implementation.

An overview of the CPSCA method is shown in Figure 4.1 for a generic matrix-void-inclusion system: from left to right the figure shows (1) a simplified representation of the material system (loosely called an RVE), with half the blue matrix material hidden showing the gray inclusion and red void; (2) contours of the xx component of strain in the matrix from a linear elastic analysis; (3) the clusters computed from the strain solution using k-means clustering (Sec. 4.2.1); (4) the plastic shear strain field from CP, computed in the prediction stage using the CP model described in 3.1.1; and (5) the FIP (as introduced in Section 3.2.3).

4.2.1. A summary of self-consistent clustering analysis

The SCA approach defines a database of training data called the Direct Numerical Solution (DNS); construction of this database is made tractable by computing only the elastic response of the RVE using an FFT or FEM solver. The database is used to redefine the number of strain degrees of freedom (DOFs). In the prediction stage, the RVE response is then solved using a self-consistent solution to the Lippmann-Schwinger equation [**70**] with *any* constitutive law, in this case a crystal plasticity model. Since the number of DOFs has been reduced, complex load paths (e.g. cyclic loading) and expensive constitutive laws can be used during the prediction stage with relatively little impact on total computational time.

4.2.1.1. Derivation. This method is derived from the first order homogenization of a boundary value problem within an RVE. The local strain field ϵ^m is defined as the sum of a macroscopic, homogeneous strain field $\overline{\boldsymbol{\epsilon}}$ and a fluctuating term, i.e. $\boldsymbol{\epsilon}^m = \overline{\boldsymbol{\epsilon}} + \boldsymbol{\epsilon}^*$. To satisfy the Hill-Mandel condition [**91**], we assume periodic displacement field and anti-periodic boundary traction. The local stress must satisfy equilibrium, that is:

$$\nabla \cdot \boldsymbol{\sigma}^m(\mathbf{x}) = 0, \ \mathbf{x} \in \boldsymbol{\Omega}, \tag{4.1}$$

where $\boldsymbol{\sigma}^m(\mathbf{x})$ is the local stress tensor at point $\mathbf{x}$ in the RVE domain Ω. The local stress $\boldsymbol{\sigma}^m$ can be computed using any constitutive equation.

It has been shown in [**70**] that Eq. 4.1 is equivalent to the Lippmann-Schwinger equation for first order homogenization, as given by:

$$\boldsymbol{\epsilon}^m(\mathbf{x}) = -\int_{\boldsymbol{\Omega}} \boldsymbol{\Phi}^0(\mathbf{x}, \mathbf{x}') : \left(\boldsymbol{\sigma}^m(\mathbf{x}') - \mathbf{C}^0 : \boldsymbol{\epsilon}^m(\mathbf{x}')\right) \mathrm{d}\boldsymbol{\Omega}(\mathbf{x}') + \overline{\boldsymbol{\epsilon}}, \mathbf{x} \in \boldsymbol{\Omega} \tag{4.2}$$

where $\mathbf{C}^0$ is a fourth order reference stiffness tensor, and $\boldsymbol{\Phi}^0$ is the periodic fourth-order Green's operator.

4.2.1.2. Training data. We would like to solve Eq. 4.2 on a set of arbitrary sub-domains within the RVE, rather than using the DNS discretization. With careful selection of these sub-domains, or *clusters*, a dramatic reduction in the number of strain DOFs is possible with little loss of accuracy.

To make this selection well, clustering is based on a training dataset. Here, we choose to use the strain concentration tensor, $\mathbf{A}^m$ defined by $\boldsymbol{\varepsilon}^m(\mathbf{x}) = \mathbf{A}^m(\mathbf{x}) : \overline{\boldsymbol{\varepsilon}},\ \mathbf{x} \in \boldsymbol{\Omega}$; how this is computed is determined by the loading conditions used during the prediction stage. In some cases, the deformation concentration tensor will be used instead (when the finite strain implementation is used). For each phase in the material, voxels with similar $\mathbf{A}^m$ are assigned to one of a predetermined number of clusters $I = 1...k$ using k-means clustering [**74**].

4.2.1.3. Predicting response. To use clusters in place of voxels, solution variables are assumed constant across each cluster $\boldsymbol{\Omega}_I$, or $(\boldsymbol{\epsilon}_i^m)_{1...k}$; $(\boldsymbol{\sigma}_I^m)_{1...k}$ and likewise for any other local variable. Using this cluster-wise-constant approximation, Eq. 4.2 is rewritten in discretized form as:

$$\boldsymbol{\epsilon}_I^m = -\sum_{J=1...k} \mathbf{D}_{IJ}^0 : \left(\boldsymbol{\sigma}_J^m - \mathbf{C}^0 : \boldsymbol{\epsilon}_J^m\right) + \overline{\boldsymbol{\epsilon}},\ I = 1 \dots k \tag{4.3}$$

where $\mathbf{D}_{IJ}^0$ is the interaction tensor between clusters I and J defined by $\mathbf{D}_{IJ}^0 = c^1\mathbf{D}_{IJ}^1 + c^2\mathbf{D}_{IJ}^2$. Numerical variables c^1 and c^2 are computed and updated by a physically-based self-consistent scheme which ensures accuracy at each load step. For the definition of $\mathbf{D}_{IJ}^0$ see [**70**]. Clustering, $\mathbf{D}_{IJ}^1$, and $\mathbf{D}_{IJ}^2$ can be precomputed and stored for future use, see [**53, 72, 91**]. Given a macroscopic, or external, strain $\overline{\boldsymbol{\epsilon}}$, Eq. 4.3 can be solved using, e.g., Newton-Raphson iterations for the unknowns $\boldsymbol{\epsilon}_1 \dots \boldsymbol{\epsilon}_k$ using these precomputed values. Verification of the accuracy of this overall method is discussed in [**72**].

The application for the CPSCA method to problem involving fatigue failure was first shown in [**54**], where the same FIP defined in Chapter 3, Section 3.2.3 was applied to model fatigue, driven by an application in Nickel-Titanium shape memory alloys for heart valve frames or stents. The implementation of an FIP in CPSCA is similar to that for FEM, although the details for volume averaging differ (due to the inherent averaging done by clustering). The schematic for the complete

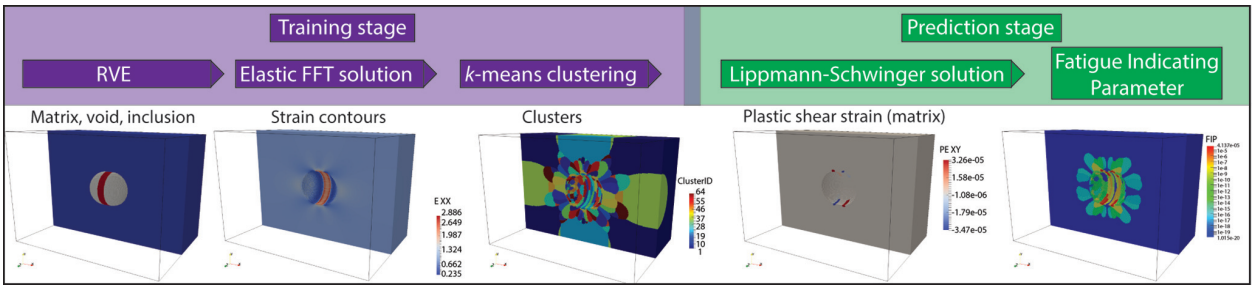

Figure 4.1. A schematic showing the essential components of the SCA method for predicting fatigue using CP like the FE method did in Chapter 3. The figures here show a demonstrative RVE from a parametric study of inclusions and voids in NiTi, with half of the matrix phase shown and the inclusion and void phases hidden. This is a tidier and easier to understand example than the AM images provide. From Kafka et al. [**54**].

workflow is reproduced from Kafka et al. [**54**] in Figure 4.1. In subsequent work, this derivation was refomulated in a finite deformation setting, see [**111**] and [**147**].

4.2.2. Application to polycrystalline metal with voids

This fatigue prediction framework was applied to the three images of voids shown in Figure 2.3. Unfortunately, crystallographic information for these specimens was not measured directly. In absence of that data, multiple possible realizations of grains were generated that were visually similar in pattern to the measurements of SS316L using the "synthetic generation" functionality of DREAM.3D (specifically the "statsgen" filter and a related pipeline). The polycrystalline models, just as in Chapter 3 do not account specifically for grain boundary effects. One future direction would be to include a Hall-Petch effect to empirically alter the mechanical behavior based on the grain boundary density in the direction of loading (such as is done in the example given in [**147**]). Another option would be to use another method that embeds a means of capturing length scale, e.g. with non-local plasticity such as Fleck and Hutchinson's strain gradient plasticity [**23**]. This length scale could then be related (likely empirically) to physically relevant features such as the grain size or void spacing.

Including voids in the model provides an opportunity to directly compare material with porosity to material without porosity, and measure the effect that has on mechanical response. This could

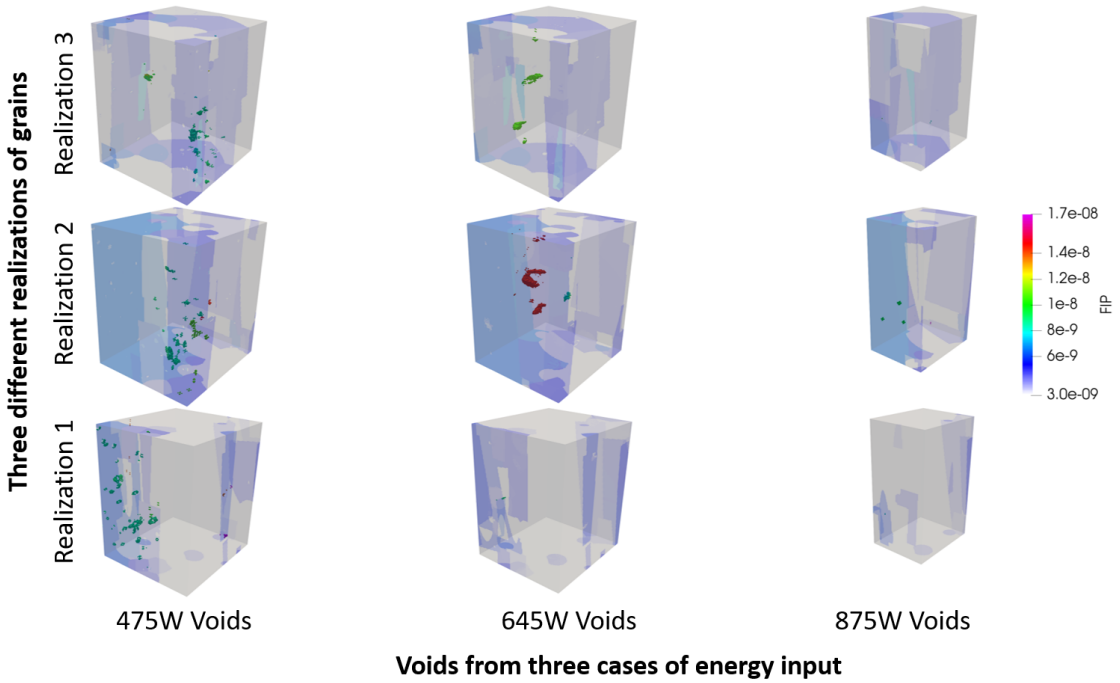

Figure 4.2. Three-by-three diagram showing heightened FIP surrounding voids in polycrystalline volumes. Each of the three different voids cases at different power levels were modeled with three different instantiations of grains

be used in future as a point of reference for building void-based homogenization-type constitutive laws, should that be of interest. By excluding the voids, a reference material condition can be obtained, and the exact role of the void could perhaps be deduced.

4.2.3. CPSCA model validation by comparison to in-situ XCT images

The void deformation captured by the experiments in Chapter 2 can also be modeled using CP-SCA, as shown in Figure 4.4. In this case, a single void deforming in a single crystal is captured using periodic boundary conditions (as implied by the CPSCA formulation, but also a reasonable assumption in this case). The speed of CPSCA allows for an inverse approach to identify the crystallographic orientation of the surrounding grain; simply by matching the orientation the observed deformation behavior, elongation in the loading direction with contraction in one transverse direction but not the other, is captured well. This modeling was conducted by Cheng Yu using the finite deformation implementation, and more details of the model are available in his thesis [**146**].

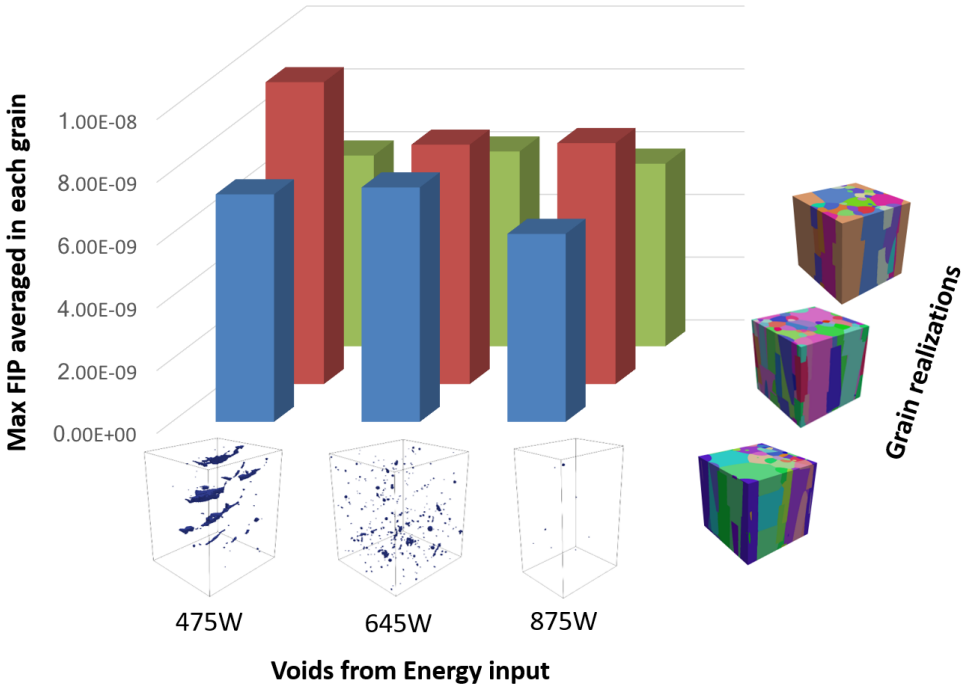

Figure 4.3. Maximum averaged FIP within one grain in each of the void and grain cases. Larger voids in the 475 W case then to increase the measured FIP, but grains have a very noticeable impact as well. The interplay between the voids and grain imply that in some cases (e.g. 645 W, realization 1 versus 875 W, realization 2) voids one would expect to produce a higher FIP are entirely mitigated by the grain configuration

4.3. Structure-properties modeling directly from modeling of AM processes

The two examples above make use of high resolution images of voids, but make some assumptions for the grains (either single crystal or synthetic reconstruction). In either case, a substantial experimental effort is required to obtain these baseline inputs to the model. However, this does not have to be the case. Parallel work on modeling additive manufacturing, indeed probably the bulk of the work in the literature at large, involves modeling the AM process-structure relationships. One realization is that our process-structure and structure properties models can be directly linked. In Yan, Lian, Yu, Kafka et al. [**141**] we presented what we believe is the first demonstration in the literature of a completely integrated process-structure-properties-performance model: one in which the input (e.g. hatch spacing) can be altered and the effect on performance (e.g. cycles to

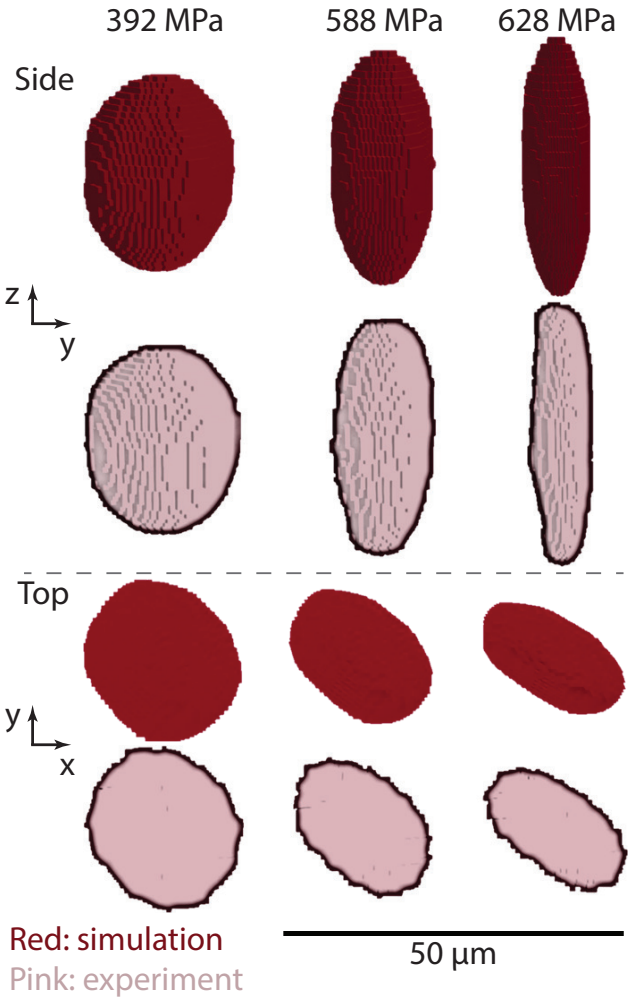

Figure 4.4. A single void deforming in a single crystal. The two rows show "side" and "top" views, with each sub-row showing the comparison of measurement (red) and model (pink). The single crystal orientation in the model was selected to optimize the similarity with fixed material properties

failure in fatigue) computed. What follows is a modified excerpt from that publication. Note that in this case, due to the process models developed at the time, this focuses on selective electron beam melting of Ti-6Al-4V. However, the principles are entirely transferable to other systems and materials (e.g. LENS IN718).

4.3.1. Integrated AM modeling framework

Here I present a process-structure-property prediction framework for metal additive manufacturing, with an implementation for SEBM of the commonly used Titanium alloy, Ti-6Al-4V. In this framework, shown schematically in Figure 4.5, each model incorporates basic material information and data provided directly from previous models in the framework to predict the mechanical response and estimated fatigue life of critical microstructures given machine-relevant processing conditions. The key idea of the framework is that structural information, data that can be represented in space using a collection of volume-filling elements, sufficiently describes the system and can thus intermediate models: a common, powerful premise.

In abstract form, the framework consists of various "modules" that are aggregated into "hubs;" there may be multiple hubs, each of which collects and passes a complete solution for one stage (e.g. process simulation) to the next stage (e.g. mechanical response prediction). One might think of our *modules* as discrete processing units capturing a unique facet of the system and *hubs* as data management facilities for database queries. To systematize the method, we group modules into hubs for (1) material processing and (2) material response.

Each module is stand-alone, designed to answer significant scientific and/or engineering questions independent of the connecting framework. As such, the models that make up our modules will only be discussed with sufficient detail to elucidate their purpose: the key points of each are provided. The interested reader is directed to published manuscripts devoted to each for further details. A detailed description of the framework implementation is given in Section 4.3.2. The process is captured by models for powder spreading (Section 4.3.3.1), heat source and paired thermal-fluid modeling (Section 4.3.3.2), and grain growth during solidification (Section 4.3.3.3). The mechanical response prediction consists of reduced order modeling (Section 4.2), constitutive law (Section 4.3.4.1), and performance metric (Section 4.3.4.2). The example results are shown in Section 4.4, with output and discussion for each model. The specific models that we use are selected to capture microstructure-level variations caused by the AM process and the impact of these variations on mechanical properties. These choices are not unique but simply elucidate the framework: this

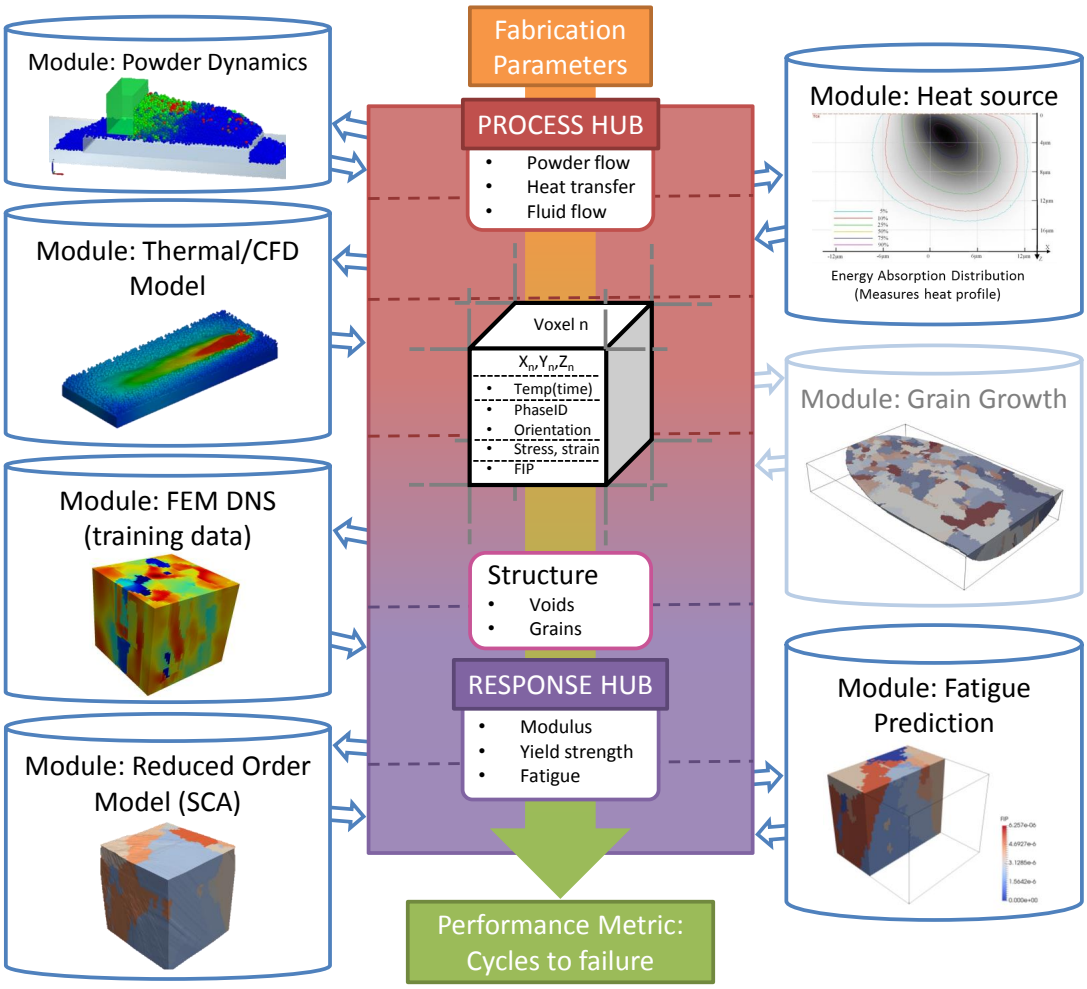

Figure 4.5. Schematic diagram of the module-hub framework conceptual layout, with images of our current implementation demonstrating the modules: a SEBM process with microstructure-based fatigue life assessment. The data used by the framework at each point in space is described by spatial coordinates and any relevant field data for the current working modules, as shown graphically by a schematic of a representative voxel. The cellular automaton model is shaded gray to indicate that results both with and without it are given, to demonstrate the flexibility of the framework.

framework could also, for example, be used with part-scale thermodynamic simulations coupled to conventional continuum plasticity modeling, with local material properties dependent upon the information derived from processing, e.g. phase fraction [**115**].

x	y	z	T(t=0)	T(t=dt)	...	T(t=tend)	phase	orientation1	...	stress1	...
1	1	1	—	—	—	—	—	—	...	—	...
1	1	2	—	—	—	—	—	—	...	—	...
⋮	⋮	⋮	⋮	⋮	⋮	⋮	⋮	⋮	⋮	⋮	...
l	m	n	—	—	—	—	—	—	...	—	...

Figure 4.6. A schematic of the flat file database used to store record data for the proposed framework. The fields are abbreviated to more clearly show the structure of the database.

4.3.2. Framework Implementation

The general framework depicted in Figure 4.5 contains mechanisms for input and output handling as well as intermediate storage. The solution domain is represented within a fixed format, flat file database as a regular grid of volume filling points, with each point described by coordinates (x, y, z location) to identify the unique record, each of which has fields that contain a datum: temperature at a point in time, phase, orientation, various stress and strain tensors expressed component-wise, and a fatigue indicating parameter (FIP) in this implementation. These field values are chosen to match the information required by all of the models used, and are not necessarily unique or optimal in their ability to describe the process. Figure 4.6 outlines the database format.

The integrated framework is mainly based on one-way coupling, which is relatively straightforward to implement and test. Each model is directly connected to the next by passing output information to a subsequent input processor: the CFD powder melting model feeds temperature profiles and voids information to the CA grain growth model through the flat file database, and the CA grain growth model feeds the grains and void information to the SCA crystal plasticity model, also through the flat file database. In this case, data is promulgated in predominately one direction (process to structure to properties): a "backwards" coupling (e.g. structure to process) is not considered. Latent heat is considered an effective simplification of the influence of microstructure evolution on the temperature field and molten pool flow. Previous thermal or thermal-fluid models with this simplification have shown simulated temperature history and molten pool behavior in good agreement with experiments [**30, 59, 101**]. Published grain growth models [**104, 121**]

have also shown qualitative agreement with experimental results using simple one-way coupling that does not incorporate the influence of mechanical deformation (e.g., thermal stress) on grain growth. Therefore, this sequentially coupled framework should be sufficient to predict the temperature profiles, material structures and mechanical behaviors. From a top-down approach as illustrated below, this framework can be used to derive process-structure-property relationships, while a bottom-up approach could be used to solve design and inverse problems. Specifically, the framework proceeds as follows:

- The powder spreading model and powder melting model exchange high-resolution geometry information of the powder bed, using an STL-format surface mesh representation. That is, the DEM powder spreading model generates the particle packing configuration within one powder layer, outputs as an STL file, and feeds into the CFD powder melting, thereby reproducing powder spreading and melting; the CFD powder melting model predicts the solidified shape, outputs as an STL file, and feeds into the DEM powder spreading model to apply a new powder layer, thereby reproducing powder spreading. The manufacturing process of multiple layers and tracks can be represented by repeating these two simulations and the data exchange between them. This part of the work was led by Wentao Yan.
- The temperature profile in the volume of interest (VOI) is predicted by the powder melting model and written to a database in the flat file format shown in Figure 4.6. By convention, void space is set to an ambient temperature to distinguish it from the dense material.
- The grain growth model reads the temperature field history from the database, and interpolates to match the grid spacing if needed. The dense material and voids are identified based on the temperature. Voids and free surfaces are thereby included in the grain growth model.
- The grain growth model simulates the grain growth process, predicts grain structure (phase and orientation), and writes grain and void information into the database. This part of the work was led by Yanping Lian.

- A sub-domain of particular interest, e.g. the largest void, of the full VOI for the grain growth model is selected as the input to the mechanical model; the grain and void information provided at each point via the database are interpreted as the center point of each voxel in a regular, uniform, cuboid mesh. This mesh can be used for all three mechanical response modules: FEM, SCA, and fatigue prediction.
- The SCA and FEM models are used to predict stress-strain response, which is added to the database.
- The fatigue prediction model reads the stress-strain behavior at each point, and computes a non-local potency estimate. The fatigue life of the highest potency location is computed to provide a scalar material response metric. Cheng Yu and I worked on these last three points.

4.3.3. Process Modeling Hub

The first hub codifies the process models. Inputs include process conditions and material information. Process conditions incorporate a multitude of factors, such as the scan pattern, input power, powder bed thickness, and build chamber conditions (e.g. temperature, degree of vacuum).

In the relatively simple case shown here, the scan pattern is a two-pass, two-layer Z configuration: each layer is added using the same path at the new height. Between layers the powder spreading model is used to place the new bed of powder particles. The temperature history of each point and the final geometry of the CFD powder melting simulation are output information, which are subsequently used as the input to the grain growth model. The grain growth model input processor identifies the voids and predicts the grain structures based on thermal information from the CFD model. The output of this hub is the overall microstructure information, crystallography and geometry, predicted with the CFD-thermal model and grain growth model.

A continuum-based thermal model using the Finite Element Method (FEM), for example, could replace the thermal predictions of the high-fidelity thermal-CFD model used here. In this study, the high-fidelity models for powder spreading and melting are intended to provide a relatively accurate

Table 4.1. Input and output for powder spreading model

Input	Particle size distribution
	Spreading tool geometry/description
	Substrate shape/material
Output	Powder bed state (STL geometry) after spreading

description of the thermal conditions and void information compared to the simpler models required for part-scale analysis. These high-fidelity models have high computational cost, limiting the total volume of material that can be investigated in the following examples.

4.3.3.1. Powder spreading. The arrangement of particles in the powder bed is determined with a DEM-based particle spreading simulation. The distribution and dynamics of particles within the bed or on a substrate can influence the final build condition, e.g. through surface roughness or defect formation between tracks or layers [**58**]. Thus, spreading is simulated with accurate process variables such as the rake geometry, substrate geometry, layer thickness, powder size distribution, and frictional contact/collisions between particles and with the rake. Further details can be found in [**143**].

4.3.3.2. Powder melting. The STL file representing powder configuration is passed to a coupled thermal-fluid solver to compute thermal response and material redistribution during melting and subsequent re-solidification. The interested reader is directed to [**139**], [**144**], [**143**], and [**138**] for more details. The results shown in the following sections are for case 1 in table 4.2. The fully coupled thermo-fluid flow equations were solved using commercial software with custom scripts developed by my co-authors, so I will not go into further detail here. A list of the inputs and outputs of this module is provided in Table 4.3.

The temperature history of each computational cell is output into the flat file database for use in the CA model. To distinguish between a solid/liquid domain and void space, i.e. above the build surface and any voids within the material, void areas are assigned ambient temperature, while the temperature of the solid/liquid domain is no lower than the initial temperature (about 900K) due to the preheating procedure in SEBM.

Table 4.2. Build parameters for cases 1 and 2

Parameter	Case 1	Case 2
Hatch spacing	200 μm	240 μm
Electron beam power	60 W	60 W
Hatch strategy	Z-pattern	Z-pattern
Scan speed	0.5 m/s	0.5 m/s

Table 4.3. Input and output for thermal-CFD model

Input	Powder bed state
	Thermal processing conditions
	Material properties
Output	Thermal history of each point in the volume
	Geometry (including voids)

Table 4.4. Input and output for grain growth model

Input	Thermal history at each point
	Material properties, parameters
Output	Phase ID (includes void phase)
	Grain orientation (Bunge Euler angles)

4.3.3.3. Grain Growth. Grain formation during solidification can be computed based on the temperature field input in the flat file format, which is provided by the thermal-CFD module. While various models (e.g., Kinetic Monte Carlo model [**104**]) can be potentially implemented into this framework, a cellular automaton (CA) model [**26**] is used in this work. More details can be found in [**68**] and [**67**]. The input and output of this module is summarized in Table 4.4.

The conditions of AM (high temperature gradient and cooling rate) result in grain growth dominated by epitaxial growth from existing grains surrounding the melt pool. Thus, the grain structure of the substrate and metal powders are obtained first before the melting process; during the melting and re-solidification process, nucleation is assumed to progress only from the solid material boundary to better capture growth conditions under AM. For more details see [**68**]. The prediction results from the CA model are written to the database as a phase ID (a unique integer) and a predicted crystallographic orientation (Euler angle triplet following the Bunge convention) for each voxel in the CA domain. This database can be read directly to construct a voxel mesh, since material properties are associated with phase ID and orientation.

These descriptions of the processing modeling have been abbreviated, as it is not my own work (rather, that of the papers cited within those sections), and is not central to this dissertation. However, the details included herein are hopefully enough to ensure that the reader understands that a full process-structure modeling effort was conducted in parallel with my work, and at some point (in 2018) we realized that these could be relatively simply combined so I initiated a project with Wentao Yan, Yangping Lian, and Cheng Yu to achieve an integration of all our methods.

4.3.4. Mechanical Response Prediction Hub

The second hub codifies our mechanical response and performance prediction methods. Input to this hub is crystallographic and geometric microstructure information, as well as material properties for constitutive model calibration. The output of this hub is a prediction of mechanical response, i.e. overall stress-strain curves, local plastic strains and stresses, and the high-cycle fatigue incubation life. All information (phase ID, grain orientation, etc.) is carried by voxels. CPSCA was used to speed up the simulations. Volumes of interest (VOIs) for computing the fatigue indicating parameter (FIP) and predicting fatigue life are selected from the larger thermal-CFD-grain growth region; a subset with known spatial coordinates can simply be queried from the database, which contains the predicted microstructure (void size, shape, location, grain size, shape, orientation, etc). All the input and output data to and from this module is listed in Table 4.5.

4.3.4.1. Crystal plasticity for material law. The same crystal plasticity model used in Section 3.1.1 in Chapter 3 is implemented in CPSCA as described in Section 4.2, and is used here with modifications to capture the primary-α phase of Ti-6Al-4V, rather than the IN718 material modeled elsewhere. The modifications to the code to do this were by Cheng Yu.

It has been observed that the microstructure of Ti-6Al-4V produced by SEBM is dominated by hexagonal-close-packed (hcp) α grains which are transformed from the prior body-centered-cubic (bcc) β grains. The α phases originating from the same parent β grain have similar orientation [**1**]. For this demonstration of the framework we make the simple, though inaccurate, assumption that each parent β grain, under thermal processing, produces a single, aligned child α grain. Slip systems

Table 4.5. Input and output for mechanical response model

Input	Phase ID (including voids)
	Grain orientations (if not provided assume single crystal in weakest orientation)
	Material properties
	Boundary/loading conditions (assumes periodic BCs)
Output	Stresses
	Strains

Table 4.6. Calibrated elastic and plastic crystal plasticity parameters for primary α phase. Parameters with a * are from [**123**]. Others are selected to match experimental results

Elasticity:	MPa	Plasticity:				
$\mathbf{C}^*$		Phase	Basal	Prismatic	Pyramidal $\langle a \rangle$	Pyramidal $\langle c+a \rangle$
$C_{11} = C_{22}$	1.7×10^5	$\dot{\gamma}_0{}^*$ s^{-1}	0.0023	0.0023	0.0023	0.0023
C_{33}	2.04×10^5	m*	50	50	50	50
$C_{44} = C_{55}$	1.02×10^5	τ_0 MPa	284.00	282.24	395.00	623.30
C_{66}	0.36×10^5	$a^{t=0}$ MPa	0.0	0.0	0.0	0.0
$C_{12} = C_{21}$	0.98×10^5	H MPa	1.0	1.0	1.0	1.0
$C_{13} = C_{31}$	0.86×10^5	R MPa	0.0	0.0	0.0	0.0
$C_{23} = C_{32}$	0.86×10^5	h MPa	500.0	500.0	500.0	500.0
other C_{ij}	0	r MPa	0.0	0.0	0.0	0.0
		χ	1.0	1.0	1.0	1.0

used for the dominant α-phase of Ti-6Al-4V are $3\langle 11\bar{2}0\rangle\{0001\}$ basal, $3\langle 11\bar{2}0\rangle\{10\bar{1}0\}$ prismatic, $6\langle 11\bar{2}0\rangle\{10\bar{1}1\}$ first order pyramidal and $12\langle 11\bar{2}3\rangle\{10\bar{1}1\}$ second order pyramidal. These are shown in Table 4.6, as provided by [**123**]. Parameters for the crystal plasticity material model used both for offline and online stages are also given in Table 4.6, where C_{ij} are the stiffness components in Voigt notation [**7**].

In this case, the strain concentration tensor for SCA of each voxel is obtained with a linear elastic finite element model conducted in Abaqus using C3D8R elements. This model computes the elastic response of a VOI with periodic boundary conditions under three uniaxial tensile loading cases (corresponding to x, y, z directions respectively). The stretch direction is the same as applied during the online stage. The elastic strains thus obtained are used in a k-means clustering algorithm for domain decomposition, where the squared Euclidean distance measure is used for clustering.

Table 4.7. Offline and online model parameters

Parameter(s)	Value(s)
Domain size	0.05 mm × 0.05 mm × 0.05 mm
Mesh size	40 × 40 × 40
Element edge length	1.25×10^{-3} mm
Material law, offline	linear elasticity
Material law, online	crystal plasticity
Strain amplitude, online	0.5%, 0.375%, 0.3%
No. of strain cycles	4
Load ratio, $R = \epsilon_{min}/\epsilon_{max}$	-1
Strain rate, $\dot{\epsilon}$	0.1 s^{-1}

Four fully-reversed unidirectional load cycles at various strain amplitudes with crystal plasticity constitutive law were simulated during the online analysis. These cycles result in a stabilized value of $\Delta\gamma^p_{max}$ and a known σ^n_{max}, used later to compute a FIP. A full accounting of the parameters used for both the offline and online modules is provided in Table 4.7.

4.3.4.2. Performance prediction: fatigue life. The same FIP as described in 3.2.3 of Chapter 3 is used here. The relationship between FIP and N_{inc} for Ti-6Al-4V is calibrated to experimental high cycle fatigue life data for wrought (nominally defect free) Ti-6Al-4V presented by [**48**]. Here, this calibration has been done to reduce the total RMS difference between the experimental data of [**48**] and the N_{inc} predicted for the polycrystalline, defect free VOI at 0.5% and 0.375% strain amplitudes simultaneously (this is the simulation condition that best matches that of the experimental conditions). As before, a moving volume average with window size of about 10% of the volume of the microstructure of interest (in this case the mean void size) is used to compute the nonlocal FIP. The maximum nonlocal FIP, $NFIP_{max}$, is correlated with fatigue crack incubation life, N_{inc}, through

$$NFIP_{max} = \bar{\gamma}_f \left(2N_{inc}\right)^c \tag{4.4}$$

where $\bar{\gamma}_f$ and c, multiplicative and exponential factors, are used to fit experimental high cycle fatigue data. The input and output of the module are summarized in Table 4.8.

Table 4.8. Input and output for fatigue prediction

Input	Stresses
	Strains
	Material properties
Output	FIP
	N_{inc}

4.4. Integrated framework results

The final result of this integrated framework is the computed performance metric for different cases. Intermediate results of each of the hubs and modules are shown in [**141**], which probably make the progression of modeling more clear, but are omitted here as they were not the focus of my work. Included here are only the structure-properties modeling results; the initial grain structure shown in the figures comes directly from the process modeling.

The important point that this demonstrates, to our knowledge for the first time in the open literature, is that the modules used to predict processing and material response to mechanical loading during service have been directly linked. A comparison of the final metric for build quality between cases with different processing conditions is made. The examples here show the influence of process parameter choices on simulated performance with two distinct cases shown in Table 4.2: one with hatch spacing 200 µm and the other with hatch spacing 240 µm. This allows us to directly show the differences in that result from different process parameters. The influence can be seen in Figure 4.9, where a larger hatch spacing results in the prediction of voids, which reduce estimated fatigue life.

4.4.1. Mechanical response prediction

When run without the CA module, we assume a single crystal oriented such that the Schmid factors, the products of the glide plane and glide orientation cosines, are maximized: the weakest orientation, representing a "worst-case" analysis. A more realistic, polycrystalline grain structure enabled by the CA model allows us to capture some of the effects of the crystalline texture on the material response. Figures 4.7 (a) and (b) show four polycrystalline VOIs selected from the CA

solution for a two-track, two-layer simulation. Three VOIs are selected throughout the height of the build (the black, purple, and green outlines) and a fourth VOI (red outline) is selected from the intertrack area. The fourth region in the CA volume is selected because the intertrack area contains a large void caused by lack-of-fusion, predicted by the thermal-CFD model, that influences the fatigue life of the component. The void space is represented by a unique phase ID in both the thermal-CFD results and the CA results and is interpreted as a void by the SCA model. When the framework is used without the CA model, the void space is directly passed to SCA, again through a unique phase ID in the voxel database, and is passed via the CA model when the CA model is used. Thus, the coupling of the framework is achieved by defining geometry and crystallographic information using the thermal-CFD and CA models and using the structures thus defined as the geometry and crystal orientation required by the crystal plasticity model. In the following examples, VOIs are selected to highlight spatial differences within the build, rather than to represent average material properties of an entire build. This is motivated by applications where failure is a concern, in which the local minimum properties are of greater importance than the mean properties.

4.4.1.1. Anisotropic response of the polycrystalline VOIs. For the polycrystalline case, where the CA model is employed, the anisotropic stress-strain response at the strain rate of 10^{-4} s^{-1} for the first three VOIs with loading in the x-, y-, and z-directions is shown in Figure 4.8; an anisotropic and location dependent response emerges from the crystallographic structure. Each of these VOIs are 40 voxels $\times$ 40 voxels $\times$ 40 voxels. A voxelated mesh is constructed directly from the VOI, with material properties assigned to each voxel corresponding to the known properties for the crystal predicted by the CA model. The periodic boundary condition assumption can result in spurious stress localizations near the boundary of these volumes. To counteract this, the five surface layers of voxels are neglected for the results presented below. This is similar to the relatively common "buffer zone" approximation. The simulation was run on a single processor and each stress-strain curve took approximately 680 s in total with 600 s to calculate elastic strain concentration, 43 s to calculate interaction tensor and 27 s for online crystal plasticity analysis for 100 loading increments.

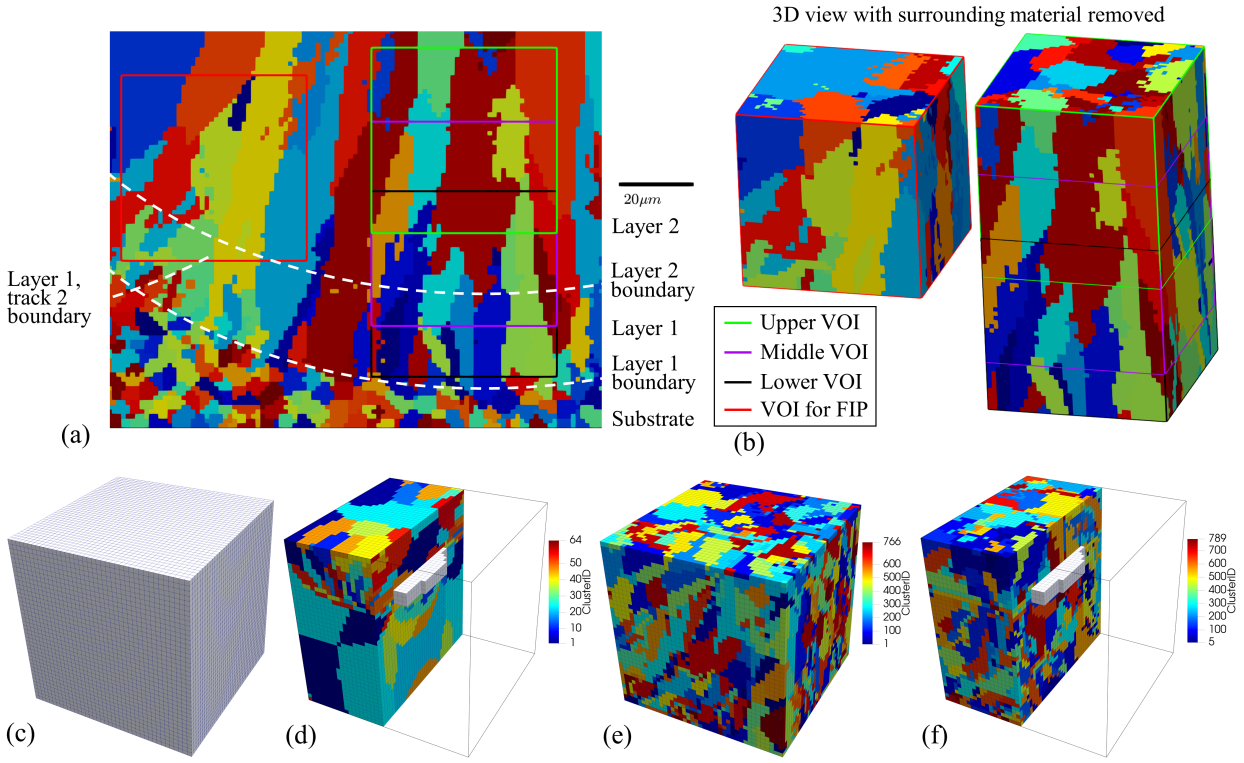

Figure 4.7. (a) a 2D section of the CA result with the relative locations of four cubic VOIs at different locations through the height of a two-layer build (color coded green, purple, and black to upper, middle, and lower) and one near the intersection of two tracks of the same build (red; for FIP with/without void). The white dashed lines show approximate melt region boundaries for each layer. (b) these VOIs in 3D with the surrounding material removed. (c) the single crystal voxel mesh used for FIP prediction. (d) clustering used for the single crystal, with a void (white) case. (e) the clusters used for the polycrystal case. (f) the clusters used for the polycrystal with void case.

4.4.2. Performance prediction: fatigue crack incubation life

Relative values of N_{inc} or FIP can provide insight into the impact a particular defect, or perhaps a class of defects such as lack of fusion voids, has upon the expected lifetime of the material under cyclic loading. For example, here we compare the computed FIP value for four different VOIs. The first two show results using the framework without the CA model, and the second two show results with the CA model. In each of these sets, one result is taken from Case 1 (which does not exhibit voids) in Table 4.2 and the other is from Case 2 (where voids are observed).

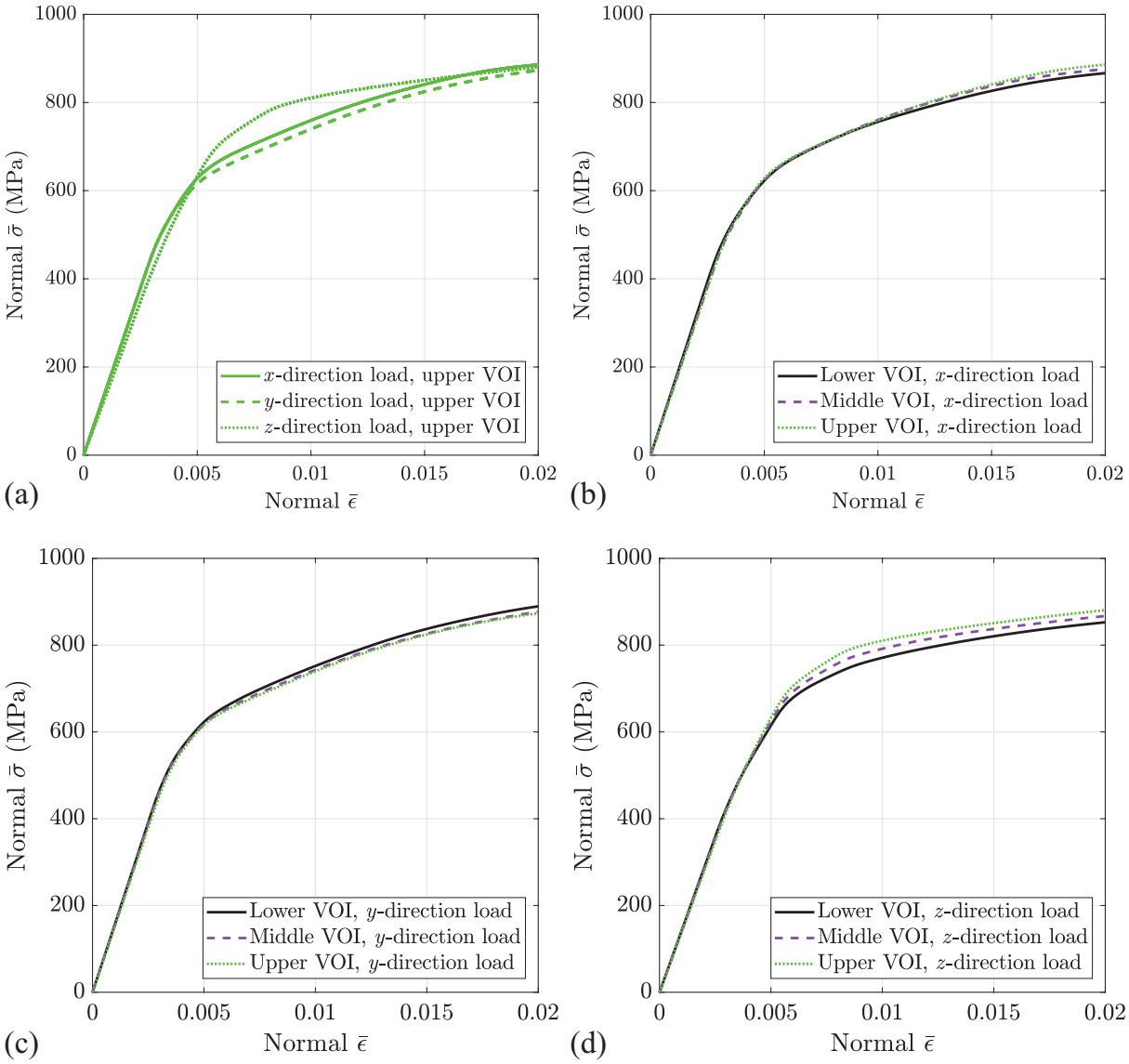

Figure 4.8. Stress-strain curves predicted by SCA with CP at the strain rate of 10^{-4} s^{-1}. (a) for the upper VOI showing the anisotropy of overall response, for all VOIs. The response for each VOI is given for x-direction loading (b), y-direction loading (c) and z-direction loading (d)

The first is a reference VOI: a simple single-crystal cube, representing a defect-free build (without the CA model). The second VOI is the same single-crystal cube, this time with a void predicted by the thermal-CFD model. This comes from Case 2 in Table 4.2, where larger hatch spacing results in insufficient fusion. The third VOI incorporates the CA model, making this a polycrystalline simulation. The fourth VOI adds the void to the polycrystalline volume. The simple, cubic voxel mesh

underlying all four of these VOIs is shown in Figure 4.7(c). The subsequent Figures 4.7(d-f) show the clusters used for SCA, computed from the elastic DNS, for the latter three RUCs, respectively.

Figure 4.9 shows the predicted strain-life behavior of these four VOIs. In the single crystal condition without a void there are no stress localizers, and the highest life is expected. The introduction of a void decreases the expected life substantially, as local stress concentrations occur around the void. In the polycrystalline VOI grain boundaries act as stress localizers, and even without a void the fatigue life is reduced from the reference VOI; however, the introduction of a void has less impact than in the single crystal VOI, since the worst case configuration – a high Schmid factor grain near the void – has not occurred.

The trends between different cases match qualitatively with experimental results demonstrated for SEBM. For example, Li *et al.* [**66**] compare experimentally measured fatigue life of Ti-6Al-4V for numerous AM technologies, including SEBM in hot isostatic pressing (HIP), heat treated, and as-built conditions. Subjecting the material to HIP is known to suppress voids, whereas heat treatment and as-built material retains any voids introduced during manufacturing. Thus, HIP SEBM results and non-HIP SEBM results present in Li *et al.* are comparable to the polycrystal no-void and void results respectively shown in Figure 4.9: in both the simulation and experiment reduction of void content results in higher fatigue life. A similar relationship, reduction of fatigue life with the introduction of a void, is presented by Gong *et al.* [**33**], where voids were intentionally built into a test coupon to study their effects.

This set of examples shows that the framework and models here can capture, at least qualitatively, the influence of process parameters (hatch spacing in the example shown) on expected material performance. This influence is captured by directly considering the change in material structure, i.e. the introduction of a void cause by lack of fusion, that results from a change in the processing conditions. The method presented is general: the impact of process parameter selection upon expected material performance can be predicted using this framework. Further, we have demonstrated that the framework is flexible enough that models can be added, removed, or

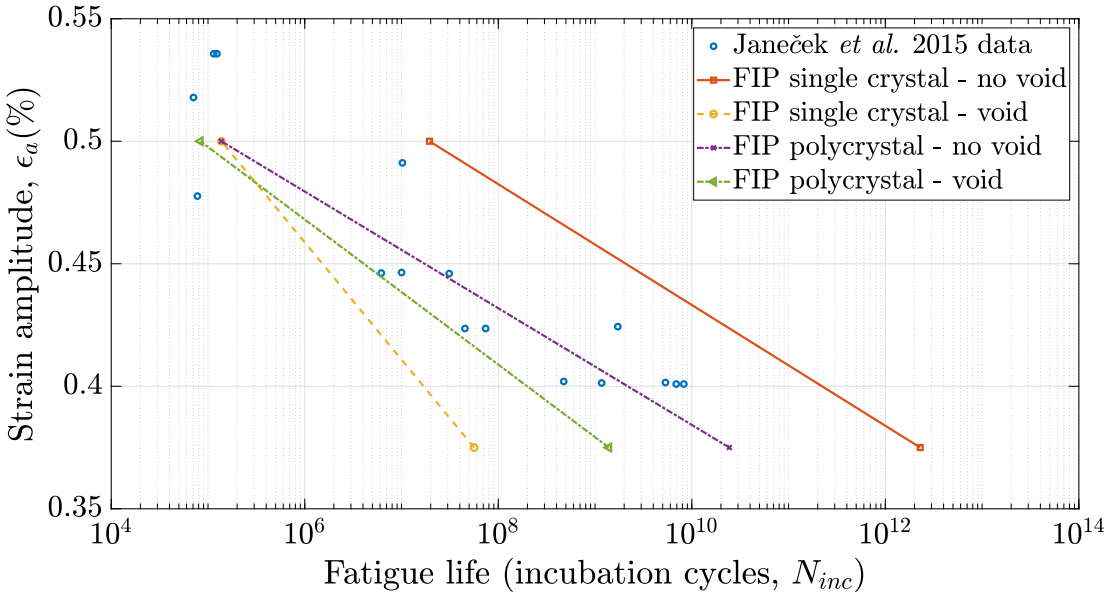

Figure 4.9. Experimental strain life data (points) for HCF replotted from [**48**], and four predictions of fatigue life at two strain amplitudes each: (1) a single crystal without any defects (baseline data), (2) a single crystal with a void predicted with the thermal-CFD model and (3) the full polycrystalline fatigue VOI shown in Figure 4.7 (4) this same growth pattern, including a void.

exchanged depending on the level of detail desired. In this case, the framework operates both with and without a prediction of grain growth via the CA model.

4.5. Summary and Conclusions

This chapter started by introducing a newly adapted reduced order modeling technique that combines the microscale basis of the crystal plasticity material model with the speedup provided by an order reduction technique based on a combination of classical micromechanics and machine learning, which we called crystal plasticity self-consistent clustering analysis, or CPSCA. For problems where the assumptions inherent in the micromechanical model are appropriate (e.g. periodic boundary conditions), the CP simulations were sped up by a factor on the order of 10^3 over the FEM for a realistic case that maintains similar accuracy to the equivalent CPFE or FFT-based solution. This level of speedup is promising: much larger problems can be attempted, and in terms

of design, previously intractable parametric studies are possible. This was demonstrated in [**54**] and [**111**].

Next, with my co-authors, we demonstrated a process-structure-properties prediction framework for additive manufacturing that connects models for each aforementioned stage and requires only basic material properties and processing conditions. The framework provides a means to capture the AM process that is extensible and flexible: additional models could be included (e.g. post-processing), and different types of analysis could be considered (e.g. continuum scale). This is enabled by a simple database format used to transport material state information between computational modules. Using this framework, we have shown a sample computation: a comparison between hatch spacings in SEBM Ti-6Al-4V, with all other process parameters held constant.

We claim the framework demonstrated here is sufficiently general to include macroscale simulations, if needed, or any other related module required. We show the addition of a CA model as an example of this. However, one could envisage the addition of further hubs. One option would be a design hub, which might include modules for CAD/CAE tools, slicing and machine control, and/or topological optimization. Another possible hub might implement models to capture post-processing steps such as HIP, heat and/or chemical treatment, and surface finishing.

In this case, the decrease in fatigue life that results from lack-of-fusion porosity occurring at too large a hatch spacing was demonstrated, consistent with experimental results. We have thereby shown that this framework enables computational design of the AM process, at least within the constraints of model applicability, using parameters derived from AM machines, raw powder, and studies of wrought material.

However, the models that make up the framework as outlined are generally applicable only for a few tracks/layers: while the larger idea of integrated PSPP modeling can be expanded to any scale, the models shown here cannot easily be expanded to capture the mechanical response across an entire build, which might consist of billions of grains. Although some scientific and engineering insight might be gained, in practice the uses might be limited.

CHAPTER 5

Heterogeneous material representation with image-based two-scale modeling

5.1. Background and motivation

This chapter introduces a new paradigm in mechanical modeling of microstructure dependent failure wherein a fast, reduced order approach is applied directly to experimentally imaged microstructures, which are used to populate a macroscale component; the behavior of these microstructures is used to predict the macroscale performance. This is a special case of what is known as concurrent multiscale modeling, with the added complexity that each microscale might be different. Knowledge of the process history (either from modeling or experiments) can be used to select which microstructure occurs at each material point in the component-level model, either deterministically or with some variability. Thus spatial, build-to-build, and part-to-part variations can be captured.

Specifically, this concept will be demonstrated by choosing, at each material point in a component, a particular microstructure based on the results of a process model for AM. The microstructures to choose from are provided by a database of x-ray computed tomography images of voids. Finally, the load history during the component's expected service life is predicted, and used to estimate the fatigue or fracture initiation (or another performance indicator). One might alternatively think of this as a virtual experiment, as each specimen tested computationally provides one data point in terms of performance, analogous to a physical experiment. In some ways this is similar to the concept of a digital twin that has been gaining popularity in the industrial sector.

The resulting framework has several unique features:

- Location- and process/history-dependent properties and performance prediction

- Scalability to components or even systems (based on the macro-scale solution method employed)
- Ability to estimate variability, in addition to mean/min/max, in behavior throughout the domain
- Use of 3D images as the microscale; this provides a sound physical basis for the microstructure selection and hopefully more accuracy than using synthetic, imagined, or idealized microstructures

In Section 5.2, a sketch of the methods employed to build our multiscale model is made, including a thermal model of the AM process (Section 5.2.2.1), an image- and modeling-based statistical description of voids (Section 5.2.3.1), and the mechanical multiscale model used to predict performance (Section 5.2.4). This is followed by two computational examples, predicting of the strain-life behavior of a sample of virtual fatigue specimens built of IN718 with several different process parameters and the fracture initiation behavior of a compact tension specimen are demonstrated (Section 5.3).

5.2. Methodology

5.2.1. Model setup

Conceptually, this multi-physics, multiscale method is composed of several different interconnected steps. A preliminary step involves building a database of images of voids in the material of interest, in this case IN718, and a relationship between those key measures of those images and a metric that describes the relevant processing history of the material, in this case relating the volume fraction of voids to final solidification cooling rate. With this information available, the workflow for a particular component of interest is as follows:

(1) Macroscale thermal model of the build process, which captures the influence of processing parameters (scan speed, and laser power are shown as examples).
(2) Macroscale stress analysis to compute deformation history of all points within the component.

(3) Generation of a possible realization of the overall specimen by picking images (microstructures) for every point in the component that match the relationship between processing history and microstructural descriptors developed in the preliminary step.

(4) For every microstructure thus associated to a point in the component, application of the deformation computed in the stress analysis of the component for that point.

(5) Computation of the performance of the component based on a performance metric applied to each microstructure. For example, the minimum fatigue life within a microstructure will give the failure location and cycles-to-failure.

(6) Repeat steps 3-5 until a reasonable confidence of the results, based on possible microstructural configurations, is obtained.

(7) Repeat 1-6 and/or 2-6 for different processing conditions and/or loading conditions as needed.

There are a number of inputs to the model. The first set are processing conditions (e.g. laser power, toolpath, beam size) and thermal material properties - this is used in the thermal modeling, and might be thought of as a pre-processing step for the material model. The material modeling phase takes in thermal results (in this case, solidification cooling rate), single-crystal material properties for the crystal plasticity model (16 fitting parameters for this CP model, plus slip systems), fitted FIP parameters for fatigue initiation prediction and/or a failure surface represented as effective plastic strain plotted on stress triaxiality versus Lode angle parameter axes for fracture initiation prediction. Finally, and most importantly, a database of microstructures of interest is used to build in the heterogeneity at the microscale. In this case, XCT images are compiled from a series of imaging experiments, however, in theory any means of microstructure generation could be used (e.g. synthetically built with DREAM3D or from simulations as is demonstrated in Chapter 4).

The overall workflow is shown schematically in Fig. 5.1 with a generic example component. The different phases of this method make use of different solution methods, conducted in several different software packages (both internal codes and commercial software). However, the data exchange between each step requires little user input and could be configured to operate completely

automatically. In the numerical examples shown here, five repeated trials are performed for four different strain amplitudes and two processing conditions for a fatigue test are completed automatically, once the input data is gathered. Two different trials are shown for a fracture test; the same underlying idea is used, so this just demonstrates that fracture initiation can also be predicted in addition to fatigue initiation.

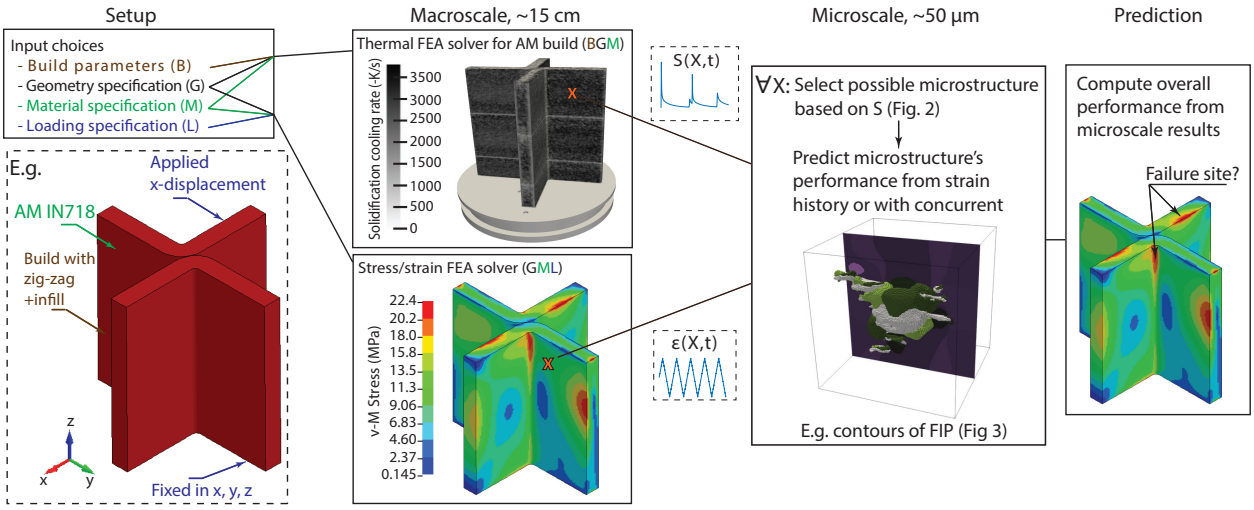

Figure 5.1. Overall diagram of the computational scheme. Geometry, build process parameters, material, and loading conditions must be specified. These are used to conduct a thermal analysis and a macroscale stress analysis. For each material point X within these two models, an element-wise sub-model is constructed to represent a possible state at that point. This uses local thermal history and strain history to determine the microstructure (void geometry) and deformation history. These are used to predict the microscale evolution of state variables such as plasticity and damage, which are homogenized (e.g. by taking the l_∞ norm of the domain) and used as element-wise estimators of part-level susceptibility to failure.

5.2.2. Macroscale

5.2.2.1. Thermal modeling for the AM build process. A thermal analysis is used to model building the component of interest using the directed energy deposition (DED) method. This analysis is done using a transient thermal Finite Element solver [**115**] (GAMMA). Thermal modeling in GAMMA was conducted by Kevontrez Jones for this project. The governing heat transfer energy

balance to be solved is:

$$\frac{\partial \rho c_p}{\partial t} = \frac{\partial}{\partial x_i}\left(k\frac{\partial T}{\partial x_i}\right) \tag{5.1}$$

where ρ is the material density, c_p is the specific heat, t is the time, x_i are the spatial coordinates, k is the conductivity of the material, T is the temperature.

A heat source Q is used to represent a moving laser. It is modeled using a moving boundary condition to apply a surface flux described by the Gaussian distribution:

$$Q = \frac{2P\eta}{\pi R_b^2}\exp\left(\frac{-2\left(x^2+y^2+z^2\right)}{R_b^2}\right) \tag{5.2}$$

where P is the power of the laser, η is an absorptivity factor to limit the amount of energy absorbed by the material from the laser which was taken to be 30%, and R_b is the radius of the laser. The variables x, y, and z are local coordinates of the laser. Heat loss on the dynamic free surfaces of the model is simulated though a combination of convection and radiation. Convective heat loss is defined by

$$q_{conv} = h_c\left(T - T_\infty\right) \tag{5.3}$$

where h_c is a convection coefficient, T is the surface temperatures, and T_∞ is the far-field (ambient) temperature. Radiation heat loss is defined using the Stefan-Boltzmann law, given by

$$q_{rad} = \sigma_s \varepsilon\left(T^4 - T_\infty^4\right) \tag{5.4}$$

where σ_s is the Stefan-Boltzmann constant and ϵ is the surface emissivity of the material.

Particular build parameters, including laser speed and power and the toolpath are selected. The material must also be specified. With this information given, the model can predict the time-temperature-history of each point within the part. This is achieved by specifying elements in the mesh to activate or de-activate based on the time-history of the toolpath: elements the tool has traversed are considered activated, and are included as fully dense material, while elements the

tool has yet to traverse are not include in there thermal solution. Moving boundary conditions are employed that account for active and inactive elements, appropriately applying the heat transfer conditions outlined above as required throughout the domain.

The solidification cooling rate (SCR) is calculated based upon the temperature history of the thermal model at each node. This is approximated, according to Eq. (5.5), as the time it takes for a material point, represented by subscript i, to reach the solidus temperature from the liquidus temperature. In order to capture this solidification behavior Eq. (5.1) is solved explicitly with an approximate time step of 9.0×10^{-4}s. If too large of a timestep is chosen, one may skip over the solidification behavior at some material points. Additionally, in the case of re-melting, only the final cooling stage is considered. The final solidification (if melting and re-solidification occurs) is saved as an output parameter.

$$SCR\left(\mathbf{X}^M\right) \approx \frac{T^{liquid}_{\mathbf{X}^M} - T^{solid}_{\mathbf{X}^M}}{t^{liquid}_{\mathbf{X}^M} - t^{solid}_{\mathbf{X}^M}} \quad \forall \mathbf{X}^M \in \Omega^M \tag{5.5}$$

where $SCR(\mathbf{X}^M)$ is the solidification cooling rate as a function of the macroscale spatial coordinates $\mathbf{X}^M$ within the macroscale domain Ω^M, $T^{solid}_{\mathbf{X}^M}$ is the solidus temperature, $T^{liquid}_{\mathbf{X}^M}$ is the liquidus temperature, $t^{liquid}_{\mathbf{X}^M}$ is the time at which the liquidus temperature is reached, and $t^{solid}_{\mathbf{X}^M}$ is the time at which the solidus temperature is reached.

5.2.2.2. Macroscale stress analysis, i.e. test conditions or service life. At the macroscale, a stress analysis representing expected services life conditions of the component or specimen is conducted; for example, to model a standard test specimens this would model the applied test conditions (e.g. uniaxial fatigue, compact tension). For loading conditions where small strains are expected, an elastic model or well-known elasto-plastic model, such as Johnson-Cook, with one-way heirarchical coupling is sufficient. From this approximation, the time history of the deformation gradient at each material point is extracted and passed to the microscale. This might be conducted with any commercial Finite Element software package, or any other means of acquiring a point-wise deformation gradient throughout the component. This history is then applied to the microscale,

where performance estimates are made. While this implies a one-way coupling (macroscale to microscale), a concurrent coupling where the effective response of the microscale is used at the macroscale is also possible if finite deformations are of interest. A concurrent implementation for materials that are well-described by an RVE has been demonstrated by [**147**]. These two operating modes are exemplified in the numerical examples for fatigue and fracture, respectively.

5.2.3. Microscale

Two primary components are required for the microscale model. First, a microstructural geometry is needed, and second the boundary conditions (loads or deformations) to be applied to that microstructure are needed. For each material point, the thermal conditions are used to select an appropriate image to represent the microstructure at that point. For that same point, the deformation gradient from the macroscale analysis is used to provide overall deformations on the bases of either one-way coupling (for the fatigue example) or two-way coupling (for the fracture example), and a scale-separation assumption.

5.2.3.1. Relate thermal conditions and defects. A relationship between the predicted thermal history and microstructure descriptors is used to identify possible defects. As a simple example, and to demonstrate the principle, in this case the relationship is generated by relating a thermal descriptor (e.g. SCR, as computed above) and microstructure descriptor (e.g. void volume fraction, V_f). This relationship is then used with a database of microstructural geometries to identify possible microstructures for each point within the component. Selecting one possible microstructure for each point gives one "realization" of that component. This process is outlined in Fig. 5.2.

In order to identify the SCR-to-void relationship and build a database, I used the two IN718 DED single-track thin wall parts built with processing parameters corresponding to parameter set 1 in Tab. 5.2. Both walls used a vertical zig-zag toolpath pattern, but while the toolpath for one wall was continuous, the other added a one-minute dwell between each layer. This results in different thermal behavior in the two walls. These are two of the specimens which were tested in Chapter 2.

X-ray tomography imaging experiments from Beamline 2-BM at the Advanced Photon Source, Argonne National Laboratory, for specimens extracted from 22 locations on the two thin walls (total 44 data points) were used. Each image was of about 1 mm^3 of material with voxel edge length 0.65 µm. Contrast from x-ray absorptivity was used to distinguish between voids and material using a series of processing steps including filtering, thresholding, and artifact removal. Eleven different descriptive statistics for voids were extracted from these images, such as void location, size, shape, orientation, and n-nearest neighbor information, just as described in Chapter 2. For simplicity, we will focus here on the void size, as represented by the single-point correlation statistic: void volume

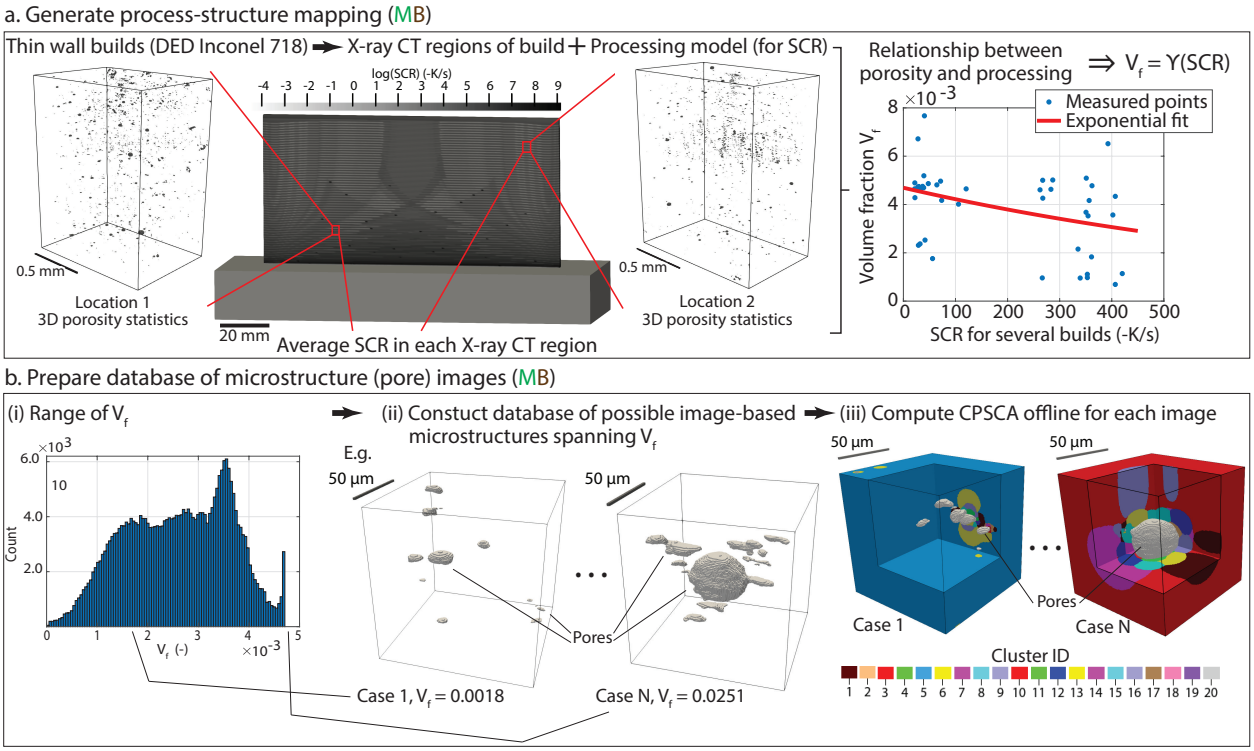

Figure 5.2. Diagram of the defect estimation and database building process. In the first part, a relationship between solidification cooling rate (SCR) and void volume fraction (V_f) is determined using process modeling and X-ray computed tomography. Second, 2(a) the subsets of the images acquired with X-ray tomography are selected based on V_f, such that the expected range of V_f for any arbitrary part (with known or predicted thermal history) is spanned. 2(b) A database of these possible microstructures is generated, 2(c) including computing the training stage of the mechanical model.

fraction V_f. The overall V_f was computed from the sum of the void sizes throughout the image for each location.

The build process of these two thin walls was modeled using the thermal analysis method outlined in Section 5.2.2.1. The parts' thermal history is summarized as a point-wise SCR throughout the build. The SCR is a useful, physically relevant single-point statistic that summarizes the thermal conditions that result from the choice of building parameters. The average SCR at the location of each of the x-ray images was computed using this processing model. Note that experimental measurements of the cooling rate, e.g. with an infrared (IR) camera, could be used to provide equivalent data; however, confidence in the thermal model is currently higher due to difficulty in calibration of the IR data and several other procedural concerns. The first part of Fig. 5.2 shows how the average SCR versus the V_f of each image is gathered and plotted. An exponential relationship, as suggested by Wolff et al. [**130**], given by:

$$V_{frac} = Ae^{-(B)(SCR)} \tag{5.6}$$

was fit to the data. The fit parameters are $A = 0.0047$ and $B = 0.0011$. Similar relationships have been made for porosity elsewhere, e.g. [**55**].

5.2.3.2. Build the image database. Next, this relationship is used to determine a range of possible microstructures that might occur within the build. Subsets of the images used in the first part were exhumed, such that the V_f range of the subsets corresponds to the range estimated to occur in a part as given by the relationship shown in Fig. 5.2. Basically, an iterative search process through the larger images was conducted, searching for subsets with appropriate V_f. These image subsets constitute a database of possible microstuctures, in this case each was of size 97.5 µm × 97.5 µm × 97.5 µm (150 voxels in each dimension) and with $V_f \approx 0.0001$ to $V_f \approx 0.03$. A total of 388 different example microstructures were extracted using a script written by Puikei Cheng. Of these, 320 were used in the examples shown below. These were tabulated according to V_f, which could be referenced to select any given subset for a particular location in the macroscale.

To complete the database, the three training steps outlined in Sect. 5.2.4.1 were conducted on each entry. Thus, the final database used for the multiscale mechanical response prediction contains proto-data used to generate response predictions for arbitrary loading, which depends upon microstructural information. Critically, all microstructures used the mechanical response predictions shown in the following sections are computed directly with 3D XCT subset images of voids in AM metal.

5.2.4. Part 3: Mechanical response prediction

In the previous two sections, we have used a database of experimental data to populate the part with a realistic, heterogeneous distribution of voids that correspond to the processing conditions used to build the part. The next step is to use this information to predict the mechanical properties of the part. However, similar predicting the defect structure directly, it would be infeasible to directly model the mechanical response of the microstructures we have generated.

As mentioned above, to capture the microstructural information required to predict mechanical performance of AM materials, a multiscale approach is taken. At the macroscale, an empirical material model is used to provide the strain boundary conditions (more specifically, deformation gradients are used) to the data-driven reduced order model used at the microscale. At the microscale, crystal plasticity is used to predict the material behavior using a single grain for each microscale (although this simplifying assumption could easily be refined given more data). This can operate with either one-way to two-way coupling. Lacking more complete or deterministic data, we simply assume that any microstructure with V_f within 20% of that specified by Eq. (5.6) has equal probability of occurring at each macroscale material point. In this way, the part is described by essentially a Monte Carlo process, where the possible states of the random variable are controlled by the process model. Box 5.1 gives a detailed alorgithm for selecting, for each material point, the entry in the database to use. A schematic of this process is shown in Fig. 5.3, where the local temperature history and strain history are taken as inputs to a micromechanics model, which then computes local and homogenized responses.

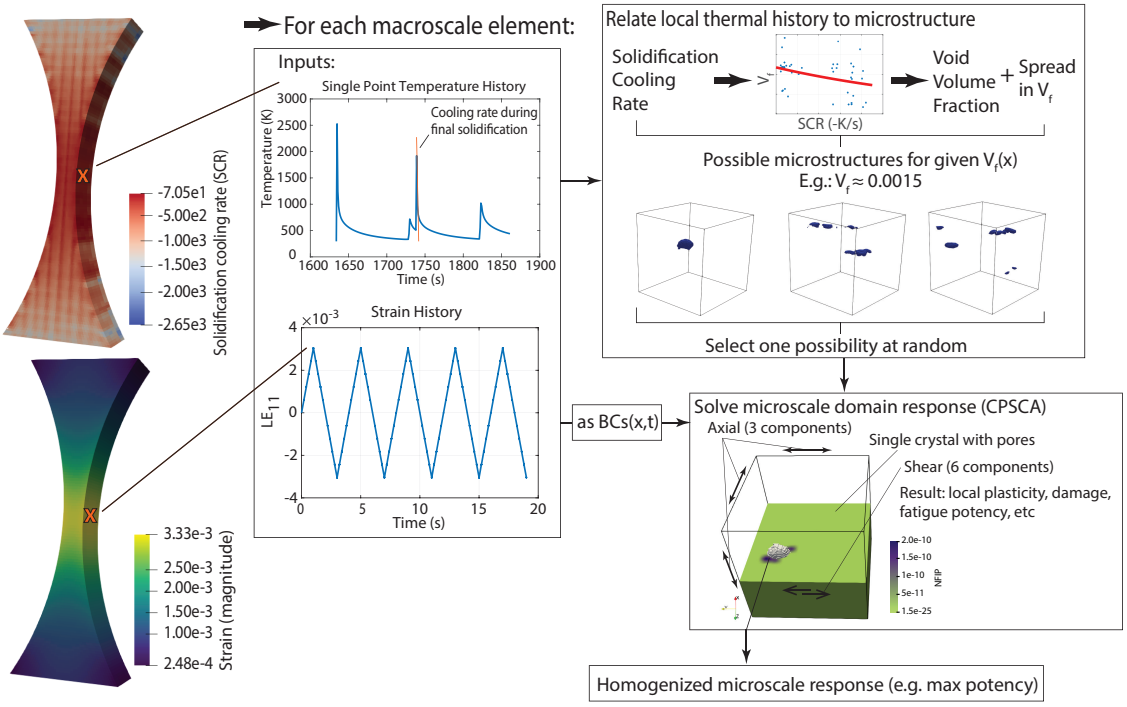

Figure 5.3. For each macroscale material point (in this case, within the dogbone specimen use in the numerical example in Section 5.3), the thermal history and strain history are passed to a microscale solver; a microstructure is selected from the database developed in Section 5.2.3.1 based on the thermal history, and deformation boundary conditions are applied according to the strain history. A crystal-plasticity-based microscale solution is computed, and a homogenized response (e.g. the l_∞-norm of the fatigue indicating parameter, if a fatigue problem is chosen) is returned to the macroscale.

Box 5.1

Algorithm for microstructure selection

(1) Initial data

  (a) Load SCR data

  (b) Load stress mesh

  (c) Load microscale database

(2) For each element in stress mesh:

  (a) Compute average SCR for element

  (b) Compute V_f from SCR with Eq (5.6)

  (c) Find all microscale in database with $\pm 20\%$ of that V_f

(d) if no microscales are within ±20%:

(i) if $V_f >$ maximum V_f: pick 1 microscale at random from 5 special "large V_f" options

(ii) if $V_f <$ minimum V_f: pick 1 microscale at random from 5 special "small V_f" options

(e) otherwise: V_f pick 1 microscale at random from the avaliable microstructures

After each element has a microscale assigned, begin concurrent (one-way or two-way) modeling:

If one-way model: solve response of each microscale with pre-computed stress-history at each point

If two-way model: in macroscale UMAT load in all microscale data, store in an element-by-element 2D and 3D arrays and access each element's data as needed (e.g. V_f is stored with one entry per phase per element in a 2D array $v_f(nP, nElem)$, where nP is the number of clusters and $nElem$ is the number of elements in the stress mesh).

5.2.4.1. Microscale reduced order model with crystal plasticity. At the microscale, the modeling approach combines a data-driven micromechanics method with computational crystal plasticity, termed crystal plasticity self-consistent clustering analysis (CPSCA). This method was first introduced by Liu et al. [**72**], and refined by [**147**]. A microstructural Fatemi-Socie fatigue indicating parameter (FIP) was computed with this approach by Kafka et al. [**54**]. Shakoor et al. [**111**] and Yu et al. [**147**] extended this to a finite strain formulation to be fully compatible with deformation-gradient-based crystal plasticity, and demonstrated a concurrent multiscale model. In essence, the microscale fatigue prediction model used here is the same as used in [**54**] and Chapters 3 and 4, with appropriate choices of model parameters for IN718. The method is derived from first order homogenization, the Hill-Mandel condition, and local equilibrium, similar to what is shown in Chapter 4. In this case, a finite deformation implementation is employed to more accurately compute the deformation gradient that the CP requires as input. The problem is defined concisely in by Yu et al. [**147**]; see that reference for details.

Recall that CPSCA solves these equations in two stages. The first "training" stage consists of three parts: data collection, data compression (or clustering), and computation of the interaction tensor. The resulting interaction tensor can be stored for future use. The second "prediction" stage makes use of the interaction tensor and solves the integral equation given in Eq. (4.3) subject to an applied strain state and material law.

This first stage is conducted for each of the subset volumes in Section 5.2.3.1, adding the clustering and interaction tensor data to the database of image subsets.

Thus, after a part is instantiated (microstructures selected for each macroscale point), only the second stage has to be used to compute the mechanical response. The second stage can be run any number of times, with independent stress-strain histories and boundary conditions, resulting in different behavior at different points in the macroscale. In this case, the behavior is are computed with a crystal plasticity (CP) material law. The crystal plasticity model is the same as is shown in [**54**] and Chapter 3, where the applied deformation gradient is decomposed into an elastic and plastic part; the plastic part of the deformation gradient is computed from the plastic velocity gradient, which itself is determined by summing the plastic shear velocity across slip systems in the intermediate configuration. In the case of one-way coupling used in the fatigue example below, deformation gradients history from the macroscale analysis is passed to the microscale via I/O operations on a simple text file. For the two-way coupling required for convergence of the CP method when the larger strains experiences in the fracture example are encountered, the entire online portion of the CPSCA is implemented (by adapting Cheng Yu's implementation) within a user material subroutine (UMAT) in Abaqus/Standard.

5.2.4.2. Example performance measure: fatigue life. Again, as in 3, fatigue life is measured using Shenoy and McDowell's modification to the Fatemi-Socie fatigue indicating parameter. The formulation is the same, implemented within SCA following [**54**] and Chapter 3. The volume averaging region is set with edge length l_{avg} equal to 10% of the edge length of the equivalent cube edge length of the total void volume (i.e. $l_{avg} = 0.1 \sum(\text{voidVolume})^{1/3}$). Volume averaging uses MATLAB's built-in imboxfilt3 routine with circular padding. Mind that the clustering solution is

already includes averaging, so interpretation of the volume averaging must be taken in the context of averaged clusters that can be either larger or smaller than the region size.

5.2.4.3. Example performance measure: fracture potency. A second example case demonstrates prediction of fracture potency by measuring the local microscale Lode parameter and stress triaxiaility and comparing that to a failure criterion applicable to microscale deformations. These measures account for, e.g., void-void interaction causing local stress enhancement. Whether or not a given load will cause failure is computed in this way. However, an ongoing fracture process was not modeled; only the point of fracture initiation is identified here due to limitation of the multiscaling method as will be discuss in Section 5.4

5.3. Numerical demonstrations

Two example cases, one for fatigue and one for fracture, are given below. Each follow the relevant ASTM standard geometry, and in both cases a mesh refinement study was conducted to ensure converged results.

5.3.1. Fatigue life of a standard test specimen

A fatigue specimen conforming to the ASTM E606 standard geometry [**5**] is numerically built and tested. The specimen geometry was meshed with two different hexahedral meshes, for one thermal and one stress analysis, as shown in Fig. 5.4. The two meshes are largely the same, except the mesh used for stress analysis is coarsened in the thickness (z-) direction. This is the build direction, and thus requires at least one element per build layer in the thermal model, but during the stress analysis the stress and strain are roughly constant through this direction. This may, however, smooth out some of the variability between process parameters, as SCR was averaged during mesh coarsening. Following the schematic shown in Fig. 5.1, this mesh was loaded into both the thermal solver then the stress solver. An in-house thermal FEA code was used for the thermal model, and C3D8R elements in Abaqus were used to compute stress and strain at the macroscale. The lower grip was fixed and the upper grip was displaced at constant strain rate over four fully reversed load

Table 5.1. Thermo-physical properties of IN718 [**88**]

Property	Notation	Value
Density	ρ $(\frac{kg}{m^3})$	8100
Solidus temperature	T_s (K)	1533
Liquidus temperature	T_l (K)	1609
Specific heat capacity	c_p $(\frac{J}{kgK})$	$360.24 + 0.026T - 4 \times 10^{-6}T^2$
Thermal conductivity	k $(\frac{W}{mK})$	$0.56 + 2.9 \times 10^{-2}T - 7 \times 10^{-6}T^2$
Latent heat of fusion	L $(\frac{kJ}{kgK})$	272

Table 5.2. Set of process parameters for thermal analysis of IN718

Parameter set	1	2
Laser power (W)	1800	1800
Scan speed (mm/s)	15	10
Beam radius (mm)	1.5	1.5
Layer thickness (mm)	0.75	0.75
Scan pattern	unidirectional	unidirectional

cycles in the macroscale FEA stress analysis (using the Static/General solver in Abaqus) at several different strain amplitudes.

Macroscale homogeneous material properties corresponding to Inconel 718 (IN718) were applied to both the thermal and macroscale stress analyzes. These thermal properties for IN718 are summarized in Tab 5.1. The Johnson-Cook parameters identified by [**39**] were used, although this choice is essentially arbitrary – under the fatigue loading specified, the macroscale response was entirely elastic.

For the thermal analysis, a zig-zag tool path with 90-degree layer-by-layer offset was selected, with the two different sets of process parameters specified in Tab. 5.2. The part was meshed and simulated with the gage section aligned normal to the build direction. A relatively fine mesh with 539216 hexahedral elements (Fig. 5.4(a), substrate not shown) was used; Fig. 5.4(b) shows a detail of the mesh in the narrowest part of the gage section.

The CP model outlined in Sect. 5.2.4.1 was used at the microscale. The parameters were calibrated by minimizing the difference between many runs of a cubic domain consisting of 64 cubic grains and a set of baseline tensile and cyclic loading data for AM IN718, with starting conditions taken from [**19**] (for m and $\dot{\gamma}_0$) and [**28**] (for elastic moduli). The resulting model parameters are

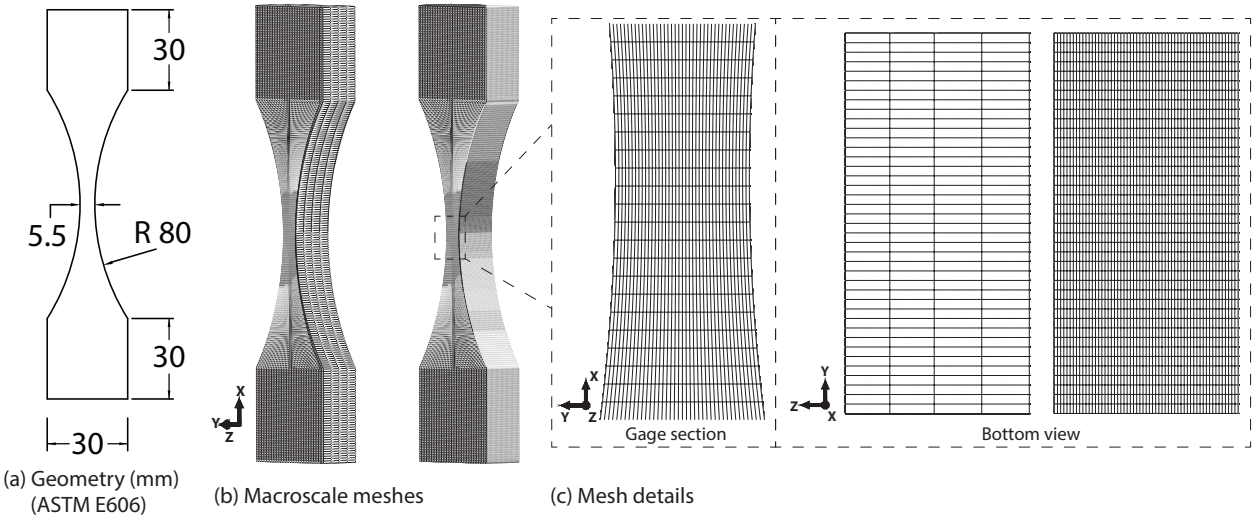

Figure 5.4. (a) example component geometry specification (ASTM E606 fatigue specimen) (b) the two meshes and (c) details of the specimen meshes, including the difference between stress (left) and thermal (right) meshes.

given in Tab. 5.3. The parameters that relate FIP to fatigue life are fit to experimental high cycle fatigue data of IN718 collected from literature in Chapter 3 [**60, 137, 122, 149, 2, 15, 6, 73**].

The imaged voids identified by the method in Sect. 5.2.3.1 were assumed to be embedded within a single crystal oriented so that the fastest growth direction ([111] for the fcc matrix) was aligned with the build direction (the Z-direction in the figures). This is consistent with experimental experience which suggests that grains in IN718 are much larger than the voids and preferentially orientated [**96, 92**]. However, this assumption could easily be refined in future work, e.g. to include grains in the microscale representation, if more information for local grain orientation is forthcoming.

A snapshot of the thermal response for the part being built under one of the processing parameter sets is shown as contours of temperature in Fig. 5.5, as an example of the thermal prediction. This thermal prediction progresses through the full building process for this specimen.

I simulated forty different virtual test specimens, each with a different, random distribution of defects, and thus estimated fatigue life. This involved selecting one of the possible microstructures for each material point in the coarsest mesh at the macroscale, in this case for the stress analysis. At each point, the solidification cooling rate was used compute the expected V_f using Eq. 5.6. A

Table 5.3. Primary crystal plasticity model parameters

Parameter	Value
C_{11} (MPa)	257,000
C_{12} (MPa)	127,000
C_{23} (MPa)	94,000
$\dot{\gamma}_0$ (s^{-1})	0.0024
m	60
τ_0 (MPa)	360

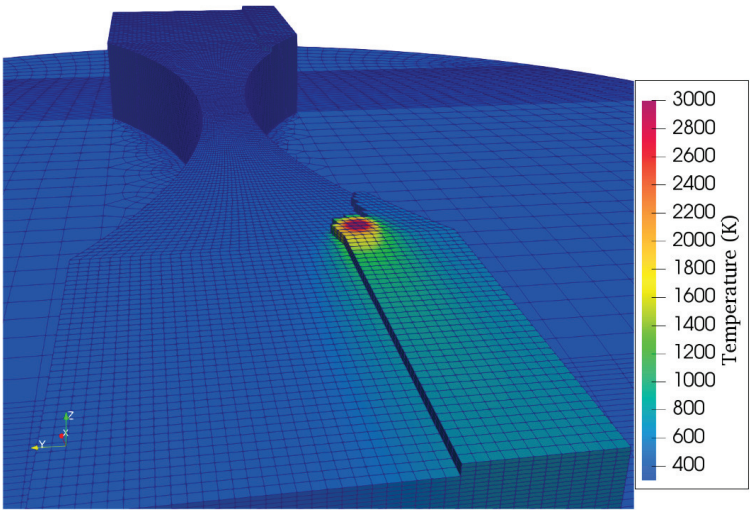

Figure 5.5. The continuous radius fatigue test specimen, showing the thermal processing prediction partway through the build. The peak temperature and temperatures gradients appear physically reasonable.

spread of 20% on either side of this expected V_f was applied to select a few possible microscale images from the sub-image database described in Sect. 5.2.3.1. One of these images was chosen at random to be the microstructure at that material point. Note that because the size of the database of images is small for this demonstration, each image might be selected multiple times in each specimen and similarly will likely be chosen in multiple specimens.

Each specimen consists of 19360 elements at the macroscale, each of which is represented by a $150 \times 150 \times 150$ voxel mesh selected from the database of microstructures (voxel meshes) at the microscale (or 3.375 million voxels). Thus, each specimen has about 65 billion voxels across all the microstructures. Direct simulation of a system this large is intractably computationally expensive except, perhaps, on some of the very largest computers (not practical for practitioners). Using

CPSCA at the microscale with 16 clusters in the matrix phase and four in the void phase reduces the computational expense to effectively solving for $19360 \times 20 = 387200$ microscale responses across the macroscale specimen, which is possible using a modern workstation computer (or one node of a cluster computer, in this case). The microscale part (the most time consuming) for each simulation takes about nine hours using 36 cores in parallel on Intel Xeon Skylake 6140 CPUs at 2.9 GHz clock speed. The macroscale solution only takes a few minutes on 72 of the same CPUs.

The resulting microstructure-based fatigue life predictions are shown in Fig. 5.6. The plotted points fall on a strain-life curve showing the overall minimum estimated life for five realizations of specimens (different sets of possible microstructures) for each of three different load amplitudes for two different processing conditions. Changing processing conditions changes the solidification cooling rate at each point, and thus changes the possible microstructure that can be chosen to represent each point in the macrocale which in the end changes predicted failure site and number of cycles to failure.

The results in Fig. 5.6 directly demonstrate the key features of this method. The contour plots of the gauge sections report an estimated number of cycles required to cause fatigue crack initiation at each macroscale point in the fatigue specimen; at any given macroscale point, the microstructure is different between different instantiations (Specimen A versus Specimen B at the top of Fig. 5.6), which results in different contours plots. Comparing the microstructures between Specimen A and Specimen B provides the reason behind this difference: features with higher fatigue potency might, by random chance, occur at the point of highest strain concentration in one instantiation but not another. This is similar to behavior seen in physical testing, e.g. [**31**]. Note that because of the relatively limited number of microstructures in the database use for this demonstration, one particular microstructure tends to result in failure throughout the specimens (see Fig. 5.6). All the coupons corresponding to the points shown in Figure 5.6 are shown with contours of fatigue life in Figure 5.7.

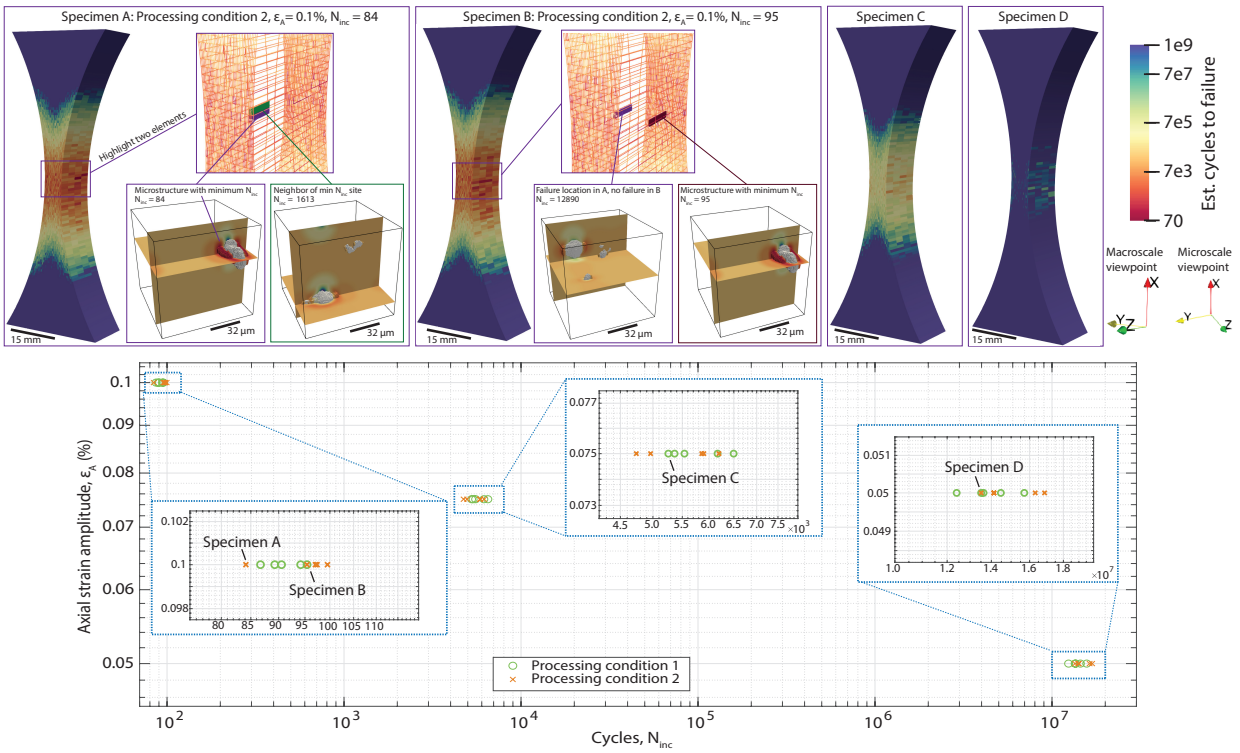

Figure 5.6. Estimated fatigue lives for multiple realizations of the fatigue coupon, run at different applied strain amplitudes, mimicking theoretical experimental conditions. Two different processing conditions (conditions 1 and 2 in Tab. 5.2) were modeled.

5.3.2. Fracture potency estimate

A compact tension specimen conforming to the ASTM E399 standard test geometry was simulated using this framework. The goals of this model are twofold: 1) to show that the fracture initiation point can be captured, and 2) to demonstrate that by using variable microstructures, predicted onset of fracture will vary and thus we can hope to predict and perhaps control fracture onset in AM builds.

A thermal simulation of the build was conducted with the Z-direction along the build axis. A converged mesh with 6220 elements was used for the stress analysis, as shown in Fig. 5.8(a). There are two elements per build layer (reduced from five in the thermal mesh). A symmetry boundary condition was applied to the +Z face, and free boundary conditions were applied on all other surfaces. Two rigid cylinders were used as pins with predefined displacements in the

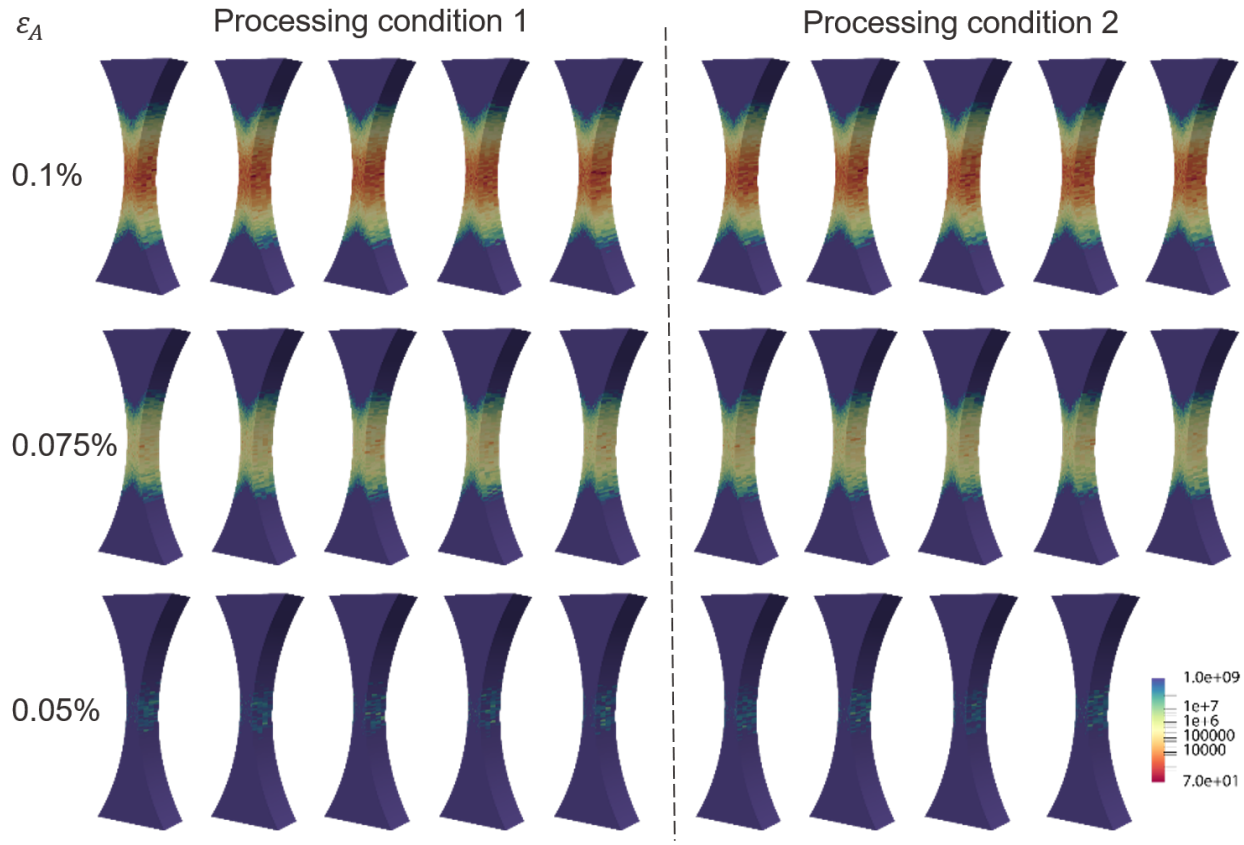

Figure 5.7. Contour plots for each of the points shown in the fatigue-life diagram, showing distributions of estimated fatigue life

Y-direction and simple contact to achieve bulk-scale Mode-I-type deformation, roughly modeling common experimental conditions (not shown in the figures). An initially-blunted crack with root radius 0.254 mm was considered, which is more easily processed in the thermal simulation than a geometry with a sharp crack tip root. The goal of the model is to estimate fracture initiation and demonstrate the impact of heterogeneous microscale on the macroscopic predictions. The model does not extend to the fracture process itself (capturing local effects such as separation with a homogenization-type model such as this makes little sense), so there is no need to use a sharp-tip initial configuration. The same database of microscale voxel meshes were used as in the fatigue example.

Because of the larger deformations involved here compared to in the fatigue problem, a concurrent coupling method [**147**] was for the mechanical solver (although mesh convergence was analyzed

at the macroscale with a Johnson-Cook material law), replacing the deformation gradient history mapping technique that was sufficient for the lower total strains observed in the fatigue example. As before, a prior thermal analysis is used for element-by-element selection of microstructures. A thorough derivation and details regarding the implementation of the concurrent scheme for two-scale coupling (used here) and the generalization to many-scale coupling can be found in [**146**] and [**147**].

In short, this scheme implements CPSCA as a material model inside of an Abaqus UMAT. The UMAT passes the deformation gradient at the beginning and end of the time step to CPSCA, and CPSCA computes the stresses and algorithmic tangent modulus required for that deformation step and passes those values back. The iterative solution scheme used by Abaqus/Standard's static solver can be used as with any other UMAT, and updates through time as normal. The biggest new contribution here is the addition of a database of microstructures, as outlined in Box 5.1, rather than the use of a single geometry at the microscale. To achieve this, when Abaqus initially loads the material subroutine, a series of additional matrices are initialized to store the database. The data is then loaded into these matrices such that for each element, the UMAT can access a different portion of the matrix which corresponded to a different microscale for CPSCA for analyze. This is all achieved with custom user routines, implemented in Fortran within the Abaqus UMAT environment and in MATLAB, Bash, and C++ for utility routines used to set up the run (e.g. select which microstructure go where in the macroscale and assign microstructures to the correct elements so Abaqus can load the matrices with the proper entries) and extract information for post-processing (with the Abaqus C++ API) and visualization of data at different scales using Paraview (after data is extracted from the Abaqus save files).

Classical fracture toughness measures (stress intensity K, fracture energy G, and the J-integral) are typically used for macroscale assessment; however, these may not be useful to measure the changes caused by microstructures. In the fracture mechanics literature, at the micro-scale, changes in void shape or spacing in the fracture zone has been proposed, for example. However, the accuracy of predicted void shape change might be limited. In this case, we simple choose to measure the

local plastic strain, and compare that value to a "critical failure strain" reported for wrought IN718 in [**102**] in terms of the Lode angle parameter and stress triaxiality. The critical failure strain was fit with a polynomial surface to experimental data points, as given by

$$\begin{aligned}(5.7)\quad \epsilon^{p}_{critical} &= 0.6975 - 0.02614(\bar{\theta}) - 0.8662(TF) - 0.03889(\bar{\theta})^2 \\ &\quad - 0.1643(\bar{\theta})(TF) + 0.4206(TF)^2 + 0.4206(TF)^3 - 0.1934(\bar{\theta})^2(TF) + 0.249(\bar{\theta})(TF)^2\end{aligned}$$

where $\bar{\theta}$ is the Lode angle parameter and TF is the triaxiality. A simple weakening factor was further applied; after a microscale cluster is marked as "failed" according to its stress state, it remains failed and for every subsequent increment its stiffness is homogeneously reduced by a factor 5% greater than the previous factor starting at zero and increasing until 95%, effective removing its load-bearing capability shortly after failure. In the current implementation, this causes the implicit macroscale FEA convergence difficulties, naturally, meaning the solver fails after just a few elements have failed. In order to predict fracture toughness, a different solution method (one that is robust to local stiffness loss) would have to be employed at the macroscale. Either that, or the fracture process could be captured with a failure parameter, but one that does not impact the strength of the system itself, for example, the model proposed by Liu et al. [**71**]. It might be possible to integrate that so-called "three-step" method with the part-scale solver; however, because that method was implemented using explicit dynamics to solve the FE-level problem reworking the currently CPSCA implementation and coupling would be required.

Single-point descriptive statistics regarding the initial microstructural configuration are shown in contour plots at the macroscale and collected in histograms in Figure 5.9. This shows a selection of the parameters that could be extracted - obviously because the full images are used to represent the microstructures, any appropriate measure of voids in images could be extracted. Only some example statistics that could be gathered for any given realization are shown in Figure 5.9. Because the void volume was used to populate the microscales, it seems reasonable that average void size appears somewhat correlated to solidification cooling rate (in Figure 5.8). In this case, the nearest

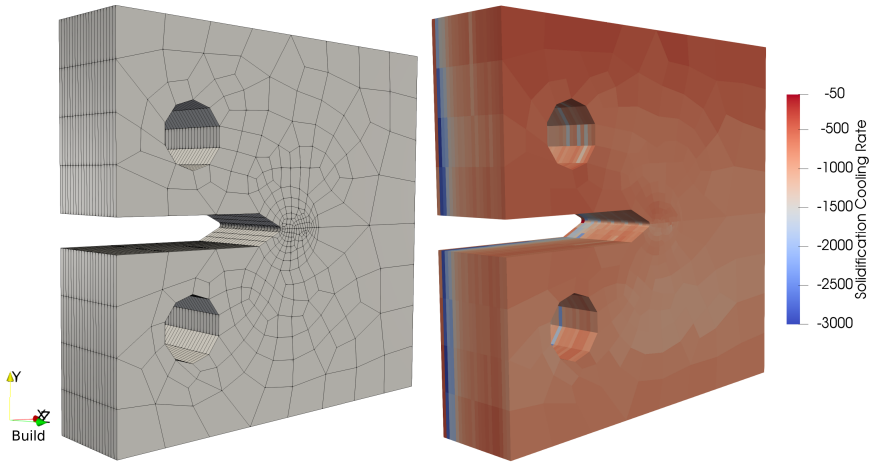

Figure 5.8. Compact tension example: (a) mesh, pin loading from rigid pins excluded from this visualization (b) solidification cooling rate prediction

neighbor statistics were not used to pick microstructure, but in future this would be possible (if some relationship with processing conditions was known). From a design perspective, a parametric study of the impact of any of the factors (e.g. using prescribed microstructural geometry) would be easily possible as well. A total of 54655 voids are represented across 320 different RVEs used to populate the 6220-element mesh (with one material point per element, because reduce integration bricks with hourglass control are used), so the total system contains about 20.9925 billion voxels. Solving this problem directly or with FE^2 would be very computational expensive. Using FE-CPSCA, this takes about 23 hr on 108 CPUs; notice that because the two-way coupling is required this is more expensive than the fatigue example. This is predominately because the time steps have to be much smaller to ensure convergence.

Figure 5.10 shows the results from this fracture initiation simulation. Subset (F) shows the deformed configuration of the compact tension specimen with YY direction stress contours after 0.114 in of total displacement of the pins in the Y-direction. Note that some elements at the crack tip have failed, and as a result no longer hold stress (e.g. near the center of the blunted crack region). The contour plot in Fig. 5.10G shows the number of failed cluster in each sub-scale mesh, tracking the progress of damage; several specific elements are numbered in Figure 5.10C, and the corresponding microstructures are shown in Figure 5.10A-E, colored by the YY component of the

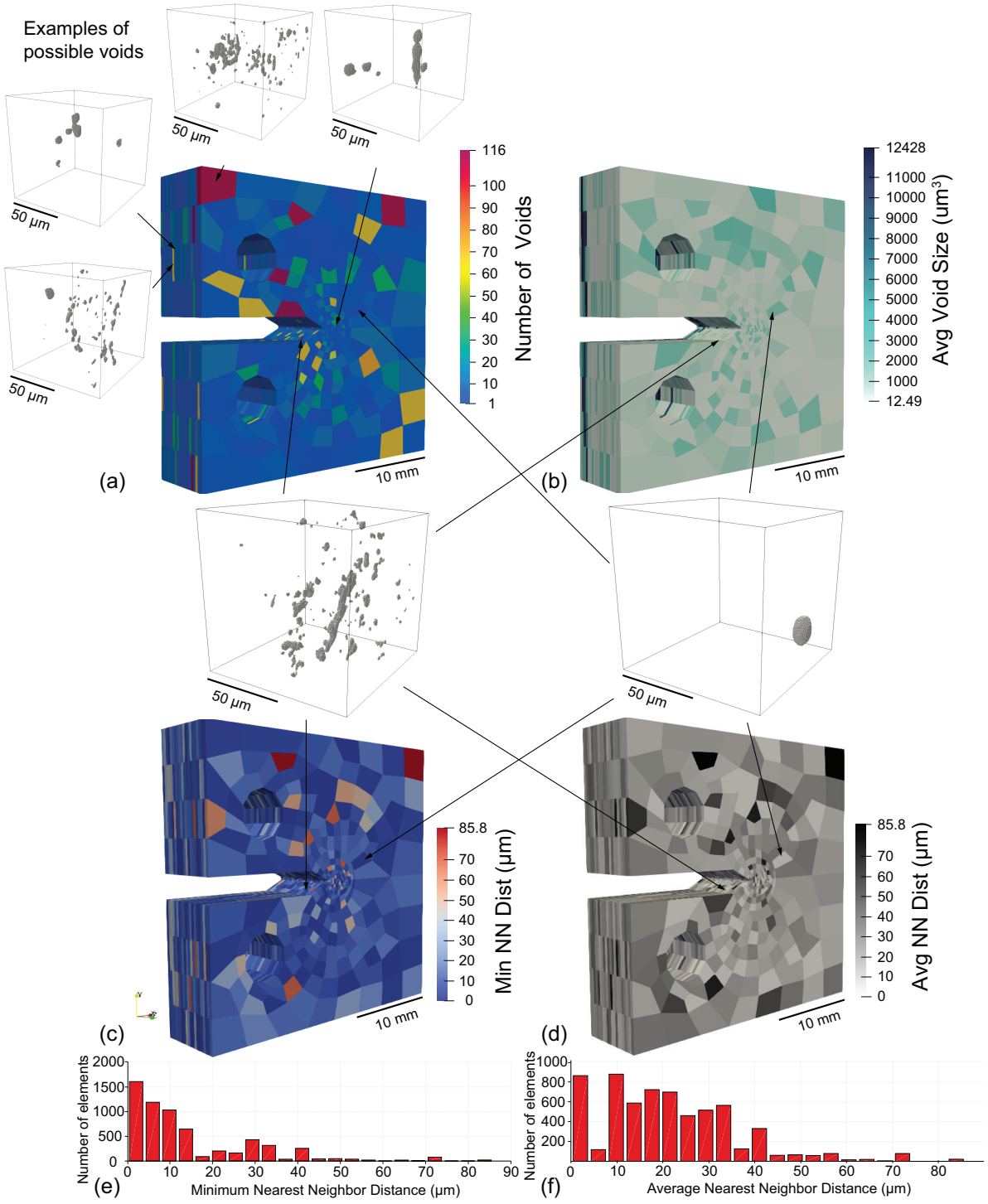

Figure 5.9. Contour plots of (a) number of voids in the microscale for each element, (b) average void size for within the microscale, (c) minimum nearest neighbor distance, (d) average nearest neighbor distance (a value of zero in (c) and (d) indicates only one void is present); (e) histogram of minimum nearest neighbor distance, (f) histogram of average nearest neighbor distance

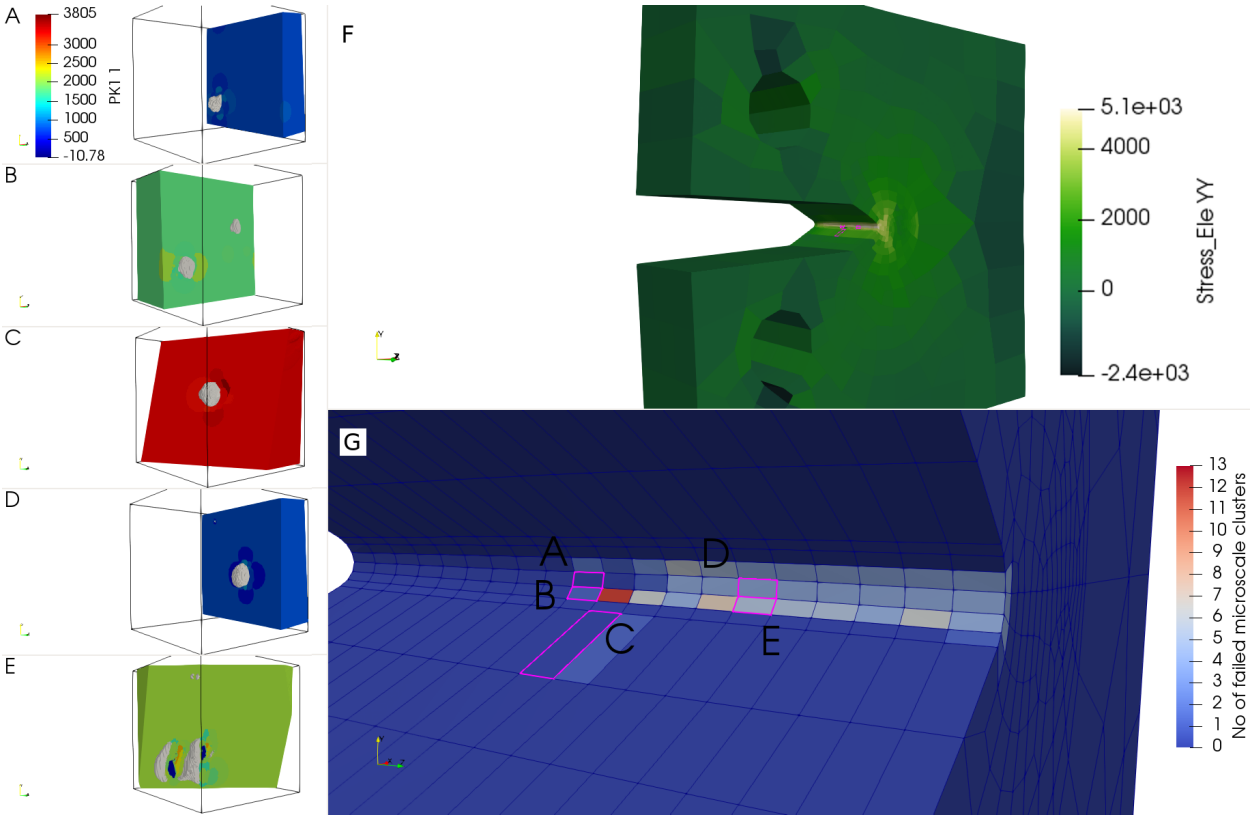

Figure 5.10. (a-e) PK1 YY (or 1 in Voigt notation) stress contours of the microscales at the elements highlighted in (g); note that some voids interact and cause larger failed zones or increase stresses; (f) contours of stress in the YY direction after fracture has begun, note "failed" elements with decreased stresses at crack tip; (g) heat map showing the prevalence of failure, the color shows the number of clusters failed at the microscale, 0 = no failures, 20 = completely failed.

PK1 stress. A, B, D, and E have failed regions and thus hold lower load than C, which has not had any microscale regions fail.

The results are compared to another run of the same system, and different results are obtained on the basis of different microstructural configurations. The comparison is shown in Figure 5.11. This demonstrates that the model is capable of application to heterogeneous systems with varying microstructure. Computing the critical stress concentration factor for mode I fracture, K_{IC}, for each of these specimens, gives about a 6% differences in estimated fracture toughness for these two realization. Using this method, fracture toughness could be taken as a design parameter with the local microstructural configuration and properties at each point as design variables.

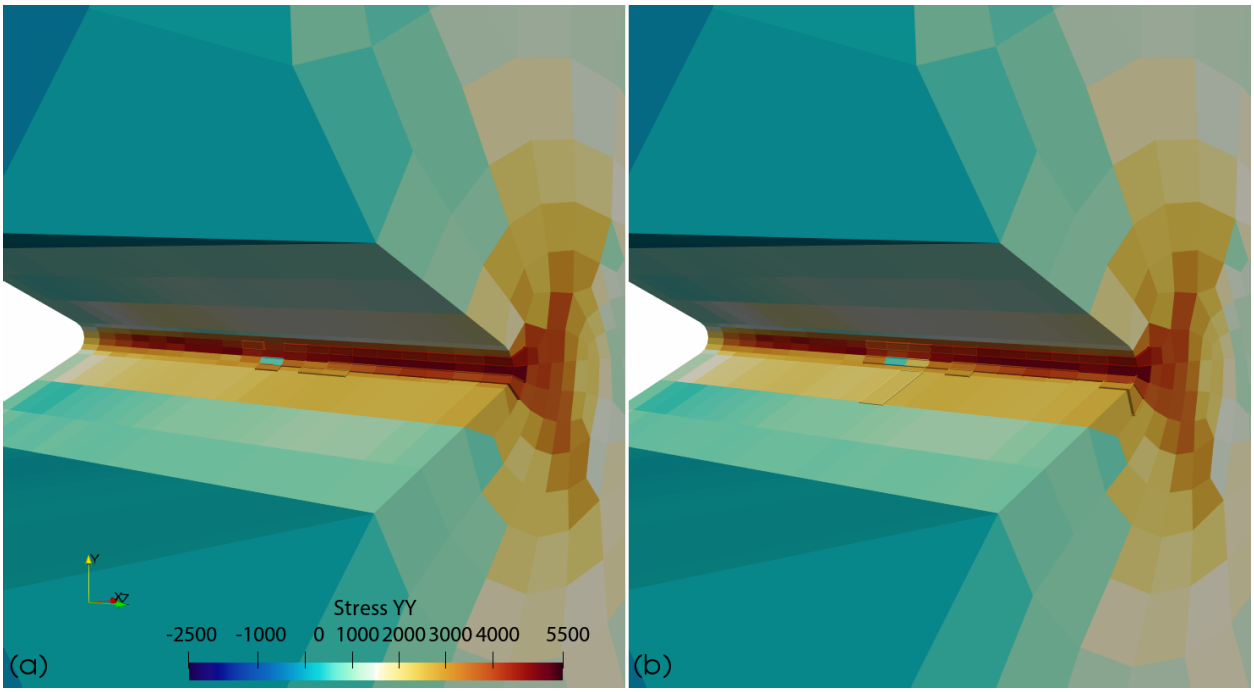

Figure 5.11. Contours of YY stress plotted for (a) Instance 1 of the fracture specimen; (b) Instance 2 of the fracture specimen. As with the fatigue example, (slightly) different local patterns of failure are caused by different microstructures selected based on thermal conditions. Failed elements are outlined heavily. Note that failure is not necessarily in the highest stress elements, because of the triaxiality/Lode angle failure criterion used on the microscale

5.4. Discussion

The most obvious difficulty with this method currently is in the descriptors that connect processing conditions to selection of a microstructure that represents that condition. One of the simplest possible approximations is made here, but further refinement in terms of the thermal model and variables used and in the microstructure descriptors is possible. For example, a measure of distribution of porosity within each microstructure (i.e., if it is one large void or many small ones) might be used in addition to V_f.

The microstructures used here do not explicitly capture surface effects for the microstructural fatigue behavior. For example, a void on the microscale near the surface of the entire part might have an impact on fatigue performance. While the macroscale effects of the boundaries are naturally included, this small scale interaction is a matter of ongoing work. Some authors, e.g. [**135**], suggest

that there is limited change in overall fatigue life, up to the high-cycle limit (runout), for as-built versus machined finish specimens; this may indicate the assumption made here is reasonable, but this is controversial.

In addition, the database used here contained only 320 possible microstructures. Thus, each microstructure was repeated many times throughout a given macroscale. This implies that the likelihood of the critical flaw (or worst-case microstructure) occurring within the most highly stress area of the specimens is quite high. This artificially decreases the observed fluctuations in fatigue life. Some relationship between the number of sub-scale microstructures required in the database and either the range of SCR or the size of the most highly stress volume could be developed to support this framework.

A simplifying assumption for the grain structure (single crystal at the microscale) was also used for this demonstration; however, we could add a step that either predicts the grain structure from thermal history, as was demonstrated in [**141**] and Chapter 4, or derives a grain structure from experiments should more of that data be available. Currently, the kind of 3D grains structures needed to include image-based grains are not available to us. Those shown in Chapter 2 give us some idea, but are to scare to use directly, although one possible direction is to use statistically similar, synthetically generated grain structures based on currently available sparse images of grains in different orientations. Future work could also use simulations, such as the cellular automata approach to predict grains throughout a build (as in [**68, 141**]). Another possibility would be to synthetically generate grain structures from literature data, which provides a statistical basis for the synthetic generation. The results shown in Chapter 4 do indicate that grains generated this way could substantially impact predicted fatigue lives when used in concert with image-based void geometries.

An implicit assumption of the images used here is that the hatch spacing and laser power were appropriate to avoid lack-of-fusion defects between tracks. This is because the images used to make the database came from single-track, thin-wall build, were no between-track porosity would

be possible. This assumption could easily be relaxed by including images of voids thought to come from lack of fusion in multi-track builds in the database.

Although for simplicity we assume that voids always occur and dominate the material response, this is not a necessary assumption of the method – given sufficient characterization data of the processed material, many classes of microstructure might be used with this framework. For example, the grain and voids combinations similar to those demonstrated in Section 4.2.2 could be used to account for the effects of grain boundaries and polycrystalline mechanics in general, as mentioned above.

Because scale separation is assumed between the microscale and macroscale, it is unclear if through-going fracture can be reasonably modeled. Certainly, a fracture process could be captured, but does it make sense? If we understand the microscale (with periodic boundaries) to represent a larger volume of material, directly capturing the fracture at a microscale level makes little sense. On the other hand, a crack tip radius of the same length-scale as the microscale is likely, and active deformation mechanisms will require mechanics of that length scale as well. Thus, modeling the crack at the macroscale, with a fine enough discretization to capture the crack tip, also makes little sense (violates the scale-separation assumption). If empiricism is introduced, this contradiction might be solved. However, to maintain a mechanistic basis would likely require a new conception that avoids the separation of length scales assumption. Perhaps a gradient-based non-local method would be a starting place. Thus, this method is not necessarily directly comparable to implicit or empirical homogenization techniques such as Gurson-type models, viz. [**84, 85, 126**].

Development of a benchmark for fatigue and fracture prediction in AM would support these modeling efforts. Currently, conflicting reports of the influence of AM, versus conventional processing, on the fatigue properties of metals exist. This can in part be attributed to the wide range of materials, but also to a range of build processes and choices made by machine operators. This makes it challenging to develop reliable, cross-cutting models. In order to calibrate the models fully, in addition to the material properties some data regarding fatigue life is required to compute the fitting factors in the FIP. For the failure model, a local measure of failure potency is needed –

in this case, we used failure surface in terms of effective plastic strain at a given stress triaxiality and Lode angle. Experiments that deduce this relationship are necessary. If further developments include fracture progression in addition to initiation, some measure of separation energy or another factor related to the ductile failure may be required as well (currently, a simple assumption for post-failure behavior is used to avoid this).

5.5. Conclusions and summary

This chapter presented a method that exploits computational efficient micromechanics techniques to perform Monte Carlo-style sampling with numerical experiments, using XCT images of real AM microscale voids. The specific microscale solutions are derived from a cluster-based solution of the Lippmann-Schwinger equation, and involve the prediction of fatigue life using crystal plasticity and a fatigue indicating parameter. A database of possible microscale geometries is developed from 3D imaging experiments. These geometries are related to AM processing conditions through the solidification cooling rate, and a process- and microstructure dependent, stochastic prediction of fatigue life and fracture initiation are achieved with reasonable computational expense.

There are two key innovations here. First, the microstructure varies according to a process model. This is unusual in concurrent multiscale modeling approaches. I hope this means that fluctuations in performance can be captured; specifically, this will enable more realistic modeling of the variability that occurs due to localized material processing such as AM than what might be accomplished with metamodels or other ways of capturing variability. Second, experimental 3D images of the microstructures of interest are used directly, drawn from a relatively extensive database. Use of this kind of image database for multiscale modeling does not, too my knowledge, appear elsewhere in the literature. This at once provides the variability needed for the first point and involves higher fidelity material representation, because simplified geometric representation commonly used for multiscale, reduced order, or homogenization type problems are avoided. The method can also be used to design microstructures that result in greater fatigue life or fracture resistance, with direct, physical representation of the underlying mechanics that control the process.

CHAPTER 6

Conclusions and future work

6.1. Summary and conclusion

The overall goal of this thesis is to understand and model heterogeneous, anisotropic metals, and the impact these factors have upon fatigue and failure. The primary motivation for this goal is to be able to relate the material microstructures generated by additive manufacturing to the expected performance of parts made with AM.

The first step in the process was to conduct experiments to understand what was happening within these materials, and what their microstructures are. To this end, an experimental effort was undertaken using both mundane and highly specialized techniques to assess grains structures in both two and three dimensions, surface characteristics, porosity in three dimensions, the spatial variability of porosity through simple builds, the variation of mechanical performance in uniaxial tension as a function of several factors including build parameters, spatial location within a build, and observed porosity in each tension specimen. Further, the progression of deformation within a batch of about 75 tension test specimens spanning nearly all these different variables was tracked using a combination of DIC and in-situ x-ray measurements to form a more complete understanding of the role of voids generated by the AM process on deformation and failure in tension. The conclusions here were mixed, indicating that voids can, but do not always have a large impact on the deformation behavior. Factors not measured, most likely grains, also had an important impact in some cases. Another important outcome of this work was the measurement and characterization of a large number of voids (about 550,000 in total) that were observed across over 150 different specimens with XCT. These images are all collected and organized to make a database of images of porosity, predominately featuring IN718 LENS-built thin walls, but also including PH48S, SS316L, and IN718 from more conventional build patterns.

Next, a microstructure sensitive model was constructed, using CPFE, to capture some of the features that were observed in the experiments. This CPFE model included a step to assess fatigue performance, a longstanding and still open issue with AM metals. The fatigue performance measure was fitted to experimental data for high cycle fatigue for IN718 collected from literature and adjusted to match just a few known data points for high cycle fatigue of AM-built specimens. This model was used to compare the effects of grain orientation, size, and shape on local fatigue potency. Size and shape do both have an effect, and in this model an unusually large grand tended to increase life marginally but also increase variability (although this may not be significantly, because it might represent the model not the material). However, when a void characteristic of the void size observed in IN718 (the material made by Honeywell) was introduced, a substantial decrease in fatigue life was noted.

This idea of microstructure-based modeling for fatigue was then transferred into a recently-developed data-driven reduced order modeling technique. The enhanced speed at little cost to accuracy provided by this method encouraged us to integrate the structure-properties predictions directly with process-structure modeling under concurrent development by my colleagues. This allowed us to demonstrate, for the first time, a model that takes as input the processing conditions and material properties, and outputs a performance measure such as estimated cycles to failure. As implemented, however, the model was difficult to scale to part-size geometries and is completely deterministic.

The culminating work presented here is a model that captures part-scale variability using an image-based, data-driven approach to multiscale modeling. This enables the model to capture the relevant features identified earlier (CP and voids) while predicting performance across an entire part at relatively modest computational expense. These unique capabilities were demonstrated both for fatigue initiation and crack initiation, relying on slightly different solution techniques (one-way to two-way coupling) depending on the application. This model directly includes the voids and their variability observed in XCT images in mechanical performance predictions at a scale relevant to part and build-strategy design.

In summary, the dissertation has described a progression of work that started with experimental characterization of the material of interest. Once we had some idea of the microstructures and deformation mechanisms that could be expected with this heterogeneous material, a model that captures the microstructurally-driven deformation was developed. We found, however, that these simulations were too computationally expensive to be used to make larger-scale predictions that would be useful to practicing designers or engineers. To this end, a reduced order model was developed and integrated with a processing prediction framework to provide a process-structure-properties-performance prediction tool. The ideas of this tool were then extended to a modeling strategy that accounts for part-scale variability using a new conception of concurrent multiscale modeling that embeds different images of microstructures at different points throughout the macroscale to capture material heterogeneity.

6.2. Ongoing projects and future work

The methods demonstrated here have exciting potential, and many possibilities to continue exploring those potential exist. Some of these have been discussed in their respective chapter, however some that have not been mentioned are the following:

6.2.1. High cycle fatigue testing

In order to understand the origins of fatigue failure in AM materials and provide a more consistent calibration and validation data set to the fatigue prediction methods shown in Chapter 3, a test machine was designed and built. Specifically, the goal is to test high cycle fatigue, which has limited study in AM currently. Under strict requirements to enable in-situ operation, the device was designed following the pattern of the in-situ tensile testing machine used in Chapter 2. To enable high cycle fatigue testing a piezo-electic actuator was selected. The design was constrained by the usual factors (e.g. stiffness, natural frequencies), but additional constraints were applied to make a suitable in-situ test device. The mass was constrained to strictly under 60 kg with a desired mass under 25 kg. The size was limited to 300 mm between the gage section and mounting table,

and the width/length constrained to allow rotation of the stage to also about 300 mm although this was not a particular concern. One further in-situ related constraint relates to the portion of swept arc that can be blocked while still being able to reconstruct 3D images. Using the method developed by Dr. Xiao, this is about 20 degrees to 25 degrees. Using a design with vertical cylindrical support columns, the ratio of column thickness to distance between the column and center point (illustrated in Fig. 6.1(a) was constrained using the chart in Fig. 6.1(b). Operating parameters of the piezo actuator selected are shown in Fig. 6.2, which can be compared against the sample force versus frequency and cycles to failure at a given force (or stress, for the specimen geometry given below) to develop a voltage profile to use for testing.

The test geometry selected at least for the initial testing is the constant radius fatigue coupon miniaturized from ASTM standard E606, shown in Fig. 6.4. The drawing is in inches, but the cross section of the gage corresponds to about 2 mm diameter – the approximate penetration depth of the x-ray beam at 2BM.

The machine was designed and initially built by Fengchun Li, under my supervision. The certain components and subsystems (collet adapter, cooling air, LabVIEW VI for control most notably adding the ability to save results) were then rebuilt by undergraduate Jose Amador, working with me in the summer of 2019, to conform more closely to my requirements. While all the equipment has now been set up, and a simple demonstration test conducted, the system has not yet been fully validated. One of the concerns is about the alignment fidelity. The current alignment method is quite rudimentary, involving simply clamping a straight rod in the collet grips when tightening the bolts that hold the load cell in place. More complete instrumentation, namely, a method to measure gage section strains, or even crosshead displacements, reliably is also still required. Optical measurement might be possible, although the small deformation levels (about 2 µm to 5 µm) makes this challenging.

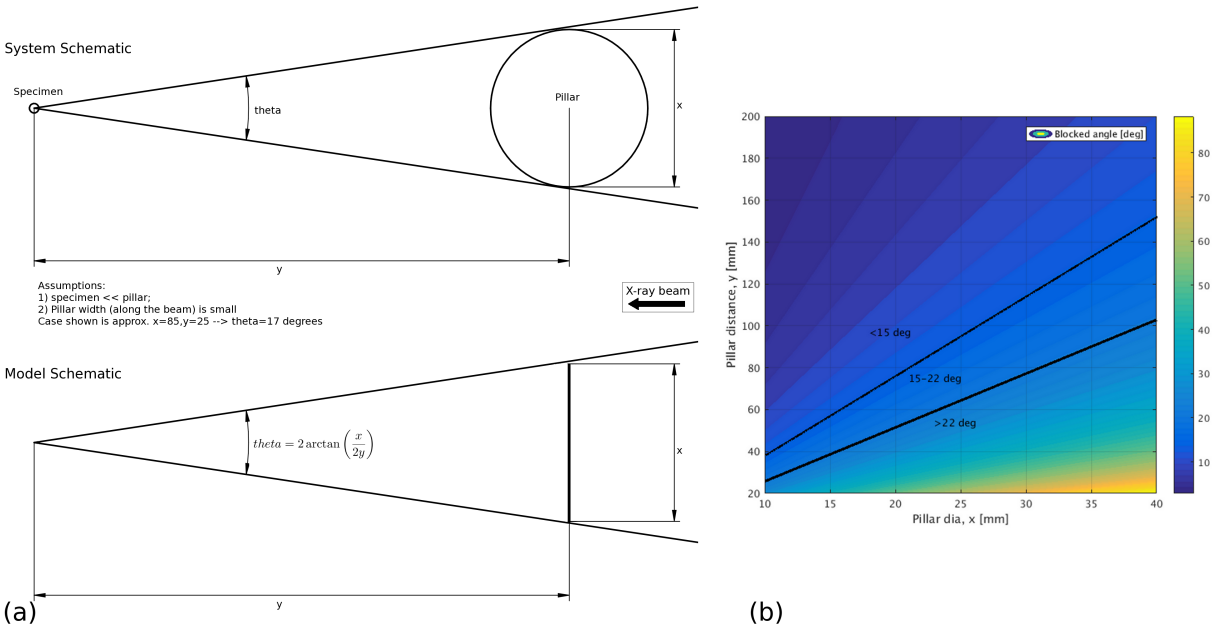

Figure 6.1. Design constraint: in-situ blocking angle

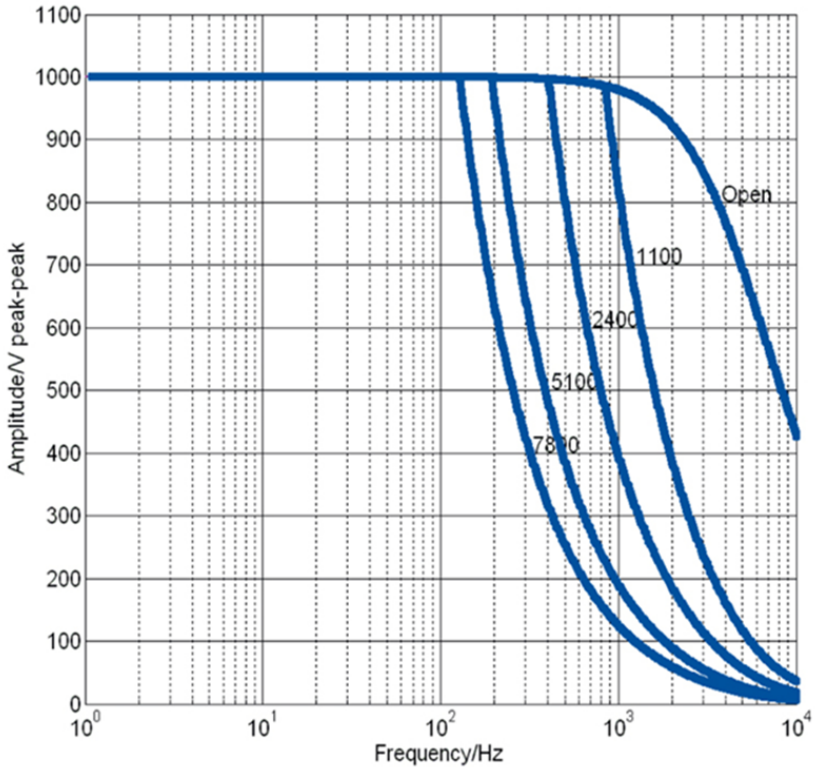

Figure 6.2. Contours of applied force on the voltage versus frequency plot show the physical limitation of the actuator itself

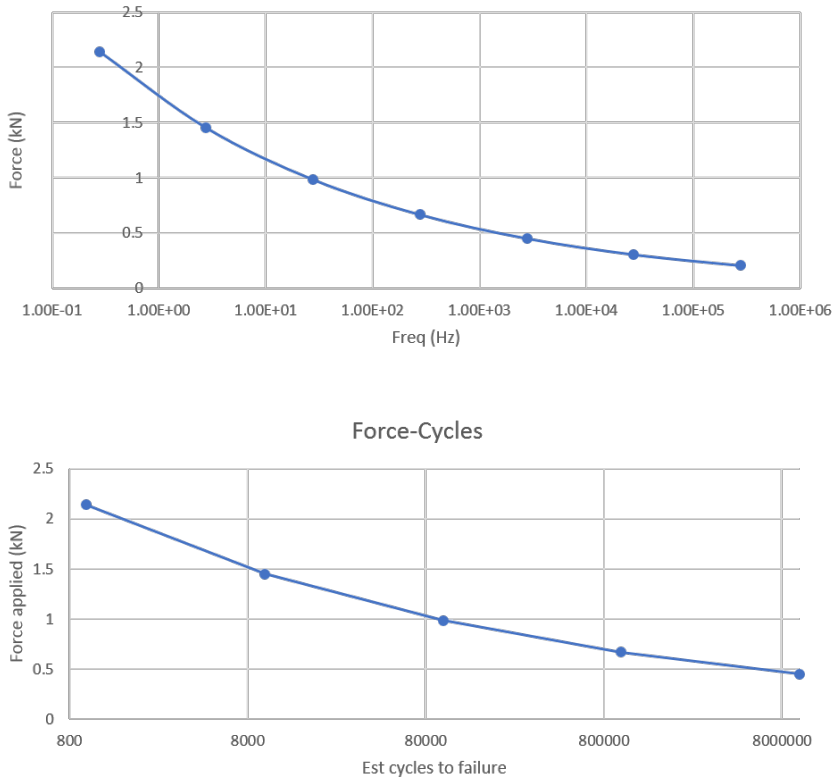

Figure 6.3. Design constraint: cyclic frequency versus force apply for the piezo-actuator

6.2.2. Deformation tracking with in-situ XCT

More robust methods for reconstructing deformation fields in the in-situ XCT measurements could be developed. Currently, the only lacking feature is a consistent reference point or location to index each subsequent image against. If that could be identified, a particle tracking approach would likely be able to capture the deformation in the system, e.g. with [**98**].

6.2.3. Image-based modeling

One future possibility is to increase the scope of the modeling to include full XCT images rather than subsets. This would require enhancements in efficiency (in particular, RAM requirements). But it would increase accuracy (or at least verisimilitude) of the model. It would probably also require including grain structures. A system for generating a pairing these structures with the

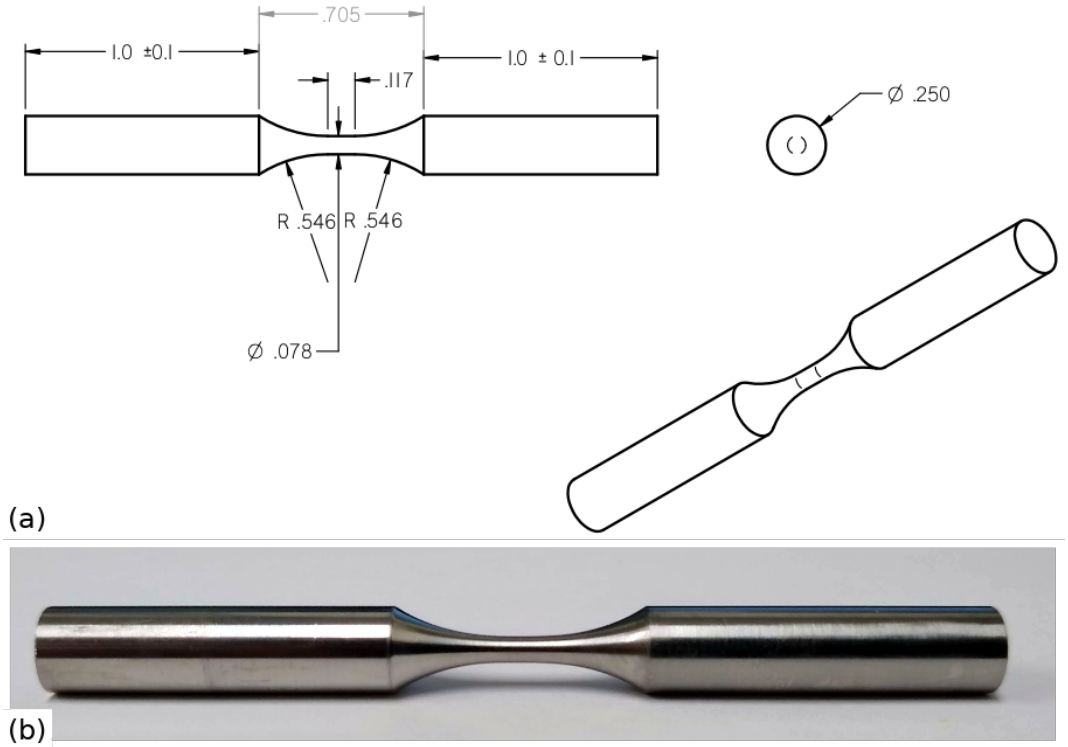

Figure 6.4. (a) Draft drawing of the fatigue test coupon to be used; dimensions are in inches, tolerances are generally ± 0.0002 inches unless otherwise marked. Roughly a miniaturized ASTM E606 standard test geometry. (b) A machined test coupon

images would be required. Either through more experiments (e.g. more diffraction work) or by some sort of synthetic generation (e.g. as shown in Chapters 3 and 4).

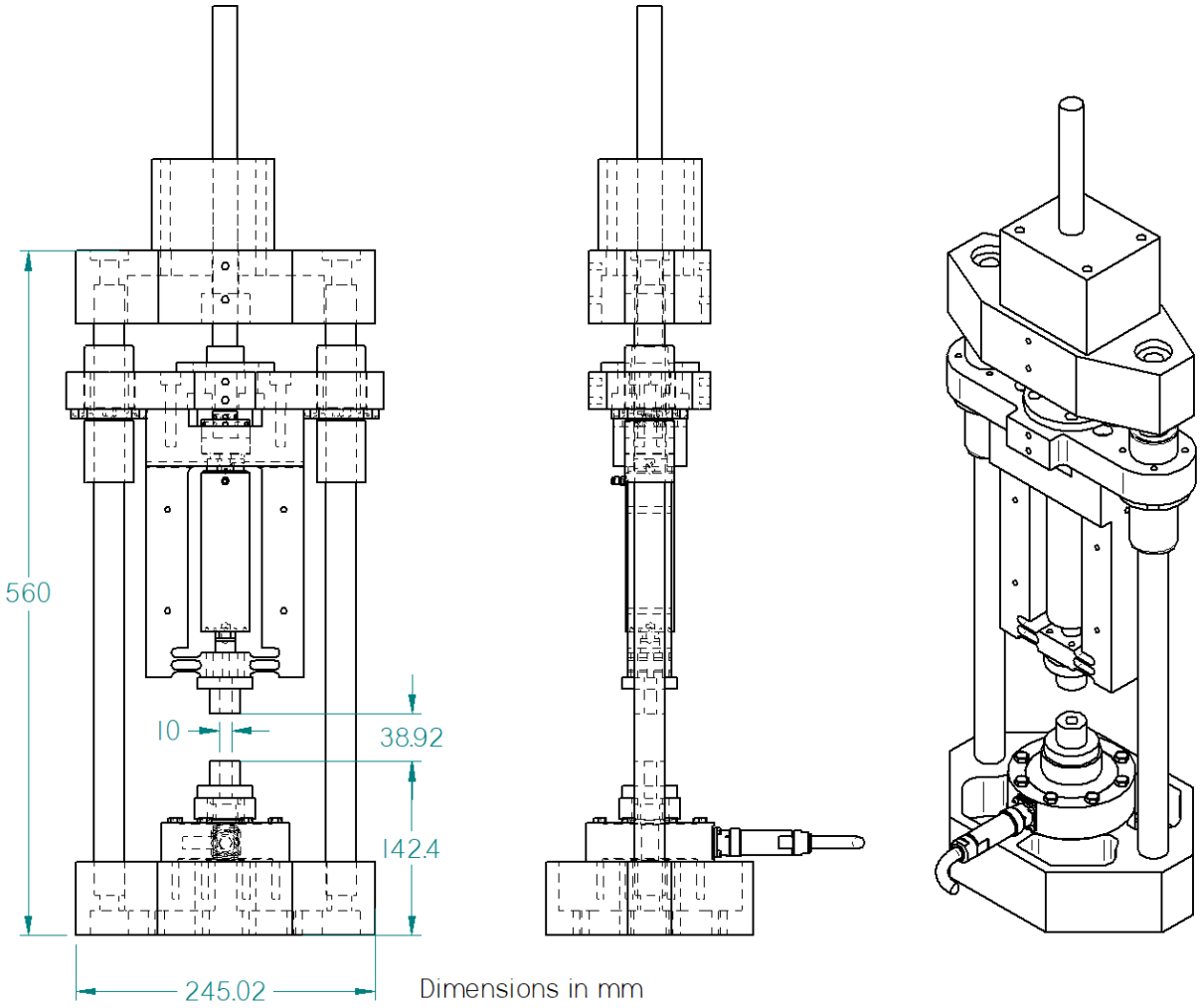

Figure 6.5. Drawings of the fatigue test machine as built; digital 3D embodiment by Fengchun Li

References

[1] S S Al-Bermani, M L Blackmore, W Zhang, and I Todd. The origin of microstructural diversity, texture, and mechanical properties in electron beam melted {Ti-6Al-4V}. *Metallurgical and Materials Transactions A*, 41(13):3422–3434, 2010.

[2] A. Amanov, Y-S Y.-S. Pyun, J-H J.-H. J-H Kim, C-M C.-M. C-M Suh, I-S I.-S. Cho, H.-D. H-D Kim, Q. Wang, and M. K. Khan. Ultrasonic fatigue performance of high temperature structural material Inconel 718 alloys at high temperature after UNSM treatment. *Fatigue & Fracture of Engineering Materials & Structures*, 38(11):1266–1273, 2015.

[3] E Amsterdam and Ga Kool. ICAF 2009, Bridging the Gap between Theory and Operational Practice. In *25th ICAF (International Committee on Aeronautical Fatigue) Symposium*, number May, pages 1261–1274, 2009.

[4] A. A. Antonysamy, J. Meyer, and P. B. Prangnell. Effect of build geometry on the Beta-grain structure and texture in additive manufacture of Ti6Al4V by selective electron beam melting. *Materials Characterization*, 84:153–168, 2013.

[5] ASTM. Standard Test Method for Strain-Controlled Fatigue Testing. *E606/E606M-12*, 96(2004):1–16, 2012.

[6] J Belan. High frequency fatigue test of IN 718 alloy–microstructure and fractography evaluation. *Metalurgija*, 54(1):59–62, 2015.

[7] Ted Belytschko, Wing Kam Liu, Brian Moran, and Khalil Elkhodary. *Nonlinear finite elements for continua and structures*. John wiley & sons, 2013.

[8] Jennifer L Bennett, O. L. Kafka, Haiguang Liao, Sarah J Wolff, Cheng Yu, Puikei Cheng, Gregory Hyatt, Kornel Ehmann, and Jian Cao. Cooling rate effect on tensile strength of laser deposited Inconel 718. In *Procedia Manufacturing*, volume 26, pages 912–919, 2018.

[9] S. Beretta and S. Romano. A comparison of fatigue strength sensitivity to defects for materials manufactured by AM or traditional processes. *International Journal of Fatigue*, 94:178–191, jan 2017.

[10] Erhard Brandl, Ulrike Heckenberger, Vitus Holzinger, and Damien Buchbinder. Additive manufactured AlSi10Mg samples using Selective Laser Melting (SLM): Microstructure, high cycle fatigue, and fracture behavior. *Materials & Design*, 34:159–169, 2012.

[11] G E Brinkman, C.R. and Korth. Strain Fatigue and Tensile Behavior of Inconel 718 from Room Temperature to 650C. *Journal of Testing and Evaluation*, 2(4):249–259, 1974.

[12] M. Bruchhausen, B. Fischer, A. Ruiz, S. González, P. Hähner, and S. Soller. Impact of hydrogen on the high cycle fatigue behaviour of Inconel 718 in asymmetric push-pull mode at room temperature. *International Journal of Fatigue*, 70:137–145, 2015.

[13] A. Cervellon, J. Cormier, F. Mauget, and Z. Hervier. VHCF life evolution after microstructure degradation of a Ni-based single crystal superalloy. *International Journal of Fatigue*, 104:251–262, 2017.

[14] Q. Chen, N. Kawagoishi, and H. Nisitani. Evaluation of fatigue crack growth rate and life prediction of Inconel 718 at room and elevated temperatures. *Materials Science and Engineering A*, 277(1-2):250–257, 2000.

[15] Qiang Chen, N. Kawagoishi, Q. Y. Wang, N. Yan, T. Ono, and G. Hashiguchi. Small crack behavior and fracture of nickel-based superalloy under ultrasonic fatigue. *International Journal of Fatigue*, 27(10-12):1227–1232, 2005.

[16] Jong Woo Choi and Namkug Kim. Clinical application of three-dimensional printing technology in craniofacial plastic surgery. *Archives of plastic surgery*, 42(3):267–277, 2015.

[17] P C Collins, C V Haden, I Ghamarian, B J Hayes, T Ales, G Penso, V Dixit, and G Harlow. Progress Toward an Integration of Process–Structure–Property–Performance Models for "Three-Dimensional (3-D) Printing" of Titanium Alloys. *JOM*, 66(7):1299–1309, jul 2014.

[18] Marie Cronskär, Mikael Bäckström, Lars-Erik Rännar, M Cronskar, M Backstrom, and L.-E. Rannar. Production of customized hip stem prostheses–a comparison between conventional machining and electron beam melting (EBM). *Rapid Prototyping Journal*, 19(5):365–372, 2013.

[19] A. Cruzado, J. LLorca, and J. Segurado. Modeling cyclic deformation of inconel 718 superalloy by means of crystal plasticity and computational homogenization. *International Journal of Solids and Structures*, 122-123:148–161, 2017.

[20] L. Denti, E. Bassoli, A. Gatto, E. Santecchia, and P. Mengucci. Fatigue life and microstructure of additive manufactured Ti6Al4V after different finishing processes. *Materials Science and Engineering A*, 755(March):1–9, may 2019.

[21] Matthew Di Prima, James Coburn, David Hwang, Jennifer Kelly, Akm Khairuzzaman, and Laura Ricles. Additively manufactured medical products – the FDA perspective. *3D Printing in Medicine*, 2(1):1, dec 2016.

[22] Ali Fatemi and Darrell F Socie. A Critical Plane Approach to Multiaxial Fatigue Damage Including out-of-Phase Loading. *Fatigue & Fracture of Engineering Materials & Structures*, 11(3):149–165, 1988.

[23] N. A. Fleck and J. W. Hutchinson. A phenomenological theory for strain gradient effects in plasticity. *Journal of the Mechanics and Physics of Solids*, 41(12):1825–1857, 1993.

[24] M M Francois, A Sun, W E King, N J Henson, D Tourret, C A Bronkhorst, N N Carlson, C K Newman, T Haut, J Bakosi, J W Gibbs, V Livescu, S A Vander Wiel, A J Clarke, M W Schraad, T Blacker, H Lim, T Rodgers, S Owen, F Abdeljawad, J Madison, A T Anderson,

J-L. Fattebert, R M Ferencz, N E Hodge, S A Khairallah, and O Walton. Modeling of additive manufacturing processes for metals: Challenges and opportunities. *Current Opinion in Solid State and Materials Science*, 21(4):198–206, 2017.

[25] R.P. P Gamble and J.K. K Tien. The Room Temperature Fatigue Behavior of Nickel-Base Superalloy Crystals at Ultrasonic. *Metallurgical Transactions*, 2(7):1933–1938, 1971.

[26] Ch A. Gandin and M Rappaz. A 3D cellular automaton algorithm for the prediction of dendritic grain growth. *Acta Materialia*, 45(5):2187–2195, may 1997.

[27] P. Ganesh, Rakesh Kaul, G. Sasikala, Harish Kumar, S. Venugopal, Pragya Tiwari, Sanjay Rai, R. C. Prasad, and L. M. Kukreja. Fatigue Crack Propagation and Fracture Toughness of Laser Rapid Manufactured Structures of AISI 316L Stainless Steel. *Metallography, Microstructure, and Analysis*, 3(1):36–45, 2014.

[28] Saeede Ghorbanpour, Milovan Zecevic, Anil Kumar, Mohammad Jahedi, Jonathan Bicknell, Luke Jorgensen, Irene J. Beyerlein, and Marko Knezevic. A crystal plasticity model incorporating the effects of precipitates in superalloys: Application to tensile, compressive, and cyclic deformation of Inconel 718. *International Journal of Plasticity*, 99:162–185, 2017.

[29] S Ghosh and J Choi. Three-dimensional transient finite element analysis for residual stresses in the laser aided direct metal/material deposition process. *Journal of Laser Applications*, 17(3):144–158, 2005.

[30] S Ghosh and J Choi. Modeling and experimental verification of transient/residual stresses and microstructure formation in multi-layer laser aided DMD process. *Journal of heat transfer*, 128(7):662–679, 2006.

[31] Haijun Gong, Khalid Rafi, Hengfeng Gu, G. D. Janaki Ram, Thomas Starr, and Brent Stucker. Influence of defects on mechanical properties of Ti-6Al-4V components produced by selective laser melting and electron beam melting. *Materials and Design*, 86:545–554, 2015.

[32] Haijun Gong, Khalid Rafi, Hengfeng Gu, Thomas Starr, and Brent Stucker. Analysis of defect generation in Ti-6Al-4V parts made using powder bed fusion additive manufacturing processes. *Additive Manufacturing*, 1:87–98, 2014.

[33] Haijun Gong, Khalid Rafi, Thomas Starr, and Brent Stucker. Effect of defects on fatigue tests of as-built Ti-6Al-4V parts fabricated by selective laser melting. In *Solid freeform fabrication symposium*, pages 499–506. University of Texas Austin, Texas, 2012.

[34] Michael Gorelik. Additive manufacturing in the context of structural integrity. *International Journal of Fatigue*, 94:168–177, jan 2017.

[35] Michael A Groeber and Michael A Jackson. DREAM.3D: A Digital Representation Environment for the Analysis of Microstructure in 3D. *Integrating Materials and Manufacturing Innovation*, 3(1):5, 2014.

[36] Yongjun Guan, Bo Chen, Jinwen Zou, T. Ben Britton, Jun Jiang, and Fionn P.E. E Dunne. Crystal plasticity modelling and HR-DIC measurement of slip activation and strain localization in single and oligo-crystal Ni alloys under fatigue. *International Journal of Plasticity*, 88:70–88, 2017.

[37] Doga Doğa Gürsoy, Francesco De Carlo, Xianghui Xiao, and Chris Jacobsen. TomoPy: a framework for the analysis of synchrotron tomographic data. *Journal of synchrotron radiation*, 21(5):1188–1193, sep 2014.

[38] Håkan Hallberg, Sigmund Kyrre Ås, and Bjørn Skallerud. Crystal plasticity modeling of microstructure influence on fatigue crack initiation in extruded Al6082-T6 with surface irregularities. *International Journal of Fatigue*, 111:16–32, jun 2018.

[39] K F Hamed, M Ketabchi, and S Zangeneh. Determination of Johnson–Cook Plasticity Model Parameters for Inconel718. *Journal of Materials Engineering and Performance*, 2017.

[40] R Hedayati, H Hosseini-Toudeshky, M Sadighi, M Mohammadi-Aghdam, and A A Zadpoor. Computational prediction of the fatigue behavior of additively manufactured porous metallic biomaterials. *International Journal of Fatigue*, 84:67–79, 2016.

[41] J C Heigel, P Michaleris, and E W Reutzel. Thermo-mechanical model development and validation of directed energy deposition additive manufacturing of Ti–6Al–4V. *Additive manufacturing*, 5:9–19, 2015.

[42] Carl Herroitt, Xuxiao Li, Nadia Kouraytem, Vahid Tari, Wenda Tan, Benjamin Anglin, Anthony D. Rollett, and Ashley D Spear. A multi-scale, multi-physics modeling framework to predict spatial variation of properties in additive-manufactured metals. *Modelling and Simulation in Materials Science and Engineering*, 27(2):025009, 2019.

[43] Luca Hirt, Alain Reiser, Ralph Spolenak, and Tomaso Zambelli. Additive Manufacturing of Metal Structures at the Micrometer Scale, may 2017.

[44] N E Hodge, R M Ferencz, and J M Solberg. Implementation of a thermomechanical model for the simulation of selective laser melting. *Computational Mechanics*, 54(1):33–51, 2014.

[45] M F Horstemeyer. Multiscale Modeling: A Review. In J Leszczynski and M K Shukla, editors, *Practical Aspects of Computational Chemistry: Methods, Concepts and Applications*, pages 87–135. Springer Netherlands, 2010.

[46] Gene E. Ice and Judy W.L. L Pang. Tutorial on x-ray microLaue diffraction. *Materials Characterization*, 60(11):1191–1201, 2009.

[47] Mahdi Jamshidinia, Fanrong Kong, and Radovan Kovacevic. Numerical Modeling of Heat Distribution in the Electron Beam Melting®of Ti-6Al-4V. *Journal of Manufacturing Science and Engineering*, 135(6):61010, 2013.

[48] M. Janeček, F. Nový, P. Harcuba, J. Stráský, L. Trško, M. Mhaede, and L. Wagner. The very high cycle fatigue behaviour of Ti-6Al-4V alloy. *Acta Physica Polonica A*, 128(4):497–502, 2015.

[49] André Luiz Jardini, Maria Aparecida Larosa, Cec\'\ilia Amélia de Carvalho Zavaglia, Luis Fernando Bernardes, Carlos Salles Lambert, Paulo Kharmandayan, Davi Calderoni, and Rubens Maciel Filho. Customised titanium implant fabricated in additive manufacturing for craniomaxillofacial surgery: This paper discusses the design and fabrication of a metallic implant for the reconstruction of a large cranial defect. *Virtual and Physical Prototyping*, 9(2):115–125, 2014.

[50] André Luiz Jardini, Maria Aparecida Larosa, Rubens Maciel Filho, Cec\'\ilia Amélia de Carvalho Zavaglia, Luis Fernando Bernardes, Carlos Salles Lambert, Davi Reis Calderoni, and Paulo Kharmandayan. Cranial reconstruction: 3D biomodel and custom-built implant created using additive manufacturing. *Journal of Cranio-Maxillofacial Surgery*, 42(8):1877–1884, 2014.

[51] Jun Jiang, Fionn P.E. E Dunne, and T. Ben Britton. Toward Predictive Understanding of Fatigue Crack Nucleation in Ni-Based Superalloys. *Jom*, 69(5):863–871, 2017.

[52] Alex S. Johnson, Shuai Shao, Nima Shamsaei, Scott M. Thompson, and Linkan Bian. Microstructure, Fatigue Behavior, and Failure Mechanisms of Direct Laser-Deposited Inconel 718. *Jom*, 69(3):597–603, 2017.

[53] Matthias Kabel, Thomas Böhlke, and Matti Schneider. Efficient fixed point and Newton–Krylov solvers for FFT-based homogenization of elasticity at large deformations. *Computational Mechanics*, 54(6):1497–1514, dec 2014.

[54] Orion L. Kafka, Cheng Yu, Modesar Shakoor, Zeliang Liu, Gregory J. Wagner, and Wing Kam Liu. Data-Driven Mechanistic Modeling of Influence of Microstructure on High-Cycle Fatigue Life of Nickel Titanium. *JOM*, 70(7):1154–1158, apr 2018.

[55] Galina Kasperovich and Joachim Hausmann. Improvement of fatigue resistance and ductility of TiAl6V4 processed by selective laser melting. *Journal of Materials Processing Technology*, 220:202–214, jun 2015.

[56] Micheal Kattoura, Seetha Ramaiah Mannava, Dong Qian, and Vijay K. Vasudevan. Effect of laser shock peening on residual stress, microstructure and fatigue behavior of ATI 718Plus alloy. *International Journal of Fatigue*, 102:121–134, 2017.

[57] Ingomar Kelbassa, Terry Wohlers, and Tim Caffrey. Quo vadis, laser additive manufacturing? *Journal of Laser Applications*, 24(5):50101, 2012.

[58] Saad A Khairallah, Andrew T Anderson, Alexander Rubenchik, and Wayne E King. Laser powder-bed fusion additive manufacturing: Physics of complex melt flow and formation mechanisms of pores, spatter, and denudation zones. *Acta Materialia*, 108:36–45, 2016.

[59] Saad A Khairallah and Andy Anderson. Mesoscopic simulation model of selective laser melting of stainless steel powder. *Journal of Materials Processing Technology*, 214(11):2627–2636, 2014.

[60] M M Kirka, D A Greeley, C Hawkins, and R R Dehoff. Effect of anisotropy and texture on the low cycle fatigue behavior of Inconel 718 processed via electron beam melting. *International Journal of Fatigue*, 105:235–243, 2017.

[61] Anton Kolyshkin, Martina Zimmermann, Edgar Kaufmann, and Hans Jürgen Christ. Experimental investigation and analytical description of the damage evolution in a Ni-based superalloy beyond 106loading cycles. *International Journal of Fatigue*, 93:272–280, 2016.

[62] Carolin Körner, Andreas Bauereiß, and Elham Attar. Fundamental consolidation mechanisms during selective beam melting of powders. *Modelling and Simulation in Materials Science and Engineering*, 21(8):85011, 2013.

[63] Eric A. Lass, Mark R. Stoudt, Maureen E. Williams, Michael B. Katz, Lyle E. Levine, Thien Q. Phan, Thomas H. Gnaeupel-Herold, and Daniel S. Ng. Formation of the Ni 3 Nb δ-Phase in Stress-Relieved Inconel 625 Produced via Laser Powder-Bed Fusion Additive Manufacturing. *Metallurgical and Materials Transactions A: Physical Metallurgy and Materials Science*, 48(11):5547–5558, nov 2017.

[64] William Scott LePage, Samantha Hayes Daly, and John Andrew Shaw. Cross Polarization for Improved Digital Image Correlation. *Experimental Mechanics*, 56(6):969–985, jul 2016.

[65] Stefan Leuders, Malte Vollmer, Florian Brenne, Thomas Tröster, and Thomas Niendorf. Fatigue strength prediction for titanium alloy TiAl6V4 manufactured by selective laser melting. *Metallurgical and Materials Transactions A*, 46(9):3816–3823, 2015.

[66] Peipei Li, Derek H Warner, Ali Fatemi, and Nam D. Phan. On the Fatigue Performance of Additively Manufactured Ti-6Al-4V to Enable Rapid Qualification for Aerospace Applications. In *57th AIAA/ASCE/AHS/ASC Structures, Structural Dynamics, and Materials Conference*, number April, pages 1–19, 2016.

[67] Yanping Lian, Zhengtao Gan, Cheng Yu, Dmitriy Kats, Wing Kam, and Gregory J Wagner. A cellular automaton finite volume method for microstructure evolution during additive manufacturing. *Materials & Design*, 169:107672, 2019.

[68] Yanping Lian, Stephen Lin, Wentao Yan, Wing Kam Liu, and Gregory J Wagner. A parallelized three-dimensional cellular automaton model for grain growth during additive manufacturing. *Computational Mechanics*, pages 1–16, 2018.

[69] P. Lipinski, A. Barbas, and A.-S. S. A-S Bonnet. Fatigue Behavior of Thin-walled Grade 2 Titanium Samples Processed by Selective Laser Melting. Applications of Life Prediction of Porous Titanium Implants. *Journal of the Mechanical Behavior of Biomedical Materials*, 28:274–290, 2013.

[70] Zeliang Liu, M. A. Bessa, and Wing Kam Liu. Self-consistent clustering analysis: An efficient multi-scale scheme for inelastic heterogeneous materials. *Computer Methods in Applied Mechanics and Engineering*, 306:319–341, 2016.

[71] Zeliang Liu, Mark Fleming, and Wing Kam Liu. Microstructural material database for self-consistent clustering analysis of elastoplastic strain softening materials. *Computer Methods in Applied Mechanics and Engineering*, 330:547–577, 2018.

[72] Zeliang Liu, O. L. Kafka, Cheng Yu, and Wing Kam Liu. *Data-Driven Self-consistent Clustering Analysis of Heterogeneous Materials with Crystal Plasticity*, volume 46. Springer International Publishing, 2018.

[73] Xian-feng Ma, Zheng Duan, Hui-ji Shi, Ryosuke Murai, and Eiichi Yanagisawa. Fatigue and fracture behavior of nickel-based superalloy Inconel 718 up to the very high cycle regime. *Journal of Zhejiang University-SCIENCE A*, 11(10):727–737, 2010.

[74] James MacQueen and Others. Some methods for classification and analysis of multivariate observations. In *Proceedings of the fifth Berkeley symposium on mathematical statistics and probability*, number 14, pages 281–297. Oakland, CA, USA., 1967.

[75] J P MacSleyne, J P Simmons, and M De Graef. On the use of moment invariants for the automated analysis of 3D particle shapes. *Modelling and Simulation in Materials Science and Engineering*, 16(4):045008, jun 2008.

[76] H. Maderbacher, B. Oberwinkler, H. P. Gänser, W. Tan, M. Rollett, and M. Stoschka. The influence of microstructure and operating temperature on the fatigue endurance of hot forged Inconel®718 components. *Materials Science and Engineering A*, 585:123–131, 2013.

[77] Eric Maire, Vincent Carmona, Joel Courbon, and Wolfgang Ludwig. Fast X-ray tomography and acoustic emission study of damage in metals during continuous tensile tests. *Acta Materialia*, 55(20):6806–6815, 2007.

[78] W. Maktouf, K. Ammar, I. Ben Naceur, and K. Saï. Multiaxial high-cycle fatigue criteria and life prediction: Application to gas turbine blade. *International Journal of Fatigue*, 92:25–35, 2016.

[79] Alexander G. Mamistvalov. N-dimensional moment invariants and conceptual mathematical theory of recognition n-dimensional solids. *IEEE Transactions on Pattern Analysis and Machine Intelligence*, 20(8):819–831, 1998.

[80] Matthias Markl and Carolin Körner. Multiscale modeling of powder bed–based additive manufacturing. *Annual Review of Materials Research*, 46:93–123, 2016.

[81] Alida Mazzoli, Michele Germani, and Roberto Raffaeli. Direct fabrication through electron beam melting technology of custom cranial implants designed in a PHANToM-based haptic environment. *Materials & Design*, 30(8):3186–3192, 2009.

[82] D L McDowell, K Gall, M F Horstemeyer, and J Fan. Microstructure-based fatigue modeling of cast A356-T6 alloy. *Engineering Fracture Mechanics*, 70(1):49–80, 2003.

[83] Robert Davis McGinty. *Multiscale Representation of Polycrystalline Inelasticity*. PhD thesis, Geogia Tech, 2001.

[84] Cahal McVeigh and Wing Kam Liu. Linking microstructure and properties through a predictive multiresolution continuum. *Computer Methods in Applied Mechanics and Engineering*, 197(41-42):3268–3290, 2008.

[85] Cahal McVeigh, Franck Vernerey, Wing Kam Liu, and L. Cate Brinson. Multiresolution analysis for material design. *Computer Methods in Applied Mechanics and Engineering*, 195(37-40):5053–5076, jul 2006.

[86] S Merkt, A Kleyer, and A J Hueber. The Additive Manufacture of Patient-tailored Finger Implants. *Laser Technik Journal*, 11(2):54–56, 2014.

[87] Jiashi Miao, Tresa M. Pollock, and J. Wayne Jones. Microstructural extremes and the transition from fatigue crack initiation to small crack growth in a polycrystalline nickel-base superalloy. *Acta Materialia*, 60(6-7):2840–2854, 2012.

[88] K C Mills. *Recommended Values of Thermophysical Properties for Selected Commercial Alloys*. Woodhead Publishing, 2002.

[89] John A Moore, Dana Frankel, Rajesh Prasannavenkatesan, August G Domel, Gregory B Olson, and Wing Kam Liu. A crystal plasticity-based study of the relationship between microstructure and ultra-high-cycle fatigue life in nickel titanium alloys. *International Journal of Fatigue*, 91, Part 1:183–194, 2016.

[90] Ahmad Mostafa, Ignacio Picazo Rubio, Vladimir Brailovski, Mohammad Jahazi, and Mamoun Medraj. Structure, Texture and Phases in 3D Printed IN718 Alloy Subjected to Homogenization and HIP Treatments. *Metals*, 7(12):196, 2017.

[91] H Moulinec and P Suquet. A numerical method for computing the overall response of nonlinear composites with complex microstructure. *Computer Methods in Applied Mechanics and Engineering*, 157(1-2):69–94, apr 1998.

[92] K Moussaoui, W Rubio, M Mousseigne, T Sultan, and F Rezai. Effects of Selective Laser Melting additive manufacturing parameters of Inconel 718 on porosity, microstructure and mechanical properties. *Materials Science and Engineering A*, 735(August):182–190, 2018.

[93] Yoshinori Ono, Tetsumi Yuri, Hideshi Sumiyoshi, Etsuo Takeuchi, Saburo Matsuoka, and Toshio Ogata. High-Cycle Fatigue Properties at Cryogenic Temperatures in Inconel 718 Nickel-based Superalloy. *Materials Transactions*, 45(2):342–345, 2004.

[94] David R Owen and Ernest Hinton. *Finite elements in plasticity*. Pineridge press, 1980.

[95] Deepankar Pal, Nachiket Patil, Kai Zeng, and Brent Stucker. An Integrated Approach to Additive Manufacturing Simulations Using Physics Based, Coupled Multiscale Process Modeling. *Journal of Manufacturing Science and Engineering*, 136(6):61022, 2014.

[96] Lakshmi L. Parimi, G. Ravi, Daniel Clark, and Moataz M. Attallah. Microstructural and texture development in direct laser fabricated IN718. *Materials Characterization*, 89:102–111, 2014.

[97] L Parry, I A Ashcroft, and R D Wildman. Understanding the effect of laser scan strategy on residual stress in selective laser melting through thermo-mechanical simulation. *Additive Manufacturing*, 12:1–15, 2016.

[98] Mohak Patel, Susan E. Leggett, Alexander K. Landauer, Ian Y. Wong, and Christian Franck. Rapid, topology-based particle tracking for high-resolution measurements of large complex 3D motion fields. *Scientific Reports*, 8(1):5581, dec 2018.

[99] Jonathan W. Pegues, Nima Shamsaei, Michael D. Roach, and Randall S. Williamson. Fatigue life estimation of additive manufactured parts in the as-built surface condition. *Material Design & Processing Communications*, 1(December 2018):e36, jun 2019.

[100] Rajesh Prasannavenkatesan and David L. McDowell. Polycrystal Plasticity Modeling of Cyclic Residual Stress Relaxation in Shot Peened Martensitic Gear Steel. *Journal of Engineering Materials and Technology*, 132(3):31011, 2010.

[101] Chunlei Qiu, Chinnapat Panwisawas, Mark Ward, Hector C Basoalto, Jeffery W Brooks, and Moataz M Attallah. On the role of melt flow into the surface structure and porosity development during selective laser melting. *Acta Materialia*, 96:72–79, 2015.

[102] Aaron Ressa. *Plastic Deformation and Ductile Fracture Behavior of Inconel 718*. Masters, The Ohio State University, 2015.

[103] I A Roberts, C J Wang, R Esterlein, M Stanford, and D J Mynors. A three-dimensional finite element analysis of the temperature field during laser melting of metal powders in additive layer manufacturing. *International Journal of Machine Tools and Manufacture*, 49(12):916–923, 2009.

[104] Theron M Rodgers, Jonathan D Madison, and Veena Tikare. Simulation of metal additive manufacturing microstructures using kinetic Monte Carlo. *Computational Materials Science*, 135:78–89, 2017.

[105] S. Romano, A. Brückner-Foit, A. Brandão, J. Gumpinger, T. Ghidini, and S. Beretta. Fatigue properties of AlSi10Mg obtained by additive manufacturing: Defect-based modelling and prediction of fatigue strength. *Engineering Fracture Mechanics*, 187:165–189, jan 2018.

[106] Horatiu Rotaru, Ralf Schumacher, Seong-Gon Kim, and Cristian Dinu. Selective laser melted titanium implants: a new technique for the reconstruction of extensive zygomatic complex defects. *Maxillofacial plastic and reconstructive surgery*, 37(1):1, 2015.

[107] F Roters, P Eisenlohr, L Hantcherli, D D Tjahjanto, T R Bieler, and D Raabe. Overview of constitutive laws, kinematics, homogenization and multiscale methods in crystal plasticity finite-element modeling: theory, experiments, applications. *Acta Materialia*, 58:1152–1211, 2010.

[108] Babis Schoinochoritis, Dimitrios Chantzis, and Konstantinos Salonitis. Simulation of metallic powder bed additive manufacturing processes with the finite element method: A critical review. *Proceedings of the Institution of Mechanical Engineers, Part B: Journal of Engineering Manufacture*, 231(1):96–117, 2015.

[109] Mohsen Seifi, Michael Gorelik, Jess Waller, Nik Hrabe, Nima Shamsaei, Steve Daniewicz, and John J. Lewandowski. Progress Towards Metal Additive Manufacturing Standardization to Support Qualification and Certification. *JOM*, 69(3):439–455, mar 2017.

[110] Nicola Senin, Adam Thompson, and Richard K Leach. Characterisation of the topography of metal additive surface features with different measurement technologies. *Measurement Science and Technology*, 28(9):095003, sep 2017.

[111] Modesar Shakoor, Orion L. Kafka, Cheng Yu, and Wing Kam Liu. Data science for finite strain mechanical science of ductile materials. *Computational Mechanics*, 64(1):33–45, nov 2018.

[112] M Shenoy, J Zhang, and D L McDowell. Estimating fatigue sensitivity to polycrystalline Ni-base superalloy microstructures using a computational approach. *Fatigue & Fracture of Engineering Materials & Structures*, 30(10):889–904, 2007.

[113] Luke Sheridan, Onome E. Scott-Emuakpor, Tommy George, and Joy E. Gockel. Relating porosity to fatigue failure in additively manufactured alloy 718. *Materials Science and Engineering A*, 727(April):170–176, 2018.

[114] Sunpreet Singh, Seeram Ramakrishna, and Rupinder Singh. Material issues in additive manufacturing: A review. *Journal of Manufacturing Processes*, 25:185–200, 2017.

[115] Jacob Smith, Wei Xiong, Jian Cao, and Wing Kam Liu. Thermodynamically consistent microstructure prediction of additively manufactured materials. *Computational Mechanics*, 57(3):359–370, 2016.

[116] Jacob Smith, Wei Xiong, Wentao Yan, Stephen Lin, Puikei Cheng, Orion L. Kafka, Gregory J. Wagner, Jian Cao, and Wing Kam Liu. Linking process, structure, property, and performance for metal-based additive manufacturing: computational approaches with experimental support. *Computational Mechanics*, 57(4):583–610, 2016.

[117] K Solberg and F Berto. Notch-defect interaction in additively manufactured Inconel 718. *International Journal of Fatigue*, 122:35–45, 2019.

[118] Bo Song, Xiao Zhao, Shuai Li, Changjun Han, Qingsong Wei, Shifeng Wen, Jie Liu, and Yusheng Shi. Differences in microstructure and properties between selective laser melting and traditional manufacturing for fabrication of metal parts: A review. *Frontiers of Mechanical Engineering*, 10(2):111–125, 2015.

[119] Amanda J Sterling, Brian Torries, Nima Shamsaei, Scott M Thompson, and Denver W Seely. Fatigue behavior and failure mechanisms of direct laser deposited Ti–6Al–4V. *Materials Science and Engineering: A*, 655:100–112, 2016.

[120] Christian Stöcker, Martina Zimmermann, and Hans Jürgen Christ. Effect of precipitation condition, prestrain and temperature on the fatigue behaviour of wrought nickel-based superalloys in the VHCF range. *Acta Materialia*, 59(13):5288–5304, 2011.

[121] Wenda Tan and Yung C Shin. Multi-scale modeling of solidification and microstructure development in laser keyhole welding process for austenitic stainless steel. *Computational Materials Science*, 98:446–458, 2015.

[122] Damien Texier, Jonathan Cormier, Patrick Villechaise, Jean-Charles Charles Stinville, Chris J. Torbet, Stéphane Pierret, and Tresa M. Pollock. Crack initiation sensitivity of wrought direct aged alloy 718 in the very high cycle fatigue regime: the role of non-metallic inclusions. *Materials Science and Engineering: A*, 678(August):122–136, 2016.

[123] J Thomas, M Groeber, and S Ghosh. Image-based crystal plasticity FE framework for microstructure dependent properties of Ti–6Al–4V alloys. *Materials Science and Engineering: A*, 553:164–175, 2012.

[124] A. Townsend, N. Senin, L. Blunt, R. K. Leach, and J. S. Taylor. Surface texture metrology for metal additive manufacturing: a review, 2016.

[125] C L Ventola. Medical Applications for 3D Printing: Current and Projected Uses. *Pharmacy and Theraputics*, 39(10):704–711, 2014.

[126] Franck Vernerey, Wing Kam Liu, and Brian Moran. Multi-scale micromorphic theory for hierarchical materials. *Journal of the Mechanics and Physics of Solids*, 55(12):2603–2651, 2007.

[127] VIC2D. VIC-2D.

[128] Andrey Vyatskikh, Stéphane Delalande, Akira Kudo, Xuan Zhang, Carlos M. Portela, and Julia R. Greer. Additive manufacturing of 3D nano-architected metals. *Nature communications*, 9(1):593, dec 2018.

[129] D.~B. David B. Witkin, Paul Adams, and Thomas Albright. Microstructural evolution and mechanical behavior of nickel-based superalloy 625 made by selective laser melting. In *Laser 3D Manufacturing II*, volume 9353 of *Proceedings of the SPIE*, page 93530B, 2015.

[130] Sarah J. Wolff, Stephen Lin, Eric J. Faierson, Wing Kam Liu, Gregory J. Wagner, and Jian Cao. A framework to link localized cooling and properties of directed energy deposition (DED)-processed Ti-6Al-4V. *Acta Materialia*, 132:106–117, 2017.

[131] Sarah J. Wolff, Hao Wu, Niranjan Parab, Cang Zhao, Kornel F. Ehmann, Tao Sun, and Jian Cao. In-situ high-speed X-ray imaging of piezo-driven directed energy deposition additive manufacturing. *Scientific Reports*, 9(1):962, dec 2019.

[132] Eric Wycisk, Claus Emmelmann, Shafaqat Siddique, and Frank Walther. High Cycle Fatigue (HCF) Performance of Ti-6Al-4V Alloy Processed by Selective Laser Melting. *Advanced Materials Research*, 816-817:134–139, 2013.

[133] Eric Wycisk, Andreas Solbach, Shafaqat Siddique, Dirk Herzog, Frank Walther, and Claus Emmelmann. Effects of Defects in Laser Additive Manufactured TI-6Al-4V on Fatigue Properties. *Physics Procedia*, 56(C):371–378, 2014.

[134] Y. Xue, A. Pascu, M. F. Horstemeyer, L. Wang, and P. T. Wang. Microporosity effects on cyclic plasticity and fatigue of LENS-processed steel. *Acta Materialia*, 58(11):4029–4038, 2010.

[135] Aref Yadollahi and Nima Shamsaei. Additive manufacturing of fatigue resistant materials: Challenges and opportunities. *International Journal of Fatigue*, 98:14–31, 2017.

[136] Fuyao Yan, Wei Xiong, Eric Faierson, and Gregory B. Olson. Characterization of nano-scale oxides in austenitic stainless steel processed by powder bed fusion. *Scripta Materialia*, 155:104–108, oct 2018.

[137] Nu Yan, Norio Kawagoishi, Qiang Chen, Qing Yuan Wang, Hironobu Nisitani, and Eiji Kondo. Fatigue properties of inconel 718 in long life region at elevated temperature. *Key Engineering Materials*, 243-244:321–326, 2003.

[138] Wentao Yan, Wenjun Ge, Ya Qian, Stephen Lin, Bin Zhou, Wing Kam Liu, Feng Lin, and Gregory J Wagner. Multi-physics modeling of single/multiple-track defect mechanisms in electron beam selective melting. *Acta Materialia*, 134:324–333, 2017.

[139] Wentao Yan, Wenjun Ge, Jacob Smith, Stephen Lin, Orion L. Kafka, Feng Lin, and Wing Kam Liu. Multi-scale modeling of electron beam melting of functionally graded materials. *Acta Materialia*, 115:403–412, 2016.

[140] Wentao Yan, Wenjun Ge, Jacob Smith, Gregory Wagner, Feng Lin, and Wing Kam Liu. TOWARDS HIGH-QUALITY SELECTIVE BEAM MELTING TECHNOLOGIES: MODELING AND EXPERIMENTS OF SINGLE TRACK FORMATIONS. In *26th Annual International Symposium on Solid Freeform Fabrication*, Austin, Texas, 2015.

[141] Wentao Yan, Yanping Lian, Cheng Yu, O. L. Kafka, Zeliang Liu, Wing Kam Liu, and Gregory J. Wagner. An integrated process–structure–property modeling framework for additive manufacturing. *Computer Methods in Applied Mechanics and Engineering*, 339:184–204, 2018.

[142] Wentao Yan, Stephen Lin, Orion L. Kafka, Cheng Yu, Zeliang Liu, Yanping Lian, Sarah Wolff, Jian Cao, Gregory J. Wagner, and Wing Kam Liu. Modeling process-structure-property relationships for additive manufacturing. *Frontiers of Mechanical Engineering*, 13(4):482–492, dec 2018.

[143] Wentao Yan, Ya Qian, Wenjun Ge, Stephen Lin, Wing Kam Liu, Feng Lin, and Gregory J Wagner. Meso-scale modeling of multiple-layer fabrication process in selective electron beam melting: inter-layer/track voids formation. *Materials & Design*, 141:210–219, 2018.

[144] Wentao Yan, Jacob Smith, Wenjun Ge, Feng Lin, and Wing Kam Liu. Multiscale modeling of electron beam and substrate interaction: a new heat source model. *Computational Mechanics*, 56(2):265–276, 2015.

[145] Daryl W. Yee, Max L. Lifson, Bryce W. Edwards, and Julia R. Greer. Additive Manufacturing of 3D-Architected Multifunctional Metal Oxides. *Advanced Materials*, 31(33):1901345, aug 2019.

[146] Cheng Yu. *Multiscale Clustering Analysis*. Phd, Northwestern University, 2019.

[147] Cheng Yu, Orion L. Kafka, and Wing Kam Liu. Self-consistent clustering analysis for multiscale modeling at finite strains. *Computer Methods in Applied Mechanics and Engineering*, 349:339–359, jun 2019.

[148] Karin Yvell, T M Grehk, Peter Hedström, A Borgenstam, and Göran Engberg. Microstructure development in a high-nickel austenitic stainless steel using EBSD during in situ tensile deformation. *Materials Characterization*, 135:228–237, 2018.

[149] YangYang Zhang, Zheng Duan, and Huiji Shi. Comparison of the very high cycle fatigue behaviors of INCONEL 718 with different loading frequencies. *Science China Physics, Mechanics and Astronomy*, 56(3):617–623, 2013.

APPENDIX A

Codes and scripts for post-processing 2BM data

A.1. Tomopy reconstruction script

The following series of scripts launches jobs for that run tomopy reconstructions assuming some basic information about file structures and locations. Prior to running the "rcon" scripts, center finding must be conducted, following the procedure outline in Appendix B.2.5 (typically done as part of the 2BM work, but could be finished elsewhere if needed).

A.1.1. tomopyRunner.sh

```
#!/bin/bash

#reconStart1=149
#reconFinish1=212

#reconStart2=81
#reconFinish2=110

#reconStart3=111
#reconFinish3=140

#reconStart4=141
#reconFinish4=175

#reconStart5=176
#reconFinish5=214

#for ((i=$reconStart1; i<=$reconFinish1; i=i+4))

reconList=(61 64 67 70 72 73 76 79 82 85 88 91 94)
reconFinish=${reconList[${#reconList[@]}-1]}

for i in ${reconList[@]}
do
# end=$(($i + 3))
# qsub -N "tomopy_exp${i}_${end}" -F "$i $end" batch_run_tomopy_11
   qsub -N "tomopy_exp${i}" -F "$i $i" batchRunRomopy
   if [ "$i -ne $reconFinish1" ]; then sleep 0.2; fi
```

```
done
exit 0

#sleep 0.2

#qsub -N "tomopy_exp${reconStart2}_${reconFinish2}" -F "$reconStart2
    ↪ $reconFinish2" batch_run_tomopy
#sleep 0.2

#qsub -N "tomopy_exp${reconStart3}_${reconFinish3}" -F "$reconStart3
    ↪ $reconFinish3" batch_run_tomopy
#sleep 0.2

#qsub -N "tomopy_exp${reconStart4}_${reconFinish4}" -F "$reconStart4
    ↪ $reconFinish4" batch_run_tomopy
#sleep 0.2

#qsub -N "tomopy_exp${reconStart5}_${reconFinish5}" -F "$reconStart5
    ↪ $reconFinish5" batch_run_tomopy
```

A.1.2. batchRunTomopy.sh

```
#! /bin/bash
#PBS -l nodes=1:ppn=24
#PBS -E
#PBS -l walltime=5:00:00:00
#PBS -N tomopy_03
#PBS -l mem=50gb
cd $PBS_O_WORKDIR

start1=$1
end1=$2

/home/olk335/anaconda2/envs/tomopyv1/bin/python rcon.py $start1 $end1
```

A.1.3. rcon.py

The recon script is based on a script originally written by Dr. Xianghui Xiao (the beamline scientist at 2BM), and adapted in both from (for batch processing) and function (a number of filters and functions were added to help clean up artifacts). Additionally, a modified version of the "write_tiff_stack" function was generated (in collaboration with Dr. Xiao) that outputs 8-bit images rather than the 32-bit default, with bit space scaling determined by the vmax and vmin parameters. This saves substantial disk space.

```
# -*- coding: utf-8 -*-
```

```
"""
Created on Sat May 23 12:26:06 2015

@author: xhxiao
@editor: okafka
"""

#from tomopy.io.reader import *
#import numpy as np
#import os.path
#from numpy.testing import assert_allclose
#import pkg_resources
import tomopy
from tomopy.recon.rotation import write_center
from tomopy.recon.algorithm import recon
from tomopy import minus_log
import os, h5py, glob, fnmatch
import numpy as np
import scipy
import time
import skimage.restoration as skr

####----------------- Section 1: Input file -- Staragt -----------------
print time.asctime()
user_top_dir = '/home/projects/APS/xctRecon/rawDataFiles/March2017/'
user_out_dir = '/home/projects/APS/xctRecon/2017_03/ring_removal/'
#centering_dir = '/home/olk335/xctRecon/March2017/data_center'

# Reconstructs experiments within the range given using the proper center
# and otherwise identical settings.
for expNum in range(2,40):
    print 'ExpID = ' + str(expNum)
    #sam_idx = 1
    Exp_idx = expNum

    #data_top_dir = user_top_dir + 's' + '{:03}'.format(sam_idx) + '*/'
    data_top_dir = user_top_dir + '/'
    data_out_dir = user_out_dir + '/'

    data_dir = glob.glob(os.path.join(data_top_dir,'Exp'+'{:03}'.format(Exp_idx)
        ↪ +'*'))[0]
    if user_top_dir == user_out_dir:
        output_dir = data_dir # Output to a folder in the original directory
    else:
        # Make an output folder with JUST the experiment number in as the name
```

```
    output_dir = os.path.join(data_out_dir,'Exp' + '{:03}'.format(Exp_idx))

data_files = np.sort(fnmatch.filter(os.listdir(data_dir),'*.hdf'))
if len(data_files) == 0:
    data_files = np.sort(fnmatch.filter(os.listdir(data_dir),'*.h'))

file_data = data_files[0]
file_flat = data_files[0]
file_dark = data_files[0]

print file_data
print file_flat
print file_dark

file_name = os.path.join(data_dir, file_data)
flat_name = os.path.join(data_dir, file_flat)
dark_name = os.path.join(data_dir, file_dark)
output_file = output_dir+'/recon_'+file_data.split(".")[-2]+'/recon_'+
    ↪ file_data.split(".")[-2] +'_'
####----------------- Section 1: Input file -- End -----------------


####----------------- Section 2: Parameter configuration -- Start
    ↪ -----------------
f = h5py.File(file_name,"r")
try:
    arr = f["exchange/data"]
except:
    try:
        arr = f["entry/data/data"]
    except:
        arr = f["MyDataDir/TomoShots"]
numProj = (arr.shape)[0]
numSlices = (arr.shape)[1]
imgWidth = (arr.shape)[2]
f.close()
print numProj,numSlices,imgWidth

offset = 0 # offset from the top slice; for full volume, set to 0
numRecSlices = 100 # For full volume, comment this out
#numRecSlices = numSlices # For full volume, uncomment this line
chunk_size = 100
if chunk_size > numRecSlices:
    chunk_size = numRecSlices
margin_slices = 30 # changed from 40 to 0
```

```
num_chunk = np.int(numRecSlices/(chunk_size-margin_slices)) + 1
if numRecSlices == chunk_size:
    num_chunk = 1

z = 20
eng = 60
pxl = 0.65e-4
rat = 1e-02

zinger_level = 300
####----------------- Section 2: Parameter configuration -- End
    ↪ -----------------


#######----------------- Section 3: Finding center -- Start -----------------
#sliceStart = 900
#sliceEnd = sliceStart+40
#f = h5py.File(file_name,"r")
#try:
# arr = f["exchange/data"]
#except:
# try:
# arr = f["entry/data/data"]
# except:
# arr = f["MyDataDir/TomoShots"]
#data = arr[0:numProj,sliceStart:sliceEnd,:]
#f.close()
#
#f = h5py.File(flat_name,"r")
#try:
# arr = f["exchange/data_white"]
#except:
# try:
# arr = f["entry/data/data"]
# except:
# arr = f["MyDataDir/TomoShots"]
#white = arr[1:9,sliceStart:sliceEnd,:]
#f.close()
#
#f = h5py.File(dark_name,"r")
#try:
# arr = f["exchange/data_dark"]
#except:
# try:
# arr = f["entry/data/data"]
```

```
# except:
# arr = f["MyDataDir/TomoShots"]
#dark = arr[1:9,sliceStart:sliceEnd,:]
#f.close()
#
#data_size = data.shape
#theta = np.linspace(0,np.pi,num=numProj-1)
#print data_size,theta.shape
#
## zinger_removal
#data = tomopy.misc.corr.remove_outlier(data,zinger_level,size=15,axis=0)
#white = tomopy.misc.corr.remove_outlier(white,zinger_level,size=15,axis=0)
#
#data = tomopy.prep.normalize.normalize(data,white,dark)
#data = tomopy.prep.normalize.normalize_bg(data,air=10)
#
##data = tomopy.prep.stripe.remove_stripe_ti(data,alpha=5.)
##data = tomopy.prep.stripe.remove_stripe_ti(-1.0*data,alpha=5.)
#data = tomopy.prep.stripe.remove_stripe_fw(data,level=6,wname='sym16',sigma
    ↪ =1,pad=True,slidir=1,fltdir=0)
#
#data = tomopy.prep.phase.retrieve_phase(data,pixel_size=pxl,dist=z,energy=eng
    ↪ ,alpha=rat,pad=True)
#
#data_size = data.shape
#
#center_shift = 45 # good to start with -5
#center_shift_w = 10
#data = tomopy.prep.normalize.minus_log(data)
#write_center(data[:,20:21,:], theta, dpath=centering_dir,
# cen_range=(data.shape[2]/2+center_shift,data.shape[2]/2+center_shift+
    ↪ center_shift_w,0.5))
#######----------------- Section 3: Finding center -- End -----------------

#z = 0
#eng = 60
#pxl = 0.65e-4
#rat = 1e-02

center = [0, # Exp001 #PH48S #1 (no center found yet)
    1240.5, # Exp002 #PH48S #3
    1245.5, # Exp003
    1241.5, # Exp004
    1219.5, # Exp005
    1223.0, # Exp006
```

```
1220.0, # Exp007
1220.0, # Exp008
1221.5, # Exp009
1220.0, # Exp010
1225.5, # Exp011
1282.0, # Exp012
1257.5, # Exp013
1255.5, # Exp014
1239.5, # Exp015
1221.5, # Exp016
1221.5, # Exp017
1324.5, # Exp018 # strange contrast, in-situ test
1323.5, # Exp019 # strange contrast, in-situ test
1334.5, # Exp020 # strange contrast, in-situ test
1294.5, # Exp021
1294.5, # Exp022
1297.0, # Exp023
1288.0, # Exp024 #PH48S #4
1291.5, # Exp025 #PH48S #3
1293.5, # Exp026
1292.0, # Exp027
1293.0, # Exp028
1294.0, # Exp029
1290.0, # Exp030
1292.0, # Exp031
1291.5, # Exp032
1294.5, # Exp033
1295.0, # Exp034
1303.0, # Exp035
1288.5, # Exp036
1301.5, # Exp037
1305.0, # Exp038
1292.0, # Exp039
1291.0, # Exp040
1296.0, # Exp041
1294.5, # Exp042
1299.5, # Exp043
1304.5, # Exp044
1302.0, # Exp045
1301.5, # Exp046
1293.0, # Exp047
1299.5, # Exp048
1296.0, # Exp049
1299.5, # Exp050
1291.5, # Exp051
```

```
1285.0, # Exp052
1294.5, # Exp053
1294.5, # Exp054
1285.0, # Exp055
1287.5, # Exp056
1295.5, # Exp057
1296.0, # Exp058
1290.0, # Exp059
1290.5, # Exp060
1295.5, # Exp061
1302.5, # Exp062
1301.0, # Exp063
1298.0, # Exp064
1299.0, # Exp065
1301.0, # Exp066
1301.0, # Exp067
1298.0, # Exp068
1298.5, # Exp069
1298.0, # Exp070
1302.0, # Exp071
1296.5, # Exp072
1306.0, # Exp073
1300.0, # Exp074
1296.0, # Exp075
1301.5, # Exp076
1299.5, # Exp077
1300.0, # Exp078
1301.5, # Exp079
1297.0, # Exp080
1299.0, # Exp081
1295.0, # Exp082
1290.0, # Exp083
1295.0, # Exp084
1295.0, # Exp085
1298.0, # Exp086
1291.5, # Exp087
1300.0, # Exp088
1295.5, # Exp089
1295.0, # Exp090
1301.0, # Exp091
1300.5, # Exp092
1300.0, # Exp093
1299.0, # Exp094
1240.0, # Exp095
1269.5, # Exp096
```

```
1303.0, # Exp097
1295.0, # Exp098
1299.5, # Exp099
1279.5, # Exp100
1300.0, # Exp101
1300.0, # Exp102
1302.5, # Exp103
1304.5, # Exp104
1295.0, # Exp105
1300.5, # Exp106
1299.0, # Exp107
1300.0, # Exp108
1305.5, # Exp109
1301.5, # Exp110
1298.5, # Exp111
1284.0, # Exp112
1289.0, # Exp113
1285.0, # Exp114
1237.0, # Exp115
1221.5, # Exp116
1238.0, # Exp117
1210.0, # Exp118
1250.0, # Exp119
1259.0, # Exp120
1267.5, # Exp121
1280.0, # Exp122 No rings anywhere
1215.0, # Exp123 No rings anywhere
1199.0, # Exp124
1198.0, # Exp125
1198.0, # Exp126 No rings anywhere
1237.0, # Exp127
1237.0, # Exp128 No rings anywhere
1205.0, # Exp129 No rings anywhere
1205.0, # Exp130
1238.0, # Exp131
1205.0, # Exp132
1211.0, # Exp133
1211.0, # Exp134
1207.0, # Exp135
1250.0, # Exp136
1226.5, # Exp137
1233.0, # Exp138
1225.0, # Exp139
1217.5, # Exp140
1217.5, # Exp141
```

```
    1219.0, # Exp142
    1230.0, # Exp143
    1217.0, # Exp144
    1231.0, # Exp145
    1235.0, # Exp146
    1231.5, # Exp147
    1237.5, # Exp148
    1233.5, # Exp149
    1225.5, # Exp150
    1239.5, # Exp151
    1262.5, # Exp152
    1239.0, # Exp153
    1234.5] # Exp154

print 'center = ' + str(center[expNum])
#######----------------- Section 4: Full reconstruction -- Start
    ↪ -----------------
for ii in range(num_chunk):
    if ii == 0:
        sliceStart = offset + ii*chunk_size
        sliceEnd = offset + (ii+1)*chunk_size
    else:
        sliceStart = offset + ii*(chunk_size-margin_slices)
        sliceEnd = sliceStart + chunk_size
        if sliceEnd > (offset+numRecSlices):
            sliceEnd = offset+numRecSlices
        if sliceEnd > numSlices:
            sliceEnd = numSlices

    if (sliceEnd - sliceStart) <= margin_slices:
        print 'Reconstruction finishes!'
        break

    f = h5py.File(file_name,"r")
    try:
        arr = f["exchange/data"]
    except:
        try:
            arr = f["MyDataDir/TomoShots"]
        except:
            arr = f["entry/data/data"]
    data = arr[0:numProj,sliceStart:sliceEnd,:]
    f.close()

    f = h5py.File(flat_name,"r")
```

```
        try:
            arr = f["exchange/data_white"]
        except:
            try:
                arr = f["MyDataDir/TomoShots"]
            except:
                arr = f["entry/data/data"]
        white = arr[1:9,sliceStart:sliceEnd,:]
        f.close()

        f = h5py.File(dark_name,"r")
        try:
            arr = f["exchange/data_dark"]
        except:
            try:
                arr = f["MyDataDir/TomoShots"]
            except:
                arr = f["entry/data/data"]
        dark = arr[1:9,sliceStart:sliceEnd,:]
        f.close()
        data_size = data.shape
        theta = np.linspace(0,np.pi,num=data_size[0])
        print 'data is read'
        print 'chunk ' + str(ii)



# remove zingers (pixels with abnormal counts)
        data = tomopy.misc.corr.remove_outlier(data,zinger_level,size=15,axis=0,
            ↪ ncore=numProc)
        white = tomopy.misc.corr.remove_outlier(white,zinger_level,size=15,axis=0,
            ↪ ncore=numProc)

        # normalize projection images; for now you need to do below two operations
            ↪  in sequence
        data = tomopy.prep.normalize.normalize(data,white,dark,ncore=numProc)
        data = tomopy.prep.normalize.normalize_bg(data,air=10,ncore=numProc)

        # phase retrieval
        data = tomopy.prep.phase.retrieve_phase(data,pixel_size=pxl,dist=z,energy=
            ↪ eng,alpha=rat,pad=True,ncore=numProc)

        # remove stripes in sinograms
        data = tomopy.prep.stripe.remove_stripe_ti(data,alpha=5,ncore=numProc)
        data = tomopy.prep.stripe.remove_stripe_sf(data,size=31,ncore=numProc)
```

```
        data = tomopy.prep.normalize.normalize_bg(data,air=10,ncore=numProc)


        # tomo reconstruction
        data = tomopy.prep.normalize.minus_log(data)
        data_recon = recon(data,theta,center=center[expNum],algorithm='gridrec')

        # Attempt to remove rings from recon

        data_recon = tomopy.misc.corr.adjust_range(data_recon, dmin=np.min(
            ↪ data_recon)/0.2, dmax=np.max(data_recon)*0.2)
        data_recon = tomopy.misc.corr.remove_outlier(data_recon, dif=100, size=9,
            ↪ axis=0, ncore=numProc, out=data_recon)
        data_recon = tomopy.misc.corr.remove_ring(data_recon, thresh=500.0,
            ↪ thresh_max=300.0, thresh_min=-100.0, theta_min=20, rwidth=45, ncore=
            ↪ numProc, out=data_recon)

# data_recon = tomopy.misc.corr.remove_outlier(data_recon, dif=100, size=5, axis
    ↪ =0, ncore=numProc, out=data_recon)
        # Subtract a gaussian blur
        data_blur = scipy.ndimage.filters.gaussian_filter(data_recon,3,1)

        data_recon = data_recon - data_blur

# data_recon = tomopy.misc.corr.remove_outlier(data_recon, dif=100, size=3, axis
    ↪ =1, ncore=numProc, out=data_recon)
        data_recon = tomopy.misc.corr.remove_outlier(data_recon, dif=100, size=3,
            ↪ axis=2, ncore=numProc, out=data_recon)

        # save reconstructions

        tomopy.io.writer.write_tiff_stack(data_recon[np.int(margin_slices/2):(
            ↪ sliceEnd-sliceStart-np.int(margin_slices/2)),:,:],
                                          axis = 0,
                                          dtype = 'uint8',
                                          vmax = 0.001,
                                          vmin = -0.0011,
                                          fname = output_file,
                                          start = sliceStart+np.int(margin_slices/2),
                                          overwrite = True)

        print 'reconstruction is saved'
        print time.asctime()

    print 'Reconstruction finishes!'
```

```
#########----------------- Section 4: Full reconstruction -- End
    ↪ -----------------
```

A.2. Matlab image processing

The following scripts embody a batch processing to convert reconstructed images into binary images using a mixed automatic and manual thresholding method (some adjustment/tuning of parameter is required if substantially different images are to be used). While this is the heart of the codes, there are other processes that might be of interest. For example, there is another script to rotate and crop images to remove unneeded background space, which interfaces with a code to fill in manually identified rings and a code t write the results to a VTK file.

A.2.1. batchBin.sh batch job runner

```
#! /bin/bash
# Script to submit matlab jobs that convert tif stacks to
# binary images and .mat files. --Orion, July 2017
basePath="/home/projects/APS/xctRecon/2017_11"
startSlice=15
numSlices=2088
#=========================================
# RANGE
# comment list lines and uncomment to do a range
reconStart=205
reconFinish=205
for ((i=$reconStart; i<=$reconFinish; i++))

#=========================================
# LIST
# comment range lines and uncomment to do a set list
#reconList=(25)
#reconFinish=${reconList[${#reconList[@]}-1]}
#for i in ${reconList[@]}

#=========================================
# main body of loop. Do not edit below this.
do
    expNum=${i}
    expNumIn=$(printf %03d $expNum)
    projNum=$(printf %04d $expNum)
    # Make the paths and a directory to place the output in
    inPath="${basePath}/Exp$expNumIn/8bit" # recon_proj_${projNum}"
    outPath="${basePath}/Exp$expNumIn/matBin"
    if [ ! -e "$outPath" ]; then mkdir "${outPath}"; fi
    inPrefix="Exp${expNumIn}_" #"recon_proj_${projNum}__"
    outPrefix="Exp${expNumIn}_"
```

```
    # Run the job
    qsub -N tif2bin $expNumIn -F "$inPath $outPath $inPrefix $outPrefix $expNumIn
        ↪ $startSlice $numSlices 11" /home/projects/APS/xctRecon/makeBin/
        ↪ run_matlab_batch.sh
    # Pause slightly before submitting the next job
    if [ "$expNum" -ne "$reconFinish" ]; then sleep 1; fi
done
exit 0
```

A.2.2. runMatlabBatch.sh submission script

```
#! /bin/bash
## note that nodes must be equal to 1, i.e., nodes=1. Max cpus is 24 on Ares.
#PBS -l nodes=1:ppn=24
#PBS -l walltime=2:00:00
#PBS -l mem=58gb

inPath="'"$1"'"
outPath=$2
inPrefix="'"$3"'"
outPrefix="'"$4"'"
expNumIn=$5
startSlice=$6
numSlices=$7

if [ $8 == 11 ]; then
   inputfile=tif2bin_11
elif [ $8 == 6 ]; then
   inputfile=tif2bin_06
fi

# place log files
#logLoc=$outPath
#logLoc+=/matlab_$expNumIn.log
logE=$outPath
logE+=/matlab_e_$expNumIn.log
logO=$outPath
logO+=/matlab_o_$expNumIn.log

logE=matlab_e_$expNumIn.log
logO=matlab_o_$expNumIn.log

outPath="'"$outPath"'"
```

```
################################################################################################
    ↪
cd $PBS_O_WORKDIR

#echo $inputfile
#echo $inPath
#echo $outPath
#echo $inPrefix
#echo $outPrefix


#/shared/matlab/R2015b/bin/matlab -nosplash -nodisplay -nodesktop -r "$inputfile(
    ↪ $inPath,$outPath,$inPrefix,$outPrefix,$PBS_NUM_PPN); exit" > $logE > $logO

#/home/olk335/matlab/r2017a/bin/matlab -nosplash -nodisplay -nodesktop -r "batch(
    ↪ $inputfile($inPath,$outPath,$inPrefix,$outPrefix,$startSlice,$numSlices,
    ↪ $PBS_NUM_PPN)); exit" > $logE > $logO

matlab -nosplash -nodisplay -nodesktop -r "batch($inputfile($inPath,$outPath,
    ↪ $inPrefix,$outPrefix,$startSlice,$numSlices,$PBS_NUM_PPN)); exit" > $logE >
    ↪  $logO
```

A.2.3. tif2bin.m main matlab script

```
function out = tif2bin(inPath,outPath,filePrefixName,outImageName,startSlice,
    ↪ numSlices,numProc)
% tif2mat
% Orion L. Kafka
% Northwestern University, Summer 2016
% A simplistic script to stack tif format grayvalue images from sectioning
% e.g. tomopy or analysis e.g. dream3d to form 3d mat files for dvc

tic
% ===== USER INPUTS =====
% Input parameters
% Set parallel processsing
%isParallel = 'true';

% Size of images
xSize = 2560; % pixels
ySize = 2560; % pixels
zSize = numSlices; % pixels (or images)

% To build file names:
startInd = startSlice;
% Ending image
```

```
endInd = startInd + zSize;
% Number of digits of postfix number
numDigits = 5;

% Output parameters
%outImageName = 'Exp021_';
outFileName = [outImageName,'.mat'];
outSmallFileName = [outImageName,'x10.mat'];

%curTime = clock;
%disp(['Start time: ',num2str(curTime(4)),'h:',num2str(curTime(5)),'m:',num2str(
    ↪ curTime(6)),'s::',...
% num2str(curTime(1)),'y:',num2str(curTime(2)),'m:',num2str(curTime(3)),'d'])

% ===== START COMPUTATIONS =====

disp('Initializing variables...')
volData = zeros(xSize,ySize,zSize,'uint8'); % will actually be logical, because
    ↪ the output is thresholded
%countz = 1;

disp('Starting data collection...')
% ii = z, jj = x, kk = y

xSlice = 1:xSize;
ySlice = 1:ySize;

if numProc ~= 1 %strcmp(isParallel, 'true'); if there is more than one processor
    ↪ provided by the scheduler
    % Make a unique MATLAB parallel pool
% pool = parpool(numProc);
    eval(['pool' outFileName ' = parpool(numProc)']);
    parfor ii = 1:zSize
        ll = ii + startInd-1;

        imgFile = fullfile(inPath,[filePrefixName,padWithZeros(numDigits,ll),'.
            ↪ tiff']);
        disp(imgFile)

        tifImage = imread(imgFile);

        % Read in file
        % Do some filtering and processing
        tifImage = localcontrast(tifImage,0.1,-0.1);
        tifImage = localcontrast(tifImage,0.1205,-0.205);
```

```
        tifImage = wiener2(tifImage,[4,4]);
        tifImage = medfilt2(tifImage,[5,5]);

        lvl = graythresh(tifImage);
        tifBin = imbinarize(tifImage,lvl*0.998);

        tifBin = bwareaopen(tifBin,25);


        % Save mat data
        volData(:,:,ii) = uint8(tifBin(xSlice,ySlice,:));

        pad = '';
        for jj = 1:numDigits
            if ll < 10^(jj)
                numPad = numDigits-jj;
                for kk = 1:numPad
                    pad = [pad,'0'];
                end
                imwrite(tifBin,...
                       fullfile(outPath,[outImageName,pad,num2str(ll),'.tif']),...
                       'tiff','Compression','none');
                pad = '';
                break
            end
        end
        disp(['Processing number ',num2str(ii)])
    end

    eval(['delete(pool' outFileName ')']); % Clean up the parallel pool
else
    for ii = 1:zSize
        ll = ii + startInd-1;
        % Build file name to read in - add proper number of padding zeros
        pad = '';
        imgFile = '';
        for jj = numDigits:-1:1
            if ll < 10^(jj)
                numPad = numDigits-jj;
                for kk = 1:numPad
                    pad = [pad,'0'];
                end
                imgFile = fullfile(inPath,[filePrefixName,pad,num2str(ll),'.tif']);
                pad = '';
            end
```

```
        end

        % Read in file
        tifImage = imread(imgFile,'tif');
        % Do some filtering and processing
        tifImage = localcontrast(tifImage,0.04,-1);
        %tifImage = wiener2(tifImage,[3,3],13e-3);
        %tifImage = medfilt2(tifImage,[5,5]);
        %tifImage = wiener2(tifImage,[5,5],7e-3);
        %tifImage = wiener2(tifImage,[7,7],5e-3);

        lvl = graythresh(tifImage);
        tifBin = imbinarize(tifImage,lvl*1.25);

        %tifBin = bwareaopen(tifBin,50);

        % Save mat data
        volData(:,:,ii) = uint8(tifBin(xSlice,ySlice,:));
        % Output tif to file
        pad = '';
        for jj = 1:numDigits
            if ll < 10^(jj)
                numPad = numDigits-jj;
                for kk = 1:numPad
                    pad = [pad,'0'];
                end
                imwrite(tifBin,...
                       fullfile(outPath,[outImageName,pad,num2str(ll),'.tif']),...
                       'tiff','Compression','none');
                pad = '';
                break
            end
        end
        disp(['Processing number ',num2str(ii),'/',num2str(zSize)])
        if ii == 5
            disp(['Estimated time = ',num2str(toc/5*zSize/60),'min']);
        end
    end
end
procTime = toc;
volSmall_10 = voxelDownsample(volData,10,'uint8');
tic
% ===== DATA OUTPUT =====
disp('Saving...')
% Save mat files
```

```
save(fullfile(outPath,outFileName),'volData','-mat','-v7.3');
save(fullfile(outPath,outSmallFileName),'volSmall_10','-mat','-v7.3');
%curTime = clock;
saveTime = toc;
%disp(['End time: ',num2str(curTime(4)),'h:',num2str(curTime(5)),'m:',num2str(
    ↪ curTime(6)),'s::',...
% num2str(curTime(1)),'y:',num2str(curTime(2)),'m:',num2str(curTime(3)),'d'])
disp(['Processing time : ',num2str((procTime)/60),'min'])
disp(['Saving time : ',num2str((saveTime)/60),'min'])
disp(['Total elapsed time: ',num2str((procTime + saveTime)/60),'min'])
disp('Process complete.')

function matOut = voxelDownsample(matIn,scaleFac,dataType)
% voxelDownsample Make a voxel image smaller
% B = voxelDownsample(A,s) makes the voxel image defined by matrix matIn
% smaller by a factor of scaleFac and returns the resulting matrix in
% matOut.
%
% Example: 20x20x20 input image with scaling factor of 2 will result
% in a 10x10x10 output image.
%
% Notes:
% 1. Slight shifting might occur for images scaled with non-integer
% factors.
% 2. Upscaling (scaleFac < 1) is currently not supported, but
% sometimes might produce reasonable results.
% 3. Currently scaling by the same factor in all dimensions is the only
% supported mode. While it might not make much sense to do, one may
% eventually wish to scale in different dimensions by a different
% factor. This might be added.
%
% +------------------------------------------------------------------------+
% | *** INPUTS *** |
% | matIn - n*m*p matrix with 0 for the matrix phase and 1 for the other |
% | phase |
% | scaleFac - value by which to scale the image (tested for 2 and 4) |
% | |
% | *** OUTPUTS *** |
% | matOut - n/sizeRatio * m/sizeRatio * p/sizeRatio (all rounded down) |
% | matrix with 0 for matrix phase and 1 for other phase. |
% +------------------------------------------------------------------------+
%
% Orion L. Kafka, Northwestern University
%
% File history:
```

```
% 1 Dec 2016 - Written
% 29 Apr 2017 - Added datatype control, changed SumA to sumA

% Check for some easy mistakes
assert(ndims(matIn) == 3,...
    'Invalid entry: matIn. Number of dimensions must = 3')
assert(size(matIn,1) > scaleFac || ...
      size(matIn,2) > scaleFac || ...
      size(matIn,3) > scaleFac, ...
    ['Invalde entry: matIn OR scaleFac.',...
     ' Matrix size in each dim must be > scaleFac'])
assert(scaleFac>0,...
    'Invalid entry: scaleFac = %f Scaling factor must be > zero.',...
    scaleFac)

if scaleFac < 1
    warning('scaleFac = %f will make the image BIGGER.',scaleFac)
    warning('Upscaling is not well supported; proceeding anyway.')
end

% Preallocate output array
matOut = zeros(floor(size(matIn,1)/scaleFac),...
             floor(size(matIn,2)/scaleFac),...
             floor(size(matIn,3)/scaleFac),dataType);

% In a region around the current point of interest, add up all the voxel
% values. If the region is more than half filled with 1's make the voxel a
% 1. If less than half, make it a 0. Region size is defined by the image
% size and scaling factor.
for I = 1:size(matIn,1)/scaleFac
    for J = 1:size(matIn,2)/scaleFac
        for K = 1:size(matIn,3)/scaleFac

            sumA = sum(sum(sum(matIn(...
                floor(I*scaleFac-(scaleFac-1)):ceil(I*scaleFac),...
                floor(J*scaleFac-(scaleFac-1)):ceil(J*scaleFac),...
                floor(K*scaleFac-(scaleFac-1)):ceil(K*scaleFac)))));

            if sumA >= (scaleFac^3)/2 + 1
                matOut(I,J,K) = 1;
            else
                matOut(I,J,K) = 0;
            end

        end
```

```
    end
end

function padStr = padWithZeros(numDigits,padNum)
%padStr = padWithZeros(numDigits, padNum)
%=========================================================================
% Add leading zeros to a number and return a character string. This is
% mostly useful for working with file names, but for reading and writing.
%
% --- INPUT ---
% numDigits - int, total width of number (number of characters)
% padNum - int, number to add padding zeros to
%
% --- OUTPUT ---
% padStr - string, padded with leading zeros to length of numDigits
%
% -------------------------------------------------------------------------
% History - Orion L. Kafka
% 12-11-2017 - written
%
%=========================================================================

pad = '';
for jj = numDigits:-1:1
    % Find the number of digits in the number
    if padNum < 10^(jj) && padNum >= 10^(jj-1)
        zerosToAdd = numDigits-jj;
        % add a zero for each digit short of the requested number of digits
        for kk = 1:zerosToAdd
            pad = [pad,'0'];
        end
    end
end
% combine the number and the padding zeros
padStr = [pad,num2str(padNum)];
```

A.3. DREAM3D porosity analysis pipeline

The following listing is a json file that defines a DREAM3D pipeline to analysis the binarized 3D images output from the MATLAB script defined in Section A.2.

A.3.1. processCTVoidPipeline listing:

```
{
    "0": {
        "CellAttributeMatrixName": "CellData",
        "DataContainerName": "ImageDataContainer",
```

```
    "FilterVersion": "1.0.367",
    "Filter_Enabled": true,
    "Filter_Human_Label": "ITK::Import Images (3D Stack)",
    "Filter_Name": "ITKImportImageStack",
    "ImageDataArrayName": "ImageData",
    "InputFileListInfo": {
        "EndIndex": 1890,
        "FileExtension": "tif",
        "FilePrefix": "Exp001_crop_600-1890_",
        "FileSuffix": "",
        "InputPath": "/home/ender/Desktop/IN718Plus_CT/Exp001/crop",
        "Ordering": 0,
        "PaddingDigits": 4,
        "StartIndex": 600
    },
    "Origin": {
        "x": 0,
        "y": 0,
        "z": 0
    },
    "Resolution": {
        "x": 0.8700000047683716,
        "y": 0.8700000047683716,
        "z": 0.8700000047683716
    }
},
"1": {
    "DestinationArrayName": "Mask",
    "FilterVersion": "1.0.179",
    "Filter_Enabled": true,
    "Filter_Human_Label": "Threshold Objects",
    "Filter_Name": "MultiThresholdObjects",
    "SelectedThresholds": [
        {
            "Attribute Array Name": "ImageData",
            "Attribute Matrix Name": "CellData",
            "Comparison Operator": 1,
            "Comparison Value": 50,
            "Data Container Name": "ImageDataContainer"
        }
    ]
},
"2": {
    "ActiveArrayName": "Active",
    "CellFeatureAttributeMatrixName": "CellFeatureData",
```

```
    "FeatureIdsArrayName": "FeatureIds",
    "FilterVersion": "6.4.197",
    "Filter_Enabled": true,
    "Filter_Human_Label": "Segment Features (Scalar)",
    "Filter_Name": "ScalarSegmentFeatures",
    "GoodVoxelsArrayPath": {
        "Attribute Matrix Name": "CellData",
        "Data Array Name": "Mask",
        "Data Container Name": "ImageDataContainer"
    },
    "ScalarArrayPath": {
        "Attribute Matrix Name": "CellData",
        "Data Array Name": "ImageData",
        "Data Container Name": "ImageDataContainer"
    },
    "ScalarTolerance": 0,
    "UseGoodVoxels": 1
},
"3": {
    "FilterVersion": "1.0.179",
    "Filter_Enabled": true,
    "Filter_Human_Label": "Replace Value in Array",
    "Filter_Name": "ReplaceValueInArray",
    "RemoveValue": 0,
    "ReplaceValue": 30000,
    "SelectedArray": {
        "Attribute Matrix Name": "CellData",
        "Data Array Name": "FeatureIds",
        "Data Container Name": "ImageDataContainer"
    }
},
"4": {
    "FeatureIdsArrayPath": {
        "Attribute Matrix Name": "CellData",
        "Data Array Name": "FeatureIds",
        "Data Container Name": "ImageDataContainer"
    },
    "FilterVersion": "6.4.197",
    "Filter_Enabled": true,
    "Filter_Human_Label": "Find Surface Features",
    "Filter_Name": "FindSurfaceFeatures",
    "SurfaceFeaturesArrayPath": {
        "Attribute Matrix Name": "CellFeatureData",
        "Data Array Name": "SurfaceFeatures",
        "Data Container Name": "ImageDataContainer"
```

```
    }
},
"5": {
    "CentroidsArrayPath": {
        "Attribute Matrix Name": "CellFeatureData",
        "Data Array Name": "Centroids",
        "Data Container Name": "ImageDataContainer"
    },
    "FeatureIdsArrayPath": {
        "Attribute Matrix Name": "CellData",
        "Data Array Name": "FeatureIds",
        "Data Container Name": "ImageDataContainer"
    },
    "FilterVersion": "6.4.197",
    "Filter_Enabled": true,
    "Filter_Human_Label": "Find Feature Centroids",
    "Filter_Name": "FindFeatureCentroids"
},
"6": {
    "EquivalentDiametersArrayName": "EquivalentDiameters",
    "FeatureAttributeMatrixName": {
        "Attribute Matrix Name": "CellFeatureData",
        "Data Array Name": "",
        "Data Container Name": "ImageDataContainer"
    },
    "FeatureIdsArrayPath": {
        "Attribute Matrix Name": "CellData",
        "Data Array Name": "FeatureIds",
        "Data Container Name": "ImageDataContainer"
    },
    "FilterVersion": "6.4.197",
    "Filter_Enabled": true,
    "Filter_Human_Label": "Find Feature Sizes",
    "Filter_Name": "FindSizes",
    "NumElementsArrayName": "NumElements",
    "SaveElementSizes": 0,
    "VolumesArrayName": "SizeVolumes"
},
"7": {
    "AspectRatiosArrayName": "AspectRatios",
    "AxisEulerAnglesArrayName": "AxisEulerAngles",
    "AxisLengthsArrayName": "AxisLengths",
    "CellFeatureAttributeMatrixName": {
        "Attribute Matrix Name": "CellFeatureData",
        "Data Array Name": "",
```

```
        "Data Container Name": "ImageDataContainer"
    },
    "CentroidsArrayPath": {
        "Attribute Matrix Name": "CellFeatureData",
        "Data Array Name": "Centroids",
        "Data Container Name": "ImageDataContainer"
    },
    "FeatureIdsArrayPath": {
        "Attribute Matrix Name": "CellData",
        "Data Array Name": "FeatureIds",
        "Data Container Name": "ImageDataContainer"
    },
    "FilterVersion": "6.4.197",
    "Filter_Enabled": true,
    "Filter_Human_Label": "Find Feature Shapes",
    "Filter_Name": "FindShapes",
    "Omega3sArrayName": "Omega3s",
    "VolumesArrayName": "Shape Volumes"
},
"8": {
    "CentroidsArrayPath": {
        "Attribute Matrix Name": "CellFeatureData",
        "Data Array Name": "Centroids",
        "Data Container Name": "ImageDataContainer"
    },
    "EquivalentDiametersArrayPath": {
        "Attribute Matrix Name": "CellFeatureData",
        "Data Array Name": "EquivalentDiameters",
        "Data Container Name": "ImageDataContainer"
    },
    "FeaturePhasesArrayPath": {
        "Attribute Matrix Name": "CellFeatureData",
        "Data Array Name": "NumElements",
        "Data Container Name": "ImageDataContainer"
    },
    "FilterVersion": "6.4.197",
    "Filter_Enabled": false,
    "Filter_Human_Label": "Find Feature Neighborhoods",
    "Filter_Name": "FindNeighborhoods",
    "MultiplesOfAverage": 10,
    "NeighborhoodListArrayName": "NeighborhoodList",
    "NeighborhoodsArrayName": "Neighborhoods"
},
"9": {
    "CellFeatureAttributeMatrixPath": {
```

```
            "Attribute Matrix Name": "CellFeatureData",
            "Data Array Name": "",
            "Data Container Name": "ImageDataContainer"
        },
        "DelimiterChoice": 0,
        "FeatureDataFile": "/home/ender/Desktop/IN718Plus_CT/Exp001/Feat001.csv",
        "FilterVersion": "1.0.179",
        "Filter_Enabled": true,
        "Filter_Human_Label": "Export Feature Data as CSV File",
        "Filter_Name": "FeatureDataCSVWriter",
        "WriteNeighborListData": 0,
        "WriteNumFeaturesLine": 1
    },
    "PipelineBuilder": {
        "Name": "processCTVoidPipeline_06_2016",
        "Number_Filters": 10,
        "Version": 6
    }
}
```

APPENDIX B

Experimental procedures

B.1. Sample preparation for in-situ tensile coupons

(1) Surface Damage Removal
   (a) Apply etch resist (clear nail polish works) to non-gage surfaces of each specimen
   (b) Immerse each specimen (in batch) in Kalling's Etchant for 1 hour to remove 30-40 microns of material
   (c) Remove etch resist (acetone); immerse in removal agent and clean
(2) Speckle Painting
   (a) Build airbrush
      (i) Attach air line to handle and compressor
      (ii) Attach paint jar connector to handle
   (b) Fill paint jar with water
   (c) Attach paint jar to handle
   (d) Spraying the water to clean the brush by pushing down and then backward on the
   (e) Simultaneously adjust the line pressure until a consistent, moderate spray is achieved
   (f) Remove paint jar and empty any remaining water
   (g) Add some alumina particles and fill with ethanol
   (h) Replace paint jar on handle
   (i) Stir the jar and spray briefly to make sure stream is acceptable
   (j) Mask specimens as required (grip ends, mostly)
   (k) Paint with dark, matte/flat spray paint; paint should cover metal, but not drip or run

(l) Quickly after painting stir paint jar and spray alumina particles onto paint (before it dries); obtain a consistent stream from the airbrush then pass the specimen through the stream at about arm's length.

(m) Inspect specimen. A good pattern will not have clumps and will be consistent particle density throughout the gage section.

(n) If a good pattern is seen proceed with steps j-l on the next specimen

(o) If a good pattern is not seen, clean with acetone or ethanol and repeat steps k and l

(p) When complete run a paint jar of ethanol or acetone through the spray nozzle to ensure it is clean. Wipe down everything and disassemble to state it was in when starting.

B.2. Procedures for in-situ testing at 2BM

2BM-B Procedure

Notes:

- Look at tomo_scan_instruction.pdf if anything goes wrong
- Lyra: username: user2bmb, password: *****
- Grayhound: computer in hutch controlling the tomo scans
- Lyra: computer in hutch controlling the camera
- Polaris: right computer at control station
- Usra: left computer at control station
- Tomography: computer in cubicle storing the data
- Handyn: computer in cubicle doing post-processing and reconstruction

B.2.1. Hutch setup:

(1) Acquire load frame (if not at 2-BM)

(2) Connect to 2BM EPICS and check that displacement control is working in both directions and the load cell detects correctly.

(3) Align collets

(a) Loosen bottom screw until slight movement is possible

(b) Raise crosshead until alignment rod can be inserted into open collets

(c) Obtain sufficiently close alignment to insert rod into both collets

(d) Lower crosshead so alignment rod can be fully seated in both collets simultaneously

(e) Move lower grip on alignment rings until until alignment rod moves easily through the collets

(f) Tighten collets

(g) Tighten lower grip alignment rings carefully to maintain position

(h) Loosen collets

(i) Check that alignment rod still slides cleanly between collets

(j) Check coaxiality with laser sheet

(k) Raise crosshead and extract alignment rod

(4) Insert and align collet-to-pin connection adapters

(a) With crosshead raised (from 3(j) it should still be) remove both collets

(b) Insert adapters into collets until the end of the slot is 3-4mm away from large end of collet

(c) Screw large end of collets into holding nuts

(d) Feed one adapter, collet and nut into the top (crosshead) holder

(e) Feed the remaining adapter, collet and nut into the bottom (load cell) holder

(f) Adjust both adapter heights until the end of the slot is 1-2mm from the top of the nut

(g) Roughly align top and bottom slot to lie in plane with the load frame columns

(h) Hand tighten the collet nuts

(i) Lower the crosshead until the adapters nearly touch

(j) Use the end of one of the slightly larger test specimens to finally align the slots; make sure the grip end passes completely through the slots from both directions without resistance. If realignment is needed, loosening the collets slightly might help.

(k) Raise the crosshead to provide working space

(l) Taking care that the alignment is not changed (fully hand tighten first), tighten collets using crossed wrenches to avoid putting torque on load frame (particularly the load cell). Tighten firmly.

(m) If axial alignment slips, return to step 4(j). If slot alignment slips return to step 3(a). Can re-check alignment with laser sheet.

(n) If no noticeable alignment slippage occurs alignment is complete

(5) Affix LF to stage

(a) Align columns to avoid blocking DIC camera and initial view from x-ray

(b) Pasha should have the proper adapter and screws

(c) Ensure ample clearance for control and data cables under rotation

(6) Configure DIC image acquisition system

Camera

(a) Attach mounting ring to optical table stand. Working distance is about 30-45mm.

(b) Unscrew extension tube

(c) Place lens through mounting ring

(d) Re-attach extension tube

(e) Tighten mounting ring so lens does not slide or rotate (do not overtighten)

(f) Remove objective-side lens cover

(g) Remove CF-2 objective from storage box, remove protective cover from back of objective (loosen mounting screws)

(h) Mount CF-2 objective on lens

(i) Mount linear polarizing filter on objective

(j) Remove camera-side lens cover

(k) Attach 49mm to C-mount adapter

(l) Carefully screw camera onto C-mount; careful not to tangle USB cord (if attached)

(m) Only when ready to acquire images, remove objective lens cover

Controller

(n) Connect camera to control computer (if using laptop); connect camera to hutch out line if using EPICS

(o) IF USING LAPTOP: launch Flycapture 2 and start live imaging

(p) IF USING EPICS: Unknown

Lighting

(q) Place lights and turn them on

(r) Cover direct light sources with horizontally aligned polarizing sheet

(s) Align imaging area (might have to be redone or adjusted for each specimen)

(i) Insert alignment grid into adapter slots unless a specimen has already been mounted

(ii) Focus camera

(iii) Zoom out (in flycap) to see the whole picture, if needed

(iv) With camera firmly screwed to lens, marginally loosen lens clamp and rotate until the long axis of the picture is along the specimen (about 90

(v) Retighten lens clamp (without rotating if possible)

(vi) Adjust location (will require re-focusing), height, azimuth, and elevation (in that order) of camera marginally until grid pattern is centered and square. A level may be used to make sure the camera is square.

(t) Rotate polarizing filter on lens until maximum blocking is achieved

(u) Adjust camera aperture and exposure time (in flycap or EPICS controller) until one point is just over-exposed (one pixel is saturated), then shorten exposure slightly (will need to be re-calibrated for each specimen)

.

(7) Configure X-rays
    (a) This should have be done by Xiao and/or Pasha; we should only need to follow procedure the proper procedure to conduct scans (as taught by Xiao and/or Pasha).

B.2.2. Change sample:

Before starting, follow *Hutch set up* procedure.

(1) Ensure that the hutch is set up correctly
(2) Mount specimen
    (a) Record specimen identifier and time in logbook
    (b) Carefully remove specimen from storage container, do not touch speckle painted surface. Use of forceps may help.
    (c) Place bottom of specimen (the side without a silver line, arrows pointing up) in the bottom adapter with speckled side facing camera
    (d) Insert pin into lower grip, slightly moving specimen if necessary to allow passage
    (e) Set pin flush with adapter on both sides
    (f) Slowly lower crosshead until top specimen hole aligns with adapter pin holes
    (g) Insert pin. If it will not go through easily, iterate with step 2(f).
    (h) Set pin flush with adapter on both sides
    (i) Make sure specimen is snug
(3) Align camera and light sources
    (a) Start live image capture (the green triangle in flycap)
    (b) Roughly focus camera on specimen
    (c) Adjust azimuth (slightly) and height of camera (keeping elevation constant using a level) slightly to center gage section of specimen. Try to keep the camera as square with the specimen face as possible.

(d) Adjust lighting if needed (see Procedure 0-6(q-u) for lighting setup), including polarizers. Try to avoid placing light sources close to the specular angle (diffuse lighting is ideal).

(e) Finely adjust camera focus

(f) Adjust camera exposure time following Procedure 0-6(u). " until one point is just over-exposed (one pixel is saturated), then shorten exposure slightly".

(g) Set fixed camera settings (e.g. exposure time, F-stop) to try to ensure consistent light quality

(4) Test DIC speckle pattern

(a) Translate stage by -100 um vertically

(b) Translate stage by +50 um vertically

(c) Translate stage by +50 um vertically

(d) Capture initial image (one frame from live feed), record stage location

(e) Translate stage by +50 um vertically

(f) Capture image, record stage location

(g) Repeat (e) and (f) about 5 more times (total of about six moves, total nominal displacement of 300 um)

(h) Import images into DIC (e.g. VIC, or NCORR and test that linear displacements are correct

(i) If DIC speckle pattern is good, continue

(j) If DIC speckle pattern is bad, repaint speckles following

B.2.3. Set up:

(1) Change the sample after each set (see "Sample change" procedure)

(2) Move "Readback" of loading stage to get the pins through (workspace 1 on Lyra)

(a) Set "Moveabs" to 9900 (um), speed to 100, and press "Go"

(b) Set load frame speed to 1.25

(3) Rotate sample to 89.5 degrees to check the camera (workspace 2 on Lyra)

(4) Wobble, shift, and focus camera until the speckles are sharp

(5) Apply pre-tension with right arrow on "Tweak" until load is 20 N (workspace 1 on Lyra)

(6) Align LAT Tomo-Y (workspace 5 on right computer)

B.2.4. Scan and loading:

(1) Scan tomo (workspace 5 on right computer)
   (a) Open Front End shutter and click Acquire in PCOEdge_User.adl window
   (b) Align 0deg_A and 90deg_A if starting a new sample, or scanning fractured ends (check 88 deg instead of 90 deg since pillar is blocking) using LAT Tomo-Y and 0deg_A
   (c) Important: check the DIC camera to make sure it's still aligned and focused!
   (d) Change sample name (Thinwalllabel-samplenumber) if starting a new sample
   (e) Record the end displacement value from the load frame and add to log book, the logbook should automatically record the LAT Tomo-Y value for the next scan
   (f) Scan -> Click "Do" in caputRecorderExecute.adl window
   (g) Wait for 4.5 minutes, when scan is done, and scanInfo window says "Scan finished!"

(2) Load and DIC (workspace 5 on right computer)
   (a) Rotate sample to 89.5 degrees in Rot (ABRS25) window
   (b) Go back to initial LAT Tomo-Y position
   (c) Check the NoMachine-Lyra camera window, the camera shifts often
   (d) Record Keithley2kDMM_cal.adl "Result" load in starting "Load range" on spreadsheet
   (e) Up arrow and enter in Logging Load window to run load_log_script
   (f) Optional: check folders (workspace 2 on left computer) to see if DIC camera is recording/adding files

(g) Click “Go” in motorx_all.adl window and right arrow on “Tweak” button (about 1000 (um)), but right arrow a few times for continuous loading

(h) When load reaches “Load Goal” on spreadsheet, click “Stop” on motorx_all.adl window

(i) Record Keithley2kDMM_cal.adl “Result” load in ending “Load range” on spreadsheet

(j) Record motorx_all.adl “Readback” in “End Displacement” on spreadsheet

(k) Wait for 2 minutes or until “Result” load stabilizes from creep

(l) Click “Action” in tk window next to Logging Load window, then “yes”, then close window

(m) Ctrl + C in “Logging Load” window

(n) If sample is intact, go to Scan Tomo for stop-stop scans

(o) If sample breaks, go to record “End Displacement” and scan fracture surfaces

(3) Transfer files while camera is scanning (workspace 6 on right computer)

(a) In command prompt window, up arrow and change number, enter

(b) In Firefox Globus window, click on the folders to transfer

(i) Don’t initiate more than one transfer at once to or from a single computer

(ii) Need to go from #grayhound to #tomography to #handyn, transfer from right to left to right endpoints using arrows

(iii) Right endpoint = b67549#grayhound, path /S/data/2017_11/Sarah/Exp00number

(iv) Transfer left to

(v) Left endpoint = petrel#tomography, path //2-BM/2017_11/Sarah

(vi) Once uploaded, transfer right to

(vii) Right endpoint = b67549#handyn, path /run/media/user2bmb/APS4/APS_2BM_2017_11/ (or APS3)

(4) Reconstruction centers while camera is scanning (Workspace 7 on left computer)

(a) Leave upper terminal window open

(b) Run python recon script in lower terminal

B.2.5. Center finding:

(1) Change “exp_inx” to new experiment number

(2) Go to “remote to handyn” terminal session with “bash-4.2$” prompt

(3) Press “up arrow key” and enter to run python script

(4) Go to the “Dolphin” file manager window

(5) Drag the “data_center” folder to Image_J

(6) “Yes” to open the images as a virtual stack

(7) Scroll through to find the image with the least artifacts

(8) Write the number of the best image into the comments section under the correct exp number “center = …”

APPENDIX C

Image-based multiscale code

C.1. Fatigue

C.1.1. Main program

The main program used to set up and run the one-way coupling is listed below. In this case, the SCA solver was implemented by Cheng Yu, and thus is not included here (e.g. the function call to function_SCA_FIP, which actually runs CPSCA and computes the FIP). For two-way coupling (the fracture example), more changes to the solver routines themselves were required; decoupling my work from that of Cheng Yu would be difficult as one is not easily understood without the other, so these routines have not be included here to avoid confusion over who's work is who's. They might be obtained upon reasonable request.

```
function [out]=coupon_fatigue(runNum,strainIn,scrCase,numProc)
%{
Orion Kafka
Northwestern University
Feb. 2019

 Scheme:
 0. Generate macro data
    a. macroscale stress/strain
    b. thermal data
 1. Load strain histories
 2. Run box picker using pre-defined stats, some number of times < N_macroElem
 3. Run offline SCA on boxes
 4. Run online CPSCA on boxes, once for each strain history
 5. Compute results across boxes, e.g. max overall FIP, and report:
    a. Overall results (e.g. min fatigue life across all elements)
    b. Port info back into the macroelements, and give color e.g. color
       contours of life (use vtk for that?)
 Run 2-5 multiple times (3? 5?), then loop on step 0 too for e.g.
  multiple strain amps

History:
02-??-2019 - first version written with placeholders for SCA and boxList
03-??-2019 - v2 introduces unequal mesh capabilities
%}
format long
```

```
strains = [0.1,0.075,0.05,0.06];
strainAmp = strains(strainIn);

% === User input options ===
disp('=== Reading input data...')
specimenPath = fullfile('thermal-mesh-strain-data','E606');
if ~exist(specimenPath)
   mkdir(specimenPath);
end
disp(['Specimen data path is ',specimenPath])

outPath = ['specimen_',num2str(runNum)];
if ~exist(outPath)
   mkdir(outPath);
end
vtuFile = fullfile(outPath,['specimen_SCR_FIP_NINC_',num2str(runNum),'.vtu']);
disp(['VTU file is ',vtuFile])
% Load solidification cooling rate data
scrPath = fullfile(specimenPath,'SCR',['Case',num2str(scrCase),'_ElementSCR.csv
   ↪ ']);
if ~exist('scrData','var')
   scrData = dlmread(scrPath,'\t',2,0);
end
disp(['Using SCR data from ',scrPath])

% Load the strain history data and reformat it
strainPath = fullfile(specimenPath,['odbSmallMeshFatigue_e',num2str(strainAmp),'
   ↪ _t0.1.out']);
if ~exist('strainData','var')
   strainData = csvread(strainPath,5,0);
end
disp(['Using strain data from ',strainPath])

% Load connectivity and nodal coordinates of the (smaller) stress mesh
nodesStr = dlmread(fullfile(specimenPath,'nodesStr.out'),'\t');
ConnStr = dlmread(fullfile(specimenPath,'connectivityStr.out'),'\t');

% Load set of elem numbers (make the file from an inp file)
elems = csvread(fullfile(specimenPath,'setElems.csv'));
elems = sort(reshape(elems,1,[],1));
numElemS = length(unique(elems));
% Load connectivity and nodal coordiantes of the (larger) thermal mesh
nodesT = dlmread(fullfile(specimenPath,'nodesT.out'),'\t');
nodesT = nodesT(:,1:4);
ConnT = dlmread(fullfile(specimenPath,'connectivityT.out'),'\t');
```

```
ConnT = ConnT(:,1:4);

startElem = min(elems);
numTimes = length(nonzeros(strainData(:,1) == startElem));

scrDataOnSElems = zeros(length(elems),2);

% Load volume fraction data
boxFiles_mid = 'midvf';
boxList_mid = fullfile('..','filled',...
    ['boxMat_',boxFiles_mid],'boxList_Matlab.csv');
boxData_mid = csvread(boxList_mid,0,0);

boxFiles_high = 'highvf';
boxList_high = fullfile('..','filled',...
    ['boxMat_',boxFiles_high],'boxList_Matlab.csv');
boxData_high = csvread(boxList_high,0,0);

boxFiles_low = 'lowvf';
boxList_low = fullfile('..','filled',...
    ['boxMat_',boxFiles_low],'boxList_Matlab.csv');
boxData_low = csvread(boxList_low,0,0);

% Time increment
dt = 0.1;

% === End user input options ===

disp(' ...completed reading data ===')
disp('=== Comparing meshes and sorting scr...')
% Build the SCR data on each of the elements of interest in the small mesh
pool_1 = parpool(numProc);

% Build the SCR data on each of the elements of interest in the small mesh
parfor ii = 1:numElemS
    %disp(['Processing elem: ',num2str(ii)])
    nodesElem = ConnStr(ConnStr(:,1) == elems(ii),2:end-1);

    % direction (2=x, 3=y, 4=z)-> |
    % sum direction -> | |
    x_top = max(nodesStr(logical(sum(nodesStr(:,1) == nodesElem,2)),2));
    x_bot = min(nodesStr(logical(sum(nodesStr(:,1) == nodesElem,2)),2));
    y_top = max(nodesStr(logical(sum(nodesStr(:,1) == nodesElem,2)),3));
    y_bot = min(nodesStr(logical(sum(nodesStr(:,1) == nodesElem,2)),3));
    z_top = max(nodesStr(logical(sum(nodesStr(:,1) == nodesElem,2)),4));
```

```
    z_bot = min(nodesStr(logical(sum(nodesStr(:,1) == nodesElem,2)),4));

    nodesTX_top = nodesT(nodesT(:,2) < x_top,1);
    nodesTX_bot = nodesT(nodesT(:,2) >= x_bot,1);
    nodesTY_top = nodesT(nodesT(:,3) < y_top,1);
    nodesTY_bot = nodesT(nodesT(:,3) >= y_bot,1);
    nodesTZ_top = nodesT(nodesT(:,4) < z_top,1);
    nodesTZ_bot = nodesT(nodesT(:,4) >= z_bot,1);

    nodesTX = intersect(nodesTX_top, nodesTX_bot);
    nodesTY = intersect(nodesTY_top, nodesTY_bot);
    nodesTZ = intersect(nodesTZ_top, nodesTZ_bot);

    inter_1 = intersect(nodesTX, nodesTY);
    TNodesInElemS = intersect(inter_1,nodesTZ);

    % Use ConnT to find elemID of elemsT in TNodesInElemS; average SCR of
    % those elements


    [~,ai] = intersect(ConnT(:,2:end-1),TNodesInElemS);

    TElemInSElem = ConnT(ai);
    %{
    count = 1;
    runningSum = 0;
    for jj = 1:length(ConnT)
        if length(intersect(ConnT(jj,2:end),TNodesInElemS)) == 8
            runningSum = runningSum + scrData(scrData(:,1) == ConnT(jj,1),2);
            %TElemInSElem(count) = ConnT(jj,1);
            count = count+1;
        end
    end
    %}

    elemS_SCR = 0;
    for jj = 1:length(TElemInSElem)
        elemS_SCR = elemS_SCR + scrData(scrData(:,1) == TElemInSElem(jj),2);
    end

    scrDataOnSElems(ii,:) = [elems(ii),elemS_SCR/jj];
    %disp(['Completed elem: ',num2str(ii)])
end
clear nodesElem;
```

```
disp(' ...completed sorting SCR...')
% Just look at the connectivities of the gauge section (or whatever is defined
% in the set loaded in elemSet.csv).
nodesElem = zeros(max(elems),size(ConnStr,2));
for ii = 1:numElemS
   nodesElem(elems(ii),:) = ConnStr(ConnStr(:,1) == elems(ii),:);
end
nE1 = zeros(numElemS,size(nodesElem,2));
for ii = 2:9
   nE1(:,ii) = nonzeros(nodesElem(:,ii));
end

Conn = nE1(:,2:end-1)-1;

CoordNew = zeros(max(nodesElem(:,1)),3);
for ii = 1:(size(Conn,1)*size(Conn,2))
   CoordNew(Conn(ii)+1,:) = nodesStr(nodesStr(:,1) == Conn(ii)+1,2:end-1);
end

% Make sure scr and strain are all sorted the same way Conn is (by elem number)
scrSorted = zeros(max(elems),2);
strainHist = zeros(numElemS,1+numTimes*6);
strainHist(:,1) = elems;
strainHistSorted = zeros(max(elems),1+numTimes*6);
startIdx = find(strainData(:,1) == elems(1));
startIdx = startIdx(1);
for ii = 1:numElemS
   % Get SRC data sorted
   scrSorted(elems(ii),:) = [elems(ii),scrDataOnSElems(scrDataOnSElems(:,1)==
      ↪ elems(ii),2)];

   % Collect strain history data
   % For small(ish) meshes, find is OK but sort of slow. For big
   % meshes, use some knowledge of the mesh structure to do direct
   % indexing.
   % Use ConnStr array, because the spacing is based on the number of
   % elements in the *extracted* data, not the number in the sub-region
   % defined by the set.
   startStrIdx = (startIdx+ii-1):max(size(ConnStr)):(max(size(ConnStr))*numTimes-
      ↪ startIdx+ii-1);
   %strains1 = strainData(strainData(:,1)==elems(ii),:);

   %startStrIdx = find(strainData(:,1) == elems(ii));
   strainsAtElemIdx = strainData(startStrIdx,2:end);
   for jj = 1:size(strainsAtElemIdx,1)
```

```
        strainHist(ii,2+((jj-1)*6):(jj)*6+1) = strainsAtElemIdx(jj,:);
    end
    % Sort strain history
    strainHistSorted(elems(ii),:) = strainHist(strainHist(:,1)==elems(ii),:);
end

% Re-fill the SCR and strain arrays, but this time we're sure they are
% sorted the same; avoid using "nonzeros" for this, because some really
% results might be zero
scrCompact = zeros(numElemS,2);
strainHist = zeros(numElemS,1+(numTimes)*6);
for ii = 1:numElemS
    scrCompact(ii,:) = scrSorted(elems(ii),:);
    strainHist(ii,:) = strainHistSorted(elems(ii),:);
end

Conn = Conn';
Coord = CoordNew';

disp(' ... completed preparing strain hist and scr ===')
disp('=== Starting SCA runs...')

% Determine the microstructure to use
vf_from_scr = [scrCompact(:,2),0.0047 * exp(-0.0011 * -scrCompact(:,2))];

elemFIP = zeros(size(strainHist,1),3);
strainHistPar = parallel.pool.Constant(strainHist);
vf_from_scrPar = parallel.pool.Constant(vf_from_scr);
scrCompactPar = parallel.pool.Constant(scrCompact);
boxData_midPar = parallel.pool.Constant(boxData_mid);
dt = parallel.pool.Constant(dt);
elemsPar = parallel.pool.Constant(elems);
runNumPar = parallel.pool.Constant(runNum);

rng('shuffle');

% Set up list of random numbers
for ii = 1:numElemS
    boxFilesIn = boxFiles_mid;
    boxDataIn = boxData_mid;
    % Find candidate boxes from boxpicker and select one at random that
    % matches the vf criteria
    clear microBoxID

    try
```

```
        micro = find((boxDataIn(:,6) > 0.8*vf_from_scr(ii,2)) &...
            (boxDataIn(:,6) < 1.2*vf_from_scr(ii,2))); % within +/-20%
        numMicro = length(micro);
% Avoid box 3 atm, because it seems to cause ALL failures... currently
    ↪ investigating
% while 1
            pickMicro = randi(numMicro,1);
            microBoxID = micro(pickMicro);
% if microBoxID ~= 3
% break;
% end
% end
        microBoxID = [1,microBoxID];
    catch
        disp('Warning: V_f not found... using backup data')
        if max(size(micro)) <=1 % vf_from_scr(ii,1) >= max(boxData_mid(:,5))
            boxFilesIn = boxFiles_high;
            boxDataIn = boxData_high;
            numMicro = 5;
            microBoxID = randi(numMicro,1);
            microBoxID = [2,microBoxID];
        elseif vf_from_scr(ii,1) <= min(boxDataIn(:,5))
            boxFilesIn = boxFiles_low;
            boxDataIn = boxData_low;
            numMicro = 5;
            microBoxID = randi(numMicro,1);
            microBoxID = [3,microBoxID];
        else
            numMicro = size(boxDataIn,1);
            micro = 1:numMicro;
            microBoxID = randi(numMicro,1); % pick a box a random
            microBoxID = [1,microBoxID];
        end
    end

    disp(['SCR = ',num2str(scrCompact(ii,2)),' --- ',...
          'Vf from SCR = ',num2str(vf_from_scr(ii,2)),' --- ',...
          'Picking boxID = ',num2str(microBoxID(2)),...
          ' from ',num2str(length(micro)),' options --- ',...
          'Boxs Vf = ',num2str(boxDataIn(microBoxID(2),6))])
   boxNum{ii} = microBoxID;
end

clear microBoxID
% Start loop over elements in stress mesh, running "online" for each element
```

```
parfor ii = 1:numElemS
    %microBoxID = randi(3,1); % use either box 1 or box 2
    microBox = boxNum{ii};
    if microBox(1) == 1
        boxFilesIn = boxFiles_mid;
    elseif microBox(1) == 2
        boxFilesIn = boxFiles_high;
    elseif microBox(1) == 3
        boxFilesIn = boxFiles_low;
    end
    microBoxID = microBox(2);
    Dhist = zeros(numTimes*9,1);
    % Farm the online job out to the SCA code (which might take a while,
    % although it just runs the online part)
    % and get the max elemental volume averaged FIP back.
    Shist = strainHistPar.Value(ii,2:end);
    %display(Shist);
    %Shist = zeros(1,12);
    %Shist(1,7) = 1.e-3;
    for i = 1:length(Shist(:))/6
        strain = Shist(6*(i-1)+1:6*i);
        dfg = [strain,strain(4:6)];
        dfg(1:3) = dfg(1:3) + 1.;
        Dhist(9*(i-1)+1:9*i) = dfg;
    end
    [nfip_max,nf] = function_SCA_FIP(...
                    boxFilesIn,...
                    microBoxID,...
                    Dhist,...
                    dt.Value,ii,runNumPar.Value); % Call SCA code
    elemFIP(ii,:) = [elemsPar.Value(ii),nfip_max,nf];
    disp(['Completed element (elemID) = ',num2str(ii),...
            ' (',num2str(elemsPar.Value(ii)),')']);
end
disp(' ...completed SCA ===')
disp('=== Saving data...')
save(fullfile(outPath,['elem_fip_run',num2str(runNum)]),'elemFIP');

% Save everything, in case we need to come back to this for
% data output later (e.g. the run crashed during ouput)
save(fullfile(outPath,['full_workspace_run',num2str(runNum)]),...
     '-v7.3','-nocompression');


disp(['Max fip = ',num2str(max(elemFIP(:,2)))])
```

```
disp(['Min Nf = ',num2str(min(elemFIP(:,3)))])

CellDataName{1} = 'SCR';
CellDataType{1,1} = 'Float64';
CellDataType{1,2} = 8;
CellDataType{1,3} = 'double';
NComC(1) = 1;

CellDataName{2} = 'nfip_max';
CellDataType{2,1} = 'Float64';
CellDataType{2,2} = 8;
CellDataType{2,3} = 'double';
NComC(2) = 1;

CellDataName{3} = 'N_inc';
CellDataType{3,1} = 'Float64';
CellDataType{3,2} = 8;
CellDataType{3,3} = 'double';
NComC(3) = 1;

CellDataName{4} = 'strains';
CellDataType{4,1} = 'Float64';
CellDataType{4,2} = 8;
CellDataType{4,3} = 'double';
NComC(4) = 6;

NodeDataName = [];
NodeDataType{1,1} = '';
NodeDataType{1,2} = '';
NodeDataType{1,3} = '';
%NodeDataArray = cell(1,1);
NodeDataArray{1} = [];
NComN(1) = 1;

CellDataArray = cell(4,1);
CellDataArray{1} = scrCompact(:,2)';
CellDataArray{2} = elemFIP(:,2);
CellDataArray{3} = elemFIP(:,3);
CellDataArray{4} = strainHist(:,end-5:end)';

offsets = 8*(1:numElemS);
types = 12*ones(numElemS,1);

WriteVTU_XML_Binary([vtuFile,'.vtu'],Coord,Conn,...
    CellDataName,CellDataType,NComC,CellDataArray,...
```

```
    NodeDataName,NodeDataType,NComN,NodeDataArray,...
    offsets,types);
disp(' ...data saved. All steps completed. ===')
end
```